THE UNIVERSITY *of* EDINBURGH

The University *of* Edinburgh
School of Chemistry

Bacterial protein complexes studied by single-molecule imaging and single-cell micromanipulation techniques in microfluidic devices

PhD Thesis

by Marcel Reuter

Edinburgh, 1 December 2009

Declaration

This thesis and the results presented within it are my own work, unless otherwise stated. Many ideas were discussed with my supervisor Dr David Dryden, my collaborators and numerous other people interested in single-molecule science.

Marcel Reuter, 1 December 2009

Acknowledgements

I would like to thank my supervisor Dr David Dryden for giving me the opportunity to work in his research group on very exciting projects, for his support, encouragement and interesting discussions.

I wish to acknowledge all members of Dr Dryden's research group for their kind support, experimental assistance and for maintaining a very friendly working environment. In particular, I want to thank Dr John White who I enjoyed sharing a lab with for numerous discussions of scientific and non-scientific matters, his continuous support and positive feedback on my work.

In COSMIC (Collaborative Optical Spectroscopy and Micromanipulation & Imaging Centre), I wish to thank Drs Jochen Arlt, Gerard Giraud and Cristina Flors for their technical and scientific support with optics matters.

Many collaborators have given me advice on my projects. I would like to especially thank Dr Garry Blakely (School of Biology) for his continuous help with all microbiology issues I had to deal with over the years, his friendly attitude and for a very productive collaboration on the AddAB enzyme.

I thank Prof Ian Booth, Dr Samantha Miller and Nicolas Hayward (University of Aberdeen, School of Medical Sciences) for giving me a valuable one-week training and many interesting discussions on hypo-osmotic shock in bacteria.

I would like to thank my collaborators within the Marie-Curie Research-Training-Network "From FLIM to FLIN" Marcel van 't Hoff and Dr Martin Oheim (Université René Descartes Paris V) for hosting me twice and giving me very valuable insights into TIRF microscopy and image analysis.

I also wish to thank the EU network "From FLIM to FLIN" for funding my PhD, enabling scientific exchange across European borders and all of its members for nice network meetings and very interesting and stimulating scientific discussions.

Last, but by no means least, I want to thank my partner Christine and my family for their continuous support, their understanding for my work and many long phone calls.

Contents

Abbreviations

Reagents

APS	ammonium persulfate
ATP	adenosine triphosphate
BSA	bovine serum albumin
Cm	chloramphenicol
DEAE	diethylaminoethyl
DMSO	dimethylsulfoxide
DTT	dithiothreitol
EDTA	ethylene diamine tetra-acetate
IPTG	isopropyl-β-D-thiogalactopyranosid
Kan	kanamycin
LB	lysogeny broth or Luria-Bertani
NADH	nicotinamide adenine dinucleotide
SDS	sodium dodecyl sulfate
TAE	Tris-acetate EDTA buffer
TEMED	tetramethylethylene diamine
YOYO-1	Quinolinium 1,1'-[1,3-propanediylbis[(dimethyliminio)-3,1-propanediyl]]bis[4-[(3-methyl-2(3H)-benzoxazolylidene)methyl]]tetraiodide

General terms

AAA^+	ATPases Associated with various cellular Activities
BP	band-pass (filter)
chi	crossover hotspot instigation
cps	counted photons
DM	dichoic mirror
DNA	deoxyribonucleic acid
ssDNA	single-stranded deoxyribonucleic acid
dsDNA	double-stranded deoxyribonucleic acid

DSB	double-stranded DNA break
EM-CCD	electron-multiplying charge-coupled device
Fl	fluorescence
GFP	green-fluorescent protein
LP	long-pass (filter)
HR	homologous recombination
LUT	look-up-table
MS^1	mechanosensitive
NA or N.A.	numerical aperture
ND	neutral density (filter)
NIR	near-infrared
NTP	nucleoside triphosphate
OD	optical density
PhC	phase-contrast
ROS	reactive oxygen species
SM	single-molecule
SF	superfamily
SNR	signal-to-noise ratio
TM	transmembrane
TEM^1	transverse electromagnetic
tRNA	transfer ribonucleic acid
UV/VIS	ultraviolet/visible

Techniques

AFM	Atomic Force Microscopy
DIC	Differential Interference Contrast
EM	Electron Microscopy
FCS	Fluorescence Correlation Spectroscopy
FRET	Fluorescence Resonance Energy Transfer
FLIM	Fluorescence Lifetime Imaging Microscopy
Laser	Light Amplification by Stimulated Emission of Radiation
MALDI-TOF	Matrix Assisted Laser Desorption Ionisation-Time of flight
MS^2	Mass Spectrometry
NMR	Nuclear Magnetic Resonance
PALM	Photoactivated Localisation Microscopy
SDS-PAGE	SDS Polyacrylamide Gel Electrophoresis
STED	Stimulated Emission Depletion
SVD	Singular Value Decomposition

TEM^2	Transmission Electron Microscopy
TIRFM	Total Internal Reflection Fluorescence Microscopy
TPM	Tethered Particle Motion

Genes

add	ATP-dependent DNase
msc	mechanosensitive channel
rec	recombination
rex	recombination exonuclease

Proteins

BfAddAB	*Bacteroides fragilis* AddAB protein
BsAddAB	*Bacillus subtilis* AddAB protein
MscL	MS channel (protein) for large conductance
MscS	MS channel (protein) for small conductance
RecBCD	heterotrimeric recombination enzyme in *E. coli*
SSB	ssDNA binding protein

(Bio)chemical structures

L-Ala	L-alanine
D-Ala	D-alanine
D-Glu	D-glutamine
m-DPA	*meso*-diamino pimelic acid
NAG	N-acetylglucosamine
NAM	N-acetylmuramic acid

Physical sizes and units

bp	base pairs
$d_{lateral}$	diffraction limit
d	decay length
D	diffusion constant
η	dynamic viscosity
$F_{friction}$	friction force
h	Planck's constant
I	intensity
k_B	Boltzmann constant
l	length

L	distance or length
L_P	polymer persistence length
λ	light wavelength
M	molar mass
n	refractive index
nS	nano-Siemens
p	momentum
Π	osmotic pressure
r	(hydrodynamic) radius of a molecule or sphere
R	gas constant
Re	Reynolds number
ρ	density
t	time
T	absolute temperature
Θ_{max}	half maximum opening angle of an objective lens
Θ_{crit}	critical angle
v	velocity or speed
z	distance from an interface

Miscellaneous

NEB	New England Biolabs
PDB	Protein Data Bank
r.t.	room temperature

Abstract

Biological systems of bacteria were investigated at the single-cell and single-molecule level. Additionally, aspects of the techniques employed were studied. A unifying theme in each project is the reliance on optical imaging techniques coupled to microfluidic devices.

Hypo-osmotic shock experiments with an *Escherichia coli* mechanosensitive channel deletion mutant were carried out at the single-cell level. *E. coli* MJF465 cells in which the three major mechanosensitive channel genes are deleted ($\Delta mscL$, $\Delta mscS$, $\Delta mscK$) show only 10% cell viability upon hypo-osmotic shock (from LB + 0.5 M NaCl into distilled water), compared to 90% viability of the wild-type strain. Bacterial cells were trapped with optical tweezers in microfluidic devices, enabling the first direct observation of single-cell behaviour upon hypo-osmotic shock. Phase-contrast microscopy revealed intra-population diversity in the cells response: Different features of lysis included cells bursting rapidly and leakage of ribosomes, DNA and protein from the cytoplasm. Fluorescence microscopy of hypo-osmotically-shocked GFP-expressing MJF465 cells showed either bursting of cells, which was a rare event, or fast leakage of GFP, indicating cell membrane ruptures. Data were analysed in terms of their kinetic behaviour and showed that lysis occurs on a timescale of milliseconds to seconds. The implications of these findings for the bacterial cell wall and cell membranes are discussed.

Enzymes involved in homologous recombination and repair of double-stranded DNA (dsDNA) breaks are essential for maintaining genomic integrity in both eukaryotes and prokaryotes. RecBCD of *E. coli* and AddAB, found widely in bacteria, are involved in these processes, carrying out the same function. Both enzymes were studied kinetically with single-molecule total internal reflection fluorescence microscopy (TIRFM). Surface-tethered, hydrodynamically stretched lambda-DNA molecules, stained with YOYO-1, were imaged with TIRFM in a microfluidic flowcell. The RecBCD enzyme is a well characterised DNA helicase and was introduced to this system for method validation purposes. The AddAB enzyme of *Bacteroides fragilis* was then characterised as a helicase acting

on lambda-DNA. It was found that AddAB helicase unwinds dsDNA with high processivity of on average 14,000 bp and up to 40,000 bp for individual enzyme complexes at an ATP-dependent rate ranging from 50-250 bp s^{-1} (for Mg^{2+}-ATP concentrations larger or equal than 0.1 mM). This activity was detected by DNA binding dye (YOYO-1) displacement from the dsDNA and studied for different Mg^{2+}-ATP concentrations, flow (shear) rates and different YOYO-1 staining ratios of DNA.

Aspects of this last experimental setup were investigated. A kinetic analysis of intercalation of YOYO-1 into lambda-DNA is presented, occurring on a timescale of minutes. Different flow rates and staining ratios that influence the apparent (stretched) DNA molecule length were also examined.

Several image analysis techniques were employed to enhance the data quality in images showing stretched lambda-DNA molecules. The Singular Value Decomposition was found to be the most effective technique which strongly reduces the noise in the obtained kymograph images.

Chapter 1

Introduction

Microorganisms count among the most adaptable forms of life on earth with hardly any niche left unexplored as a living habitat by bacteria (Postgate, 1994). Principally, they are divided into archaeal and eubacteria. Archaea have adapted themselves to very harsh environmental conditions, for example acidic, high-salt and high-temperature environments. Eubacteria generally live in environments that are less extreme in terms of physical and chemical conditions, but equally versatile, e.g. soil, water and vertebrates. Microorganisms are the object of intense study because of their relevance as human pathogens and in biotechnological applications, for example the food industry.

The entity of a bacterial cell comprises the chromosome (or nucleoid), at least one membrane, the cell wall and flagella attached to it (Neidhardt *et al.*, 1996). The latter two structures are not essential to the bacterial cell, however they are found in most species. Figure 1.1 shows a sketch of a wild-type *Escherichia coli* cell and its entities.

1.1 Bacterial stress conditions and their regulation

Bacterial growth and division requires the concerted action of many proteins and protein complexes performing biochemical reactions to regulate and maintain pathways within a living cell. The most important enzymatic functions control the cell wall biosynthesis, DNA transcription, ribosomal protein synthesis and DNA replication. Hence, these mechanisms are a primary target for antibiotics. The citric acid cycle and glycolytic pathway are responsible for the generation of chemical energy in form of the molecular currencies adenosine and guanosine triphosphate (ATP and GTP). The reduced species of nicotinamide adenine dinucleotide, NADH, is a third very important cofactor used in all living cells to

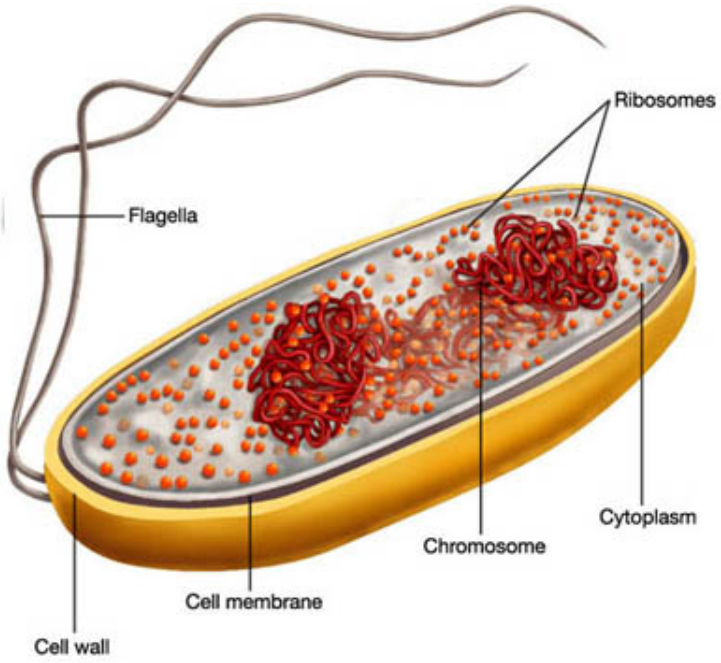

Figure 1.1: Sketch of an *E. coli* cell by R. T. Dame showing relevant cell structures. (Source Molecular Genetics Website, Leiden Institute of Chemistry)

carry out redox reactions under physiologiocal conditions.

As bacteria inhabit changing environments and biological niches that challenge and act against them, they experience constant physical and chemical threats which may kill them. However, these "masters of life" have evolved numerous survival strategies that allow at least part of the bacterial population an escape route from death (Schumann, 2006). Changes in the surrounding temperature are alleviated by heat shock and cold shock proteins which either degrade or refold impaired proteins. The cold shock response also involves the synthesis and integration of unsaturated lipids into the membranes to keep them in a fluid state which is a prerequisite for all molecular processes. The osmotic shock response regulates water and ion flow across bacterial cell membranes during an osmolarity change in the environment. Reactive oxygen species (ROS) occur as a result of bacterial respiration during aerobic growth or as a directed immune response from a host organism. ROS include singlet oxygen, peroxide and hydroxyl radicals which alter DNA, membrane lipids and proteins in a way that negatively affects cellular pathways and eventually destroys bacterial cells. The oxidative stress response, hence, initiates the expression of genes whose products remove ROS, repair damaged DNA, proteins and lipids and maintain the reducing conditions in bacterial cells. Many bacteria are also highly adaptive to pH changes in

their habitat and manage to grow under acidic and alkaline (stress) conditions. Upon moderate pH changes, cells are able to keep a constant internal H_3O^+ concentration and maintain growth while upon extreme changes fasting is induced which prevents cell death but stops growth.

Depletion of nutrients or specific amino acids also results in a stress response. The stringent response is induced when bacterial cells are starved for an amino acid which, in *E. coli*, results in cessation of rRNA and tRNA synthesis. This saves the cell precious metabolic energy during such periods. Starvation stress is akin to the stringent response and a product of nutrient limitation. It is regulated by the alternative sigma factor σ^S which is also produced during shifts to high osmolarity, to high and low temperature and to pH < 7.

Bacterial individuality greatly contributes to bacterial survival under harsh environmental and stress conditions.

1.1.1 Individuality in bacteria

Bacterial populations display individuality which, at the single-cell level, can be measured as phenotypic diversity. This phenotypic diversity of isogenic populations can be created by a variety of mechanisms (Davidson & Surette, 2008):

- bistability
- persistence
- variation in chemotactic response
- phase and antigenic variation
- and aging effects.

The two classic examples for bacterial individuality are bistability and persistence. Persistence refers to the fact that in every bacterial population a subpopulation exists that survives antibiotic treatment, as first found in staphylococcal infections (Bigger, 1944). This surviving population displayed exactly the same behaviour upon repeated cultivation and subsequent challenging with antibiotic agents. First speculations which were later proven assumed that the resistant sub-population is in a dormant state. As antibiotics target mechanisms relevant for active cell growth, e.g. cell wall biosynthesis, DNA transcription, protein translation and DNA replication, the hypothesis of a dormant state seems plausible. Using a microfluidics approach Balaban *et al.* (2004) recently proved this hypothesis to be true.

Bistability was found in bifurcating gene expression levels when the inducer was kept at subsaturating concentrations. This was found to be a result of noise and stochasticity of chemical reactions in DNA transcription and protein translation. The bacterial culture eventually splits in two populations, one in which protein induction is fully induced and another one where it is fully uninduced (Novick & Weiner, 1957).

The first direct observation of single-cell individuality was the swimming behaviour of *E. coli* (Spudich & Koshland, 1976) when exposed to new concentration levels of attractant. The adaptation time after which individual cells resumed a steady-state tumble frequency and the steady-state tumble frequency itself were found to vary within the population.

Bacterial pathogens frequently experience rapidly changing environments, e.g. elevated levels of reactive oxygen species (ROS) produced by their host cells as a result of the immune response. Phase and antigenic variation helps the bacteria to evade these attacks which usually results in bacterial cell surface changes, e.g. variation in lipopolysaccharide and lipoprotein content and number of flagella and pili. Bacteria have evolved different mechanisms to switch protein expression between two distinct states (Lederberg & Iino, 1956).

All microorganisms show aging effects which lead to individuality. This is particularly true for asymmetric bacteria with distinguishable cell ends. *E. coli* cells are symmetric with two poles of the same kind. During cell division, one pole is newly formed whereas the other one is inherited from the parental cell. In *E. coli*, old-pole inheriting cells are smaller and grow and divide more slowly which was suggested to originate from damaged lipids in the cell membranes which impede cellular mechanisms, e.g. old poles were shown to prevent incorporation of newly synthesised lipids and membrane proteins (Nystrom, 2007; Stewart, 2005).

Common approaches to reveal single-cell behaviour and to uncover individuality in bacterial populations use microscopy techniques, theoretical considerations and computer simulations which predict the behaviour of a bacterial population or a specific pathway in response to a stimulus (Locke & Elowitz, 2009).

1.1.2 Bacterial protein complexes

Processes in living cells are controlled by proteins, the whole collection of which is referred to as the proteome. The proteome is highly regulated by itself, environmental conditions and its genetic blueprint, DNA. Likewise, proteins interact with DNA in numerous ways.

Proteins are polymeric condensates of 20 naturally occurring amino acids.

These polypeptide chains fold locally into typical secondary structure motifs, i.e. the α-helix and the β-sheet. Proteins fold further into complex, but well-defined tertiary structures which are predetermined by the amino acid sequence. Individual protein subunits can then interact with each other to form aggregates, also referred to as quaternary structure. Proteins adopt all kinds of shapes, e.g. globular (sphere-like), rod-like and filamentous. Based on their shape, polarity and charge distribution, proteins can interact with other components of the living cell, e.g. some can bind negatively charged DNA and others integrate into hydrophobic lipid membranes.

Many proteins carry out enzymatic functions, thus catalysing specific biochemical reactions. Indeed, proteins are amazing catalysts in the sense that most of the reactions take place at room temperature and atmospheric pressures. The range of biochemical reactions spans metabolic activity, *de novo* synthesis of molecular precursors, DNA transcription, protein synthesis, folding, degradation, control of water and ion flux through cell membranes as well as movement and transport along cellular templates, like DNA, actin and tubulin. Many of these proteins require cofactors to fulfil their enzymatic function, e.g. ATP for energy consumption, NAD(P)H for chemical reductions and S-adenosyl-methionine for DNA and protein methylation.

1.2 Single-molecule experiments

1.2.1 Behaviour of single-molecules

Many bulk experiments give only access to the average value of an observable, thereby hiding the underlying distributions of physical parameters. One major aim of single-molecule studies is to extract this distribution by looking at single entities, in many cases one by one, and their interaction pathways which are obscured by the ensemble.

Single-molecule behaviour originates from several basic aspects of chemical and physical interactions:

- Individual events in large, often heterogeneous ensembles can take different biochemically and physiologically relevant paths than the rest of the bulk. The basis for these can be e.g. various stable conformations.

- Processes at the single-molecule level are stochastic, discrete and occur randomly.

- The lack of synchronisation in most bulk experiments obscures the individual time trajectories and interaction pathways.

Hence, looking at single-molecule behaviour gives unique insights into any biochemical system.

1.2.2 Techniques and approaches

In order to achieve single-molecule resolution, the system of observation needs to be magnified which directly implies that microscopy techniques are most suitable. In addition, a sufficient dilution of the observed species is required.

Electron microscopy (EM), that can reach magnifications of up to 2 million times, is capable of resolving single atoms and counts as one of the first single-molecule techniques. The main disadvantage of this technique is that it requires a specific stain (e.g. using gold or graphite) or a frozen sample which fixes and kills all biological materials. This aspect precludes the observation of any dynamic process and limits the technique to purely static interaction.

Atomic force microscopy (AFM) uses a nanometre-sized tip, also called a cantilever, to scan across a sample. It can reach resolutions of up to one nanometre on static samples and clearly breaks the diffraction limit encountered in optical microscopy. Disadvantages of AFM are the sample interference with the tip, which is particularly seen with soft samples, and long search and acquisition times. Atomic force microscopes that work at video rate have been constructed but are not yet widely available (Crampton *et al.*, 2007).

Although classically limited by diffraction most single-molecule experiments rely on optical microscopy, the main reason being that biological samples are least affected in terms of preparation and actual (technique) manipulation. Most approaches use single-molecule fluorescence. While sample staining with a fluorescent probe is required, this approach is very sensitive because the measured effect of generated light at a certain wavelength is much more pronounced than the absorbance of a miniscule amount of an intense light source. An impressive number of individual techniques has become available in recent years and are briefly summarised and explained below.

- Optical tweezers which serve as a means of particle trapping are described in detail in section 1.3.2. In a standard single-molecule assay, a micron-sized bead is optically trapped while a second one is usually held with a micropipette. Onto these two beads, DNA, RNA and protein molecules can be tethered using molecular linkers. By varying the bead-to-bead distance

and measuring the bead deflections, force-extension curves can be taken which are characteristic for ssDNA, dsDNA and polypeptide chains. The latter traces are specifically dependent on the polypeptide secondary structure. Specific interactions with proteins and enzymes will alter these force-extension curves and, hence, give insight into underlying molecular interactions (Bockelmann, 2004; Mangeol *et al.*, 2006; Hormeno & Arias-Gonzalez, 2006). Magnetic tweezers are similar to optical tweezers. However, this technique uses small magnetic particles that are trapped in a magnetic field gradient (see e.g. Seidel *et al.*, 2005).

- Tethered particle motion (TPM) uses bright-field video microscopy to monitor the Brownian motion of a microsphere which is connected to a coverslip surface via a DNA molecule (Schafer *et al.*, 1991; Blumberg *et al.*, 2005; van den Broek *et al.*, 2006). A fitting procedure determines the centroid position of the microsphere. The mean-square-displacement of bead fluctuations has to be averaged for about 50 subsequent image frames and is directly related to the DNA tether length. Upon DNA-protein looping interactions for example, the effective DNA length (radius of gyration) becomes shorter which results in a decrease of the bead's Brownian motion. The TPM method can thus be used to characterise enzyme-mediated DNA loop formation times and DNA loop lifetimes.

- Confocal microscopy is widely used as an imaging technique. Using two micrometre-sized pinholes, it advances standard epi-fluorescence microscopy by suppressing light that comes from regions that are out-of-focus. The sample needs to be scanned in all three dimensions in order to produce a complete 3D image.

  Fluorescence correlation spectroscopy (FCS) is based on confocal microscopy and works at high sample dilutions to achieve conditions under which only one molecule at a time diffuses through the volume of observation (Haustein & Schwille, 2003; Haustein & Schwille, 2007). This results in discrete fluorescence bursts which can be autocorrelated. The obtained autocorrelation function has a characteristic decay which gives access to the diffusion behaviour of the single-molecules. This is dependent on molecule size and the embedding matrix, e.g. a cell membrane, and specific interactions with other molecules.

- It was mentioned that classical optics encountered a limit in resolution of about 200 nm which is a result of the diffractive nature of light. This limit

served for a paradigm for more than a century and has now been overcome using single-molecule fluorescence techniques. The underlying principle employs a point-spread-function fitting procedure (Cheezum *et al.*, 2001; Thompson *et al.*, 2002) to determine the localisation of a single-molecule with high precision of up to 1.5 nm (Yildiz *et al.*, 2003). Several techniques that use this concept have emerged in recent years, e.g. Photoactivated Localisation Microscopy (PALM) and Stimulated Emission Depletion (STED) (Hell, 2007). In PALM, all fluorescent molecules of a sample are first bleached and, upon photoreactivation with a second laser, fluorescent single-molecules reappear and are fitted with the PSF. Combining all determined single-molecule positions yields an image with very high resolution. STED (Hell, 2003) employs two different laser beams with different TEM (transverse electromagnetic) modes. A focussed laser with the TEM_{00} (Gaussian) mode excites all the fluorophores in a diffraction-limited spot. The second laser with the TEM_{10} (Donut) mode is superimposed on the first one and depletes all excited fluorophore molecules in the edge region, thereby leaving a central area, now smaller than the diffraction limit, with excited molecules. Scanning across the sample yields an image with enhanced resolution.

- Fluorescence Resonance Energy Transfer (FRET) is a radiationless energy transfer from a selectively excited donor molecule to an acceptor molecule in the ground state that takes place when several parameters are met: The donor emission and acceptor excitation spectrum must overlap, the two molecules have to be in close proximity ($\leq$ 8-10 nm) and the two transition dipole moments must have a non-vanishing scalar product. This technique is particularly suited to study the interaction between two molecular species as acceptor fluorescence is only observed upon direct donor excitation. It has proven particularly useful for studying conformational dynamics of DNA, RNA and proteins and intermolecular intercations of these biopolymers with each other (Wozniak *et al.*, 2008). In combination with Fluorescence Lifetime Imaging Microscopy (FLIM) FRET studies become very powerful as the fluorescence lifetime is a very sensitive parameter, characterised by a decrease in donor lifetime and a rising acceptor lifetime when FRET takes place (Liu *et al.*, 2007). In addition, the fluorescence lifetime is independent of protein concentration and less affected by variations in laser intensity, the photon-detection efficiency and spectral cross-talk.

- TIRF is a method that selectively excites fluorophores near a dipolar interface, usually a glass-buffer interface. Using this confinement single-molecule

detection becomes possible. Deeper insight into this technique is given in section 1.3.3.

In recent years a variety of biophysical mechanisms have been elucidated by the application of single-molecule techniques. A wealth of information has been gained on the action and mechanisms of molecular motor proteins. In particular, SM techniques enable the direct observation of motor step sizes, enzyme rates, processivities, pauses, backtracking and looping interactions on their respective template molecules. A few typical examples may illustrate this: Optical tweezers studies revealed the transcriptional pausing and arrest by individual *E. coli* RNA polymerase molecules (Davenport *et al.*, 2000); Myosin V was shown to translocate along actin using a "hand-over-hand" mechanism, rather than an inchworm mechanism (Yildiz *et al.*, 2003); the translocation, termination and reinitiation of the Type I Restriction/Modification enzyme EcoR124I was studied in detail using magnetic tweezers (Seidel *et al.*, 2005); the tension dependence of the disassembly of the Rad51 protein from nucleoprotein filaments revealed the burst-wise unbinding of patches of the Rad51 protein from the DNA (van Mameren *et al.*, 2009). A current challenge that remains is to carry out SM experiments in living cells (Xie *et al.*, 2008). An unfortunate disadvantage *in vivo* is that the used scaffold molecules, e.g. DNA, RNA or actin, cannot be stretched and concomitantly visualised. Because of cellular movement the high precision of SM localisation is strongly reduced.

1.2.3 DNA molecules as a scaffold for single-molecule helicase experiments

Figure 1.2 illustrates various SM approaches to probe the action of RecBCD (Dillingham & Kowalczykowski, 2008) which is one of the best studied helicases to date. Lambda-DNA molecules can be tethered to an optically trapped microbead. Using a hydrodynamic flow, YOYO-1-stained DNA molecules can be stretched out and directly visualised by fluorescence microscopy (fig. 1.2A). The enzyme (depicted as blue triangle) binds to a dsDNA end and its action is triggered by the cofactor Mg^{2+}-ATP. Subsequent DNA unwinding can be monitored via the continuous length decrease of DNA (Bianco *et al.*, 2001). Some translocases are sensitive to the YOYO-1 dye. However, they can be tagged to a fluorescent nanoparticle whose migration indicates the enzymatic action (Spies *et al.*, 2003) (fig. 1.2B). Helicase enzymes can be also tethered to a glass surface and act upon dsDNA which is stretched out between the surface-bound enzyme and an optically trapped bead linked to its second molecule end (fig. 1.2D). The

molecular force which is continuously exerted on the bead by the DNA is measured and a feedback mechanism coupled to stage movement ensures a constant force during enzymatic translocation upon the DNA. This assay gives insight into force-dependent DNA translocation and is able to detect the enzyme motion with nanometre precision (Perkins *et al.*, 2004). TPM is another elegant way to observe the continuous translocation of a surface-bound RecBCD enzyme acting upon two-site tethered plasmid dsDNA (Dohoney & Gelles, 2001) (fig. 1.2C). The amplitude of the bead fluctuations resulting from Brownian motion steadily decreases and thereby reveals enzyme translocation. This latter approach is easily scaled up by monitoring a whole microscope field of view where many individual complexes can be analysed simultaneously.

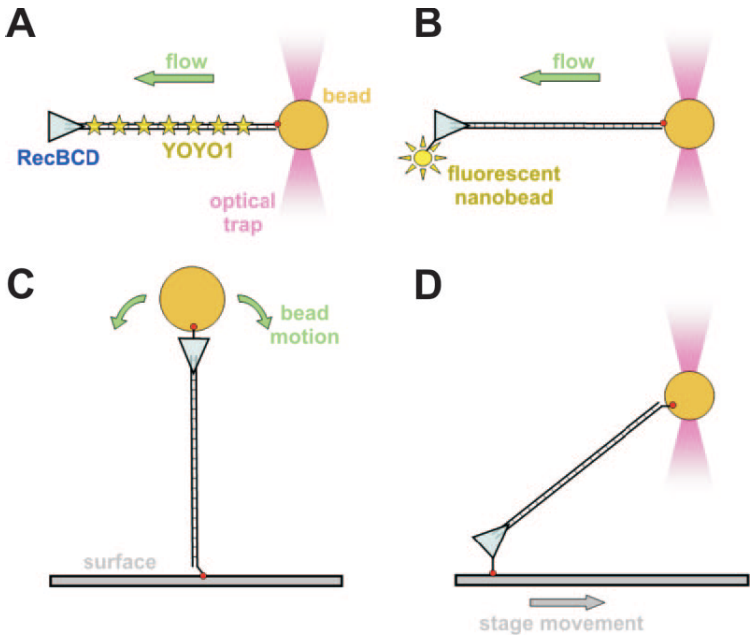

Figure 1.2: Single-molecule assays to probe the action of helicases (taken from Dillingham & Kowalczykowski (2008)).

In an effort to combine the advantages of both TPM which has a high throughput and optical tweezers based assays which offer a direct way of translocation visualisation, the research group of Eric Greene has developed a TIRFM assay which monitors many surface-tethered, fluorescently labelled lambda-DNA molecules simultaneously (Graneli *et al.*, 2006; Visnapuu *et al.*, 2008). The DNA molecules can be randomly distributed on the glass surface, but also be arranged in parallel arrays using lithographic techniques in combination with fluid lipid bilayers.

1.3 Optical Microscopy

The classical optical microscope consists of an illumination source, a condenser, a specimen holder, an objective and an eyepiece. In bright-field microscopy the condenser is needed for a constant illumination of the specimen (Köhler illumination) and consists of a simple lens. Nowadays objectives comprise a sophisticated lens system reaching magnification factors between 5 and 100 and also account for different optical aberrations, e.g. chromatic aberration. Furthermore, both the condenser and objective can be combined with plates that enable contrast enhancement of images, such as phase-contrast and differential interference contrast. The eyepiece further magnifies the image that is directly viewed by the eye.

Ernst Abbe introduced the term numerical aperture NA which is defined as

$$NA = n_0 sin\Theta_{max} \tag{1.1}$$

with n_0 and Θ_{max} denoting the refractive index of the immersion medium and half the maximum opening angle of the first objective lense, respectively. The diffraction limit $d_{lateral}$ in the specimen plane is then given by

$$d_{lateral} = \frac{0.61\lambda}{NA} \tag{1.2}$$

with λ denoting the light wavelength (Hecht, 1992).

1.3.1 Epi-fluorescence microscopy

Epi-fluorescence microscopy (figure 1.3) makes use of strong light sources emitting in the UV-VIS region, e.g. mercury arc and xenon lamps or lasers, to excite a fluorescent sample. Typically, fluorophores excited at a certain light wavelength emit light that is spectrally shifted towards longer wavelengths (also called Stokes shift). Filter cubes contain two filters and one dichroic mirror which are characterised by wavelength dependent light reflection or transmission. This principle is used to separate excitation and emission light. The excitation light which is reflected on the dichroic mirror passes through the objective and excites the sample. The fluorescent light of a longer wavelength is scattered more or less equally in all directions and, therefore, also back through the objective. The dichroic mirror transmits the emission light which is passed through a suitable emission filter and then collected with a CCD camera or observed through the eyepiece (Hecht, 1992).

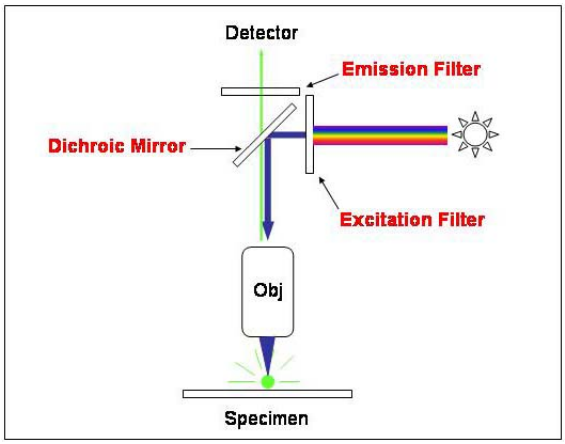

Figure 1.3: Principle of epi-fluorescence microscopy (explained in the text).

1.3.2 Optical tweezers

Trapping principle

Optical tweezers make use of strongly focussed, high-intensity laser light to trap particles of a higher refractive index than their surrounding medium either in solution or in the gas phase (Ashkin *et al.*, 1986). According to a quantum mechanical phenomenon, photons carry a momentum or impulse p based on the de Broglie relation

$$p = h/\lambda \tag{1.3}$$

where h denotes Planck's constant (Winter & Noll, 1998).

For theoretical considerations of the trapping effect two cases need to be distinguished: When the radius r of a trapped particle is much smaller than λ the Rayleigh scattering model applies, whilst when $r \gg \lambda$ the ray optics regime applies (Neuman & Block, 2004). Only the latter case is discussed since *E. coli* cells, which are larger than the used laser light wavelength, were exclusively used for optical trapping.

Two counter-acting forces arise when photons interact with matter: The scattering force is due to scattered and absorbed light which pushes a particle away from the light source because the direction of the photon's momentum is either changed in space or the momentum is taken up. The second force is the gradient force (fig. 1.4) which occurs when a light beam is refracted through a particle and changes its direction. Due to Newton's second law stating that every force provokes a force of equal amount pointing in the other direction the bead is pushed

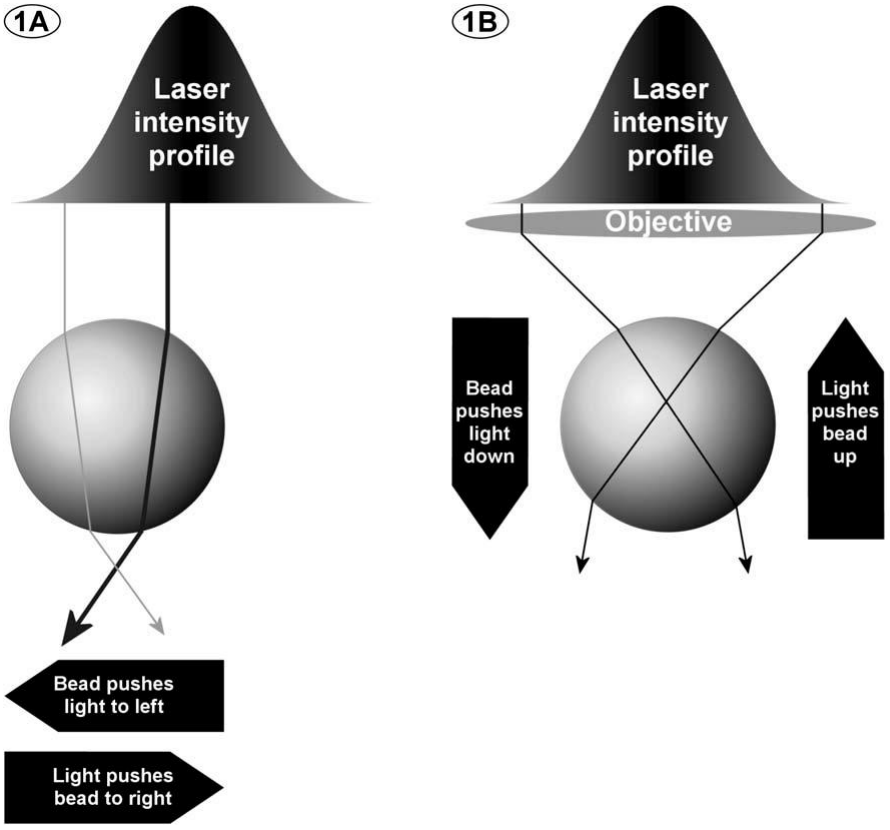

Figure 1.4: Sketch illustrating the gradient force exerted on a spherical object with higher refractive index than the surrounding medium (taken from Wright *et al.*, 2007).

into the direction of highest intensity until it reaches the equilibrium position which is in the focus of the optical trap. In order to stably trap a particle the gradient force must exceed the scattering force which is only achieved when the light intensity gradient is very steep. This is realised by using objectives with high numerical aperture ($NA > 1.2$).

The procedure of force calibration in an optical trap is sophisticated and was extensively described and analysed by Berg-Sorensen and Flyvbjerg (2004) who calibrated the power spectrum of a sphere in a laser trap. A much easier method is to use a sphere with radius r which is trapped in a flowcell with a well-defined flow speed v. The trap stiffness κ, defined as $\kappa = \Delta x/\Delta F$ can be obtained by measuring the bead's displacement Δx while obtaining the friction force $F_{friction}$ $= \Delta F$ from the Stokes equation

$$F_{friction} = 6\pi\eta r v. \tag{1.4}$$

η is the viscosity of the buffer medium.

1.3.3 Total Internal Reflection Fluorescence Microscopy (TIRFM)

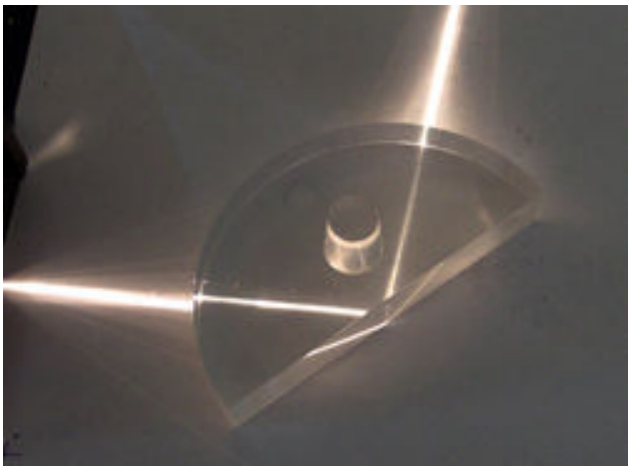

Figure 1.5: Total internal reflection in a prism

When a light beam hits a phase boundary between two media, it is normally both reflected on the surface and refracted through the second medium. Depending on the optical properties of both media, described by their refractive indices n_i and n_r, the angles of the incoming light beam Θ_i and of the refracted light beam Θ_r (with respect to the optical axis which stands perpendicular on the interface plane) follow a ratio which is termed after its discoverer Snell's law (Hecht, 1992)

$$\frac{sin\Theta_i}{sin\Theta_r} = \frac{n_r}{n_i}. \tag{1.5}$$

In the special case of medium i being an optically dense medium, such as glass or water, and medium r being air (n_r around 1), this law simplifies to

$$\frac{sin\Theta_i}{sin\Theta_r} = \frac{1}{n_i}. \tag{1.6}$$

When the angle of the incident light beam is increased, one reaches a stage where the angle of the refracted light becomes 90°. This special angle (of the incident light) is termed the critical angle Θ_{crit} because for all values bigger than Θ_{crit} the optical phenomenon of total reflection occurs (see fig. 1.5) with

$$sin\Theta_{crit} = \frac{1}{n_i}. \tag{1.7}$$

which means that all incident light is reflected. However, a so-called evanescent wave is able to penetrate into the optically thinner medium r which is described within the framework of the Maxwell equations. The evanescent-field intensity

$I(z)$ decays exponentially with increasing distance z from the interface according to

$$I(z) = I(0)exp(-\frac{z}{d}). \tag{1.8}$$

The decay length d is a characteristic measure

$$d = \frac{\lambda_0}{2\pi\sqrt{n_i^2 sin^2\Theta_i - n_r^2}} \tag{1.9}$$

and is dependent on the refractive indices n_i and n_r, the angle of light incidence Θ_i and the light wavelength λ_0 (de Fornel, 2001). Depending on the actual physical parameters the decay length can vary between 10s and 100s of nanometres.

	prism-TIRF	objective-TIRF
Establishment of TIRF	Using a quartz prism.	Using an expensive high NA objective (NA $\geq$ 1.49).
Sample requirements	Thin microfluidics, usually home-made (see e.g. Brewer & Bianco (2008)) or thin capillaries (from VitroCom via Composite Metal Services, Ltd., Ilkley).	Any microfluidic device is suitable provided one side has coverslip properties.
Sample manipulation	Limited to flow and buffer control via polypropylene tubing.	Good sample access, not limited to manipulation via flow, useful e.g. for patch-clamp manipulation.
Alignment	Very complicated due to many degrees of freedom: The TIRF excitation spot needs to match exactly the camera field of view through the objective.	Relatively simple, the beam is steered via displacement along the optical axis of the objective.
S/N ratio and contrast	Usually better because of complete separation of excitation and fluorescence collection path.	Excitation light contamination may occur if optical filters are not perfect.

Table 1.1: Comparison of prism- over objective-TIRF applied to imaging in microfluidic devices.

This effect is used in TIRFM to selectively excite fluorophores near the surface which is one approach to single-molecule imaging both *in vivo* and *in vitro* because

it strongly constrains the excitation volume (Axelrod, 2001 a,b; Axelrod, 2003). Practically, there are two ways to establish TIRFM, either using an objective with a high numerical aperture or a quartz prism. Table 1.1 compares the two different approaches with each other and discusses their advantages and disadvantages for use with microfluidic devices.

1.4 Microfluidics

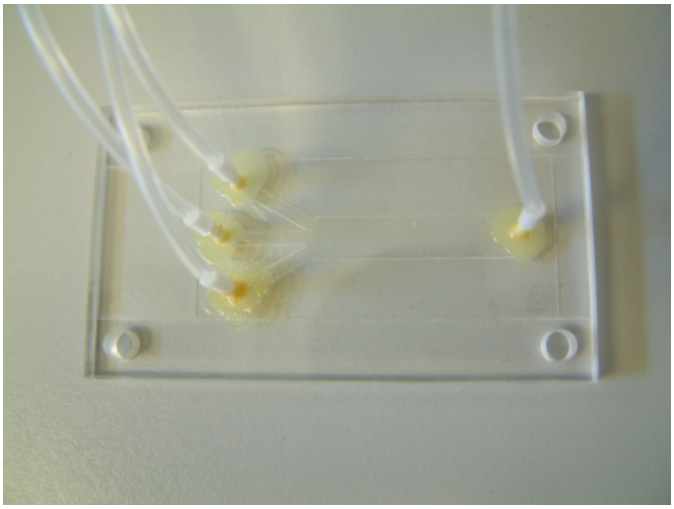

Figure 1.6: Flowcell with three inlet channels used for trapping and buffer manipulation of bacteria.

Both the optical tweezers and the single-molecule fluorescence experiments, described in this thesis, were carried out in microfluidic devices. These home-made devices with multiple inlet channels allow both sample manipulation by means of optical trapping and buffer flow and concomitant imaging of single-molecules or single cells in small buffer volumes (microlitre scale). This approach saves precious material and enables rapid exchange of buffer media to trigger reactions (Brewer & Bianco, 2008).

The fluid flow in typical multi-inlet channel microfluidics (fig. 1.6) is laminar and its profile is parabolic. The inner dimensions of the device shown are 6 mm (width) and 70 ± 10 μm (height). Typical flow rates of a water-based buffer (with a density ρ of 1 g cm^{-3} and η of 1 cP) are 50 μm s^{-1}. The Reynolds number Re

$$Re = \frac{v \cdot l \cdot \rho}{\eta} \tag{1.10}$$

which serves as a criterion for flow change from laminar to turbulent flow is

much lower than 1 for these parameters. Only at $Re > 2{,}000$ does the flow become turbulent. Interchannel mixing occurs, however, when colloidal particles or bacterial cells (which can physically considered to be of the same nature) undergoing Brownian motion are used in the flow buffer. Otherwise, mixing between different streams is governed by transverse diffusion. The mean-square displacement $\langle x^2 \rangle$ of a diffusing species in one dimension can be calculated according to

$$\langle x^2 \rangle = 2Dt \tag{1.11}$$

where D and t are the diffusion constant and time, respectively. Using the Stokes-Einstein equation

$$D = \frac{k_B T}{6\pi\eta r} \tag{1.12}$$

and considering that the travelled molecule distance L from a flowcell junction is related to flow velocity and time via $L = tv$, this leads to

$$\langle x^2 \rangle = \frac{k_B T L}{3\pi\eta r v} \tag{1.13}$$

for the mean-square displacement. Assuming the same conditions as before, i.e. a water-based buffer at room temperature, the same flow rate and a distance L of 100 μm, one obtains average transverse diffusion distances of 53 μm for molecules with hydrodynamic radii r of 0.3 nm. Hence, transverse diffusion leads to smeared flow boundaries in microfluidic devices. This is an important aspect for multi-inlet channel flowcells, because shifting optically trapped objects from one medium into another can take a few seconds while the objects of interest feel a changing gradient in condition, rather than a sudden and abrupt change.

1.5 Motivation

Bacteria experience permanent physical and chemical threats from their environment against which they have evolved an arsenal of defense and protection strategies. Two of these many strategies have been studied in detail within the context of this thesis.

Bacteria sustain a very high outwardly directed turgor pressure that maintains cell shape and growth. This pressure is well-balanced by solutes present in the cell cytoplasm and the medium of suspension. During a change in environment this pressure can, however, rapidly and dramatically rise in fractions of a second. This may for example happen when soil bacteria experience rain fall after a long

drought period leading to hypo-osmotic shock. To escape cell death by lysis, bacteria have evolved pressure safety valves known as mechanosensitive (MS) channels which can open and close within a few milliseconds to release cell solutes. This counteracts the sudden pressure difference and ensures cell survival.

DNA contains all the genetic information needed to ensure proper functioning of an organism. Hence, during cell division DNA replication has to take place with extremely high fidelity to avoid loss of this information. A common threat in each living cell is the occurrence of double-stranded DNA breaks (DSBs) or single-stranded DNA (ssDNA) lesions which arise through the action of reactive-oxygen species (ROS), UV light or chemicals. ROS are for example produced by the respiratory pathway or as an immune response of host cells against a bacterial pathogen. Enzymes responsible for DNA recombination and repair have been shown to be crucial for processing DSBs and ssDNA lesions (Dillingham & Kowalczykowski, 2008) and to maintain cell viability and pathogenicity (Cano *et al.*, 2002; Amundsen *et al.*, 2008). The RecBCD enzyme from *E. coli* (Smith, 2001; Dillingham & Kowalczykowski, 2008) has set the paradigm for homologous recombination in bacteria. However, very recently it was shown that the functionally analogous protein AddAB is much more prominent in the bacterial world (Cromie, 2009). To examine whether these structurally different enzymes behave similarly, the *Bacteroides fragilis* AddAB protein was studied.

To probe both bacterial protein complexes, AddAB and the MS channels, single-molecule experiments and single-cell manipulation was carried out. Individual AddAB molecules unwinding large strands of dsDNA were observed with TIRF microscopy. The relevance of the MS channel complexes was assayed by subjecting single, optically trapped *E. coli* cells which either possess or lack three types of their MS channels to a strong hypo-osmotic shock. Both techniques explore the power of looking at single entities: Individuality in bacteria has been appreciated almost since the discovery and use of antibiotics (Bigger, 1944; Davidson & Surette, 2008). Looking at individual bacteria has provided much deeper insight into population dynamics and, in particular, bacterial defense mechanisms. The basis of this dynamism is in part purely molecular and, indeed, analogous phenomena are discovered at the level of single molecules. Rather than observing an ensemble average, single-molecule observations give access to individual interaction trajectories and are, thus, able to reveal distributions of physical parameters which may uncover different underlying mechanisms.

Over the past 10 years, single-cell manipulations and single-molecule imaging experiments have made their procession into many laboratories and are actively being used by a wide research community (Joo *et al.*, 2008; Bustamante,

2008). Both techniques in this thesis are based on optical laser microscopy and have proven particularly powerful in combination with microfluidics (Brewer & Bianco, 2008). This combined approach allows the use of minimal amounts of bacterial cell cultures, buffers and protein samples which saves both costs and time consumption of otherwise expensive experiments. Hence, relying on such equipment is an ideal and straight-forward way to probe the relevance of MS channel complexes *in vivo* and to study HR enzymes at the single-molecule level.

While exploiting the power of single-cell and single-molecule approaches towards the application of biophysical questions there is a permanent quest for technical development, hence improving scientific instruments, data analysis to withdraw a maximum amount of information from results obtained and method validation. Two relevant questions that occurred during the course of the single-molecule study of the *Bacteroides fragilis* AddAB enzyme were pursued within the frame of this thesis. The lambda-DNA scaffold is affected by the intercalation dye YOYO-1 iodide. Both static and kinetic DNA parameters influenced by this stain were characterised. In addition, image analysis techniques were applied to refine the extraction of quantitative information from these experiments.

1.6 Organisation of this thesis

This first chapter has provided insight into the biological background of microorganisms and the threats they constantly face. It has introduced concepts of single-molecule imaging and outlined current state-of-the-art techniques. The reader was also familiarised with optical microscopy techniques used within this thesis, concepts of optics and microfluidics.

Chapter 2 addresses the fate of single *E. coli* cells when they experience a hypo-osmotic shock. It explains the structure, functioning and gating mechanism of different mechanosensitive channel proteins and introduces different models for the cell wall structure that are currently under debate. Optical tweezers combined with microfluidics revealed the diverse cellular response to hypo-osmotic shock which is discussed in the light of the cell wall and membrane structure.

In chapter 3 single surface-tethered, hydrodynamically stretched lambda-DNA molecules were used as a scaffold for probing interactions of highly processive and fast enzymes. This scaffold was first evaluated with detailed studies on apparent DNA molecule length under varied shear rate and intercalation dye concentrations. In addition, the effect of rapid YOYO-1 dye intercalation into dsDNA was analysed. The experiment was then used to examine the *Bacteroides*

fragilis AddAB protein and the well-studied RecBCD enzyme. Bulk biochemical experiments complemented the single-molecule studies.

The fourth chapter addresses image analysis questions on stretched lambda-DNA molecules imaged with a parabolic-reflector TIRF setup. Different image analysis approaches are introduced and applied to improve the resolution of single-DNA molecules. It further analyses whether one can determine the length of individual stretched DNA molecules with high(er) accuracy for improved enzyme detection.

The fifth chapter concludes and summarises the presented findings.

The chapters 2-4 are self-contained and have independent introductory sections with more detailed background, materials and methods, as well as results and discussion sections. Supplementary material containing video files and MatLab programmes is provided on a CD and documented in appendices A-C.

Chapter 2

The relevance of bacterial mechanosensitive channel proteins during hypo-osmotic shock

This project was carried out in collaboration with the School of Medical Sciences at the University of Aberdeen. People involved were Prof Ian Booth, Dr Samantha Miller and Mr Nicolas Hayward. I received a one-week training at the School of Medical Sciences to learn certain microbiological techniques in more detail. In case data are presented that were generated together with the PhD student Mr Nicolas Hayward, this is clearly stated.

2.1 Mechanosensitive channel proteins

Bacteria have four major classes of ion channels embedded in their (inner) membrane: Ligand-gated , shaker-like, chloride and mechanosensitive channels (MS) (Booth *et al.*, 2003). The first three classes show ionic selectivity, whereas MS channels are nonspecific and have no ligand binding site. Four MS channel proteins are known in *E. coli* which are MscL, MscS, MscK and MscM, each being characterised by a well-defined conductance, open dwell time and pressure sensitivity (Edwards *et al.*, 2004; Booth *et al.*, 2007). These channel proteins are essential for bacterial cells in order to exchange nutrients and to account for osmolarity changes (either hyper- or hypo-osmotic) in their environment. The four channel proteins MscL, MscS, MscK and MscM have a characteristic conductance of 3 (L = large) , 0.3 - 2 (S = small), 1 (K = potassium) and 0.1 - 0.2 nS (M = mini), respectively; MscK is a potassium dependent channel. The electrical conductance measures how easily dissolved ions flow through the MS channels.

Hence, MscM is opened by low pressures, MscS by moderate pressures and MscL activity is triggered at a membrane tension which is close to what would cause membrane disruption. MscK was found to have similar conductance as MscS (Li *et al.*, 2002). The gating mechanism is triggered by specific chemical, physical or electrical signals leading to ion movements at the rate of free diffusion (10^7 ions s^{-1}). Solutes smaller than 400-500 Da are able to pass open MS channels. This includes disaccharides, amino and organic acids, polyamines and aminosugars (Schleyer *et al.*, 1993; Li *et al.*, 2002). The patch-clamp method was the first technique used to identify the different MS channels and also enabled the characterisation of the electrophysiological behaviour in giant protoplasts (liposome based technique) under different pressures and membrane potentials (Martinac *et al.*, 1987; Sukharev *et al.*, 1994). The technique uses a micron-sized glass electrode tip which is tightly connected to a patch of a (cell) membrane to monitor the flow of ions through single ion channels. Based on that, MS channel genes could be identified and were related to a certain electrophysiological response. The relevance of these channels for bacterial life was then shown using *E. coli* deletion mutants. A bacterial strain (MJF465) which lacks the three MS channel proteins MscL, MscS and MscK is largely unviable when subjected to a hypo-osmotic downshock (Levina *et al.*, 1999). The missing MS channels are activated in a wild-type cell below the critical pressure difference that would cause the cells to lyse. Following a hypo-osmotic shock from LB medium + 0.5 M NaCl into LB only 10% of the mutant cells in this culture were still identifiable under the microscope. Cell plating and counting assays have established a survival rate in this range.

2.1.1 Structural insights

The crystal structures (fig. 2.1) have been solved for the MscL (from *Mycobacterium tuberculosis*) and MscS (from *E. coli*) channel revealing a homopentameric and homoheptameric structure, respectively (Chang *et al.*, 1998; Bass *et al.*, 2002). Both MS channel structures adopted closed conformations; MscS (Bass *et al.*, 2002) was initially assumed to be in an apparently open state which was later corrected by Anishkin & Sukharev (2004) who could show by modelling that the channel is actually in a closed conformation. Continued efforts have yielded the structure of an open form of a mutant (A106V) MscS channel (Wang *et al.*, 2008) which *in vivo* protects against hypo-osmotic shock and gates at slightly larger pressures than the wild-type protein. Also, the channel structure of an expanded intermediate of the carboxy-terminal truncated mutant (Δ95-120) of

the MscL protein from *Staphylococcus aureus* (Liu *et al.*, 2009) could be solved. Interestingly, this channel exists as a tetramer. The MscL and MscS families were reviewed for different bacterial organisms (Pivetti *et al.*, 2003).

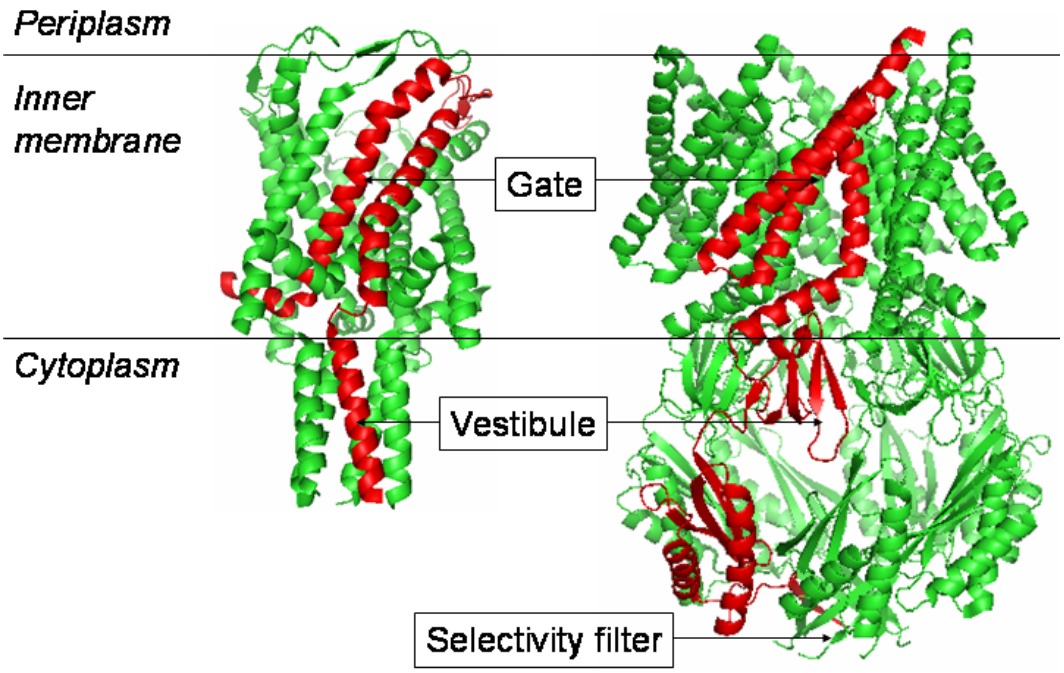

Figure 2.1: Structures of the MscL channel from *Mycobacterium tuberculosis* (left) and the MscS channel from *Escherichia coli* (right) (PDB files 2OAR and 2VV5, respectively). Single monomer subunits in each channel are highlighted in red. Each channel has a transmembrane region and a cytoplasmic region (indicated in the sketch). Each MscL and MscS subunit is characterised by two and three transmembrane helices, respectively, embedded in the inner cell membrane. In the complete channel these TM helices form the MS channel gate. Each of the MS complexes has a vestibule residing in the cytoplasm. MscS is additionally equipped with a selectivity filter.

In *E. coli*, MscS, whose subunit contains 286 amino acid residues, is a much more complex channel aggregate than MscL with 136 residues (Miller *et al.*, 2003). A characteristic feature of these protein aggregates is that each individual subunit is equipped with transmembrane (TM) spans (2 for MscL and 3 for MscS). Upon pore opening, major changes in the subunit orientation including a strong displacement of the transmembrane helices occurs (Liu *et al.*, 2009; Wang *et al.*, 2008; Edwards *et al.*, 2004; Miller *et al.*, 2003). Sketching the channel

structure between the cytoplasm and the periplasm (fig. 2.1) it can be seen that each channel is composed of a gate, a vestibule and, in the case of MscS, a selectivity filter which has dipole moments oriented in such a way that anions are preferentially gated (Edwards *et al.*, 2004). In the closed state, both the MscL and MscS pore are narrow and the latter uses a so-called vapour-lock mechanism to prevent the passing of water or ions.

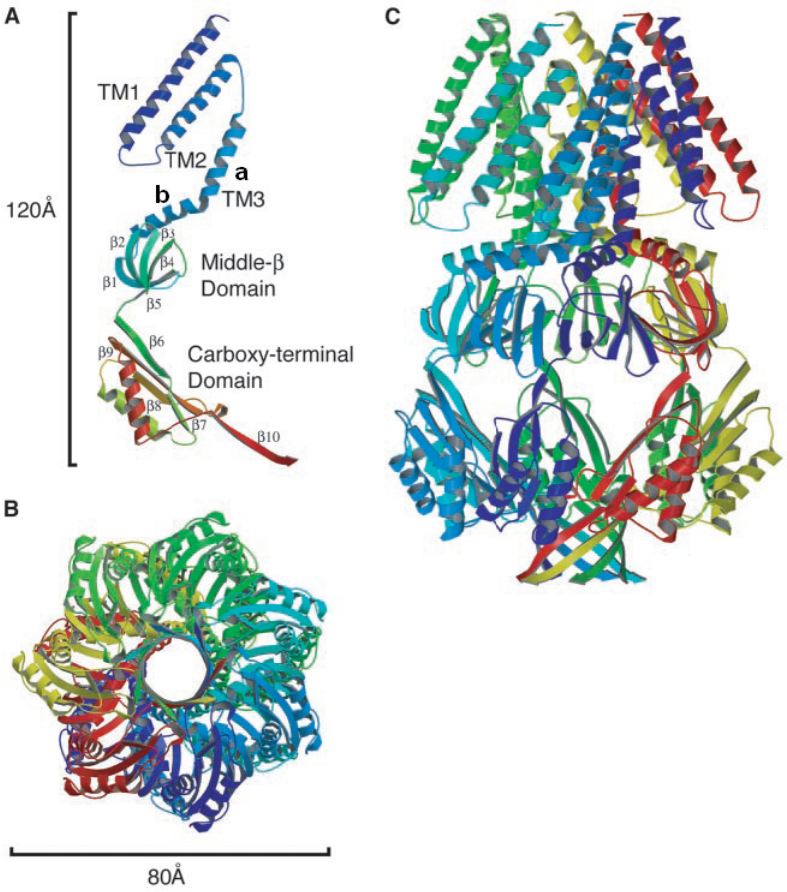

Figure 2.2: Closed structure of the MscS channel (taken from Bass *et al.*, 2002). The ribbon diagram is shown for a single protein subunit (A) shown perpendicular to the seven-fold axis which itself coincides with the lipid membrane normal. The amino-terminus (blue) is located in the periplasm and the carboxy-terminus (red) is located in the cytoplasm. The transmembrane helices located in the membrane are labelled (TM1, TM2 and TM3). The middle-β domain and the carboxy-terminal domain reside in the cytoplasm.
One homoheptamer forming the complete channel is shown as seen from the top (looking from the periplasm and along the seven-fold axis) (B) and from the side (C). The colour-code in B and C is changed to a different colour for each individual subunit.

The MscS channel pore essentially behaves like a carbon-nanotube (Wang *et al.*, 2008) due to the exposure of hydrophobic amino acid residues (fig. 2.3). During channel opening the TM helices are moved away from the central axis of the pore, thus allowing wetting and ion conduction through the opened pore.

The MscS channel (figs. 2.2 and 2.3) is described in more detail (Bass *et al.*, 2002; Wang *et al.*, 2008). Each of the seven subunits has three transmembrane helices: TM1 and TM2 make close contact to the lipid membrane with membrane-embedded arginine residues being probable sensors for tension and voltage changes. Leucine residues at positions 105 and 109 are positioned in the pore lumen to form the vapour-lock of the closed state. The TM3 helices line the pore and form a right-handed bundle. A conserved pattern of glycine and alanine residues in the TM3b helix (also known as "knobs" and "holes") play a crucial role during gating. The cytoplasmic part of the channel comprises the middle-β and the carboxy-terminal domain which form a large chamber that resembles a molecular filter which explains the preference for anions (Edwards *et al.*, 2004). The membrane and cytoplasmic domain have a length of 50 and 70 Å, respectively, and are both 80 Å wide. In the closed form the TM helices are tilted with respect to the membrane normal by 27 to 35°. Different effects can trigger MscS channel gating. Osmotic pressure differences lead to tension within the lipid bilayer, i.e. perpendicular to the membrane normal. Depolarisation which is a result of voltage change across the lipid bilayer results in a force which is parallel to the membrane normal and directed out of the cell. Both the tension and voltage sensitivities are coupled while TM1 and TM2 mediate both forces (Martiniac, *et al.*, 1987; Cui, *et al.*, 1995). During channel gating TM1 and TM2 rotate around 45° and tilt by 15° acting as a lever for TM3a which pivots around the Cα atom of G113 to move out from the centre and align parallel to the seven-fold axis (fig. 2.3). TM3b remains unchanged in position. The concerted movement of the TM helices is often compared to a camera iris which opens and closes. This movement is accompanied by a displacement of L105 and L109 out of the pore centre which breaks the vapour-lock and gives rise to a pore diameter of 13 Å amenable to ion flux.

2.1.2 Beyond structural insights

Although the crystal structures have allowed fundamental insights into MS channel function and behaviour, one important classic limitation is that they did not shed light on dynamic aspects, e.g. channel opening and closure. In part, this was very recently compensated by solved structures for both open and closed channel

conformations which allowed detailed insights into the gating pathway.

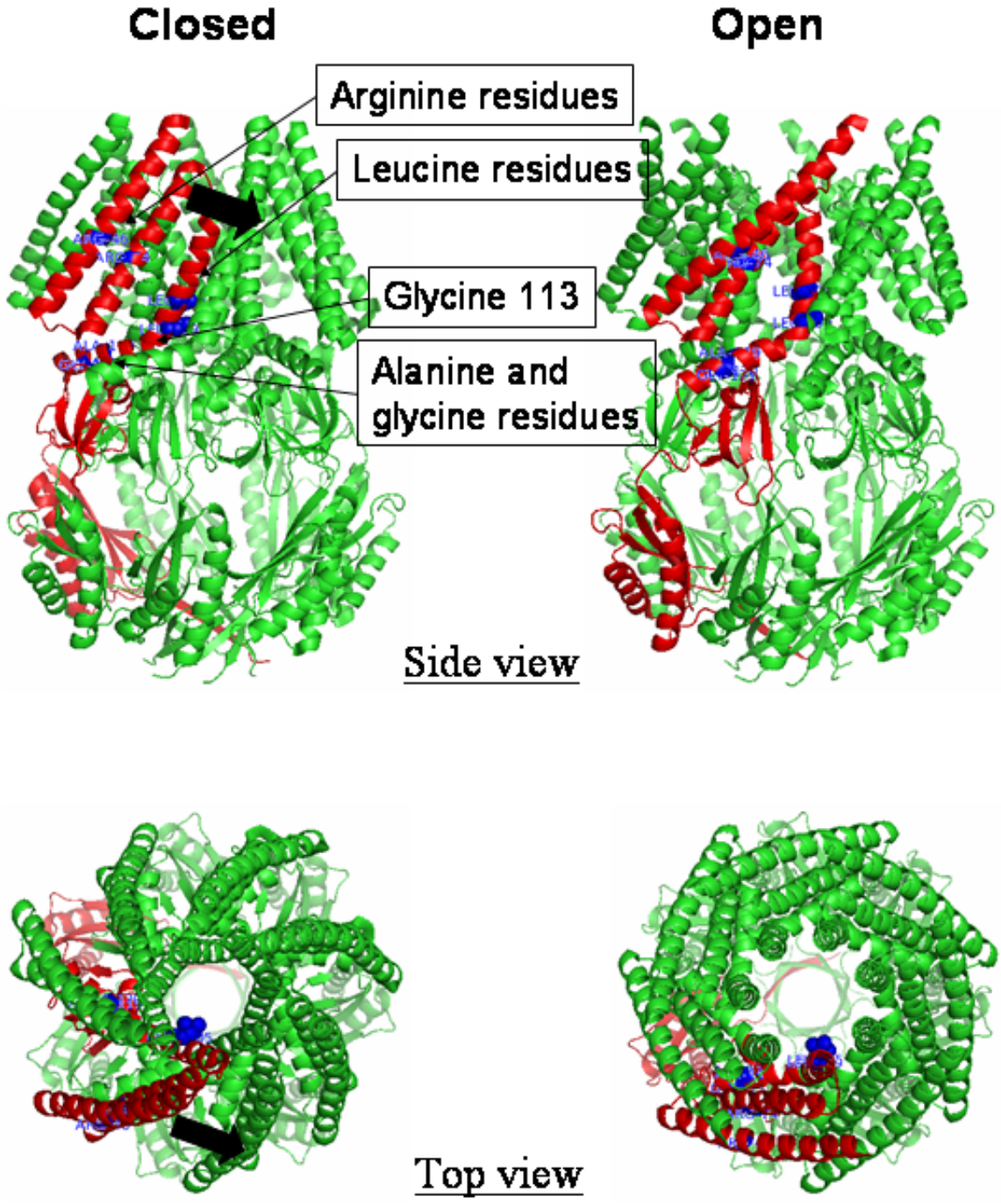

Figure 2.3: Closed and open conformation of the MscS channel (PDB files 2OAU and 2VV5, respectively) viewed from the side and the top. Crucial amino acid residues are indicated and described in the text. Block arrows indicate the movement of TM1 and TM2 during channel gating.

Based on the first crystal structures (Chang *et al.*, 1998; Bass *et al.*, 2002), more detailed studies could address the dynamic aspects of MS channel gating including internal structural rearrangements. Within this context, different gating substates were also analysed. Sukharev *et al.* (2001) modeled the protein subunits in the MscL channel and already showed at that time that, during gating and channel opening, the TM helices recline and rotate in analogy to a camera iris. Further to this, tryptophan fluorescence (Powl *et al.*, 2003) and, in particular EPR spectroscopy, have identified the open and closed conformation as well as several intermediate and subconducting states (Perozo *et al.*, 2002a,b). Edwards *et al.* (2005) have also found that the opening of these channels under osmotic stress conditions occurs on the millisecond time scale via several substates and conformations (more than 2 for MscL in *E. coli*).

Protein-membrane interactions were studied theoretically (Wiggins & Phillips, 2005) and experimentally (Perozo *et al.*, 2002b). This has revealed the crucial role of the lipid membrane in pressure sensing and its interplay with the conformation and function for the case of the MscL channel. Kung (2005) has further generalised this view and found that force detection occurs at the channel-lipid interface.

2.2 The bacterial cell wall

Historically, bacteria are divided according to a staining reaction into the two classes of Gram-negative and positive. Typical examples for either of the classes are *E. coli*, *Salmonella* and *Enterobacter* (Gram-negative), and *Streptococcus*, *Staphylococcus* and *Bacillus* (Gram-positive).

2.2.1 Cell wall organisation

Gram-negative bacteria have an inner plasma membrane and an outer plasma membrane (Alberts *et al.*, 2002) which both have an approximate thickness of 5 nm. Phospholipids are the main component of the inner membrane which is penetrated by different transmembrane proteins, e.g. ion channel proteins. The external leaflet of the asymmetric outer membrane consists of lipopolysaccharide molecules and the inner leaflet of lipoproteins (Dmitriev *et al.*, 2005). Typical components of the outer plasma membrane are mono- and trimeric transmembrane porins. Between both inner and outer plasma membrane there is the periplasm with the peptidoglycan layer, also called murein, which has a thickness between 2.5 nm (75-80% of the surface) and 7 nm (20-25% of the surface)

(Vollmer & Höltje, 2004; Labischinski *et al.*, 1991). According to Labischinski *et al.* (1991), this finding reflects the existence of either single- or triple-layered murein. Gram-positive bacteria have only one plasma membrane and a much thicker murein layer of 25 to 30 nm.

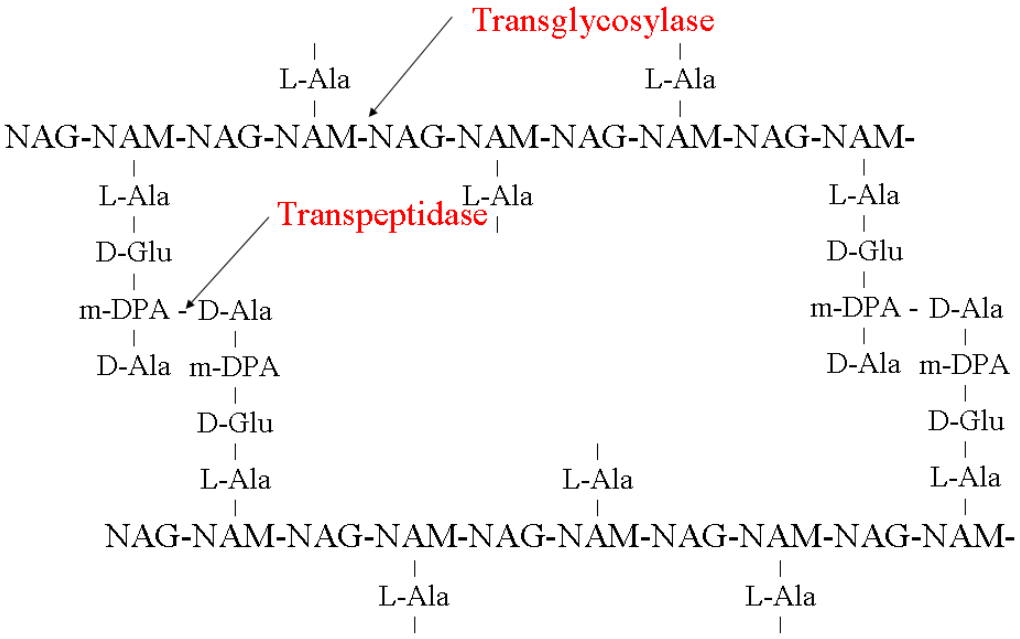

Figure 2.4: Chemical composition of the *E. coli* peptidoglycan layer: The murein precursor (shown in fig. 2.6) is integrated into the murein network by the two enzymes transpeptidase and transglycosylase. The terminal D-Ala group gets first cleaved from the precursor and the carboxy terminus of the second D-Ala group is then linked to the ϵ-amino group of the *meso*-diamino pimelic acid (m-DPA) in a peptide moiety of the existing network. A transglycosilase cleaves the pyrophosphate bond between N-acetylmuramic acid (NAM) and the undecaprenyl group (not shown) and forms then a glycosidic bond between NAM and the hydroxyl group at the carbon atom 4 of N-acetylglucosamine (NAG). (Image reproduced after Höltje, 1998).

The peptidoglycan layer is important to microorganisms to maintain shape, cell growth and to resist the high internal turgor pressure of 3-5 atm for Gram-negative and 20-50 atm for Gram-positive bacteria, respectively (Arnoldi *et al.*, 2000). The peptidoglycan layer is composed of glycan strands which are made of the aminosugars N-acetylglucosamine (NAG) and N-acetylmuramic acid (NAM) which are linked by β-1,4 glycosidic bonds (figs. 2.4 and 2.6) (Höltje, 1998). The

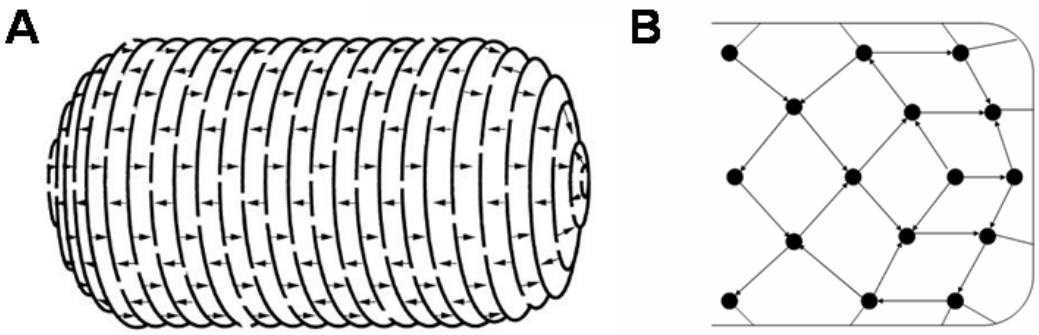

Figure 2.5: Sketch of the murein sacculus. A: "Horizontal Layer Model" (taken from Höltje, 1998): The parallel lines represent the glycan strands which lie parallel to the cell membrane(s) and the arrows symbolise the peptide bridges. B: "Scaffold Model" sketched after Dmitriev *et al.* (2005): The filled circles represent the glycan strands which are oriented perpendicularly to the cell membrane(s) and the arrows symbolise the peptide crosslinks.

oligosaccharides are covalently (cross)linked by short peptide strands making up a 3D-network (see figs. 2.4 and 2.5). Interestingly, in *E. coli*, the D-forms of glutamate (D-Glu) and alanine (D-Ala) are used and *meso*-diamino pimelic acid (m-DPA) has to be present in order to arrange peptide crosslinking in either three or four directions seen from a sugar strand (fig. 2.6) depending on which model is used (discussed in the next section). Murein digestion and (reversed-phase) HPLC analysis of the products has revealed a large variety of both peptide and sugar molecules across different microorganisms, as well as in chemical composition and molecule length (Höltje, 1998).

2.2.2 Models for the cell wall structure

In the past decades different models of the peptidoglycan layer have been formulated (Vollmer & Höltje, 2004) and two of them are under active debate. The structure of the more widely accepted model, called the "Horizontal Layer Model", is depicted in fig. 2.5A in which sugar strands lie parallel to the membrane surface. This model suggests that subsequent peptide units along a sugar strand assume a 90° angle with respect to each other which explains cell wall crosslinking within one murein layer and, if present, to neighbouring murein layers.

The alternative model was proposed by Dmitriev *et al.* (1999, 2003) which is called the "Scaffold Model" (fig. 2.5B). According to this model, sugar strands are perpendicularly orientated to the membrane surface, but are also crosslinked

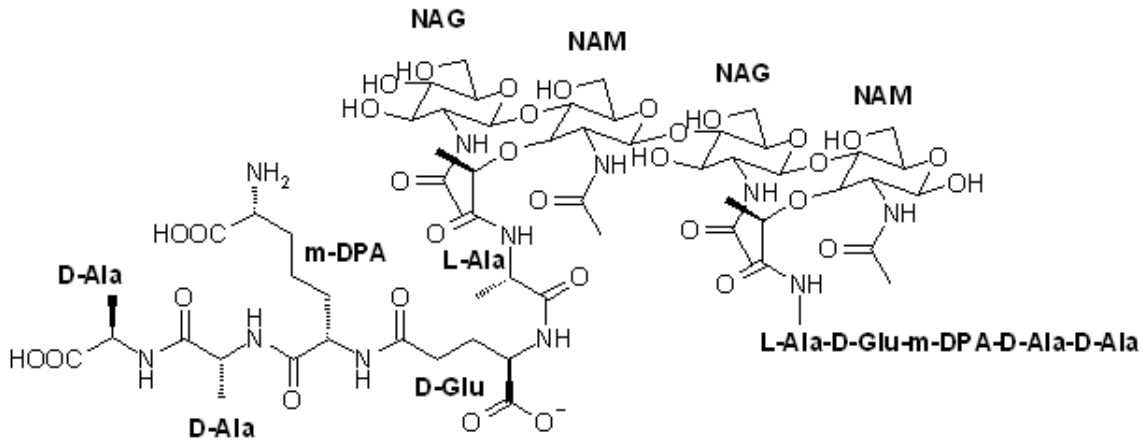

Figure 2.6: Chemical structure of a dimer of the basic unit, the disaccharide of N-acetylglucosamine and N-acetylmuramic acid (NAG-NAM) linked to a pentapeptide, to build the *E. coli* cell wall. The pentapeptide consists of L-Alanine, which is attached to the N-acetylmuramic acid via its amino group, D-glutamate, *meso*-diamino pimelic acid which is linked via its α-amino group and the first carboxylic acid and two D-alanine amino acids. (Reproduced after Meroueh *et al.* (2006).)

via oligopeptides. This model is based on cell wall synthesis insights which is described as and termed the patch-insertion mechanism. Murein synthesis complexes, embedded in the inner plasma membrane, are assumed to translocate the murein precursor from the cytoplasm into the periplasm where it is directly incorporated (in this orientation) into the cell wall. Because of the turgor pressure, the inner membrane bulges to fill the cavity in the old cell wall (Bayer *et al.*, 1990; Ishidate *et al.*, 1986) with the murein synthesis complexes being located on the bulge top. This model explains the cell wall synthesis in a more consistent way because there is no need for breakage of previously synthesised peptide crosslinks. However, it is not very obvious how a cylindrical cell like *E. coli* and *B. subtilis* can grow in the direction of its long axis. Further support for the scaffold model has been gained from gradual cell lysis experiments which are accompanied by a thinning of the cell wall without any visible holes or long cuts (Kitano *et al.*, 1986; Leduc *et al.*, 1985). In addition, Dmitriev *et al.* (2005) argued that branched cell morphologies as obtained by the group of Young (Young, 2003; Varma & Young, 2004) are only compatible with the scaffold model. Meroueh *et al.* (2006) have arrived at the scaffold model independently by solving the NMR structure of the NAG-NAM(pentapeptide)-NAG-NAM(pentapeptide) synthetic fragment which is a dimer of the basic primary unit of the cell wall (fig. 2.6). This structure has

revealed an ordered, right-handed helical saccharide conformation corresponding to three NAG-NAM pairs per helix turn. In addition, they reasoned that the AcrAB/TolC efflux system (Akama *et al.*, 2004; Koronakis *et al.*, 2000; Tamura *et al.*, 2005), present in Gram-negative bacteria, which connects the cytoplasm with the outer membrane can only be sterically well-fitted when the cell wall adopts the scaffold model.

Vollmer & Höltje (2004) challenge this model arguing that some of the sugar molecules present in *E. coli* are too long to be arranged perpendicularly to the the cell membrane normal. Hence, they must lie parallel to the cell surface automatically suggesting the horizontal layer model. Although this model has difficulty to explain cell wall synthesis because of continuous breakage, precursor insertion and synthesis of new crosslinks, it is understandable how rod-shaped cells elongate during growth. In addition, the horizontal-layer model predicts correctly that 50% of the peptides are crosslinked which was shown by experiment earlier (Glauner *et al.*, 1988). The scaffold model, however, predicts 100% crosslinking.

Touhami *et al.* (2004) performed AFM and TEM measurements on the bacterial cell wall, but were not able to confirm either of the existing models.

2.3 Osmotic pressure

The osmotic pressure Π of a diluted solution can be calculated according to the van 't Hoff relation which resembles the ideal gas law

$$\Pi M = c_m RT \tag{2.1}$$

with M, c_m, R and T denoting molar mass, mass concentration (in g cm^{-3}), gas constant and absolute temperature (Winter & Noll, 1998; Nelson, 2004). The solutions of macromolecules, and in particular the crowded environment in cells, are non-ideal. Hence, equation 2.1 has to be extended using a virial expansion

$$\Pi = RT(\frac{c_m}{M} + Bc_m^2 + ...) \tag{2.2}$$

The introduced virial coefficient B contains the effects of non-ideality and depends on the size and form of the polymers, the solvent and interactions of both. If two solutions of different nature are separated by a membrane, usually an osmotic pressure develops between them which can be calculated as the difference of the osmotic pressures on each side of the membrane according to equation 2.2.

Bacterial cells naturally maintain a high internal pressure of at least a few atmospheres by accumulating solutes. The osmolarity is a measure of the number of osmotically active substances dissolved in a certain volume and given in the unit mosmol/l. A 5-10 mosmol/l solute change corresponds to a 0.1-0.2 atm pressure change, which is the threshold value that activates MscS channels in patch-clamp experiments (Booth *et al.*, 2007). In living *E. coli* K12 cells a hypo-osmotic shock of 300 mosmol/l (equals a concentration difference of e.g. 150 mM NaCl corresponding to 2 atm) was found to be required for MS channel activation. The reason for the larger required pressure or osmolarity change is that the inner membrane is shielded and protected by the cell wall and the outer membrane of the cell.

2.4 Aim and motivation

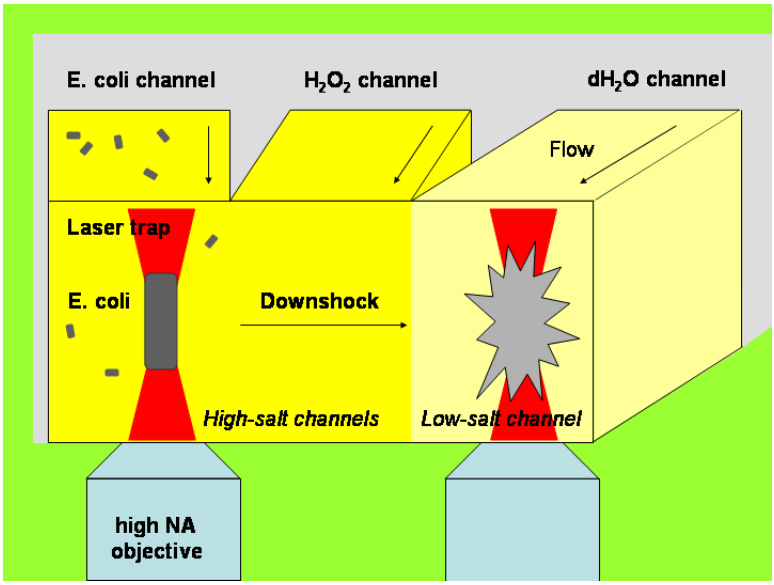

Figure 2.7: Single-cell hypo-osmotic shock experiment in a microfluidic device. An *E. coli* cell grown and maintained under high-salt conditions is optically trapped in the left channel (laser trap depicted in red) and then shifted into minimal medium containing a small amount of hydrogen peroxide. This revives the cell which is necessary to observe cell lysis after subjection to distilled water (low-salt) conditions.

From bulk observations it is known that *E. coli* cells which are deficient in three MS channels lyse upon hypo-osmotic shock (Levina *et al.*, 1999). The aim of this project was to image this lysis event for single bacterial cells using optical

trapping combined with microfluidics. The successful lysis event allows one to address numerous questions on bacterial behaviour during these naturally occurring extreme changes in environment:

- Is the time scale of lysis similar to the time scale of MS channel gating, i.e. in the millisecond range?
- Does lysis happen always in the same way or is there cellular diversity?
- Which information for the cell wall and membranes can be extracted from the direct observation of cell lysis? Is there a total failure of these elements or does a reversible adaptation take place?

Figure 2.7 sketches the experiment. Microfluidic devices allow reasonably controlled subjection of individual, trapped *E. coli* cells to media of different osmolarity. Wide-field microscopy observation then gives direct insight into the single cell's response.

2.5 Materials and Methods

2.5.1 Optical tweezers

The optical tweezer system was built in COSMIC by Wright *et al.* (2007). Two NIR laser diodes (λ = 785 nm) with a maximum output power of 70 mW (Laser Class IV) served as trapping lasers that were coupled into a Nikon Eclipse TE2000-U microscope (Nikon Instruments Europe B.V., Kingston) through the objective back aperture (100x, 1.3 N.A. PhC 3, oil immersion, plan apo). Because of the attenuation of the laser beam through the microscope, particularly the objective lenses, the laser power at the specimen was roughly 50% diminished compared to its normal output. One of the beams was held in a fixed position whereas the other beam was directed towards two galvanometric mirrors before entering the objective. These two mirrors could be controlled by the self-created software, written in LabVIEW 6.1 (National Instruments, Austin, TX, USA), to change x- and y-position of this trap. The system was combined with phase-contrast and fluorescence imaging (see following section). Images were taken with a CCD camera (Applied Vision Technologies, Dolphin 145-F, from Firstsight Vision Ltd., Farnham) run at lowest gain and 50 ms exposure time. The software allowed moving the trap in a straight line and at constant, well-defined speeds of 1 to 10 μm s^{-1} to any position in the field of view. Video imaging was done with the HyperCam2 software which captured time-courses visualised on the computer

screen through the optical tweezers software. 5 image frames were captured per second.

2.5.2 Epi-fluorescence microscopy

A mercury vapour lamp (Nikon) was used for widefield fluorescence microscopy providing a high light intensity in the UV/VIS. For YOYO-1 iodide and GFP (green fluorescent protein) imaging a Nikon B-2A filter cube with the following properties was used: excitation range (Ex) 450-490 nm, dichroic mirror (DM) 505 nm, emission range (Em) 515-555 nm.

2.5.3 Microfluidic devices

Microfluidic cells were fabricated from Perspex (block 70 x 40 x 6 mm) with channels milled out to a depth of 0.07 $\pm$ 0.01 mm using a 0.4 mm diameter end mill (STUBSD-0.4; Drill Service Ltd, Surrey). Two or three inlet channels of 2 mm width merged at an angle of 30°. The width of the resulting main channel was the sum of the single inlet channel widths. Only one outlet channel was used. The inlet and outlet holes were drilled 1.0 mm in diameter and attached to dispenser (precision) tips (EFD, Inc., East Providence, RI, USA) which were connected to polypropylene tubing (bore 1.0 mm, wall 0.5 mm; Altec Products Ltd., Bude). The flowcell was sealed by gluing (Norland Optical Adhesive No. 61, UV curing; Thorlabs, Ely) a coverglass over the channels and exposing it for 20 min to UV light (350-360 nm) using a standard C-10P Chromato Vue Cabinet (Ultra-Violet Products Ltd., Cambridge) found in organic chemistry laboratories. 1ml syringes (Fisher Scientific UK Ltd, Loughborough) were used to load the flowcell via the polypropylene tubing.

The syringe pump used in microfluidic experiments was the KDS200 (model no. 789200) from KD Scientific Inc. (Holliston, MA, USA).

2.5.4 Bacterial strains and plasmids

The bacterial strains used for this study were the *E. coli* wild-type strain FRAG1 and a mutant strain, MJF465 (DE3), in which three MS channel genes were deleted. The exact genotype of the MJF465 strain is Frag1 Δ*mscL::Cm* Δ*mscS* Δ*mscK::kan* which was created by Levina *et al.* (1999). (The old designation of the MJF465 strain was Δ*mscL* Δ*yggB* Δ*kefA*.) Additionally, a lysogen strain of MJF465, designated MJF465 (DE3), was used for GFP expression. All strains were obtained from Dr Samantha Miller (University of Aberdeen).

Bacterial stocks were prepared from exponential-phase growth cultures which were diluted with 60% (w/v) sterile glycerol to obtain a final concentration of 15% (w/v) glycerol and stored at -80 °C.

Dr John White (School of Chemistry) created the pET20 GFPuv plasmid which he kindly donated for this study. As this is the first report of its use, I document the cloning procedure carried out by Dr White. The *GFPuv* allele of pTYB1GFP (a gift from Derek MacMillan, Department of Chemistry, University College London) was amplified by the polymerase chain reaction, employing 5'CCGGGACTTCACATATGAGTAAAGGAGAAGAAC3' and 5'ATGCCTCGAGAAGCTTGAATTCTTAATGATGATGATGATGATGCTTGTACAGCTCGTCCATGCC3' as primers. The resulting fragment was ligated into the NdeI-HindIII interval of pET20. The DNA sequence was determined and dramatic expression of GFPuv was previously confirmed in BL21 (DE3) cells. The plasmid pET20 GFPuv carries ampicillin resistance. The analogous antibiotic carbenicillin was used for cell screening.

2.5.5 Media and reagents

All chemicals were purchased from Sigma-Aldrich Company Ltd. (Dorset), unless otherwise stated.

The growth medium used was either LB broth, Miller (from Fisher Scientific UK Ltd, 25 g/l based on 10 g tryptone, 5 g yeast extract and 10 g NaCl) or LB broth prepared from the single components from Oxoid Ltd (Cambridge) with 10 g/l tryptone, 5 g/l yeast extract and 5 g/l NaCl (Sigma). Note the changed salinity which was adopted for the single-cell hypo-osmotic shock experiments in microfluidics to be consistent with my collaborators. For LB agar plates 1.5% agar (Oxoid) was added. These media were also prepared in double-strength concentration (twice the amounts of reagents per litre). Additionally, 1 M NaCl solution and sterile distilled water was prepared. All solutions were autoclaved separately (2 min at 123 °C and 20 min at 121 °C) and mixed to reach the desired NaCl concentration prior to use as bacterial growth medium.

McIlvains minimal medium was prepared with the following components (per litre): 310 ml 0.2 M Na_2HPO_4 (Fisher), 25 ml 0.2 M K_2HPO_4, 70 ml 0.1 M citric acid and 595 ml distilled water for pH 7. NaCl was added to the distilled water to match a final concentration of 0.5 M or 0.3 M, respectively. The pH was checked prior to autoclaving the minimal medium. After this step filter-sterilised supplements needed to be added for *E. coli* cells to grow (final concentrations given): 0.4 mM $MgSO_4 \cdot 7H_2O$ (Fisher), 0.1% $(NH_4)_2SO_4$ (Fisher), 1 mg/l thiamine·HCl,

6 μM $(NH_4)_2SO_4 \cdot Fe_2SO_4 \cdot 6H_2O$ (Fisher) and 0.2% glucose.

The MJF465 strains were grown with the selective antibiotic markers chloramphenicol (25 μg/ml) and kanamycin (50 μg/ml) at standard-salt conditions. FRAG1 did not have any antibiotic resistance. In case of plasmid expression, an additional antibiotic was added. For the pET20 GFPuv vector this was carbenicillin.

2.5.6 Growth of bacterial cell cultures

Liquid cultures of MJF465 and FRAG1 cells were grown from a single colony with aeration at 37 °C (230 rpm, innova 4000 incubator shaker, New Brunswick Scientific (UK) Ltd., St. Albans) in 5 ml LB broth during the day (between 8 and 9 hours) or overnight after which they reached an OD600 around 5 (measured as 1/10 dilution using an eppendorf BioPhotometer, Fisher).

LB agar plate cultures were incubated in a stationary incubator at 37 °C (Function Line, Heraeus, via DJB Labcare Ltd, Newport Pagnell).

2.5.7 Preparation of liquid bacterial cultures for hypo-osmotic shock

A liquid overnight culture of the strain MJF465 was grown in LB. All subsequent growth media were prewarmed to 37 °C in order to prevent a cold shock. The next morning the (overnight) culture was diluted to an OD600 of 0.05 into 5 ml fresh LB broth. This culture was grown to an OD600 of 0.4 and was then diluted 1 in 10 into prewarmed LB + 0.5 M NaCl (Oxoid recipe without added antibiotics) and grown to an OD600 in the range from 0.2 to 0.4 with aeration. In this early-exponential growth phase cells were subjected to hypo-osmotic shock.

2.5.8 Preparation of plate bacterial cultures for hypo-osmotic shock

In order to be independent from the fast growth rate of liquid bacterial cultures, an assay based on plate cultures was developed by our collaborators in Aberdeen. The agar medium used was based on the Oxoid recipe and NaCl was added to increase the salt content by 0.5 M.

5 ml of an overday culture with a typical OD600 value of 5 was diluted serially to 10^{-5} giving roughly 1000 cells per ml. 1 ml of this solution was spread on an agar plate with LB + 0.5 M NaCl (without added antibiotics) using sterile ColiRollers Plating Beads (Novagen, via Merck Chemicals Ltd., Nottingham) and incubated overnight for 14-15 hours. (Our collaborators have shown that all cells in these colonies are in exponential-growth phase under these conditions. An

incubation time of 16 to 18 hours must not be exceeded as cells go into stationary phase by then.) *E. coli* cells were harvested by adding 1 ml LB + 0.5 M NaCl to the plate and suspended using a sterile plastic spreader (Fisher). The plate was tilted and as much suspension as possible was withdrawn (usually 0.5 ml) which subsequently was added to 4 ml fresh LB + 0.5 M NaCl.

2.5.9 Bulk hypo-osmotic shock of bacteria in solution

A 1/20 dilution of an *E. coli* cell culture, grown in LB + 0.5 M NaCl, into both sterile distilled water (shock) and LB broth + 0.5 M NaCl (control) was performed (0.5 ml cell culture in 9.5 ml medium). The resulting cell culture was shaken slightly, incubated at 37 °C or r.t. for 10 min and then imaged with phase-contrast microscopy. The cell number was counted from 10 microscope images (both control and shock) and the cell viability was determined after averaging the cell numbers.

In order to further analyse these downshocked cell cultures the DNA specific stain YOYO-1 iodide (Invitrogen Ltd, Paisley) was added in a separate experiment at a concentration of 25 nM (derived from a 1 mM stock in DMSO). The cell cultures were incubated for 10 min at r.t. in the dark and then analysed with phase-contrast and epi-fluorescence microscopy (the latter using a mercury lamp HBO 100). The microscope used for this experiment was an upright Zeiss Axioskop 2 mot plus equipped with a 100x oil objective (Ph3, 1.4 NA). The exposure time of the Q Imaging QICAM camera was 210 and 2.1. ms for fluorescence and phase-contrast microscopy, respectively (Gain 2.72, Offset 0). The FITC filter cube had the following spectral properties: Excitation BP 450-490 DM 510 Emission BP 515-565. Comparative pictures in both imaging modes were acquired for all four preparations. The switching time between each mode was 10 to 15 s.

2.5.10 Single-cell hypo-osmotic shock in a microfluidic device

Approach I: Microfluidic devices with two inlet channels and one outlet channel were used in combination with optical tweezers in order to subject single cells to a hypo-osmotic shock from LB + 0.5 M NaCl into distilled water. One 1 ml syringe was loaded with the bacterial culture, the second with sterile distilled water. During the experiment a hydrodynamic flow between 20 and 40 μl/hr per syringe was maintained which was the maximum flow speed for not losing bacterial cells from the laser traps. The laser input power was kept at 100 mW when cells were trapped, moved across the flow boundary by shifting the translation stage

in y-direction onto which the flowcell was fixed. Two individually trapped *E. coli* cells could be observed simultaneously. The experiment was repeated 20 to 25 times within an hour, i.e. giving data for 40 to 50 cells. A generic problem in all assays was the smearing of the flow boundary between the two solutions because of Brownian (and flagella) motion of *E. coli* cells.

Approach II: In order to account for oxygen depletion in the microfluidic devices the hypo-osmotic shock assay was modified. *E. coli* cells were grown overnight on LB agar plates + 0.5 M NaCl and harvested as described before, but with minimal medium + 0.5 M NaCl. Microfluidics with a third inlet channel were used. This middle channel contained minimal medium + 0.5 M NaCl + 50 μM hydrogen peroxide (6% stock solution from Fisher) where the *E. coli* cells resided for 30 s to 1 min to recover before they were dragged into the channel containing sterile distilled water.

There is a slight difference in osmolarity between LB agar + 0.5 M NaCl and minimal medium + 0.5 M NaCl. In the Aberdeen laboratory where an osmometer was available it was shown that this osmolarity difference is very small and neither affects the *E. coli* cells in any way nor triggers any MS channel activity in the wild-type strain FRAG1.

2.5.11 GFP expression in *E. coli*

This section describes the transformation of the MJF465 (DE3) lysogen strain with the pET20 GFPuv plasmid used for single-cell epi-fluorescence microscopy. MJF465 DE3 cells were grown overnight in LB broth on selective markers. In the next morning a growing culture in 100 ml fresh LB (initial OD600 = 0.05) was setup and grown to an OD600 = 0.35, then cooled 10 min to 0 °C, and spun down (10 min, 2k rpm, 4 °C, Sorvall RC 3B plus, Thermo Fisher Scientific Inc., Loughborough). After the cell culture was drained it was resuspended in 10 ml ice-cold 80 mM $MgCl_2$, 20 mM $CaCl_2$ solution (Standard Transformation Buffer) and put on ice for another 10 min. One further spinning and draining cycle was done and the culture was transferred to 4 ml 100 mM $CaCl_2$ 15% glycerol. (Frozen stocks were prepared from this culture after 24 hr and kept at -80 °C.) 1 μl of the plasmid pET20 GFPuv stock (concentration 200 ng DNA/μl) was added to 100 μl of cell culture and left on ice for 30 min. (A control experiment in which no plasmid-DNA was added to the cell culture was also performed.) This culture was incubated at 42 °C for 20 s (in a water bath) and chilled to 0 °C for 1 to 2 min. 900 μl fresh LB broth was added to the cell culture with subsequent incubation for 1 hour at 37 °C without aeration (no antibiotics added).

100 and 10 μl of this culture were used to inoculate two separate LB agar plates, supplemented with carbenicillin, chloramphenicol and kanamycin (100, 25 and 50 μg/ml), respectively and incubated at 37 °C overnight.

Single colonies from these plates were used to inoculate overnight LB cultures. In the morning of the next day the cells were twice spun down (2k, 10 min, r.t.) and resuspended in LB and then used immediately as an inoculant for a fresh culture (6 ml). This culture was grown to an OD600 around 0.35 and diluted 1/10 into 6 ml prewarmed LB broth + 0.5 or 0.3 M NaCl (without antibiotics), respectively. At an OD600 around 0.1, IPTG was added to a final concentration of 0.1 mM to induce GFP expression and cells were grown to an OD600 between 0.2 and 0.25 where they were used for hypo-osmotic downshock as described in section 2.5.10.

2.5.12 Image processing

Videos were cropped and reduced in frame number using ImageJ. The same software was also used to read out fluorescence intensity values of single brightly fluoresceing *E. coli* cells over the time course of a few minutes. For this purpose a short macro was written.

2.5.13 Statistical analysis

The generated data sets for mutant and wild-type cells, as well as hydrogen peroxide supported *vs.* non- hydrogen peroxide supported downshock and harvesting media dependent downshock behaviour, were statistically analysed using a significance test. As described in more detail in the next section, the cellular downshock response was classified into four single categories. For the statistical analysis, however, only the number of lysing over surviving cells was analysed. Two data sets are significantly different, i.e. the likelihood that differences between them arise through randomness is less than 5%, if a $test-parameter$ is larger than the value of 3.84 (Henkel, 1976). The $test-parameter$ can be obtained as follows. The number of lysing and surviving cells of the cell culture A will be denoted L_A and S_A, respectively. For culture or condition B the index changes accordingly. The $test-parameter$ is then calculated with the equation

$$test-parameter = \frac{(N-1)\cdot(L_A\cdot S_B - L_B\cdot S_A)^2}{(L_A+L_B)\cdot(S_A+S_B)\cdot(L_A+S_A)\cdot(L_B+S_B)} \qquad (2.3)$$

where

$$N = L_A + S_A + L_B + S_B. \tag{2.4}$$

2.6 Results

2.6.1 Bulk hypo-osmotic shock experiments

The research group of Prof Ian Booth has established that only 10% of *E. coli* MJF465 cells survive a hypo-osmotic shock from LB + 0.5 M NaCl into LB, whereas the *E. coli* wild-type strain FRAG1 survives to 90% (Levina *et al.*, 1999). I had the opportunity to carry out bulk hypo-osmotic shock experiments using bacterial cultures grown on LB agar plates and in LB solution in Prof Booth's laboratory under the guidance of Mr Nicolas Hayward. The resulting hypo-osmotically shocked cultures were analysed by optical density readings, bright-field microscopy and were, separately, regrown on LB agar plates to recover the extent of cell lysis and survival (by counting colony forming units) of both wild-type and mutant strain, respectively. The results obtained reproduced what was previously found by Levina *et al.* (1999).

2.6.2 YOYO-1 staining of hypo-osmotically shocked cell cultures in bulk solution

YOYO-1 is a common DNA stain which brightly fluoresces upon DNA bis-intercalation. This dye is not able to penetrate prokaryotic cells. However, if lesions in the cell wall or cell membrane(s) occur, YOYO-1 can access and stain the bacterial nucleoid which can be assayed with epi-fluorescence microscopy. Hence, it is an ideal probe to assess the extent of cell wall and cell membrane lesions during a hypo-osmotic shock in both wild-type *E. coli* (FRAG1) and mutant (MJF465) cells which lack MS channels. Figure 2.8 shows example images of *E. coli* cell cultures taken under different hypo-osmotic shock conditions following the method described by Levina *et al.* (1999). The left panel shows phase-contrast images where all non-lysed cells can be clearly observed. The right panel shows the corresponding image (same field of view) taken in epi-fluorescence mode which reveals to which extent cell wall or membrane disruptions occurred. Wild-type and mutant cells under control conditions did not show any fluorescence. This result is expected as MS channel activity is not challenged. During a hypo-osmotic shock of a FRAG1 cell culture from LB + 0.5 M NaCl into LB, less than 10% of all cells (see also table 2.1) showed bright fluorescence which proves

that the majority of the *E. coli* cells was protected by MS channel activity. However, when a culture of the mutant strain was subjected to the same conditions, 50% of all cells lit up fluorescent which indicates that this cell culture suffered from cell wall or membrane lesions.

The absolute cell number determined from 4-5 images for both wild-type and mutant strain under hypo-osmotic shock and control conditions does not reflect the number of lysed cells. The figures are very similar because the *E. coli* cells imaged have settled on the coverslip.

YOYO-1 staining of hypo-osmotically shocked *E. coli* cultures									
FRAG1	shock		control		**MJF465**	shock		control	
	PhC	Fl	PhC	Fl		PhC	Fl	PhC	Fl
Total number of cells	154	10	100	9		211	109	204	44
% fluorescent cells		**6.5**		**9**			**51.7**		**21.6**

Table 2.1: Summary of YOYO-1 staining of hypo-osmotically shocked *E. coli* cultures (from LB + 0.5 M NaCl into LB). For each strain and each imaging mode, phase-contrast (PhC) *vs.* epi-fluorescence (Fl), the number of observable cells under control and hypo-osmotic shock conditions is given. The percentage of fluorescent cells reflects to which extent cell wall or cell membrane lesions appeared. (These data were generated together with Nicolas Hayward at the University of Aberdeen.)

2.6.3 Single-cell hypo-osmotic shock in microfluidic devices

To address questions on the cellular diversity, the timescale of hypo-osmotic shock response and failure or support of the cell wall and cell membranes, single-cell experiments were carried out using optical tweezers combined with microfluidic devices. Such an experimental setup allows the manipulation of individual *E. coli* cells in different buffer media. The different buffers were maintained in a laminar flow beside each other, as sketched in figure 2.7. Individual cells were trapped with an optical laser tweezer in the region between the first and second inlet channel and shifted from a high-salt into a low-salt buffer by systematic microscope stage displacement. Simultaneous wide-field imaging through the microscope objective monitored the fate of individual bacterial cells.

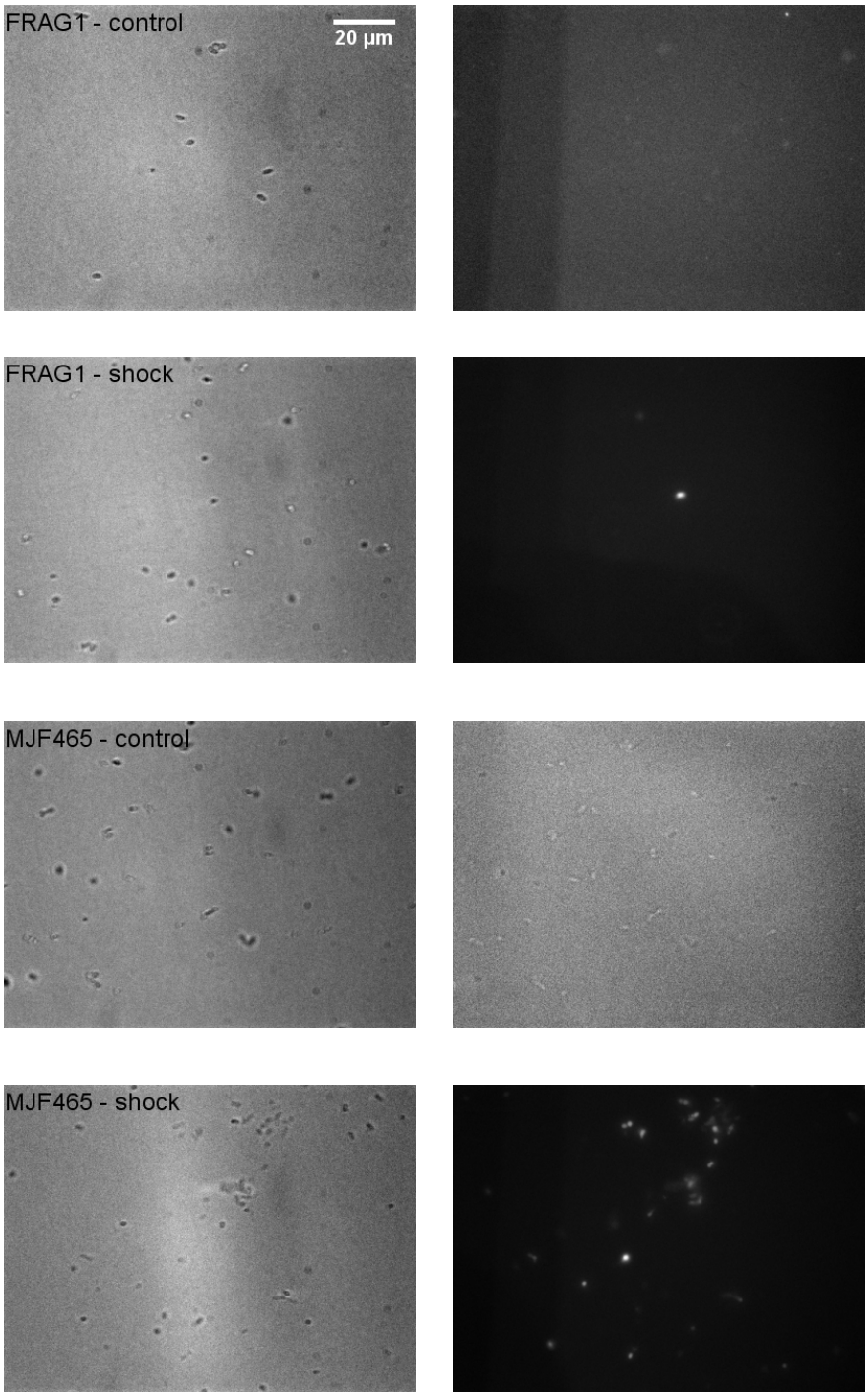

Figure 2.8: Hypo-osmotically shocked *E. coli* cultures (from LB + 0.5 M NaCl into LB). Both the wild-type (FRAG1) and mutant (MJF465) strain are displayed. The left panel shows phase-contrast images and the right panel shows the epi-fluorescence images of the same (YOYO-1 stained) cultures in exactly the same field of view. (These data were generated together with Nicolas Hayward.)

Using a NIR trapping laser at a wavelength of 785 nm was shown to induce

only very little optical damage in *E. coli* cells by a local heating effect compared to the wavelength region between 870 and 930 nm; the least damaging laser wavelengths were found to be 830 and 970 nm (Neuman & Block, 2004; Neuman *et al.*, 1999).

As outlined in chapter 1.4, mixing of laminar flows in microfluidic devices is governed by transverse diffusion. While working at low flow rates to ensure stable trapping of bacterial cells, one has to take into account that the NaCl and hydrogen peroxide gradients smear out between the different inlet channels. Hence, there is an intrinsic uncertainty in the exact hypo-osmotic shock condition as well as in the exposure to hydrogen peroxide to revive the bacterial cells. This effect was not evaluated within this thesis, but could be principillay investigated using fluorescence lifetime imaging and a solvent sensitive fluorescent dye to characterise the extent of diffusional mixing between different laminar streams under the conditions chosen (see e.g. Magennis *et al.*, 2005). In order to minimise the variablity of the hypo-osmotic shock conditions for different cells, a constant trajectory close to the merging site of the different inlet channels (around 100 μm away) was chosen and maintained throughout all experiments. The microfluidic device used could be improved by physical separation of the different media streams and their connection by small (e.g. 10 μm wide) junctions through which trapped *E. coli* cells can be transferred from one medium into another.

For the phase-contrast single-cell experiments, all *E. coli* cultures were harvested from an LB agar plate + 0.5 M NaCl grown for 14 hr. Initially, a two-inlet flowcell was used where individual *E. coli* cells were directly hypo-osmotically shocked from the harvesting medium + 0.5 M NaCl into distilled water (approach I). This experimental configuration, at that early stage, did not allow successful imaging of cell lysis. The experimental setup suggested that the *E. coli* cultures suffered from oxygen depletion in the microfluidic device which induces the stationary growth phase which leads to physiological conditions where cell lysis is prevented. Nicolas Hayward (personal communication) showed in a bulk experiment later that a MJF465 *E. coli* culture has a survival rate of 50% when it is kept for 10 min in a syringe prior to hypo-osmotic shock from LB + 0.5 M NaCl into LB.

Consequently, in the single-cell experiments a three-inlet flowcell was introduced (approach II). My collaborators in Aberdeen, namely Prof Ian Booth, suggested to harvest all *E. coli* cultures from a LB plate with minimal medium + 0.5 M NaCl and to subject each individual cell to 50 μM H_2O_2 for 30-60 s in the middle channel of the flowcell. This agent was previously shown to provide the *E. coli* cells with enough oxygen to reenter or remain in the exponential growth

phase (Ian Booth, personal communication). As a direct result, cell lysis could be clearly imaged using phase-contrast microscopy. Longer or shorter hydrogen peroxide exposure times were not assayed within this thesis because shorter exposure times were practically impossible to reach as the transit time through the middle channel was around 30 s. Longer exposure times would have further reduced the throughput of the assay. Given the aim of observing individual lysis events and to provide a qualitative and kinetic description of cell lysis, the experimental design was not further modified or investigated from that stage on. With grown experience on the difficult assay, a few lysis events were detected even without hydrogen peroxide support in the final stage of this project. Using a hypo-osmotic shock from LB + 0.3 M NaCl or minimal medium + 0.3 M NaCl into distilled water did not permit phase-contrast observation of cell lysis. Each individual experiment series was run for one hour aiming to acquire as much data as possible within that time frame.

2.6.4 Phase-contrast results of single hypo-osmotically shocked *E. coli* cells

Using phase-contrast microscopy, the different events seen on the single-cell level could be principally divided into four categories:

1. Cell lysis.
2. Loss of *E. coli* cells from the optical trap during channel crossing, so that lysis or survival could not be evaluated. (Supplementary video S2-1)
3. Cells surviving the hypo-osmotic downshock remaining totally unchanged in phase-contrast appearance. (Supplementary video S2-1)
4. In a few cases, no proper discrimination between these three categories (in most cases between 1 and 2) was possible making the experimental outcome for the single cell unclear. (Supplementary video S2-2)

Referring to category 1 there are three possible ways of cell lysis which can be clearly distinguished. A sudden vanishing of the an *E. coli* MJF465 cell (fig. 2.9) is thought to be accompanied, or better preceded, by cell bursting. However, this lysis event happened on a timescale which is faster than the image acquisition, i.e. 200 ms. No remnants like cell wall or membrane debris could be detected in this event. A stably trapped cell (not shown) in the second laser tweezer ensured in many cases that no mechanical interference or disturbance on the microscope took place. Cell bursting releases the ribosomes which are responsible for the dark

cell appearance in phase-contrast microscopy (Neidhardt *et al.*, 1996), most of the proteins and probably DNA (fig. 2.10). Interestingly, this event is slower than the case of the vanishing cell. After prolonged incubation in minimal medium (at 37 °C) some *E. coli* MJF465 cells swelled before they experienced sudden lysis from one video frame to another (fig. 2.11). Figure 2.12 shows single MJF465 cells which leak suddenly when they are subjected to hypo-osmotic shock conditions. This, again, must be due to loss of the ribosomes, protein and probably DNA through relatively large cell wall ruptures.

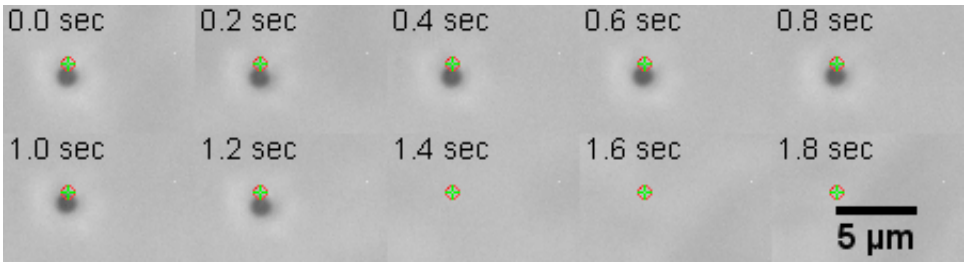

Figure 2.9: Phase-contrast video image sequences of a vanishing *E. coli* MJF465 cell upon hypo-osmotic shock from minimal medium + 0.5 M NaCl via minimal medium + 0.5 M NaCl + 50 μM H_2O_2 into distilled water. No remnants could be observed in the entire field of view which is 70 fold larger than the sub-images. The green cross and red circle were slightly displaced from the actual laser trap position to allow a clear view of the *E. coli* cell in the trap. (Supplementary video S2-3)

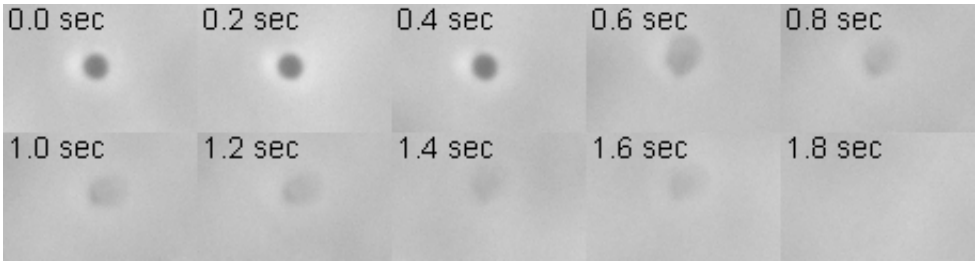

Figure 2.10: Phase-contrast video image sequence showing a bursting *E. coli* MJF465 cell upon hypo-osmotic shock from minimal medium + 0.5 M NaCl via minimal medium + 0.5 M NaCl + 50 μM H_2O_2 into distilled water. (Supplementary video S2-4)

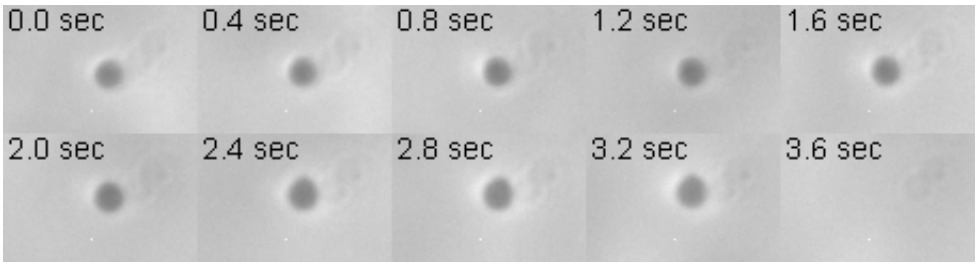

Figure 2.11: Phase-contrast video image sequence showing a swelling *E. coli* MJF465 cell upon hypo-osmotic shock from minimal medium + 0.5 M NaCl via minimal medium + 0.5 M NaCl + 50 μM H_2O_2 into distilled water. The cell was incubated for 1.5 hr at 37 °C in minimal medium + 0.5 M NaCl which may provoke this artefact which was never observed in one of the cultures without further incubation. Eventually, the cell bursts and vanishes within 200 ms (frame at 3.6 s). (Supplementary video S2-5)

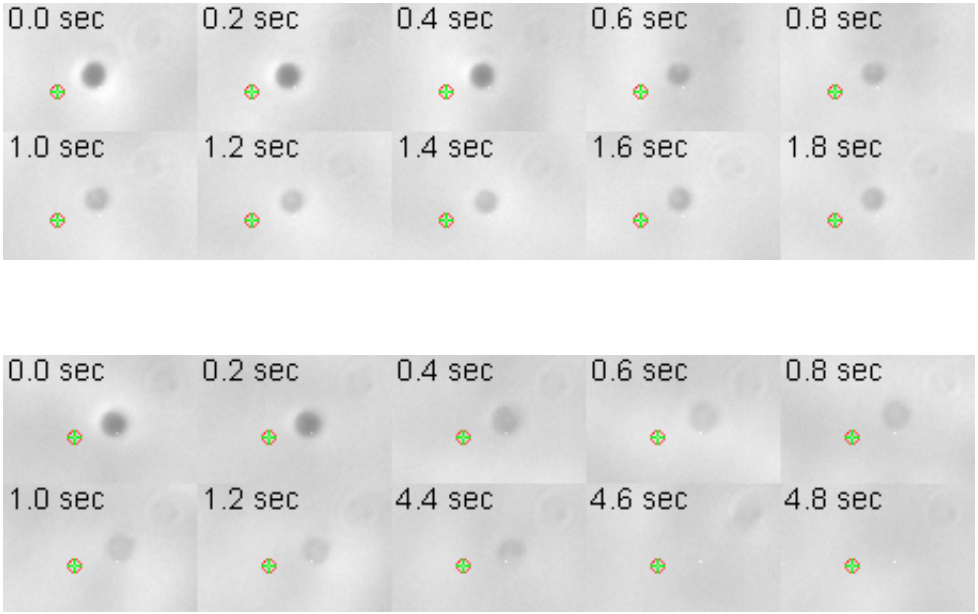

Figure 2.12: Phase-contrast video image sequences showing leaking *E. coli* MJF465 cells upon hypo-osmotic shock from minimal medium + 0.5 M NaCl via minimal medium + 0.5 M NaCl + 50 μM H_2O_2 into distilled water. Both cells suffer from cell wall and membrane lesions which cause the ribosomes and protein to leak out from the cell seen as a loss of contrast. In the upper panel the cell ghost remains in the laser trap, whereas in the lower panel the cell ghost is lost after a few seconds (frame 9 at 4.6 s). (Supplementary videos S2-6 and S2-7)

In some cases the cell remnants remained trapped by the laser tweezers (upper panel), in other cases the cell ghost disintegrated and was lost from the trap (lower

Summary of hypo-osmotically shocked single *E. coli* MJF465 cells							
Harvesting medium	Channels	Further incubation	Cat. I	Cat. II	Cat. III	Cat. IV	Viability (%)
McIlvaine's + 0.5 M NaCl	3		8	17	6	3	43
Reproduction			17	4	12	7	41
McIlvaine's + 0.5 M NaCl	2		4	13	25	0	86
Reproduction			3	14	21	3	88
McIlvaine's + 0.5 M NaCl	2	1.5 hr (37 °C)	18	7	22	3	55
McIlvaine's + 0.5 M NaCl	2	2.5 hr (r.t.)	27	15	6	2	18
LB + 0.5 M NaCl	2		8	20	20	2	71

Table 2.2: Summary of hypo-osmotically shocked single *E. coli* MJF465 cells. The hypo-osmotic shock was carried out from medium + 0.5 M NaCl into distilled water. Cells were grown on LB agar + 0.5 M NaCl plates (at 37 °C for 14-15 hr) and harvested with minimal medium (McIlvaine's) or LB broth + 0.5 M NaCl. The middle channel (only present when 3 channels were used) contained minimal medium + 0.5 M NaCl + 50 μM H_2O_2. Further incubation was carried out after the *E. coli* cells were harvested from the plate. The cell viability is calculated from the number of survivors (Cat. III) divided by the sum of the numbers of cells lysed and survived (Cat. I and III).

panel). The term "cell ghost" refers to a cell without nucleus which essentially consists of the cell membranes, the cell wall and some proteins. Compared to cell bursting, cell lysis through leakage is a slower event taking place over a few seconds. However, the first sign of leakage takes place within less than 200 ms.

The complete data sets for the hypo-osmotic shock experiments with MJF465 and FRAG1 cells are shown in table 2.2 and 2.3, respectively. The figures in the table refer directly to the number of cells following the characteristics of the above defined categories (1 to 4). Hypo-osmotic shock experiments were performed under varied conditions, such as the harvesting medium, hydrogen peroxide assistance and additional incubation time. Figure 2.13 visualises these results in a histogram.

For statistical aspects it is only useful to look at the number of lysing and surviving cells (category 1 and 3), respectively. Cells in category 2 were lost from the optical trap and ones in category 4 showed unclear behaviour. The cell viability was hence calculated taking only the number of surviving and lysing cells into account. An apparent problem is that reproduction of certain data

Summary of hypo-osmotically shocked single *E. coli* FRAG1 cells							
Harvesting medium	Channels	Further incubation	Cat. I	Cat. II	Cat. III	Cat. IV	Viability (%)
McIlvaine's + 0.5 M NaCl	3		7	7	19	7	73
Reproduction			13	17	13	3	50
McIlvaine's + 0.5 M NaCl	2		12	4	31	3	72
Reproduction			5	8	32	5	86
McIlvaine's + 0.5 M NaCl	2	1.5 hr (37 °C)	6	5	38	0	86
McIlvaine's + 0.5 M NaCl	2	2.5 hr (r.t.)	9	7	40	0	82
LB + 0.5 M NaCl	2		3	3	42	2	93

Table 2.3: Summary of hypo-osmotically shocked single *E. coli* FRAG1 cells. The hypo-osmotic shock was carried out from medium + 0.5 M NaCl into distilled water. Cells were grown on LB agar + 0.5 M NaCl plates (at 37 °C for 14-15 hr) and harvested with minimal medium (McIlvaine's) or LB broth + 0.5 M NaCl. The middle channel (only present when 3 channels were used) contained minimal medium + 0.5 M NaCl + 50 μM H_2O_2. Further incubation was carried out after the *E. coli* cells were harvested from the plate. The cell viability is calculated from the number of survivors (Cat. III) divided by the sum of the numbers of cells lysed and survived (Cat. I and III).

sets, particularly with the FRAG1 strain (see first four rows in table 2.3) led to quite different results. The outcome of the statistical comparison to the mutant strain offen depended on which data set for FRAG1 was picked. In addition, all used data sets are quite small. Hence, the results of the presented statistical significance tests should not be overinterpreted.

Using equation 2.3, it was calculated if the difference between surviving and lysing cell number under different conditions and using different strains was significant, i.e. whether the likelihood that observed changes were the result of randomness is less than 5%.

The data obtained for MJF465 and FRAG1 harvested with minimal medium + 0.5 M NaCl were reproduced on different days so that we can compare them in different combinations. Exactly two of these data sets show statistically significant downshock behaviour differences when the *E. coli* cells were treated with minimal medium + 0.5 M NaCl + 50 μM H_2O_2 in the middle channel. Comparison of the other data sets does not lead to statistically satisfying differences. Hence, a result as clear as the bulk assay where cell survival was determined

from bacterial cultures regrown on an LB agar plate cannot be obtained with this single-cell assay. In case of the data sets where the middle channel was omitted, no statistically significant data between wild-type and mutant strain were obtained. Curiously, FRAG1 cells seem to be even more prone to lysis than the MJF465 mutant cells. However, when cells from both strains were harvested with LB broth and subjected to hypo-osmotic shock directly (without the middle "hydrogen peroxide" channel), the data satisfy the statistical significance with more mutant cells lysing.

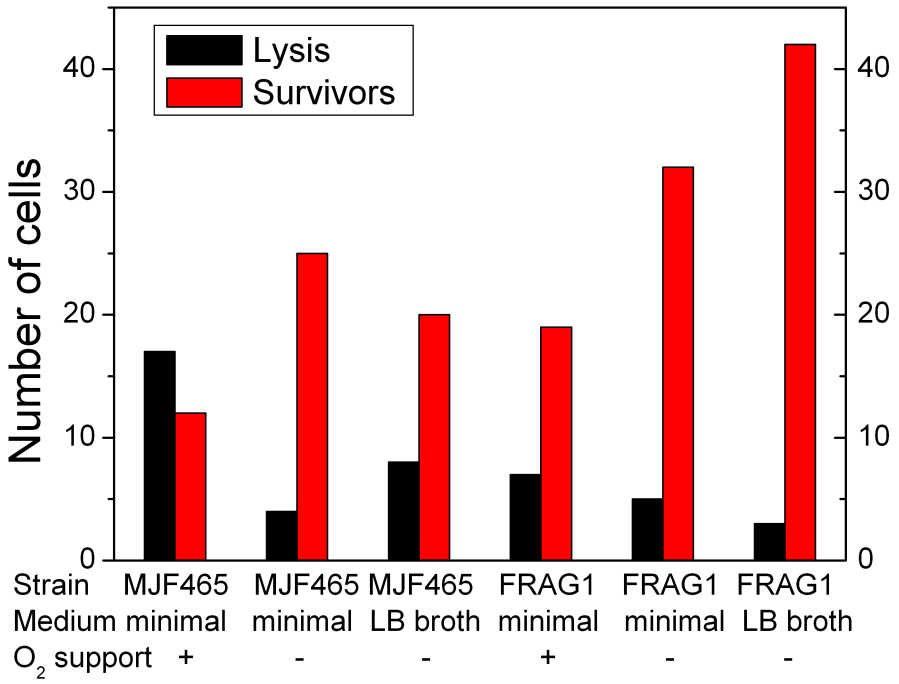

Figure 2.13: Phase-contrast summary of cell survival and lysis of wild-type and mutant strain under different hypo-osmotic shock conditions.

The effect of hydrogen peroxide in the middle channel on hypo-osmotic shock behaviour of both mutant and wild-type-strain was evaluated. For the mutant strain MJF465 all generated data sets (one reproduction for each condition) are statistically significantly different from each other showing the fundamental influence of this oxygen supporting system. For the wild-type strain only two of the generated data sets are statistically significantly different from each other. The importance of the hydrogen peroxide additive is also seen in the GFP-expressing cultures (next section). Using high-salt conditions (+ 0.5 M NaCl), all cells leak

out GFP quickly, i.e. on a timescale of 8-24 s whereas, when H_2O_2 is omitted, the cell culture seemed to split in two populations, one that leaked GFP fast (around 10 s) and one whose GFP decay resembled control conditions (around 80 s, photobleaching).

Furthermore, the effect of the harvesting medium on the downshock behaviour was investigated in two-inlet flowcells (i.e. without hydrogen peroxide assistance). Interestingly, for MJF465 the harvesting medium has no significant influence on the number of lysing and surviving cells, whereas for FRAG1 two data sets show a significant influence of the harvesting medium. Using minimal medium to harvest the cell culture leads to two- to four-fold enhanced cell lysis. When MJF465 cells are additionally incubated at 37 °C/r.t. for a 1.5/2.5 hr period of time after harvesting they are much more susceptible to lysis upon hypo-osmotic downshock. This is not the case for FRAG1 cells.

The results of the statistical significance test are also reflected in the calculated cell viability in tables 2.2 and 2.3.

2.6.5 Epi-fluorescence results of single hypo-osmotically shocked GFP expressing *E. coli* MJF465 (DE3) cells

An interesting variation of the above assay was GFP expression in the mutant strain MJF465 (DE3) and the assessment of the cellular response of these cultures to a hypo-osmotic shock. Epi-fluorescence imaging was used instead of phase-contrast imaging to determine the extent of GFP leakage. Unfortunately, the combination of high-salt-growth and GFP expression puts additional stress on the *E. coli* cells. These cultures show filamentation which indicates an SOS response which has many effects on the cell physiology. In particular, cell division is blocked until DNA or other damage is repaired which leads to reduced formation of septa (cell division sites) (Neidhardt *et al.*, 1996). These constricted rings are the weakest points in the cell wall of a growing cell, hence rupturing is likely to propagate from the septa. For hypo-osmotic shock experiments, GFP expressing cells of a maximum length of 4-5 μm were preferentially chosen.

Hypo-osmotic shock experiments with GFP expressing MJF465 cells were carried out for different salt conditions (minimal medium + 0.5 M NaCl and minimal medium + 0.3 M NaCl into distilled water) and under use or omission of hydrogen peroxide assistance in an additional microfluidic channel.

Cell bursting, as observed many times with phase-contrast microscopy, is an absolutely rare event under these conditions which was observed only twice during all experiments carried out (fig. 2.14). A fluorescence cloud of GFP could be seen

directly after the failure of the cell wall and membranes. A much more prominent event for these cell cultures is the systematic leakage of GFP through small cell wall or membrane lesions that occur as a result of the hypo-osmotic shock, seen for every condition used (upper panel in fig. 2.15). The lower panel in the same figure monitored the GFP fluorescence of a single cell that was kept in the high-salt channel. To further analyse the decrease in GFP concentration, either as a result of pure photobleaching (control) or through mainly active leakage from the cells, fluorescence traces were derived from the video sequences and plotted for the different NaCl and hydrogen peroxide conditions used (figures 2.16 and 2.17). Note that there is no proper laminar flow between the different inlet channels in the microfluidic device. To some extent the different media mix and smear the boundary region which is a result of transverse diffusion. For this reason, GFP leakage starts with a delay of around 10 seconds. Interestingly, the fluorescence traces obtained with H_2O_2 assistance show a remarkable artifact. Upon transferal into the middle (H_2O_2 containing) flowcell channel, the fluorescence intensity of the cells rises. This effect occurs systematically and depends on for how long the cells have been kept in the first channel. As oxygen depletion takes place in the first channel, the GFP chromophore cannot reach its mature state because the last reaction step requires molecular oxygen (Tsien, 1998) which is provided in the middle channel (due to the decomposition of H_2O_2 into H_2O and O_2). The fluorescence intensity reaches a maximum after 10 seconds, after which the cells are either transferred into the third channel for hypo-osmotic shock or kept in the second channel to evaluate control, i.e. in this case high-salt, conditions. The difference between the upper and lower panel in fig. 2.16 (0.5 *vs.* 0.3 M NaCl) is due to the fact that the hypo-osmotic shock traces were acquired at different stages of the experiment. The ones for 0.5 M NaCl were acquired immediately after the start of the experiment whereas the traces at 0.3 M NaCl were acquired between 20 and 30 min after the experiment start. The control traces were taken in both cases towards the end of the experiment, explicitly after around 40 min. Comparison of figures 2.16 and 2.17 shows that the initial "GFP maturation effect" under the assistance of hydrogen peroxide does not affect the downshock traces as quantitatively similar kinetic traces are observed with and without this reagent.

Both the GFP leakage and the bleaching process are first-order mono-exponential kinetic/decay processes that can be described with the equation $I = I_0 * exp(-t/\tau)$. I, t and τ denote the intensity, time and the time constant. (By stating this, one has to neglect the initial delay observed in the GFP leakage traces which is a result of smeared flow boundaries.) The time constants for GFP bleaching are

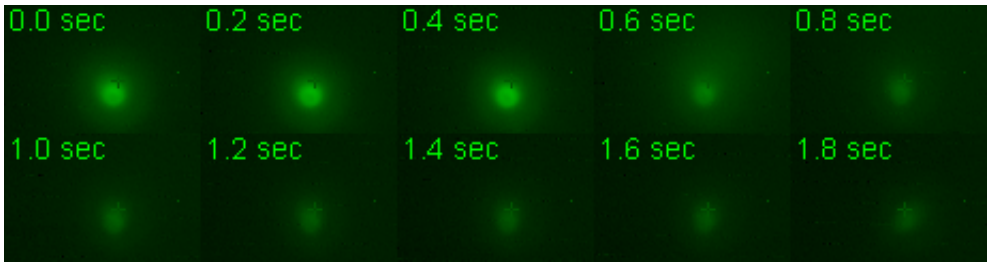

Figure 2.14: Epi-fluorescence video image sequence showing a bursting GFP expressing *E. coli* MJF465 (DE3) cell upon hypo-osmotic shock from LB + 0.5 M NaCl via minimal medium + 0.5 M NaCl + 50 μM H_2O_2 into distilled water. A fluorescence cloud is visible in frame 4 (at 0.6 s). (Supplementary video S2-8)

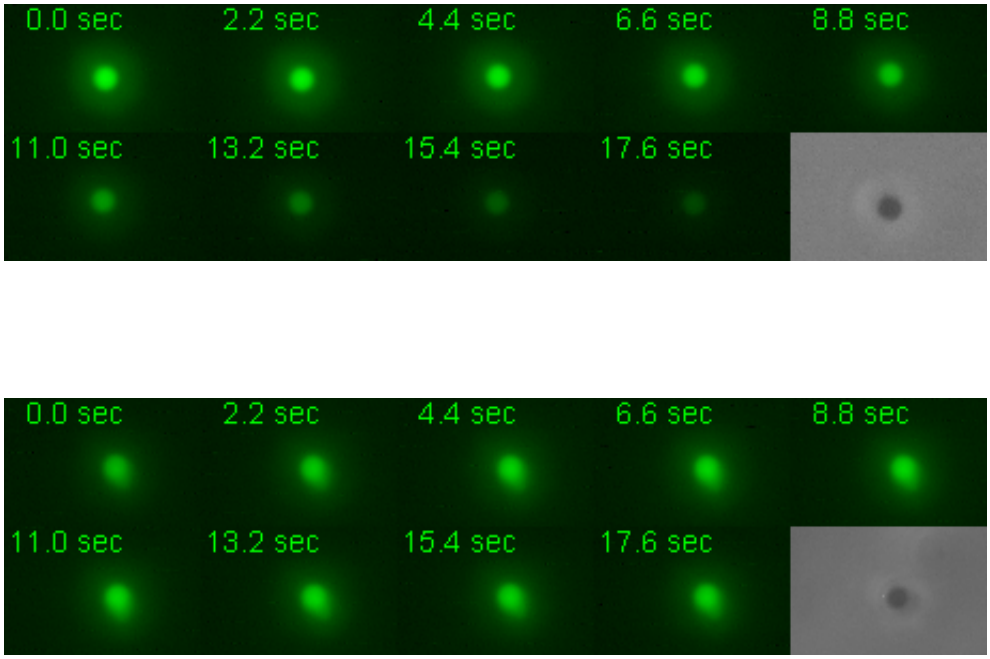

Figure 2.15: Epi-fluorescence video image sequence showing a leaking GFP expressing *E. coli* MJF465 (DE3) cell (upper panel) upon hypo-osmotic shock from LB + 0.5 M NaCl via minimal medium + 0.5 M NaCl + 50 μM H_2O_2 into distilled water. The lower image shows a GFP expressing *E. coli* MJF465 (DE3) cell which was kept under control conditions (first channel with LB + 0.5 M NaCl). These conditions purely led to photobleaching of GFP. The phase-contrast image in each panel was taken after finished GFP loss, i.e. after 30 and 300 s for leakage and bleaching, respectively. (Supplementary videos S2-9 and S2-10)

independent of the salt content and cover a range of 75 s to 125 s. Under hydrogen peroxide assistance, GFP leakage upon hypo-osmotic shock happened fast and on time scales from 8 to 24 s. This range is similar for both investigated salt concentrations (+ 0.3 M NaCl and + 0.5 M NaCl). This situation changed when the hydrogen peroxide support was omitted. Each cell culture seemed to split into two species of cells, ones that showed fast GFP leakage with time constants from 5 to 9 s, which is even faster than under hydrogen peroxide support, and cells that behaved like under control conditions where no GFP leakage occurred at all. In a few rare cases, e.g. the blue trace in figure 2.17 (lower panel), individual *E. coli* cells first leaked out GFP and then suddenly switched to a state that was dominated and could be characterised by pure GFP bleaching. Generally, cell growth at lower NaCl concentration (LB + 0.3 M NaCl) still yielded cell cultures that were susceptible to lysis upon hypo-osmotic shock. Cells grown in LB + 0.5 M NaCl showed mostly a hypo-osmotic shock reponse that resembled the behaviour under control conditions. This again underlines the importance of the oxygen supporting system H_2O_2.

An intriguing feature of all GFP leaking MFJ465 cells was their dark appearance in phase-contrast mode after completed and often fast GFP loss (last images in both panels of fig. 2.15). As shown in the previous section, without GFP expression, the lysed *E. coli* cells leaked the ribosomes and protein or burst upon hypo-osmotic shock which indicates that the observed cell wall or membrane lesions are larger than the ones occurring during GFP expression.

A lysogenic strain (DE3) of the *E. coli* wild-type FRAG1 was not available. Hence, hypo-osmotic shock experiments with GFP expressing FRAG1 cells could not be performed. However, it can be reasonably assumed that such a strain would behave similar during hypo-osmotic shock to MJF465 cells kept under control (i.e. high-salt) conditions.

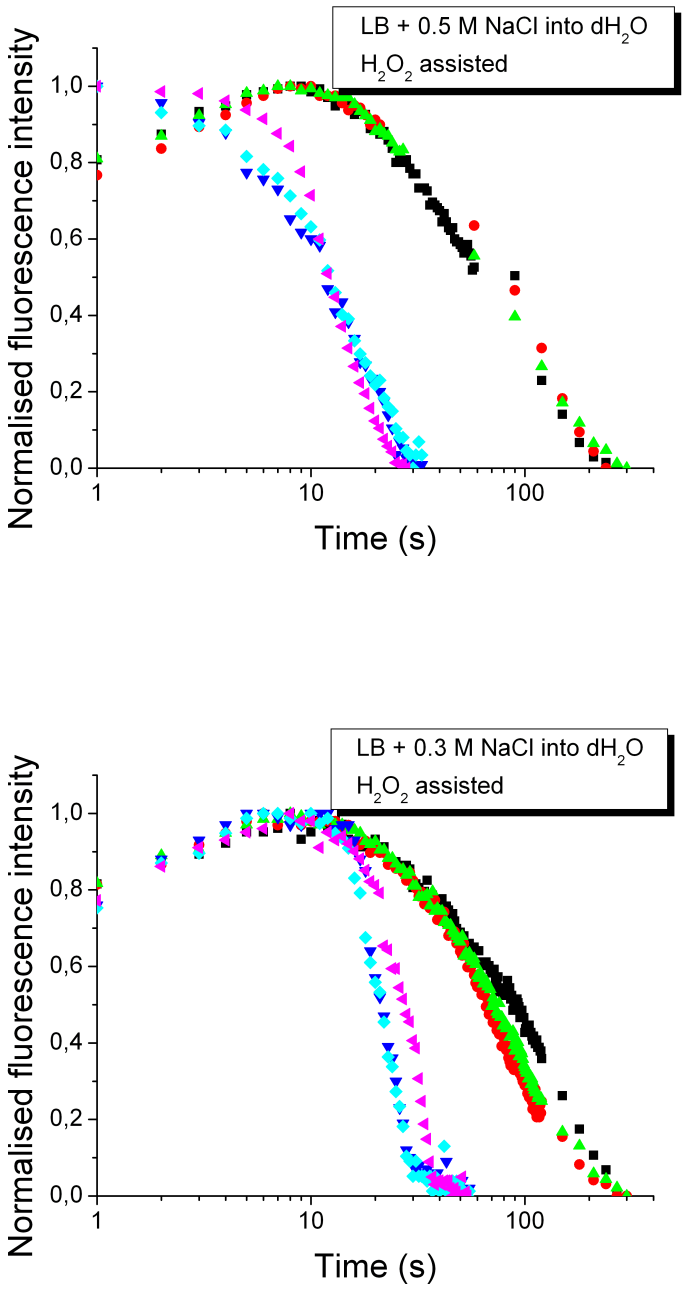

Figure 2.16: Fluorescence traces of hypo-osmotically shocked GFP expressing MJF465 cells (blue, cyan, magenta traces). In both panels the hypo-osmotic shock was assisted by a hydrogen peroxide containing (middle) channel in the microfluidic device. The hypo-osmotic shock condition is given in the panels. The black, red and green traces are control cells that were kept in the high-salt channel and purely subject to GFP photobleaching. The number of individual cells analysed for the hypo-osmotic shock from LB + 0.5 M NaCl into distilled water was 14 (shock) and 8 (control). The number of individual cells analysed for the hypo-osmotic shock from LB + 0.3 M NaCl into distilled water was 14 (shock) and 10 (control).

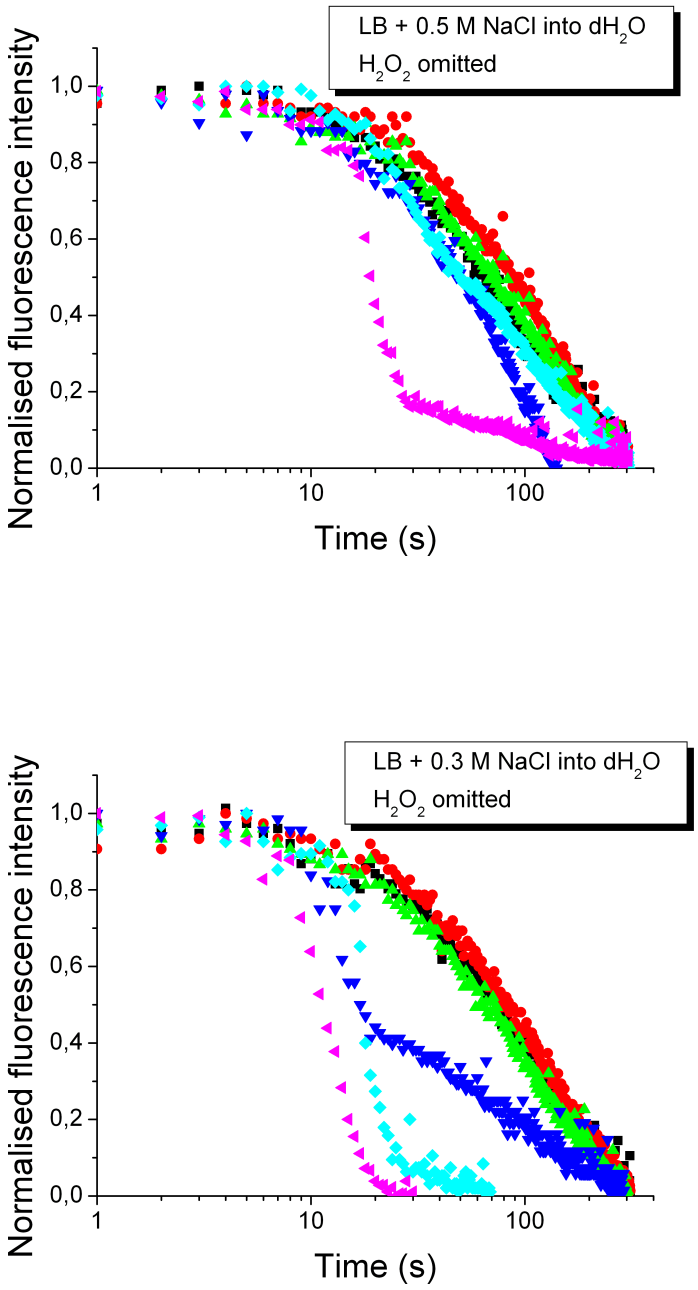

Figure 2.17: Fluorescence traces of hypo-osmotically shocked GFP expressing MJF465 cells (blue, cyan, magenta traces). In both panels hydrogen peroxide assistance was omitted during the hypo-osmotic shock . The hypo-osmotic shock condition is given in the panels. The black, red and green traces are control cells that were kept in the high-salt channel and purely subject to GFP photobleaching. The number of individual cells analysed for the hypo-osmotic shock from LB + 0.5 M NaCl into distilled water was 14 (shock) and 9 (control). The number of individual cells analysed for the hypo-osmotic shock from LB + 0.3 M NaCl into distilled water was 18 (shock) and 9 (control).

2.7 Discussion

Many wild-type bacterial cells possess four different kinds of mechanosensitive channels, MscL, MscS, MscK and MscM, whose action is triggered when the single cell experiences a sudden drop in osmolarity in its environment. Such an event may happen to soil bacteria during a rain fall after a drought period, to uropathogenic bacteria upon urinary dilution or to bacteria inhabiting the gut of mammals, e.g. *E. coli*, as a result of the mammal's daily routine. Patch-clamp experiments of cell spheroplasts or membrane reconstituted MS channel proteins have shown that MS channel gating happens on the timescale of a few milliseconds (Martinac *et al.*, 1987; Sukharev *et al.*, 1994). However, until very recently it remained elusive on which timescale single bacterial cells react if these channels fail to gate or when MS channel activity is deleted.

Optical tweezers combined with microfluidics have provided a powerful tool to successfully image single-cell lysis of *E. coli* during a hypo-osmotic shock, thus addressing questions of cell integrity and time response.

2.7.1 What happens to an *E. coli* cell during a hypo-osmotic shock?

The present results clearly show that cell wall and cell membrane lesions occur on a very rapid timescale in individual *E. coli* cells during a hypo-osmotic shock. Phase-contrast imaging confirmed that both wild-type and MS-channel deficient *E. coli* cells are susceptible to lysis on a timescale faster than the image acquisition rate, i.e. 200 ms. The time gap between a few and 100 milliseconds could, unfortunately, not be bridged at the time the experiments were carried out due to camera availabilities. The finding that also wild-type cells lyse is not unexpected as previous bulk experiments have shown that a small fraction of these cultures dies during a hypo-osmotic shock.

Figure 2.18 shows characteristic hypo-osmotic shock timetraces for the different classes of cellular events observed. Two predominant events were observed using phase-contrast microscopy: Fast cell bursting accompanied by subsequent vanishing of all debris occurs within less than 200 ms. In some instances cell bursting happened during one second and could be visualised in several image frames. The second path to cell lysis displayed leakage of ribosomes and protein from the cytoplasm. Within 200 ms, individual *E. coli* cells suddenly lost contrast. The cell ghost, i.e. the cell membranes and cell wall, usually remained for a few seconds in the optical trap and then mostly disintegrated.

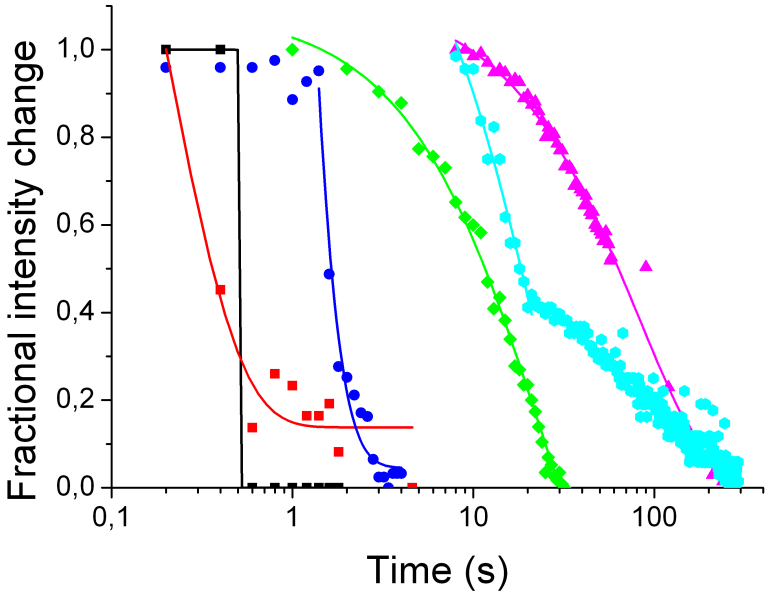

Figure 2.18: Summary of individual downshock traces characterising the different classes of cellular events. Cell bursting with subsequent vanishing of all debris (black squares) occurs in less than 200 ms and has been approximated by a sigmoidal function (fit not meaningful). All other events were fitted with a mono-exponential decay function ($I = I_0 * exp(-t/\tau)$). Phase-contrast leakage (red squares) happens fast and on a time scale of 200 ms. The bursting of a GFP expressing cell (blue circle) is rare (time constant τ 0.38 s). GFP leakage (green diamonds) and GFP photobleaching (magenta triangles) happen on time scales τ of 23 s and 83 s, respectively. Individual traces of GFP-expressing cells that were hypo-osmotically shocked without hydrogen peroxide support (cyan hexagons) showed switching from GFP leakage to GFP bleaching behaviour (time constants 28 s and 91 s, respectively).

The visualisation of GFP expressing *E. coli* cells added a new dimension to our understanding of hypo-osmotic shock. GFP is a protein (Tsien, 1998) with a hydrodynamic radius of 1.6 nm (Busch *et al.*, 2000). *A priori*, it has to be mentioned that these cell cultures were in a physiologically stressed state indicated by cell filamentation. This is most likely the result of an SOS response in which cell division is blocked accompanied by reduced formation of septa (Neidhardt *et al.*, 1996) which are the weakest points of the cell wall. Hence, without triggering the SOS response, rupturing observed with phase-contrast microscopy is likely to propagate from the septa. On this basis it can be understood why the leakage of ribosomes is frequently observed without GFP expression, however becomes extremely rare when GFP expression (leading to stress) is switched on. The ob-

servation of GFP leakage from individual *E. coli* cells happened on a timescale of 7 to 24 s for individual cells (fitted time constants). This is between 1 and 2 orders of magnitude larger than cell leakage observed with phase-contrast microscopy. Interestingly, these cell cultures seem to leak only GFP and most likely other proteins. After completed GFP leakage, in phase-contrast mode, all previously GFP expressing cells appeared dark which unambiguously shows that the ribosomes did not leak from the cells. This finding, in turn, indicates that the picture obtained through phase-contrast measurements may be incomplete and, in particular, that the cell numbers (lysis *vs.* survival) must not be overinterpreted.

2.7.2 Which lesions occur in the cell wall and membrane?

In summary, there appear to be four distinct, observable cell categories, namely, bursters, two types of leakers - ribosomes and the majority of protein *vs.* small proteins only - and survivors. These results raised questions about the cell wall and membrane integrity during hypo-osmotic shock. The model for the bacterial cell wall is still under debate and has not yet been elucidated. Hence, this is a first attempt to interpret the present findings in the light of current structural knowledge.

In principle, it is unusual that such discrete classes of events are observed which happen on very different time scales. Clearly, specific structural rearrangements of the *E. coli* cell wall and membrane must be created leading to either bursting or one of the two types of leakage.

Using the same experimental conditions as Levina *et al.* (1999), bulk hypo-osmotic shock experiments which employ the DNA intercalating dye YOYO-1 in the shock medium have shown that the majority of wild-type cells are protected by use of their MS channels. Only in a small subfraction of 6.5% do the *E. coli* FRAG1 cells suffer from cell wall or membrane lesions which allow the dye to penetrate the cell and stain the bacterial nucleoid. In case of the mutant MJF465 strain which has no means to protect itself against a hypo-osmotic shock, 51.7% of all cells suffer from lesions large enough to allow YOYO-1 penetration. A disadvantage of this assay is that completely lysed cells with their ribosomes dissoluted cannot be analysed and are not reflected in these figures. Nevertheless, this YOYO-1 staining assay shows that cell wall or membrane lesions occur to a large extent in an unprotected mutant during hypo-osmotic shock.

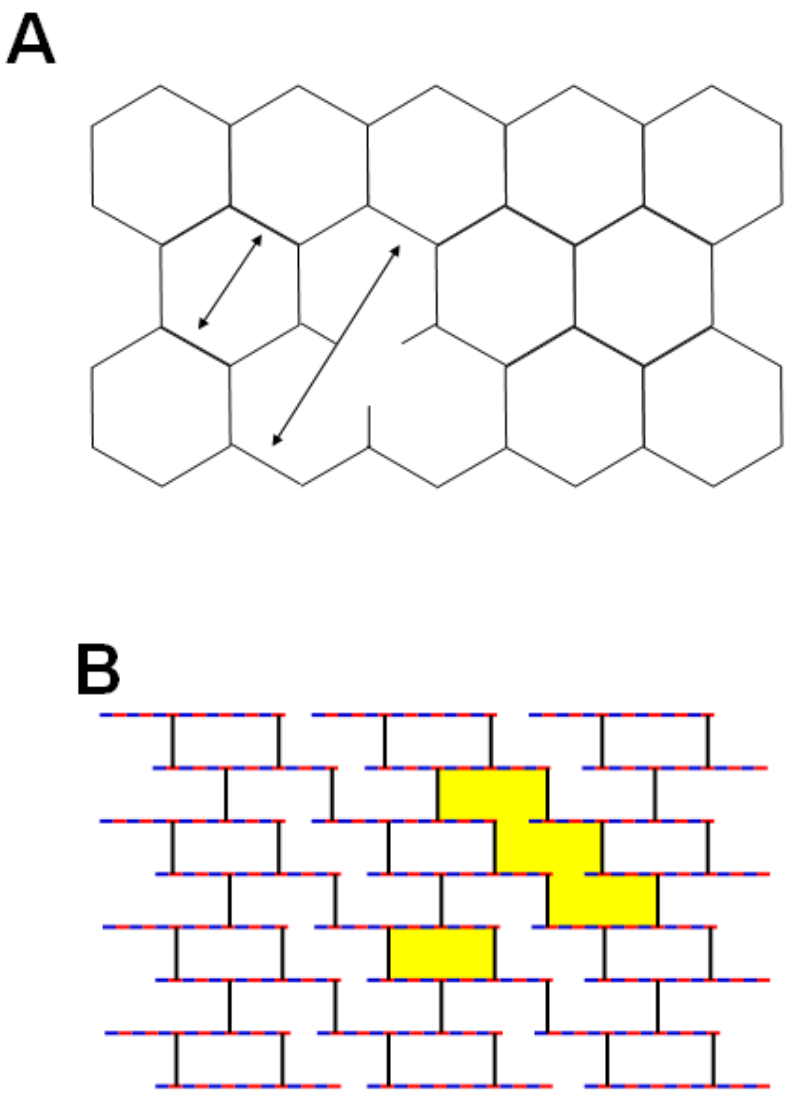

Figure 2.19: Two different models for the cell wall shown with pores of different size. The peptide strands are shown in black and the two sugars NAG and NAM are shown in blue and red colour, respectively. Both patches shown are viewed from outside the cell and lie parallel to the cell membrane. **A** In the scaffold model, the sugar strands stand perpendicular to the cell membrane (and paper) plain. Following Meroueh *et al.* (2006), the peptide strands assume 120° angles and, thus, form hexagonal pores of 7 and 12 nm (diameter) size indicated by arrows, respectively. **B** In the horizontal layer model, drawn for uniform glycan strand length (of 7 NAG-NAM units), only every second peptide chain is shown which is linked to a neighbouring glycan strand. The other peptide chains (not shown) point above and below the paper plain and link to other murein layers, if present. Analogously to the scaffold model, two different pores may form (shown in yellow shade). *In vivo* measurements found that the largest pores have a radius of up to 3 nm (Demchick & Koch, 1996; Vazquez-Laslop *et al.*, 2004).

At the single-cell level, the hypo-osmotic shock response appeared more drastic and could be monitored in real-time using video imaging. GFP-expressing MJF465 cultures have revealed that, at both NaCl concentrations used (0.5 M NaCl and 0.3 M NaCl), the cell wall and cell membrane lesions that occur during a hypo-osmotic shock are large enough to leak GFP which has a hydrodynamic radius of 1.6 nm (Busch *et al.*, 2000) and most likely other proteins of that size range. Compared to YOYO-1 uptake which is a smaller organic molecule this sets a new size limit for the cell wall and membrane lesions. Interestingly, these particular cultures still appear dark under a phase-contrast microscope which confirms that the majority of protein and ribosomes remain in the cell. GFP leakage can theoretically occur without ruptures in the cell wall which, under exponential-phase growth conditions, has pores in the nanometre size range (Vollmer *et al.*, 2008). Earlier, Demchick & Koch (1996) estimated that the isolated and relaxed peptidoglycan has pores with a mean radius of 2.06 nm. In the living cell, under the influence of turgor pressure, the stretched murein was shown to allow penetration of proteins up to 100 kDa in size matching radii of 3.1 nm (Vazquez-Laslop *et al.*, 2001). Hence, it seems plausible that solely membrane disruptions occur and the cell wall remains intact. GFP leakage and YOYO-1 penetration occurs through these disrupted membranes which may later reseal themselves to regain cell integrity. Individual GFP leakage traces (fig. 2.17), obtained without hydrogen peroxide support, show two states. The first state is characterised purely by GFP leakage. Suddenly, individual cells switch to a second state which is purely characterised by GFP bleaching. Between these two states, probably membrane resealing, driven by the hydrophobic effect, takes place which prevents further GFP leakage and gives rise to pure GFP photobleaching.

Theoretical considerations of the pore sizes according to the two different cell wall models manifest that no cell wall ruptures are required in order to allow penetration of middle-sized proteins and organic molecules in and out of the cell. As a direct response to a hypo-osmotic shock, the murein sacculus may further stretch out to maximise the size of its pores (shown in fig. 2.19 for the different models). Based on the number and type of chemical bonds involved in the cell wall structure, the maximum pore sizes can be calculated. To calculate the pore circumference, an all-trans chain of all chemical bonds is assumed. Data for the C-C, C-N and C-O bond lengths as well as for the C-C-C, C-O-C and C-N-C angles were taken from Kaye and Laby (1986). Using the equation $\mathrm{effectivebondlength} = \sin(\mathrm{angle}/2) * \mathrm{bondlength}$, this leads to effective C-C, C-N and C-O bond lengths (in the chain) of 1.25, 1.20 and 1.17 Å, respectively. No matter which model is considered, upon reaching maximum cell wall stretching even the small pores

become large enough, i.e. 5.9 and 10.7 nm diameter for the horizontal layer and scaffold model, respectively, to allow leakage of small proteins, such as GFP. Thus, although given that stressed and starving cells strengthen their cell wall by synthesis of additional peptide crosslinks (Stokes *et al.*, 2003; Vollmer *et al.*, 2008), GFP leakage from GFP-expressing *E. coli* can be explained and understood. Table 2.4 summarises the calculated figures for both models and the two smallest pores known.

Pore sizes in the cell wall					
Horizontal layer model: smallest pore (Tessera)					
Structural unit	# N-C	# C-C	# C-O bonds	Circumference	Diameter
2 peptide bridges	28	28	0		
8 NAG-NAM repeats	0	48	32		
4 muramic acid linkers	4	4	8		
Sum	32	80	40	**18.5 nm**	**5.9 nm**
Horizontal layer model: larger pore					
6 peptide bridges	84	84	0		
16 NAG-NAM repeats	0	96	64		
12 muramic acid linkers	12	12	24		
Sum	96	192	88	**45.9 nm**	**14.6 nm**
Scaffold model: smallest pore					
6 peptide bridges	84	84	0		
6 NAG-NAM repeats	0	36	24		
12 muramic acid linkers	12	12	24		
Sum	96	132	48	**33.7 nm**	**10.7 nm**
Scaffold model: larger pore					
12 peptide bridges	168	168	0		
12 NAG-NAM repeats	0	72	48		
24 muramic acid linkers	24	24	48		
Sum	192	264	96	**67.3 nm**	**21.4 nm**

Table 2.4: Calculation of pore sizes for the different cell wall models.

On the other hand, standard MJF465 cultures grown in LB + 0.5 M NaCl sub-

jected to a hypo-osmotic shock clearly leak out protein and ribosomes suggesting that the cell wall and membrane lesions in these cultures are larger. This hypothesis is corroborated by cryo-electron microscopy images of hypo-osmotically shocked cell cultures (Nicolas Hayward, personal communication). Besides intact cells containing a nucleoid, *E. coli* cells suffering from lesions in the size range of 100 nm were found (fig. 2.20). These are big enough and explain the escape of large cellular structures, such as the nucleoid (500 nm) and the ribosomes (20 nm diameter) from the cell (Neidhardt *et al.*, 1996; website on *E. coli* statistics). The latter are the cause for the dark contrast of cells in phase-contrast microscopy (Neidhardt *et al.*, 1996). Interestingly, the largest well-defined known pores consistent with the scaffold model would just allow the escape of ribosome structures without necessary cell wall breakage. The nucleoid, however, would remain inside the cells. Nevertheless, as can be clearly seen from the EM and many phase-contrast images, leakage always occurs to completion releasing both the nucleoid and the ribosomes and leaving a disintegrating cell ghost behind. Unfortunately, EM data using GFP-expressing *E. coli* cultures are currently not available, but would be desirable for a direct comparison with the optical tweezer assays.

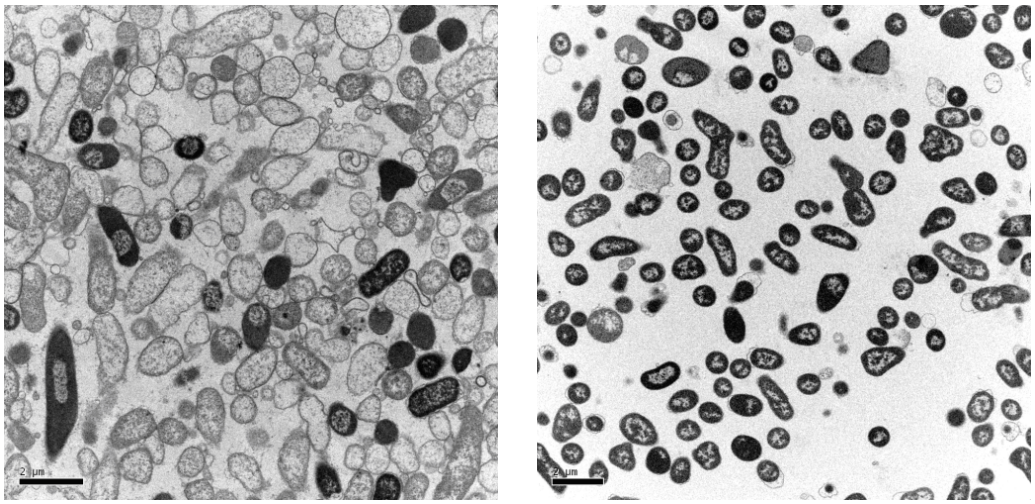

Figure 2.20: Cryo-Electron microscopy images of freeze-fractured MJF465 cultures subjected to hypo-osmotic shock (left image) and control conditions (right image) (data from Nicolas Hayward). The *E. coli* cultures were grown in LB + 0.5 M NaCl and harvested with minimal medium + 0.6 M NaCl and then either diluted (1/19 vol/vol) in minimal medium (shock) or minimal medium + 0.6 M NaCl (control). The scale bar is 2 μm.

Furthermore, many apparently intact cell ghosts and small vesicles were found using EM. This, however, may be the result of the freeze-fracture technique which

images only an arbitrary sample plane. Thus, one may miss out the ruptured region of lysed cells. No patches of the cell wall and the membranes were seen with this method which may reflect that these entities rupture only at their weakest point giving rise to leakage. A reason for the observed differences in cell leakage behaviour with and without GFP-expression may be that no septum formation takes place in the GFP-expressing *E. coli* which, apart from one observed exemption, prevents the occurrence of large-scale lesions (100s of nanometres). The cell wall lesions observed with EM look like the ones computed by Huang *et al.* (2008). In their study, single missing glycan or peptide bridges were the starting points for large cell wall cracks which lead to the fatal consequence of cell leakage during a hypo-osmotic shock challenge. This model also explains why in many cases cell ghosts can be clearly observed after the first quick step of cell lysis.

2.7.3 Outlook

The presented data allowed a first detailed insight into the single-cell fate during hypo-osmotic downshock and could shed new light on bacterial responses during extreme environmental changes. Nevertheless, fundamental issues remain to be solved, namely and most prominently the solution of the 3D cell wall structure of *E. coli* and other, Gram-positive, bacteria. AFM and EM are promising tools that may address this question in a suitable manner. A verified and commonly accepted model would also give a proper basis for the modelling of forces resting on the cell wall elements and, thus, elucidate the progression of cell wall failure during osmotic stress.

Based on the described assays, future work may address the following aspects and implement experimental modifications to pave the way to a more complete understanding of cellular hypo-osmotic downshock. The use of faster, commercially available EM-CCD cameras that can image on the millisecond time scale would allow kinetic characterisation of the fastest lysis events observed in this study in more detail. Besides staining the cytoplasm with GFP, a fluorescent cell membrane stain, e.g. FM 4-64, may be applied to the cell cultures before hypo-osmotic shock to allow a better assessment of what happens to the cell membranes. Such an assay would also shed light on the nature of membrane bulges (see for example Huang *et al.*, 2006), if present in these bacterial cultures. The firing of solutes like potassium and glutamate ions from wild-type *E. coli* cells during channel gating could be also imaged using specific solute stains and fast EM-CCD cameras which can give insight into single-MS channel dynamics.

Besides elucidating the failure of the cell wall and membranes during a hypo-

osmotic shock, the major effort of the research community will be directed towards a detailed and comprehensive understanding of MS channel gating. Several intermediate, sub-conducting states were found in the past (Powl *et al.*, 2003; Perozo *et al.*, 2002a,b) which may be further characterised by X-Ray crystallography and computer simulation. Advanced analysis of the cell membrane interactions with the MS channels is also required (Wiggins & Phillips, 2005) which in turn may answer under which circumstances MS channels fail to gate in wild-type bacterial cells.

An interesting side aspect has arisen from the observation of downshock traces of GFP-expressing *E. coli* MJF465 (DE3) cells. Tsien (1998) has reported a rate constant of 4 hours for the last (oxygenation) step of GFP chromophore maturation when molecular oxygen was readmitted to a growing bacterial cell culture. Under the conditions chosen in the presented experiment, i.e. hydrogen peroxide assistance, this process was much faster and happened within seconds. Further investigation of this finding may reveal fundamentally new insights into GFP and hydrogen peroxide assisted cell maintenance.

The findings reported in this chapter along with the EM data of Nicolas Hayward are currently being published.

Chapter 3

Homologous recombination in *Bacteroides fragilis* studied by single-molecule TIRF microscopy of the AddAB enzyme

3.1 Recombination

Genetic recombination is a biological process that rearranges genes or gene fragments both within one chromosome and between chromosomes of different organisms (Schumann, 2006). It is found in eukaryotes and prokaryotes with analogous proteins carrying out the same functions in these two domains of life. On a molecular basis, all recombination events involve cutting and ligation of DNA into new combinations. Three different recombination mechanisms are known: site- (or sequence-)specific, illegitimate and homologous recombination. The latter mechanism is of interest in this thesis and described in detail in the following subsection.

Site-specific recombination occurs at specific single sites within a recombining sequence. Two site-specific recombinase families exist: the resolvase/invertase and the integrase family. Integration systems are used by many bacteriophages, such as lambda, to integrate their genome into a bacterial chromosome and produce a lysogenic strain. Inversion systems regulate gene expression and generate genetic diversity within a population by rearranging DNA in a well-controlled manner happening at low frequency.

Illegitimate recombination occurs between DNA sequences that share little homology. The resulting DNA rearrangements can be deletions, translocations

or insertions. An important mechanism is the transposition of genetic elements which relates to gene mobility with simultaneous gene duplication. Insertion elements are usually short (600 to 1,500 bp) and code for their transposition and regulation. Transposons can be up to 25 kbp long and code additionally for antibiotic resistance genes. Transposable bacteriophages, such as Mu, use this mechanism to propagate their own DNA into a bacterial chromosome.

3.1.1 Importance of homologous recombination

Homologous recombination (HR) occurs between DNA strands of sufficient homology and is an important mechanism involved in three different biological functions:

- Reparation and restart of broken or stalled replication forks
- DNA repair
- Exchange of genetic information by DNA rearrangements.

Different cellular events can produce dsDNA breaks (DSBs) which pose a threat to the living cell which needs to be dealt with. DSBs can result through the action of ionising radiation, oxygen radicals and DNA-damaging agents (McGlynn & Lloyd, 2002). During the progression of replication forks DSBs can arise when a nick, i.e. a single bond in the sugar-phosphate backbone broken, on one of the DNA strands is encountered (Fig. 3.1). The replication fork can also be stalled because of defects in the replisome machinery or a block in the DNA strands, such as DNA base damage, chemical crosslinks or a DNA lesion in one of the template strands that block the progression of the DNA polymerase.

3.1.2 DNA replication and restart of broken replication forks

The replisome is a complex machine comprising many different enzymes in *E. coli*: A γ-complex loader is the central part and holds the replicative helicase DnaB and the polymerase complexes which are attached to and stabilised on the DNA by β-sliding clamps (Schumann, 2006). DnaB runs ahead of the replication fork and has to unwind the parental DNA which is a necessary step for the leading- and lagging-strand-polymerase complex to synthesise the daughter strands. Both DNA polymerase complexes proceed in the 5' to 3' direction. As a result of this, the leading-strand is synthesised continuously whereas the lagging strand is synthesised discontinuously and requires to be primed by small

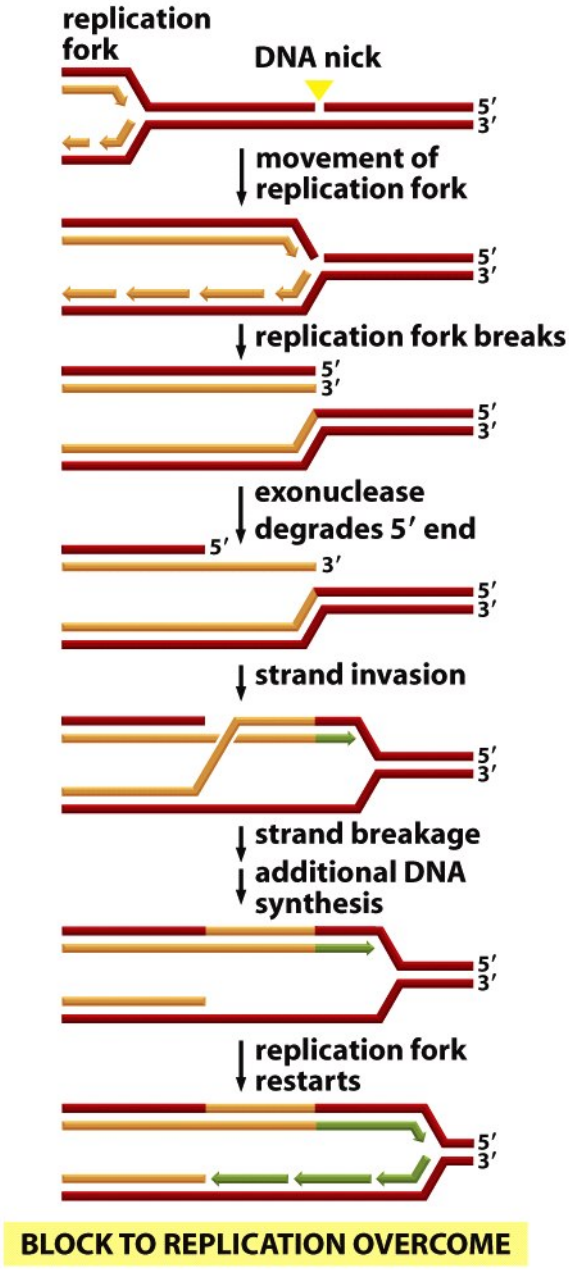

Figure 3.1: The replication fork has a leading (upper) and a lagging (lower) strand that both proceed in the 5' to 3' direction (represented by arrows). Upon encountering a DNA nick, the replication fork collapses and is then repaired by homologous recombination. An exonuclease will first bind to the DSB and preferentially degrade the 5' DNA end. A homologous sequence is the basis for recombination where strand invasion takes place. Subsequently, DNA synthesis is reinitiated. Controlled strand breakage and additional DNA synthesis enable resumption of the usual replication process.) (Figure taken from Alberts *et al.* (2008))

RNA oligonucleotides, made by the primase DnaG. These discontinuous lagging-strand fragments are called Okazaki fragments. After degradation of the RNA primers, DNA polymerase I first seals these gaps and DNA ligase then completes the lagging-strand synthesis.

In order to cope with DNA lesions during DNA replication, the cell employs two mechanisms (McGlynn & Lloyd, 2002; Michel *et al.*, 2007). Special "translesion" polymerases can bypass the obstacle in order for the replicative polymerase to continue DNA strand synthesis. This process can lead to mutation. The alternative, which diminishes mutations, is recombination. Recombination enzymes are able to form an intermediate from two sister duplexes, known as the "Holliday junction" (Holliday, 1964). A Holliday junction is a structure in which two dsDNA molecules are linked in such a way that they form a cross. In *E. coli* two possible ways exist to resolve these structures and to restart replication which are both only poorly understood: Either the RuvABC helicase/endonuclease complex cleaves two opposing strands at the branch point of the junction which are then sealed by DNA ligase or a cleavage-free pathway is followed. The first way using cleavage can temporarily result in either two independent sister chromatids or in an intermediary D-loop (which is a DNA triplex involving RecA binding to ssDNA and dsDNA). Two sister chromatids can be rejoined by homologous recombination and the D-loop is thought to be targeted by the PriA protein which is able to recreate an active replisome. Both options would thus bypass the lesion and enable the resumption of DNA synthesis. The second way involves the RecG protein which is a helicase that unwinds forked DNA structures and thereby produces a Holliday junction from stalled replication fork strands which spontaneously reanneal. Exonuclease digestion of the ssDNA overhang and rewinding of the Holliday junction recreates a fork structure from which replication can be restarted.

3.1.3 DNA repair

In *E. coli* there are two different pathways for HR which come into play when damaged DNA is encountered and that are named after the enzymes RecBCD and RecF which are responsible for and involved in the above described processes.

The RecF pathway is used during DNA replication and acts upon DNA base lesions or gaps. The 5' to 3' ssDNA exonuclease, RecJ, first recognises such a gap and digests the 5' DNA end. This step may be assisted by the RecQ helicase which unwinds DNA. In the living cell ssDNA is protected by the ssDNA binding protein (SSB) which readily binds to the DNA. In a poorly understood

mechanism, the RecFOR complex recognises this template and replaces SSB by RecA which forms filaments on the ssDNA (Morimatsu & Kowalczykowski, 2003). The RecA-ssDNA filament is capable of invading homologous sequences of dsDNA (Cox, 2007). The resulting Holliday junctions are then resolved by RuvABC.

Fig. 3.1 shows how RecBCD starts processing a broken replication fork. RecBCD (exonuclease V) preferentially binds to and continuously degrades dsDNA ends until it encounters the recombination hotspot, termed chi (crossover hotspot instigation) (Dillingham & Kowalczykowski, 2008; Smith, 2001; Smith *et al.*, 1981; Lam *et al.*, 1974; Stahl *et al.*, 1974). RecBCD then switches its activity from an exonuclease to a recombinase and loads the RecA protein onto the 3' ssDNA end. After homologous strand invasion, RuvABC-mediated strand breakage and additional DNA synthesis, the replication fork restarts after PriA-guided replisome reassembly.

3.1.4 Exchange of genetic information

Although the main function of recombination is replication fork repair (Cox *et al.*, 2000), HR also serves as the fundamental mechanism for horizontal gene transfer, i.e. the transfer of genetic information between two bacterial cells or species (conjugation) or the integration of DNA from a bacteriophage (transduction). The creation of genetic diversity is thought to have arisen as a side function of recombination. In case the genetic material comes from another bacterium, ssDNA is injected into the cell which is subsequently converted to linear duplex DNA by replication. Bacteriophages, on the other hand, inject double-stranded DNA. RecBCD immediately targets the newly presented dsDNA end and promotes recombination using the chi site. If, however, phage DNA is lacking the chi site, it will most likely be completely degraded by RecBCD, unless it is armed with a mechanism that helps it to escape this process. Such means can be for example phage-encoded inhibitors of the RecBCD enzyme that mimic dsDNA, e.g. the Gam protein from phage lambda.

In summary, the chi site is the pivotal element in the action of RecBCD because it regulates whether DNA is repaired or subject to degradation. Its importance can be derived from the fact that it is the third most overrepresented octamer with 1,008 chi sequences being present in *E. coli* (Arakawa *et al.*, 2007). In addition, 75% of all chi sites are oriented towards the origin of replication. The presence of chi enables a discrimination of host *versus* foreign DNA and may be compared to restriction/modification enzymes which recognise and methylate host DNA, but destroy phage DNA.

3.1.5 Homologous recombination enzymes

RecBCD

RecBCD is one of the best studied enzymes and has thus served as a paradigm for understanding homologous recombination and repair. It is composed of the three subunits RecB, RecC and RecD which have a size of 134 kDa, 129 kDa and 67 kDa, respectively (Dykstra *et al.*, 1984; Eichler & Lehmann, 1977). The RecB protein contains seven motifs that are characteristic of superfamily I (SF1) DNA helicases present in the half belonging to the N-terminal part and nuclease motifs which are located near the C-terminus (Gorbalenya & Koonin, 1993; Aravind *et al.*, 2000). RecC was not found to have domains in common with other known proteins. RecD has the same seven helicase motifs that were also identified in RecB (Gorbalenya & Koonin, 1993). The primary structure of RecBCD reveals the presence of two helicase domains and one nuclease domain in the holoenzyme.

RecB has both a DNA-dependent ATPase activity and a DNA helicase activity which acts upon dsDNA in the 3' to 5' direction (Hickson *et al.*, 1985; Boehmer & Emmerson, 1992). For a standard helicase this usually implies the presence of a 3' ssDNA overhang. The RecB protein alone was found to be a weak helicase, but upon interaction of its N-terminal subunit, where the helicase domain is located, with the RecC protein, it switches to a rapid and processive DNA helicase (Masterson *et al.*, 1992). The C-terminal domain in RecB functions as a DNA endo- and exonuclease and is solely responsible for all nuclease activities of the RecBCD holoenzyme (Wang *et al.*, 2000). The same domain interacts directly with RecA (Churchill & Kowalczykowski, 2000) which forms the nucleoprotein filament during DNA repair. The RecC protein binds ssDNA and stimulates the ATPase and helicase activities of RecB. The isolated RecC protein itself does not possess these activities (Masterson *et al.*, 1992). The RecD subunit possesses ssDNA-dependent ATPase and 5'→3' DNA helicase activity (Chen *et al.*, 1997; Dillingham *et al.*, 2003). It binds RecC to form, together with RecB, the RecBCD complex. *In vitro* studies have shown that RecD activates the nuclease functions of RecB and that it enhances the processivity of the RecBCD holoenzyme compared to the RecBC enzyme (Anderson *et al.*, 1997; Korangy & Julin, 1993). It was also shown to be responsible for chi-specific RecA loading of the RecBCD enzyme (Amundsen *et al.*, 2000).

Biochemical activities of RecBCD

The RecBCD holoenzyme possesses many biochemical activities, such as RecA and DNA binding, DNA-dependent ATPase, DNA helicase, ssDNA exonuclease, ssDNA endonuclease, dsDNA exonuclease, as well as Chi-site regulated nuclease and helicase functions. ATPases are enzymes that use the energy gained from ATP hydrolysis (into ADP and phosphate) to carry out biochemical processes. DNA helicases unwind dsDNA into two single strands of DNA. Exonucleases cleave nucleotides one at a time from the end of a polynucleotide chain whereas endonucleases cleave the phosphodiester bond within a polynucleotide chain.

RecBCD is a heterotrimer and has a high binding affinity for dsDNA ends, at a 1:1 binding ratio (Taylor & Smith, 1995). Its optimal DNA binding substrate is a ssDNA overhang of either 6 or 10 bases for the 3' and 5' strand, respectively (Wong *et al.*, 2005). The helicase and ATPase activities of RecBCD are coupled. Double-stranded DNA digestion was observed to be very fast (1,000 bp s^{-1} at room temperature) accompanied by highly processive DNA unwinding (30,000 bp) (Roman & Kowalczykowski, 1989 b,c; Bianco *et al.*, 2001). Both the processivity and rate are much higher for the complete RecBCD complex rather than for the RecB and RecD subunit alone (Dillingham *et al.*, 2003). The ATP-dependent dsDNA exonuclease activity is a result of the coupling of endonucleolytic cleavage of ssDNA which is produced during DNA unwinding by the two helicases (Dixon & Kowalczykowski, 1993). Mg^{2+} ions are required as a cofactor for RecB nuclease activity which is inhibited in the presence of Ca^{2+} ions (Rosamond *et al.*, 1979; Sun *et al.*, 2006). The absolute Mg^{2+} concentration also determines the frequency of ssDNA cleavage and, hence, the size of the nucleotide fragments. Because of its location in the RecB subunit, the nuclease domain degrades the two newly produced ssDNA strands asymmetrically, with a strong preference for the 3' strand (Dixon & Kowalczykowski, 1993) which is hydrolysed into polynucleotides of a length range between 10s to 100s of bases whereas the 5'-terminated strand is cut into kilobase fragments (at physiological conditions) (Dixon & Kowalczykowski, 1995). When the chi-site is encountered, this behaviour switches: Cleavage of the 3' strand nearly stops completely and the 5' strand becomes the main target of the RecBCD endonuclease activity (Dixon & Kowalczykowski, 1993; Anderson & Kowalczykowski, 1997). This polarity switch is a key element in the RecBCD mechanism which downregulates DNA unwinding and digestion and initiates DNA repair. The 3' ssDNA overhang provides the molecular basis for the formation of the RecA nucleoprotein filament. RecBCD thus regulates the competition for ssDNA binding between

the ssDNA binding protein (SSB) and RecA in favour of RecA after chi recognition (Arnold & Kowalczykowski, 2000). Chi recognition happens on a stochastic basis with a maximum probability of 30 to 40% of a successful response (Dixon & Kowalczykowski, 1993). The chi sequence was found to be 5'-GCTGGTGG-3' (Smith, 1981; Bianco & Kowalczykowski, 1997). However, very similar nucleotide sequences can also trigger the RecBCD switch (Arnold *et al.*, 1998).

As already mentioned, RecBCD is an unusual enzyme because it contains two DNA helicases of opposite polarity which each translocate along one of the unwound single DNA strands. Electron microscopy found that RecB is acting on the 3' and RecD on the 5' ssDNA strand (Taylor & Smith, 2003). The same study also found that RecD is the faster and RecB the slower motor which became apparent because of DNA loop formation in addition to the production of two ssDNA tails ("loop-2-tails" model). Nevertheless, RecBCD mutants with only one active motor are still acting as DNA helicases demonstrating the independent action of both the RecB and RecD motor (Dillingham *et al.*, 2005). The rate and processivity of these mutant RecBCD enzymes are largely decreased. But an active RecB motor is required for chi-site recognition and response, whilst an active RecD motor is not (Spies *et al.*, 2005). Depending on the free Mg^{2+} concentration, the motor speeds of both RecB and RecD change. At a limiting Mg^{2+} concentration, RecD is the lead motor, i.e. the helicase, and RecB is the slower motor, i.e. the translocase (Taylor & Smith, 2003). This situation changes, however, after chi recognition. RecBCD moves more slowly with RecB becoming the lead motor. The RecD motor is now known to be inactivated. Earlier explanations assumed RecD ejection from the holoenzyme which was disproved by single-molecule experiments, e.g. using the tethered-particle assay with the bead being attached to the RecD subunit (Dohoney & Gelles, 2001) and using a fluorescent nanoparticle attached to the RecD subunit via a biotin site (Handa *et al.*, 2005). Other single-molecule experiments which looked at continuously unwound lambda-DNA molecules gave a much better insight into RecBCD translocation dynamics and chi interactions (Bianco *et al.*, 2001; Spies *et al.*, 2003). These studies have directly shown that the unwinding rate of RecBCD largely varies within a population due to static heterogeneity and that enzyme pausing at an engineered chi site happens on a timescale of 1 to 15 s. Dynamic disorder for individual RecBCD enzymes was not observed, i.e. a single active RecBCD complex always unwinds dsDNA at a constant rate.

Many of the insights into the RecBCD mechanism gained from biochemical and single-molecule studies were complemented by the solved crystal structure of RecBCD bound to a DNA substrate (Singleton *et al.*, 2004).

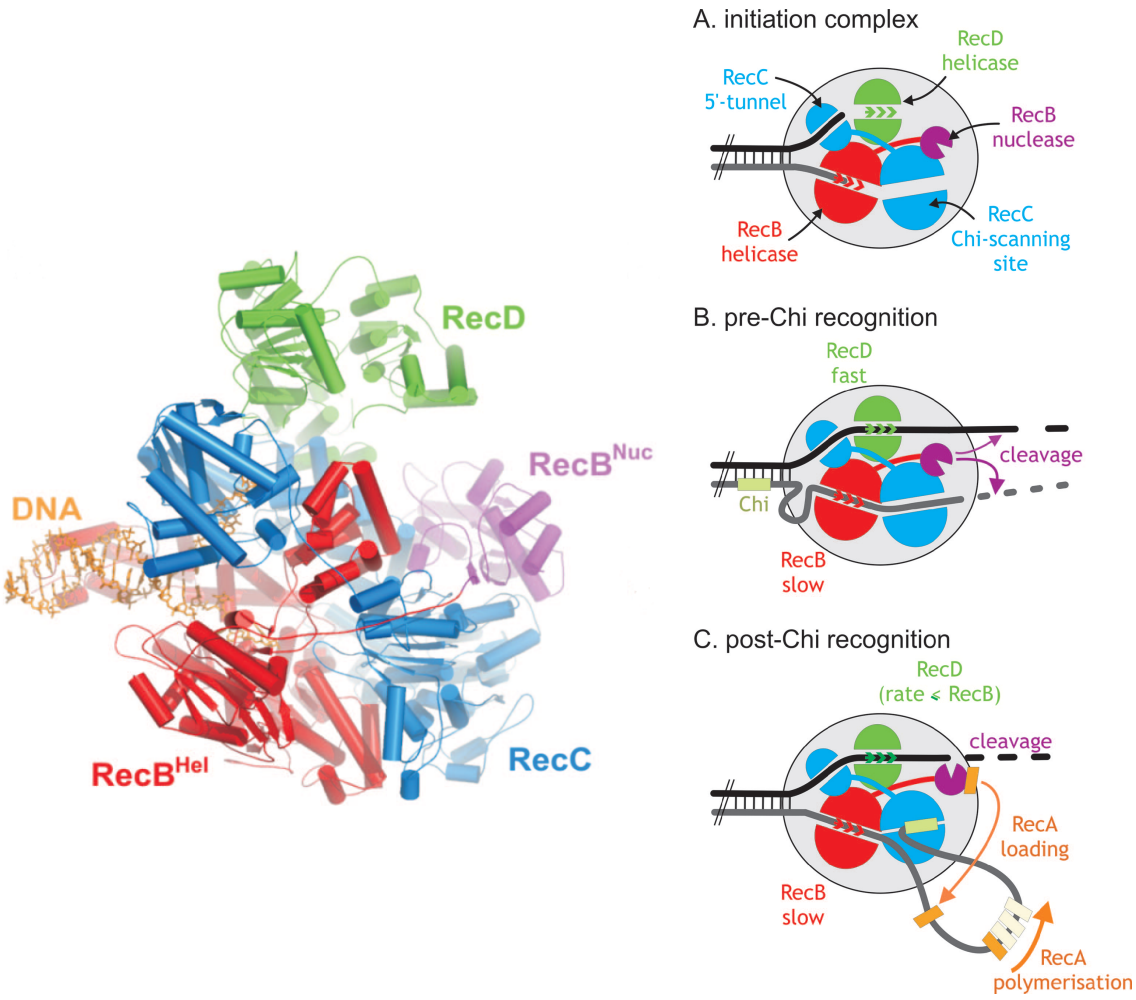

Figure 3.2: RecBCD-DNA crystal structure (left) and model (right) of the initiation complex (taken from Dillingham & Kowalczykowski, 2008). The RecB helicase, RecB nuclease domain, the RecC protein and the RecD helicase are depicted in red, purple, blue and green, respectively. The hairpin DNA substrate is depicted in orange. (A) Cartoon representation of the RecBCD-DNA complex during initiation. After encountering the "pin" in the RecC subunit, the two single-strands of DNA are guided into the RecB helicase and towards the RecD helicase. (B) Before chi site recognition, the faster RecD helicase actively unwinds dsDNA while RecB translocates upon the 3' ssDNA tail, thereby extruding a DNA loop. The RecB nuclease is positioned in such a way that it preferably digests the 3' DNA strand. Between the helicase and nuclease domain of the RecB protein the chi-scanning unit, positioned in a tunnel of the RecC domain, is located. (C) Upon chi site recognition this sequence becomes tightly bound in the RecC tunnel and the whole RecBCD machinery pauses. Translocation resumes then at a diminished rate with the 5' strand still leaving the complex through the RecD tunnel where it is now cleaved more often by the RecB nuclease. A ssDNA loop starts to develop downstream of the chi sequence. The RecB nuclease unbinds from the RecC subunit and actively loads RecA molecules onto the growing ssDNA loop in order to form the nucleoprotein filament required for homologous recombination.

The crystal structure of RecBCD

The crystal structure (fig. 3.2) could elucidate how RecBCD processes the ds-DNA substrate with a blunt end into the two single-stranded DNA molecules which are subsequently degraded into polynucleotide fragments of different size. An enzyme "arm" first makes contact to the dsDNA. A pin structure, located in the RecC subunit, then splits the incoming dsDNA into two strands which are guided into separate tunnels, one in the RecB and one in the RecD subunit. Both these subunits employ their helicase activity and drive ssDNA translocation. In the wild-type RecBCD enzyme the RecD motor is the faster helicase which results in ssDNA loop formation in front of the slower RecB motor. A chi-scanning site located towards the exit of the enzyme searches for a recombination hotspot. The nuclease domain which is positioned in the RecB subunit and at the rear of the enzyme cuts the nascent 3' strand coming out of the RecB tunnel with high preference. The 5' strand is cut less often and only when the dynamically located nuclease domain flips over. A model for the RecBCD enzyme derived from its structure is depicted in figure 3.2. The RecBCD structure confirms that RecC is the central subunit in the holoenzyme binding both the RecB and RecD subunit which themselves do not have any direct binding interaction. Furthermore, it nicely shows how the different subunit tunnels are linked with each other to effectively process DNA.

AddAB and RexAB proteins

A second class of homologous recombination enzymes is the AddAB or RexAB family which is found widely in the proteobacteria (Rocha *et al.*, 2005; Cromie, 2009; Chedin & Kowalczykowski, 2002; el Karoui *et al.*, 1998; Quiberoni *et al.*, 2001). Add stands for "ATP-dependent DNase" and Rex for "recombination exonuclease". Both enzymes carry out the same functions as RecBCD, i.e. DNA recombination and repair. Bacterial cells which are deficient in this enzyme are sensitive to UV light and subsequent DNA damage. Cell viability is also reduced. Likewise, an *E. coli* strain deficient in the *recBCD* genes can be rescued by the expression of the *Bacillus subtilis* AddAB protein (Kooistra *et al.*, 1993) or the *Bacteroides fragilis* AddAB protein (Garry Blakely, personal communication).

Analysis of the protein sequence (fig. 3.3) has revealed that AddA proteins are homologous to RecB because AddA contains an N-terminal SF1 helicase domain, apparent by the presence of seven typical motifs, and a C-terminal nuclease domain. The AddB proteins show only little homology to UvrD-like SF1 DNA

helicases, e.g. RecB and AddA, and RecC. Near the N-terminus the *B. subtilis* AddB contains the Walker A motif (helicase motif 1) which is responsible for the binding and hydrolysis of NTP. This motif is present only in a small subset of the AddB proteins and its helicase activity is apparently inactivated in all of them (Cromie, 2009). AddB also has a nuclease motif towards the C-terminus which was thought to be equivalent to those present in RecB and AddA (Dillingham & Kowalczykowski, 2008). More recently, however, it was shown that *B. subtilis* AddB contains an iron-sulfur cluster within the nuclease domain (Yeeles *et al.*, 2009). This cluster was shown to be crucial for the local structural integrity of this domain and for AddAB binding to dsDNA. Both the Walker A motif and the iron-sulfur cluster were only identified in subsets of AddB proteins which suggests the existence of different kinds and mechanisms of AddB proteins (Cromie, 2009).

As for RecBCD, AddAB proteins are also regulated by the recombination hotspot chi (Chedin *et al.*, 2000) which controls the enzymes' helicase and nuclease activity. The *B. subtilis* chi site was found to be only 5 DNA bases long (5'-AGCGG-3'). AddAB-mediated DNA cleavage occurs symmetrically on both nascent single strands of DNA producing equally sized DNA fragments. Each of the nuclease domains cuts one specific DNA strand (Yeeles & Dillingham, 2007) with the 3' strand being cut by AddA and the 5' strand being cut by AddB.

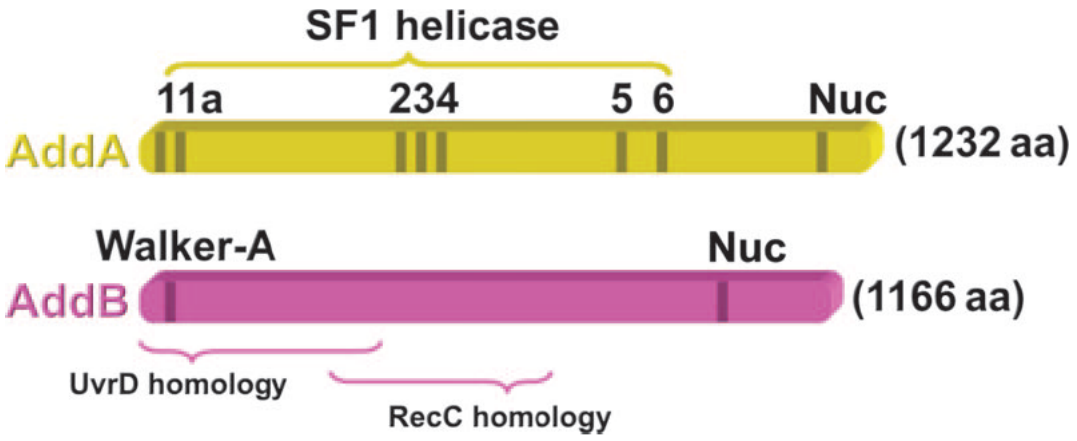

Figure 3.3: Primary structure of the *B. subtilis* AddAB enzyme (taken from Dillingham & Kowalczykowski, 2008). The N-terminal domain in the AddA subunit (shown in yellow) is characterised by seven motifs which are typical of superfamily 1 helicases. The C-terminal domain contains nuclease motifs. The AddB protein (magenta) exhibits weak homology to UvrD-like SF1 DNA helicases and to the RecC protein. The Walker A motif (helicase motif 1), present also in AddA, is found close to the end of the N-terminus. Several nuclease motifs, like the ones in RecB and AddA, are found near the C-terminus.

3.2 Overview on helicases and translocases

AddAB and RecBCD belong to a ubiquituous and diverse group of enzymes known as nucleic acid helicases and translocases. These enzymes play important roles in all domains of life where nucleic acids are processed, e.g. DNA replication, repair, transcription, translation, ribosome synthesis, RNA maturation and splicing, as well as nuclear export processes (Singleton *et al.*, 2007). Both helicases and translocases are DNA- or RNA-dependent ATPases that move in a pre-defined direction along nucleic acids. DNA helicases couple ATP-hydrolysis to the unwinding of dsDNA and RNA duplexes into the component single strands and form part of the main group of nucleic acid translocases. It is to be noted that the presence of helicase motifs does not necessarily imply a helicase activity; NTP hydrolysis of such (translocase) enzymes may be solely coupled to protein directional motion along a nucleic acid template. The translocation rates span a range of three orders of magnitude from a few to 1000s of DNA base pairs (bp) unwound per second. The enzyme processivity is usually high, up to several 10,000 bp, and is regulated by protein-protein interactions (in addition to the chi paradigm for HR enzymes).

Based on current knowledge, Singleton *et al.* (2007) have delineated six superfamilies (SF) of the helicases/translocases and attempted to define a common nomenclature for these enzymes. A recurring motif in many translocases is the AAA^+ fold (ATPases Associated with various cellular Activities) for energy transduction. A core domain comprising tandem-repeats of RecA-like folds is present in all translocases and is the structure responsible for mechanochemical coupling (Ye *et al.*, 2004). NTP binding and hydrolysis induces protein conformations and, thus, provokes mechanical movement. Conserved amino acid residues responsible for NTP binding and hydrolysis, which are equivalent to the Walker motifs of many ATPases (Walker *et al.*, 1982) and an "arginine finger" which is central in energy coupling (Scheffzek *et al.*, 1997) are universal features of the core domains of all superfamilies.

The largest groups of nucleic acid translocases are SF1 and SF2 from which seven classic signature motifs are known (Gorbalenya & Koonin, 1993) which were later extended. Characteristically, for SF1 and SF2 a single polypeptide chain comprises two RecA-like folds whereas the other superfamilies contain hexameric or double-hexameric rings formed from either 6 or 12 RecA folds. All groups are further subdivided according to translocation polarity and ss- *vs.* ds-DNA specificity. SF1 enzymes are always ss-DNA translocases, whilst the SF2 and the ring helicases families contain both ss-DNA and ds-DNA translocases.

A relatively small number of known crystal structures has set the foundation of the classification of superfamilies according to Singleton *et al.* (2007). As this knowledge increases, this topic will have to be revisited. Classical examples of SF1A enzymes which move in a 3' to 5' direction along nucleic acids are the Rep, UvrD and the Pcr helicases (Subramanya *et al.*, 1996; Korolev *et al.*, 1997). SF1B enzymes which move in a 5' to 3' direction include RecD and Dda (Singleton *et al.*, 2004; Nanduri *et al.*, 2002). SF2 is the largest family which includes the DEAD Box RNA helicases (Cordin *et al.*, 2006), the ReQ-like family (Bennett & Keck, 2004) and Snf2-like enzymes (Flaus *et al.*, 2006; Flaus & Owen-Hughes, 2004). The helicases of the SFs 3-6 are homohexameric and share very similar structures, e.g. a RecA or an AAA^+-like ATPase core. The NTP binding sites are located between the monomer interfaces. The SFs 4, 5 and 6 are DnaB-like (Ilyina *et al.*, 1992; Yu *et al.*, 1996), Rho/V-F-ATPase (Skordalakes & Berger, 2003) and AAA^+-like (Erzberger & Berger, 2006), respectively (Singleton *et al.*, 2007).

In summary, all helicases have the RecA/AAA^+-fold in common which is used for the coupling of chemical energy into mechanical motion. These domains can either appear in tandem or in different subunits of the helicase complex to enable translocation along either DNA or RNA.

3.3 Michaelis-Menten kinetics

Important parameters for the kinetic characterisation of an enzyme are the Michaelis constant K_M and the maximum rate constant r_max of the catalysed reaction (Winter & Noll, 1998). The generally assumed reaction scheme is

$$\mathrm{E} + \mathrm{S} \underset{k_{-1}}{\overset{k_1}{\rightleftharpoons}} \mathrm{ES} \xrightarrow{k_2} \mathrm{E} + \mathrm{P}. \tag{3.1}$$

An enzyme E first reacts reversibly with a substrate S to form an enzyme-substrate complex ES, at a rate constant k_1. Thereafter, this complex can either react back to the initial compounds, at a rate constant k_{-1}, or react to product P and enzyme E at a rate constant k_2. The latter reaction step is irreversible. Initially it was assumed that the equilibrium is very fast and, hence, the product reaction is determining the overall rate. The reaction rate r can be calculated according to the dissociation of the ES complex

$$r = -\frac{\mathrm{d}c_\mathrm{ES}}{\mathrm{d}t} = k_2 \cdot c_\mathrm{ES}. \tag{3.2}$$

Taking the equilibrium constant K_D into account

$$K_{\mathrm{D}} = \frac{c_{\mathrm{E}} \cdot c_{\mathrm{S}}}{c_{\mathrm{ES}}} = \frac{k_{-1}}{k_1} \tag{3.3}$$

and that the concentration of free enzyme c_{E}, calculated from the total enzyme concentration $c_{\mathrm{E,tot}}$ and the concentration of the enzyme-substrate complex c_{ES}, is

$$c_{\mathrm{E}} = c_{\mathrm{E,tot}} - c_{\mathrm{ES}} \tag{3.4}$$

this leads to

$$c_{\mathrm{ES}} = \frac{c_{\mathrm{E,tot}} \cdot c_{\mathrm{S}}}{c_{\mathrm{S}} + K_{\mathrm{D}}}. \tag{3.5}$$

Combination with equation 3.2 yields

$$r = \frac{k_2 \cdot c_{\mathrm{E,tot}} \cdot c_{\mathrm{S}}}{c_{\mathrm{S}} + K_{\mathrm{D}}} \tag{3.6}$$

At a very high substrate concentration ($c_{\mathrm{S}} \gg K_{\mathrm{D}}$) every enzyme is saturated with substrate and the rate reaches the limit $r_{\max} = k_2 \cdot c_{\mathrm{E,tot}}$.

The Michaelis-Menten equation can thus be written as

$$r = r_{\max} \cdot \frac{c_{\mathrm{S}}}{c_{\mathrm{S}} + K_{\mathrm{D}}} \tag{3.7}$$

This model was later refined by Briggs and Haldane. Their model assumes that the concentration of the enzyme-substrate complex ES stays constant until all substrate is used. During this so-called steady-state phase, it holds that

$$\frac{\mathrm{d}c_{\mathrm{ES}}}{\mathrm{d}t} = k_1 \cdot c_{\mathrm{E}} \cdot c_{\mathrm{S}} - k_{-1} \cdot c_{\mathrm{ES}} - k_2 \cdot c_{\mathrm{ES}} = 0 \tag{3.8}$$

Hence, c_{ES} can be written as

$$c_{\mathrm{ES}} = \frac{k_1 \cdot c_{\mathrm{E}} \cdot c_{\mathrm{S}}}{k_{-1} + k_2} \tag{3.9}$$

All reaction constants are combined in the Michaelis constant K_{M}

$$K_{\mathrm{M}} = \frac{k_{-1} + k_2}{k_1} \tag{3.10}$$

which, after substitution into equation 3.2, leads to the reaction rate of

$$r = \frac{k_2 \cdot c_{\mathrm{E,tot}} \cdot c_{\mathrm{S}}}{c_{\mathrm{S}} + K_{\mathrm{M}}} \tag{3.11}$$

This equation is still referred to as the Michaelis-Menten equation. In analogy to equation 3.7 $r_{\max}$ is introduced which leads to

$$r = r_{\max} \cdot \frac{c_S}{c_S + K_M} \tag{3.12}$$

By analysing equation 3.12 one finds that if the substrate concentration S is K_M, the reaction rate r becomes $\frac{r_{\max}}{2}$. The Michaelis constant hence represents the substrate concentration at which half of all enzyme active centres are bound to a substrate molecule.

RecBCD and AddAB are two-substrate enzymes. DNA as one substrate is tightly bound to the enzyme and this complex can be assumed as one fixed species (seen as E in the above equations) which uses ATP as a second substrate that is continuously recruited and consumed during the enzymatic reaction.

3.4 Aim and motivation

Homologous recombination is an important mechanism in all living cells of both bacteria and mammalia. In bacteria, the RecBCD enzyme from *E. coli* has served as the paradigm. Recent phylogenetic analysis has shown, however, that the functionally analogous AddAB enzyme is much more prominent in the bacterial world (Cromie, 2009) while the AddAB enzymes have only started being characterised.

RecBCD and AddAB proved to be relevant for bacterial pathogenicity, e.g. in *Salmonella* and *Helicobacter* species (Cano *et al.*, 2002; Amundsen *et al.*, 2008). HR enzymes protect the cell's DNA against the influence of reactive oxygen species, which are produced by the affected host organism, and hence maintain bacterial viability during a resulting SOS response (Dillingham & Kowalczykowski, 2008).

It is currently not known whether the AddAB proteins, equipped with only one single motor helicase but two nuclease domains, behave similar to RecBCD in terms of enzyme rate and processivity. So far, one could only speculate about these relevant aspects because a kinetic analysis of any AddAB enzyme has not been carried out yet.

To address these questions, the AddAB protein from *Bacteroides fragilis* was studied at the single-molecule level within this thesis. *B. fragilis* is a Gram-negative, obligate anaerobic bacterium which inhabits the gut of humans and animals with 10^{11} individual cells found in one gram of faeces. It forms a capsule which protects the bacterium against phagocytosis. *B. fragilis* develops fimbria for adherence and produces several ectotoxins. As an opportunistic pathogen it is involved in infections, such as peritonitis, intra-abdominal abscesses, aspiration pneumonia and brain abscesses (Wexler, 2007; Patrick, 2002).

Studying the *B. fragilis* AddAB enzyme is key for understanding the pathogenic behaviour of this bacterium. In a wider context investigations of the AddAB enzyme give insight into the predominant mechanism of HR and DNA repair in a large range of bacteria. Furthermore, the AddAB enzymes are crucial for horizontal gene transfer and thus related genetic diversity including antibiotic resistance (Cromie, 2009).

3.5 Materials and Methods

3.5.1 TIRF microscopy

The objective-TIRF setup was built around a NIKON Eclipse TE2000-U microscope (Nikon Instruments Europe B.V., Kingston) and is shown in figures 3.4 and 3.5. The microscope was used in conjunction with a 60x (N.A. 1.49) apo-TIRF oil objective (Nikon). Zeiss oil for fluorescence microscopy (Goettingen, Germany) was preferentially chosen as immersion liquid as it does not contain any fluorescent contamination.

Most optical components, except where otherwise stated, were purchased from Thorlabs (Ely) and were mounted on a metric optical table. A collimated Ar ion laser beam (Spectra Physics, Newport, Mountain View, CA, USA) was sent through a 488 nm line filter (Chroma Technology Corp, Rockingham, VT, USA) and varying combinations of neutral density (ND) filters to spectrally clean and attenuate the laser light, respectively. A 10x beam expander (Linos Photonics Ltd, Milton Keynes) was used to spread the collimated laser beam which was then focussed by a f = 400 mm plano-convex lens (with the convex side of the lens facing the incoming collimated beam) onto the objective back-focal plane. The focussing lens and the upper periscope mirror were mounted onto a vertically actuatable 1-dimensional stage. This allowed the systematic displacement of the laser beam parallel to the optical axis of the objective. In this way one can either establish epi-fluorescence, oblique illumination or evanescent-field excitation conditions.

The excitation beam was reflected into the objective by a dichroic mirror separating light at a wavelength of 495 nm. A bandpass filter centred 50 nm around 530 nm which removes the Raman band of water and a 500 nm longpass filter (all from Chroma) were used to collect the emitted fluorescence light that passed back through the microscope objective.

Laser powers		
ND filter	Laser power after ND filter	Laser power after objective (epi-fluorescence mode)
none	2.16 mW	1.22 mW
ND1.0	200 μW	114 μW
ND1.6	49 μW	28.7 μW
ND2.0	16 μW	9.15 μW

Table 3.1: The laser powers on the presented objective-TIRF setup were measured in combination with different Neutral Density filters before the beam expander and after passing the objective.

Figure 3.4: Front view of the TIRF setup:
The TIRF setup was built around a microscope (1) with a sensitive EM-CCD camera (2) attached to the front microscope port. A syringe pump (3) was placed to the left of the microscope with plastic syringes connected via polypropylene tubing to the microfluidic flowcell which was fixed on the microscope table (4).

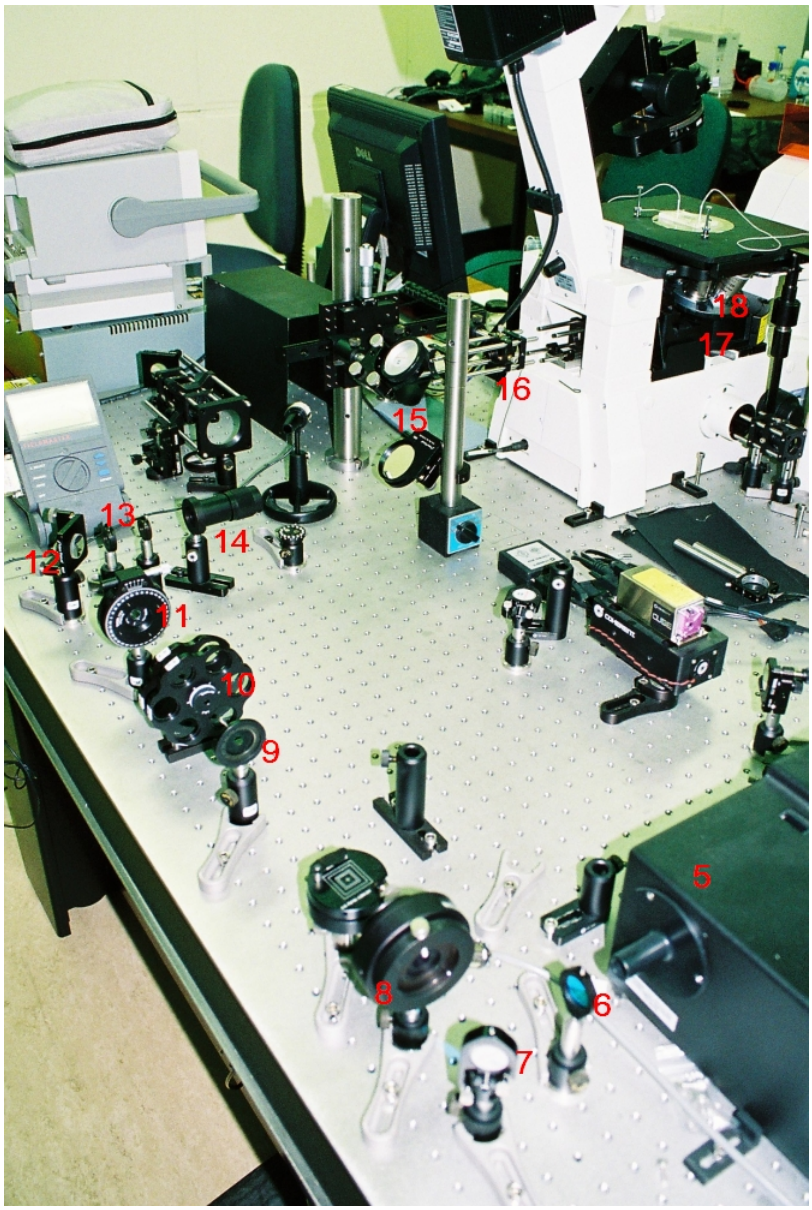

Figure 3.5: Back view of the TIRF setup:
A collimated Ar ion laser beam (5) was sent through a 488 nm filter (6) and different ND filters (10) for spectral beam cleaning and attenuation purposes, respectively. Different mirrors (7, 12) and a periscope (15) enabled steering of the laser beam on and into miscellaneous optical components mounted on the optical table. One mechanical (8) and one manual shutter (11) were used. Apertures (9, 13) were used to suppress reflected and laser stray light. A laser beam expander (14) widened the laser beam 10-fold before being focused by a plano-convex lens (16) into the rear of the microscope.
Inside the microscope the laser beam was reflected on a dichroic mirror housed in the box (17) and focused in the back-focal plane of the high-NA TIRF objective mounted in the revolver (18).

Digital images were acquired with a Luca EM-CCD camera from ANDOR (Belfast), usually attached to the front port of the microscope. Autocooling maintained a stable temperature of -20 °C at the detector. The standard settings for single-molecule imaging were an EM DAC value of 190 (enabled), which enhances the fluorescence signal at the detector, and an exposure time of 0.2 s. For the acquisition of all single-molecule time courses (YOYO-1 intercalation, AddAB-mediated and RecBCD-mediated DNA unwinding), a USB-6218 shutter (National Instruments, Austin, TX, USA) was run at a frequency of 0.5 Hz and a 10% duty cycle, thereby producing 0.2 s pulse trains matching the camera exposure time. Thus, during each time course the sample was illuminated only 10% of the time.

Laser powers were measured with a Fieldmaster (Coherent, Santa Clara, CA, USA) directly after the ND filter and after the microscope objective (while being in epi-fluorescence mode) and are presented in table 3.1. A Richardson test slide (Richardson Technologies Inc., model 80302; Bolton, ON, Canada) was used for microscope length calibration.

3.5.2 Reagents

All chemicals were purchased from Sigma-Aldrich Company Ltd. (Dorset), unless otherwise stated.

3.5.3 Preparation of microfluidic flowcells

Microfluidic flowcells were prepared as described in chapter 2.5.3, except that they had only one inlet and one outlet channel of 2 mm width.

3.5.4 Protein handling

AddAB enzyme expression

The isolation, cloning and expression of the *addA* and *addB* genes was done by Ms Frances Parry and Dr Garry Blakely (School of Biology, The University of Edinburgh). Briefly, an *E. coli* strain deficient in all the *recBCD* genes (denoted ΔBCD) was transformed with the pTrcAB plasmid (derived from pTrc99a, New England Biolabs, Inc. (NEB), Hitchin) harbouring the open reading frames of the *addA* and *addB* genes and the pRARE plasmid (Invitrogen Ltd, Paisley) encoding for rare *E. coli* tRNA codons. An overnight starting culture of this bacterial strain was used to inoculate 2 l of fresh LB broth which was induced

overnight at a temperature of 18 °C when it reached an optical density (OD) of 0.5 with 1 mM IPTG.

All subsequent steps after overnight AddAB expression prior to AddAB purification were carried out in collaboration with Dr Garry Blakely.

Sodium dodecyl sulfate-polyacrylamide gel electrophoresis (SDS-PAGE) was applied to determine the extent of AddAB protein expression at the start of induction and after 18 hr overnight induction.

Cell lysis was done according to a method described in Chedin *et al.* (2006). The cell pellet (from 2 l bacterial culture) was collected by centrifugation (6,000 g for 20 mins at 4 °C, Sorvall RC-5B centrifuge; from Block Scientific, Inc., Nutley, NJ, USA), stored at -20 °C, and resuspended later (after 30 min thawing) in 25 ml 50 mM Tris-HCl (pH 7.4) buffer containing 0.1 mM phenylmethylsulfonyl fluoride, 0.2 mg/ml lysozyme and 1.5 mM EDTA by stirring for 30 min at 4 °C. Solid Brij-58 was slowly added in six individual portions in order to finally reach a concentration of 0.3% w/v. All subsequent purification steps were also carried out at 4 °C. The lysed cell culture was centrifuged twice at 20,000 g for 30 min in order to remove cell debris. Solid $(NH_4)_2SO_4$ was added slowly to the supernatant up to a final concentration of 50% w/v which produced a precipitate containing the AddAB protein that was collected by centrifugation. The protein pellet was resuspended in 20 mM Tris-HCl (pH 7.4), 0.1 mM EDTA, 0.1 mM DTT and 100 mM NaCl and dialysed overnight against 1 l of this buffer. A SDS-PAGE gel was run to examine the amount of AddAB protein in the preparation.

SDS-PAGE

Polyacrylamide gels were prepared according to Sambrook *et al.* (2001) and consisted of a running gel (3.5 ml) and a stacking gel (0.5-1.0 ml) layered on top of the running gel in a PAGE assembly unit. The running gel contained 4.8 ml 30%/0.8% w/v acrylamide/bis-acrylamide solution, 3 ml 4x buffer (1.5 M Tris, pH 8.8), 120 μl 10% w/v SDS solution, 4 ml distilled water, 8 μl TEMED and 100 μl APS. The stacking gel contained 1.5 ml 30%/0.8% w/v acrylamide/bis-acrylamide, 2.25 ml 4x buffer (1.5 M Tris, pH 6.8), 90 μl 10% w/v SDS solution, 5 ml distilled water, 8 μl TEMED and 100 μl APS. After pouring both individual gel precursor solutions, 60 min gel polymerisation time was allowed. Where precast protein gels were used, these were obtained from Invitrogen.

The collected cell pellets taken at different stages of expression, protein samples and a protein ladder (10-250 kDa, New England Biolabs) were boiled for 10 min in 9 aliquots of SDS-PAGE loading buffer (1x: 50 mM Tris-HCl, pH 6.8, 2%

w/v SDS, 10% w/v glycerol, 1% w/v β-mercaptoethanol, 12.5 mM EDTA, 0.02% w/v bromophenol blue). Between 10 and 20 μl of these samples were loaded into the gel lanes. The gel was completely covered with SDS running buffer (25 mM Tris-HCl, 0.2 M glycine, 0.1% w/v SDS). A starting voltage of 200 V was applied along the direction of the lanes for 90 min. Thereafter, the protein gels were stained for 1-2 hr by gentle shaking in staining solution (10% glacial acetic acid, 30% isopropanol, 60% distilled water and 0.5% w/v Coomassie brilliant blue) and subsequently treated for 2-16 hr with a destaining solution (10% glacial acetic acid, 30% isopropanol and 60% distilled water). This last solution was applied fresh at least twice and until clear bands originating from the proteins were visible. Gels were dried and photographed with a CCD camera (Fujifilm FinePix S602Zoom) and processed further with the freely available software IrfanView.

Identification of the AddA and AddB protein was first done according to molecular size resolved on the SDS-PAGE gel. The theoretically calculated protein sizes are 122.126 and 112.236 kDa, respectively.

AddAB enzyme purification

Purification of the AddAB protein was done together with the group technician Mr Laurie Cooper mainly according to a method described in Chedin *et al.* (2006).

The protein purification unit used a TRIS pump (Part 69-1613-297, from Teledyne Isco, Inc., Lincoln, NE, USA) connected to a Gradient Mixer GM-1 (Code No. 90485, Pharmacia Fine Chemicals, Uppsala, Sweden). A UV/VIS Detector UA-6 (Teledyne Isco, Inc.) was used to continuously monitor the eluted protein concentrations (at a wavelength of 280 nm). 10 ml fractions were collected with an ISCO Cygnet Fraction Collector (008590 DBS, Teledyne Isco, Inc.).

Precast protein gels were used for SDS-PAGE after each individual column purification step in order to monitor the amount of AddAB protein and to select for the AddAB protein containing fractions to be used in the subsequent purification step. A 40 cm long and 2.5 cm diameter wide column was filled with DEAE (diethylaminoethyl) sepharose (GE Healthcare, Little Chalfont) suspended and equilibrated for 3 hr in 20 mM Tris-HCl buffer (pH 7.5) containing 0.1 mM EDTA, 0.1 mM DTT and 100 mM NaCl. The crude protein extract was loaded onto the column which was then washed with the same buffer for an hour to remove any proteins and impurities that did not bind to the column. To elute the protein from the column, a NaCl gradient from 100 to 600 mM NaCl was applied over a time course of 15 hr while maintaining a constant flow rate of 25 ml/hr. 10 ml

fractions were collected.

The fractions that contained AddAB protein were combined and dialysed against 50 mM potassium phosphate buffer (pH 7.5) containing 1 mM DTT. The sample was then loaded in the same buffer onto a hydroxyapatite column (DNA grade, 15 cm long, 2.5 cm diameter, Bio-Rad, Hemel Hempstead) and after one hour of washing eluted with a gradient to 300 mM potassium phosphate.

The part of the eluate containing AddAB protein was dialysed against 20 mM Tris-HCl buffer (pH 7.5) containing 0.1 mM EDTA, 0.1 mM DTT and 100 mM NaCl for four hr before being loaded onto a Mini Hi-Trap Heparin (GE Healthcare) column (5 ml volume). The protein was eluted with a NaCl gradient to 500 mM NaCl. After identifying the fractions that contained AddAB protein these fractions were merged and concentrated to yield a 17 μM AddAB stock solution.

UV spectrometry

The final protein concentration in the prepared samples was assayed by UV absorption in the range from 250 to 300 nm using a HITACHI U2900/2910 Double Beam Spectrometer (Hitachi High Technologies America, Inc., Schaumburg, IL, USA). Based on the content of aromatic amino acids and cysteine residues in the AddAB protein an absorption coefficient ϵ_{280nm} = 240,380 M^{-1} cm^{-1} was determined using a protein calculator software found on the website www.scripps.edu/cgi-bin/cdputnam/protcalc3. The basis for the theoretical calculation of protein extinction coefficients was laid by Gill & von Hippel (1989).

Nucleic acids have an absorption value around 1 at 260 nm which corresponds to 50 μg/ml of dsDNA (Sambrook *et al.*, 2001). In case a protein preparation is contaminated with nucleic acids, the ratio of the absorbance values at 260 nm and 280 nm would strongly deviate from 0.65 hence indicating that further purification was required.

Protein concentration and storage

Protein samples were concentrated using 30,000 molecular weight cut-off ultrafiltration columns (Vivascience, Sartorius, Epsom Surrey). These columns were flushed with 5 ml distilled water prior to use for protein concentration, with both operations being carried out at 4,000 g and 4 °C in a centrifuge (Heraeus Biofuge Stratos; from DJB Labcare Ltd, Newport Pagnell)

All purified protein samples were stored in 20 mM Tris-HCl buffer (pH 7.5) containing 50% glycerol (v/v) and kept at -20 °C.

RecBCD

RecBCD enzyme was prepared by a previous group member, Mr Jacob Zipprich, according to methods developed by Dykstra *et al.* (1984) and Roman & Kowalczykowski (1989b).

3.5.5 DNA agarose gel electrophoresis

DNA agarose gel electrophoresis is able to resolve DNA molecules of different sizes and was used to control the activity of DNA interacting enzymes, specifically to prove the Mg^{2+}-ATP-dependent digestion of lambda-DNA by the homologous recombination enzyme AddAB.

To resolve lambda-DNA and its digestion products using gel electrophoresis, 0.7% w/v agarose (Fisher Scientific UK Ltd) was melted at 100 °C in 1x TAE (Tris-acetate EDTA) buffer (50x: 242 g Tris base, 57.1 ml glacial acetic acid and 100 ml 0.5 M Na_2EDTA (pH 8.0), filled up with distilled water to give 1 l) (Sambrook *et al.*, 2001).

0.5 μg/ml of ethidium bromide (final concentration; Invitrogen) was added to the still molten agarose before the gel was set at r.t. (for about one hour), in order to visualise the DNA.

DNA ladder (NEB) with a size range from 1 to 10 kbp was used as a size marker for DNA.

Lambda-DNA (NEB) at a concentration of 50 μg/ml was reacted with 170 nM AddAB in 40 mM $NaHCO_3$ (pH 8.0) buffer (Fisher Scientific) containing 12.5% w/v sucrose, 2 mM magnesium acetate and 1 mM ATP. The systematic omission of either ATP or magnesium acetate proved that the AddAB-mediated DNA unwinding was Mg^{2+}-ATP-dependent. The time dependence of the Mg^{2+}-ATP-dependent DNA unwinding reaction was monitored by stopping the reaction with a 5x excess of Na_2EDTA over Mg^{2+}. 18 μl reaction sample aliquots were titrated into 2 μl 100 mM $EDTANa_2$ aliquots after 1, 2, 3, 5, 7, 10 and 15 min reaction time.

Reacted samples were mixed with DNA loading buffer (10x: 20% w/v Ficoll 400, 0.1 M Na_2EDTA (pH 8.0), 1% w/v SDS and 0.25% w/v bromophenol blue) and 20-25 μl aliquots were loaded into the lanes of the gel. Electrophoresis was carried out for 90 min at a starting voltage of 125 V. The DNA was visualised using a UV transilluminator (TFM-30, UVP, LLC, Upland, CA, USA) and images were acquired with a CCD camera (Fujifilm FinePix S602Zoom) and processed with IrfanView.

3.5.6 Mass Spectrometry of AddAB

Mass spectrometry (MS) was applied to confirm that the isolated AddAB protein was the right protein by comparison with entries in the NCBInr database using the MS-Fit search engine. All experiments including the analysis were done by Mr Jim Creanor who runs a departmental MS service for protein analysis.

Briefly, a protein gel of the AddAB sample was run in a way similar to the one described in section 3.5.4 and gel pieces with separated protein and peptide species were cut out and subjected to a tryptic digest (modified sequencing grade, Promega UK Ltd, Southampton). The mass spectra were acquired on a Voyager DE-STR MALDI-TOF Mass Spectrometer (Applied Biosystems Inc, Foster City, CA, USA). The NCBInr database was used to identify the AddAB protein fragments.

3.5.7 Sample preparation for single-molecule TIRF experiments

Buffers and solutions

Buffer A contained 100 mM NaCl, 10 mM Tris (pH 8.0) and 1 mM EDTA. The buffers B1 and B2 contained, respectively, 10 mM Tris (pH 8.0), 1 mM EDTA and 40 mM Tris (pH 7.8), 1 Mm $MgCl_2$, 1 mM DTT and 0.2 mg/ml BSA (bovine serum albumin).

Buffer C1, used during TIRF imaging experiments, contained 40 mM $NaHCO_3$ (pH 8.0), 2 mM magnesium acetate, 0.04 mg/ml catalase, 0.5 mg/ml glucose oxidase and 4 mg/ml β-mercaptoethanol and 12.5% w/v glucose.

Buffer C2 which is derived from C1 and used to trigger AddAB and RecBCD enzyme activity contained ATP in different concentrations ranging from 0.01 to 5 mM. In case of 2 and 5 mM ATP an excess of 1 mM magnesium acetate over ATP was used.

All buffers and solutions were sterilised by passing them through 0.2-μm filters (Millipore UK Ltd, Watford). Pure buffers and ultrapure water (18.2 MΩ, MilliQ, Millipore) were previously autoclaved (for 20 min at 121 °C) before adding temperature-sensitive supplements as for example BSA or NeutrAvidin (Pierce Biotechnologies, Rockford, IL, USA). The first 1 ml was systematically discarded to wash the filter.

Preparation of flowcells

Prior to experiments, flowcells with one inlet and one outlet (see chapter 3.5.3) were rinsed by first flushing 9 ml ultrapure water and washed with 2 ml 2% v/v

Hellmanex detergent solution (Hellma GmbH & Co. KG, Müllheim, Germany). Thereafter, the flowcells were rinsed a second time with 9 ml water, then flushed with 2 ml buffer A and subsequently incubated for 30 min with 0.5 ml buffer A containing NeutrAvidin (20 μg/ml). Finally the flowcells were rinsed again with 9 ml buffer A and 2 ml buffer B2 to remove unbound NeutrAvidin. 0.2 mg/ml BSA in buffer B2 was incubated for 30 min. The result is a flowcell whose inner surface is coated with individual NeutrAvidin molecules and larger BSA patches for surface passivation. Prior to loading the biotinylated DNA samples, the flowcells were purged with 2 ml buffer B2 and 0.5 ml buffer C1. The biotinylated lambda-DNA preparations were applied and incubated for at least 30 min before purging the flowcell with 1 ml buffer C1 which removed DNA that was not bound to the surface.

Buffer C2 was used to trigger the enzymatic activity of AddAB and RecBCD. C1 containing 20 nM YOYO-1 iodide was used to study the kinetics of dye intercalation.

All single-molecule experiments were performed at 22 °C.

All rinsing and incubation steps prior to the application of the DNA samples were carried out at flow rates of 1 ml/min. In the DNA sample loading and kinetic experiments using TIRFM the flow rates were 0.1 and 0.05 ml/min, respectively.

Biotinylation of lambda-DNA

50 μl ultra-pure water was mixed with 20 μl lambda-DNA (500 μg/ml, NEB), 8 μl (10x) T4 DNA ligase buffer (NEB) and 2 μl (200 μM) of an oligonucleotide with sequence 5'-GGGCGGCGACCT-3', tagged with biotin-TEG 568 at its 3' end (Eurogentec, Seraing, Belgium) which is complementary to the 5'-AGGTCGCCGCCC-3' cohesive site (generally termed cos1) of bacteriophage lambda. This mixture was heated for 30 min at 75 °C in a water bath and allowed to cool down overnight. 2 μl of T4 DNA ligase was added and the solution was incubated for 2 hr at 16-20 °C after which the enzyme was heat-inactivated for 10 min at 65 °C. This preparation was purified twice on MicroSpin S-400 HR columns (Amersham Biosciences, Piscataway, NJ, USA) by centrifugation at 2,000 g for 2 min (Heraeus Biofuge Pico; from DJB Labcare Ltd). This step removes remaining ATP and excess oligonucleotides. Buffer B1 was added to obtain five 50 μl biotinylated lambda-DNA stocks. The yield of DNA was determined to be between 50 and 65% using an Eppendorf Biophotometer (Fisher Scientific UK Ltd). The 50 μl stocks were kept frozen at -20 °C until used.

For final sample preparation, 50 μl of the DNA stock was dissolved in 2 ml

buffer C1 and stained with 10 μl (10 μM) YOYO-1 iodide and was left for incubation at 0 °C and in the dark for 5 min. The estimated staining ratio was roughly 1/20 dye molecules per DNA base pair. For other staining ratios the volume of dye stock solution was adjusted accordingly. For AddAB and RecBCD kinetic experiments, aliquots of the enzyme stock solutions were added to the YOYO-1 stained DNA preparations to produce final enzyme concentrations of 17 and 5 nM, respectively, and left for at least 30 min further incubation at 0 °C and in the dark before application to the flowcells.

3.5.8 Michaelis-Menten bulk assays

To monitor the ATPase and DNA helicase activity of the AddAB enzyme in bulk, two different photometric assays were carried out using a similar buffer to that used for the single-molecule experiments, i.e. 40 mM $NaHCO_3$ (pH 8.0), at least 2 mM magnesium acetate (for ATP concentrations $\leq$ 1 mM; in case of 2 and 5 mM ATP an excess of 1 mM magnesium acetate over ATP was used), 0.04 mg/ml catalase, 0.5 mg/ml glucose oxidase and 4 mg/ml β-mercaptoethanol.

The pUC18 plasmid (NEB, 2,686 bp, 1 μg = 0.57 pmol) was digested for 1 hour at 37 °C with the EcoRI enzyme (NEB) to produce linearised DNA with a cohesive end (5' ssDNA overhang of the nucleobase sequence AATT). An aliquot of this stock was diluted in buffer to a final concentration of 1.2 nM DNA ends. This solution was chilled to 0 °C for 5 min and then AddAB was added to a final concentration of 40 nM.

YOYO-1 iodide displacement assay

The helicase activity of the AddAB enzyme was monitored through the displacement of the DNA intercalating dye YOYO-1 iodide from the unwound dsDNA. In this assay, 33 nM YOYO-1 iodide was added to the buffer in order to bind to pUC18 DNA 5 min before the enzyme was added to the preparation.

Fluorescence spectra and kinetic time courses were acquired on an Edinburgh Instruments Spectrometer (CD920, Edinburgh Analytical Instruments Ltd, Livingston) that was equipped with two photomultiplier tubes attached to a cooler controller (that maintained a fairly constant temperature of -30 °C) and a Xenon lamp (Xe900, Edinburgh Analytical Instruments Ltd) for fluorescence excitation. A sample thermostat (NESLAB RTε-200, Edinburgh Analytical Instruments Ltd) was used to maintain a constant reaction temperature of 22 °C. Both the excitation and emission paths were each blocked with two adjustable slits. Prior to the experiments, all four slits were opened by five screw turns (referring to a spectral

bandwidth of 5 nm). For spectra and kinetic time course acquisitions a step size of 1.0 nm and a dwell time of 0.5 s were chosen, respectively. Fluorescence emission and excitation spectra were taken before the kinetic experiments in order to verify the maximum absorption and emission wavelengths of YOYO-1 of 491 and 509 nm, respectively, which were used for the collection of all kinetic time traces. A 100 μl fluorescence microcuvette was used for all bulk experiments. This cuvette was completely dark apart from three sides which had small UV-VIS light transparent windows of a size of 1 mm x 3 mm each.

63 μl sample buffer aliquots were incubated for 1 min in the cuvette (placed in the spectrometer holder) prior to the start of each experiment which had a duration of 200 s in total. After 60 s of fluorescence signal acquisition, AddAB activity was triggered by adding 7 μl (10x) concentrated Mg^{2+}-ATP solution in working buffer which resulted in a drop of fluorescence intensity. All experiments at one specific Mg^{2+}-ATP concentration were carried out at least in triplicate. The linear region of the fluorescence intensity decay was determined and the mean and standard deviation of the slope values from the three repeats were calculated and plotted (in arbitrary units) against the Mg^{2+}-ATP concentration. Control experiments without adding Mg^{2+}-ATP confirmed a Mg^{2+}-ATP-dependent AddAB activity. There was no significant drop in fluorescence intensity over the time course of this control experiment.

Coupled ATP hydrolysis assay

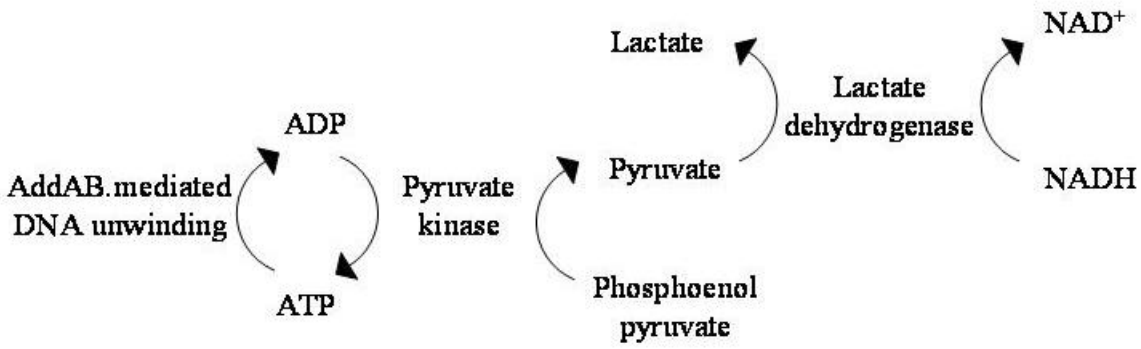

Figure 3.6: Mechanism of the coupled enzyme assay to monitor ATPase activity.

The ATPase activity of AddAB was monitored via the ATP-coupled consumption of NADH and its subsequent decrease in photometric absorption (at a wavelength of 340 nm) using an enzyme system consisting of pyruvate kinase and lactate

dehydrogenase (Pullman *et al.*, 1960). The reaction pathway is shown in figure 3.6.

The buffer was supplemented with 250 μM NADH, 1 mM phosphoenol pyruvate and the enzymes pyruvate kinase and lactic dehydrogenase (7 and 10 enzyme units/ml, respectively).

Kinetic absorption time traces were acquired on a Cary 50 UV-Visible Spectrometer (Varian Inc., Shropshire). At the beginning of each day the maximum absorption wavelength of NADH was confirmed and set to be 340 nm.

A thermostat was used to ensure a constant reaction temperature of 22 °C.

The sample was treated and assayed in the same way as in the YOYO-1 iodide displacement experiments, with the only exceptions being that kinetic timetraces were taken for 120 s using an integration time of 1 s and that the AddAB-mediated digestion was triggered after 30 s of observation.

The fitting of the kinetic curves and the statistical analysis was carried out as before.

3.5.9 Image analysis

Raw data obtained with the ANDOR Luca camera were exported as .tif (video stream) files from the ANDOR software. Image J was the software of choice to crop the videos, to label them with a scale bar, to place a timestamp and to export them as .avi files which can be shown with common players, e.g. the Windows Media Player. Kymographs were also produced in Image J by line selection of individual stretched lambda-DNA molecules and excision from each video frame and recombination into one image. Enzyme kinetic data of RecBCD-mediated and AddAB-mediated DNA unwinding were derived from these kymograph images by analysing the extent to which the DNA molecules have been gradually shortened as a function of time. Both these parameters were first determined in pixel values from the two different image dimensions, but then converted back into a time difference (seconds) and a length (micrometers) which was further converted into a number of DNA base pairs.

A MatLab (The MathWorks, Inc., Cambridge) routine for reading out length data from the kymographs for the YOYO-1 intercalation experiments was written (see next subsections for routines with and without data smoothing; programmes as electronic files on CD). In case of the initial staining ratios of 1/100 and 1/200 dye molecules/bp, the pronounced intensity increase with time, which is a direct result of YOYO-1 intercalation, needed to be corrected in the kymographs before the length readout. This signal-to-noise ratio (SNR) correction was accomplished

by multiplying all rows in the image matrix until 100 s (dead time) with a factor of 4. Each subsequent row (time lines $>$ 101 s) was then multiplied with a correction factor $f_{time} = 4 - (2.5/(300\text{s})) * (time - 100\text{s})$. The data with the 1/50 ratio do not show this pronounced intensity increase and, hence, were not corrected in this way. This routine then set all pixel values in the image that were below the average value to zero and took the first and last two subsequent non-zero values in one kymograph time line (row) as molecule start and end, respectively. In addition, these raw DNA molecule length data were smoothed by removing all DNA molecule lengths of zero, because these are a result of dark camera frames, and by performing adjacent averaging of five neighbouring values. No robust routine for reading out DNA molecule length data from the RecBCD and AddAB kinetics could be implemented because the SNR in these data was much lower due to lower YOYO-1 concentrations. A MatLab routine was also written to present kymographs with a length and time scale.

Origin was used for fitting and presenting the kinetic data.

Extraction of DNA molecule length traces with smoothing

1. Read in kymograph image and convert to double values.
2. Perform SNR correction for intensity increase during YOYO-1 intercalation.
3. Normalisation of image intensity values to LUT.
4. Smooth image (pixel values) in one row by adjacent averaging of 5 consecutive values.
5. Calculate average pixel value in whole image and set all pixel values smaller than average to zero.
6. Determine DNA molecule length in one kymograph row (one previous video image frame) by calculating the position difference between the first and last two subsequent non-zero pixels in this row.
7. Additional data smoothing
   - Calculate the mean and standard deviation of 5 subsequent DNA molecule length values.
   - If the absolute value of the difference between the initial length value in pixel and the mean exceeds the standard deviation, set this initial length value to the calculated mean value.
     -> This will remove DNA length values from dark frames (ususally 0

length).
-> One obtains improved DNA molecule lengths.

- Based on improved DNA lengths, do adjacent averaging of 5 subsequent length values.
- Discard last 10 determined DNA molecule length values.

8. Plot DNA molecule length values against time (apply factor 2 on x axis to obtain seconds).
9. Export all data (write to results matrix).
10. Do this for all files.

Extraction of DNA molecule length traces without smoothing

1. Read in kymograph image and convert to double values.
2. Perform SNR correction for intensity increase during YOYO-1 intercalation.
3. Normalisation of image intensity values to LUT.
4. Calculate average pixel value in whole image and set all pixel values smaller than average to zero.
5. Determine DNA molecule length in one kymograph row (one previous video image frame) by calculating the position difference between the first and last two subsequent non-zero pixels in this row.
6. Plot DNA molecule length values against time (apply factor 2 on x axis to obtain seconds).
7. Export all data (write to results matrix).
8. Do this for all files.

3.6 Results: TIRFM and hydrodynamic stretching of surface-tethered lambda-DNA

3.6.1 TIRF microscopy

In order to achieve evanescent-field excitation conditions (fig. 3.7) a thin-waist light beam needs to hit the glass-buffer interface at a hypercritical angle. Despite using theoretical considerations about the beam geometry, it may be difficult to practically establish whether TIRF conditions have been reached or only oblique-illumination has been established. Particularly with biochemical samples, differences between these two excitation modes are subtle and cannot easily be discriminated by means of contrast and signal-to-noise ratio. Also, optics considerations are affected by refractive index changes of interfaces covered with cells or surface passivation layers, such as BSA, casein or lipid bilayers.

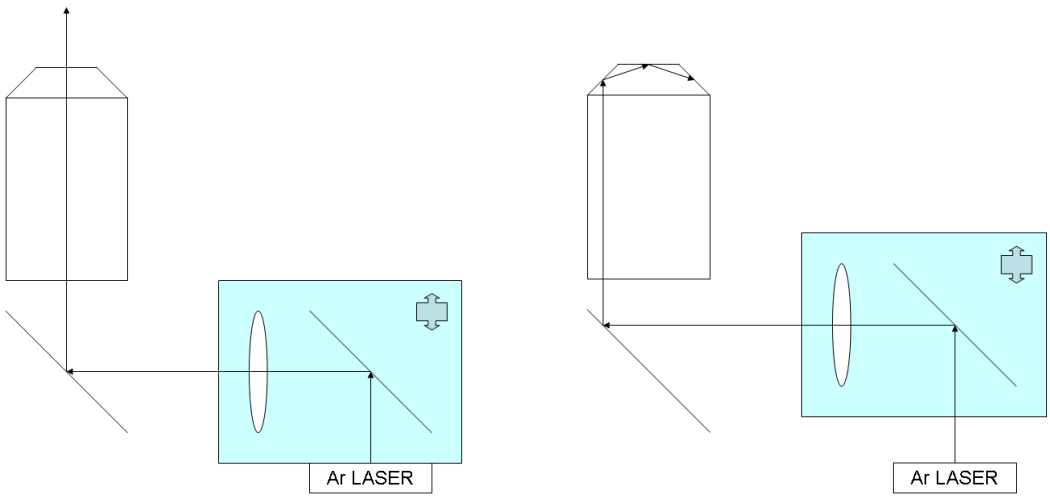

Figure 3.7: Principle of TIRFM. Left panel: Using a focussing lens (mounted on a 1D stage, shown in blue) a collimated laser beam is focussed into the objective back-focal plane along its optical axis which produces epi-fluorescence conditions. Right panel: Shifting of the 1D stage displaces the focussed laser beam parallel to the optical axis which results in total internal reflection, provided the laser incidence angle at the glass-air/buffer interface excedes the critical angle.

One of the best guiding samples during the alignment of a TIRF microscope are micrometer sized, fluorescent polymer beads suspendend in the buffer medium. Under epi-fluorescence conditions these fluorescent beads produce a characteristic blur when imaged out of focus. This blur can still be seen, but is less pronounced

when the incidence angle of the laser light is changed towards oblique excitation conditions. During TIRF conditions, the fluorescent beads are only excited when they are close to the glass-buffer interface. Diffusing beads near this surface, hence, produce a characteristic blinking which gives a qualitative confirmation of TIRF conditions (fig. 3.8).

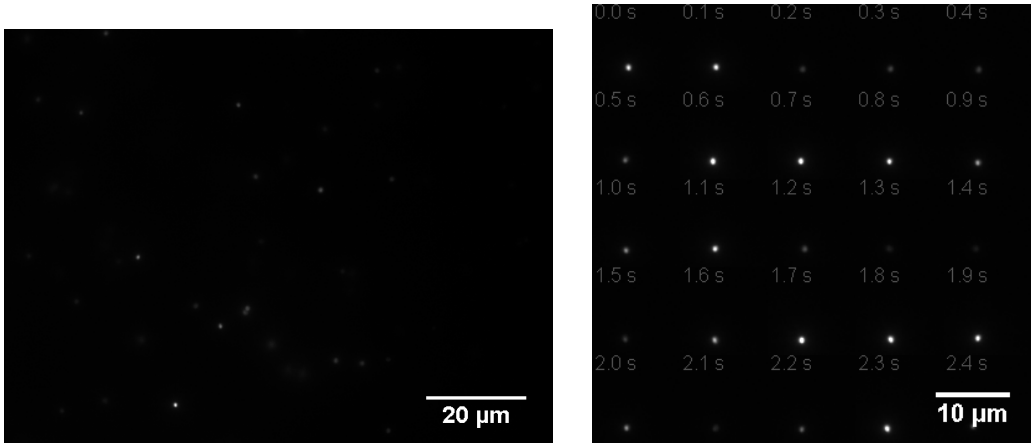

Figure 3.8: 1 μm sized green fluorescent beads suspended in 40 mM Tris buffer (pH 8.0) and imaged with TIRFM. Left panel: One frame of the whole camera field of view showing beads with different fluorescence intensity dependent on their distance from the glass surface (Supplementary video S3-Add-1). Right panel: Individual video frames showing one green fluorescent bead diffusing near the surface. When the bead is in close proximity to the surface (e.g. at 1.6 s), it is highly fluorescent. Subtle diffusion away from the surface (e.g. at 1.7 and 1.8 s) does not allow for sufficient evanescent-field excitation giving only faint fluorescence.

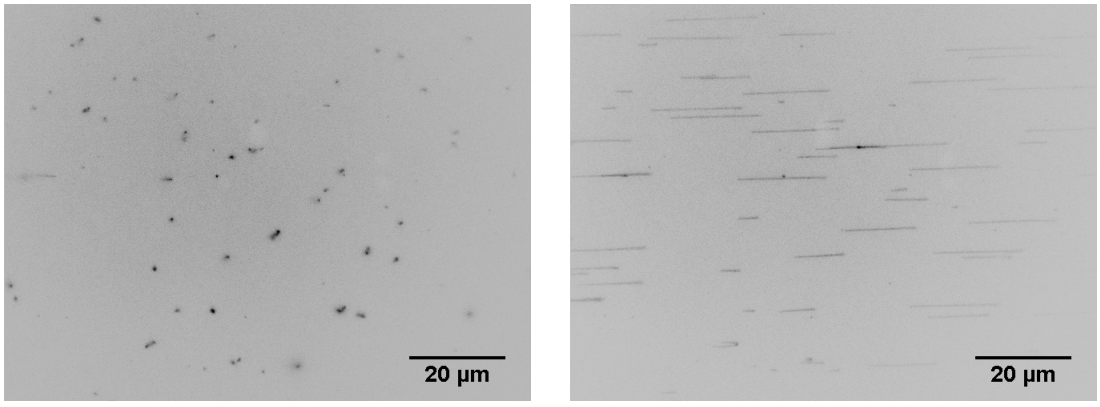

Figure 3.9: Colour-inverted TIRFM image of YOYO-1 stained lambda-DNA molecules deposited on a coverslip surface inside a microfluidic flowcell. The left panel shows the DNA coils without the application of hydrodynamic flow, the right panel shows the streched DNA molecules at a shear rate of 510 s^{-1}

3.6.2 Hydrodynamic stretching of surface-tethered lambda-DNA

Biotinylated DNA molecules can be tethered to a glass surface via the NeutrAvidin protein which is a biotin-binding protein that itself attaches to surfaces. Depending on the surface density of NeutrAvidin and the concentration of the biotinylated lambda-DNA sample, up to 50 DNA molecules can be tethered and well-resolved within a usual camera field of view (using 40x/60x objective magnification and a commercial EM-CCD camera). Inside microfluidics that are capable of maintaining a constant flow rate, lambda-DNA molecules can be stretched out (fig. 3.9).

Instead of referring to flow rates we introduce the shear rate which is a flowcell geometry independent measure defined as

$$\sigma = \frac{3Q}{2(h_0/2)^2 w_0} \tag{3.13}$$

where Q is the volummetric flow rate, h_0 and w_0 are the height and width of the rectangular flowcell, respectively (Busscher & van der Mei, 2006). This refers to σ values of 306, 510 and 714 s^{-1} for a 0.03, 0.05 and 0.07 ml min^{-1} flow rate in the used microfluidics with the measures of 0.07 mm and 2 mm for h_0 and w_0, respectively.

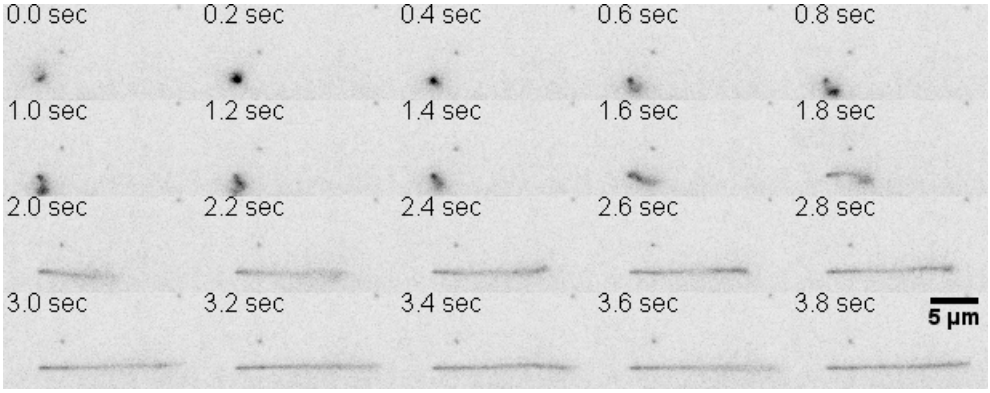

Figure 3.10: Colour-inverted image sequence showing the hydrodynamic stretching of a surface-tethered single-molecule of lambda-DNA that was subjected to a shear rate of 510 s^{-1}. The original image was taken with objective-TIRFM. (Supplementary video S3-Add-2)

Fig. 3.10 shows a TIRF image sequence of lambda-DNA uncoiling obtained during the establishment of a constant shear rate of 510 s^{-1}. Within 4 s after actuating the syringe pump, the DNA molecule gets almost fully stretched out. It can be clearly seen that both the polymer coil and the stretched molecule are

less well excited when the polymer tail fluctuates upwards into the bulk buffer phase (as in the frame taken at 3.6 s).

In order to perform and observe kinetic experiments on lambda-DNA molecules, it is necessary to maintain a constant flow rate which keeps the molecules stretched at a constant length. Reactions can then be triggered by simply changing the buffer conditions containing the inducing agent, for example a required enzyme cofactor.

Video microscopy is performed to record changes in the DNA molecule length and the general sample appearance. A particularly useful way for analysing the obtained data is to produce kymographs from the videos. This is done by line selection of a molecule of interest, subsequent excison of this line from all video frames and merging into one image. Hence, one can look at single-molecule kinetic processes in individual images. Proper assignment of time and length increments offers straight-forward access to kinetic data.

3.7 Results: YOYO-1 intercalation into lambda-DNA

During experiments with homologous recombination enzymes on stretched single molecules of lambda-DNA, it was noticed that YOYO-1 intercalation into lambda-DNA proceeds very rapidly, i.e. on a timescale of minutes, when a flow buffer containing YOYO-1 was in use. This section characterises not only the kinetics of dye intercalation, but also the influence of the shear rate and the staining ratio on the apparent lambda-DNA molecule length which is important for using this scaffold for enzyme single-molecule experiments. Despite its use in numerous assays, the process of YOYO-1 intercalation into dsDNA has surprisingly never been studied.

Note that all reported staining ratios assume 100% YOYO-1 binding to DNA and that lambda-DNA is always used in excess over YOYO-1. In this and the next two sections many data are presented as histograms. Please note that when multiple conditions are plotted in one histogram, the bars belonging to one data bin do not overlap and, hence, may be off centre.

3.7.1 Shear rate influence on apparent DNA molecule length

Using a constant lambda-DNA staining ratio of 1/50 dye molecules/bp, several camera fields of view were analysed and the apparent DNA molecule length was measured at three shear rates (fig. 3.11). For each field of view, the flow was increased in steps from the smallest to the highest shear rate. After reaching

equilibrium, an image was taken. During the image acquisition, obvious sample degradation, i.e. DNA molecule cutting by bleaching, did not occur. But it seems that the sample was previously degraded as for each shear rate each profile seems to split in mostly two peaks that are about 1 μm in length apart.

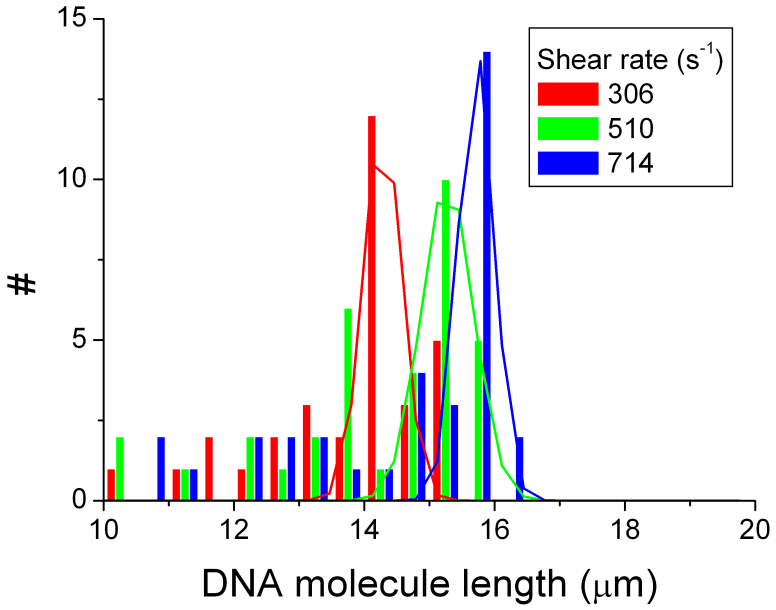

Figure 3.11: Shear rate influence on apparent DNA molecule length. For a shear rate of 306, 510 and 714 s^{-1} the mean apparent molecule length of stretched lambda-DNA is 14.3 $\pm$ 0.6, 15.3 $\pm$ 0.8 and 15.7 $\pm$ 0.5 μm, respectively. The bin size is 0.5 μm. 42 DNA molecules were analysed. (Note that for presentation purposes DNA molecules smaller than 10 μm are not shown.) The staining ratio was 1/50 dye molecules/bp.

Fitting multiple Gaussians, unfortunately, did not yield stable results. Hence, the optimum value at each shear rate was fitted by a single Gaussian and further analysed and discussed. To resolve the problem of multiple species, one would need to acquire a much larger data set or, in this case, where multiple species should naturally not occur, work with a fresh and undegraded DNA preparation. In the ideal case, all lambda-DNA molecules would have exactly the same well-defined contour length. At a certain shear rate condition, the distribution of the contour length obtained from different individual DNA molecules should hence be symmetric and centred around a mean value that we wish to derive from the data set. Fitting of alternative symmetric functions, e.g. a Lorentzian function, did neither yield qualitatively nor quantitatively improved results. As DNA

degradation occurs randomly, there is good reason to use a Gaussian function for routine fitting of all presented data sets. Although suffering from previous DNA degradation, the results still show a clear influence of an increased shear rate on the apparent DNA molecule length which rises from 14.3 to 15.3 and 15.7 μm, respectively.

3.7.2 Influence of the staining ratio on apparent DNA molecule length

Johansen & Jacobsen (1998) found that the intercalation of one YOYO-1 molecule lengthens dsDNA by 0.4 nm. Hence, different dye/bp staining ratios were investigated in order to further evaluate the experimental scaffold and to compare the results obtained with those from the literature. Using common staining ratios of 1/50, 1/100 and 1/200 dye molecules/bp the mean apparent lambda-DNA molecule lengths were 15.3 $\pm$ 0.8, 14.9 $\pm$ 0.7 and 14.0 $\pm$ 0.8 μm at a constant shear rate of 510 s^{-1}, respectively (fig. 3.12). This trend is expected to be small and occurs in the right order. The apparent DNA molecule lengths were also measured after complete saturation of the DNA with YOYO-1 intercalation dye. The determined values of 18.9 $\pm$ 1.5 (1/50), 19.2 $\pm$ 0.8 (1/100) and 19.6 $\pm$ 0.7 μm (1/200) lie quite closely together (initial staining ratios are given in brackets) and are all within the standard deviation. Besides, there is no reason why these apparent lengths should be different from each other.

3.7.3 Kinetics of YOYO-1 intercalation into lambda-DNA

The kinetic rate of YOYO-1 intercalation into lambda-DNA has been characterised for three different initial staining ratios. The figures 3.13, 3.14 and 3.15 show typical kymograph images of this process for initial staining ratios of 1/50, 1/100 and 1/200 dye molecules/bp, respectively. The intercalation reaction was triggered at 100 s using 20 nM YOYO-1 in the flow buffer. Without adding YOYO-1, the DNA length remained constant.

Using a MatLab routine the intercalation traces, yielding apparent DNA molecule lengths over time, were extracted for each condition. All single-molecule data are usually noisy and, therefore, a smoothing algorithm needed to be applied in order to read out interpretable traces. An intrinsic feature of simple smoothing algorithms, e.g. Kernel functions, is that they slightly affect the original absolute DNA molecule lengths, hence the length values in the presented graphs are given in arbitrary units (figure 3.16). This aspect is illuminated in some more detail in chapter 4 which deals with image analysis techniques.

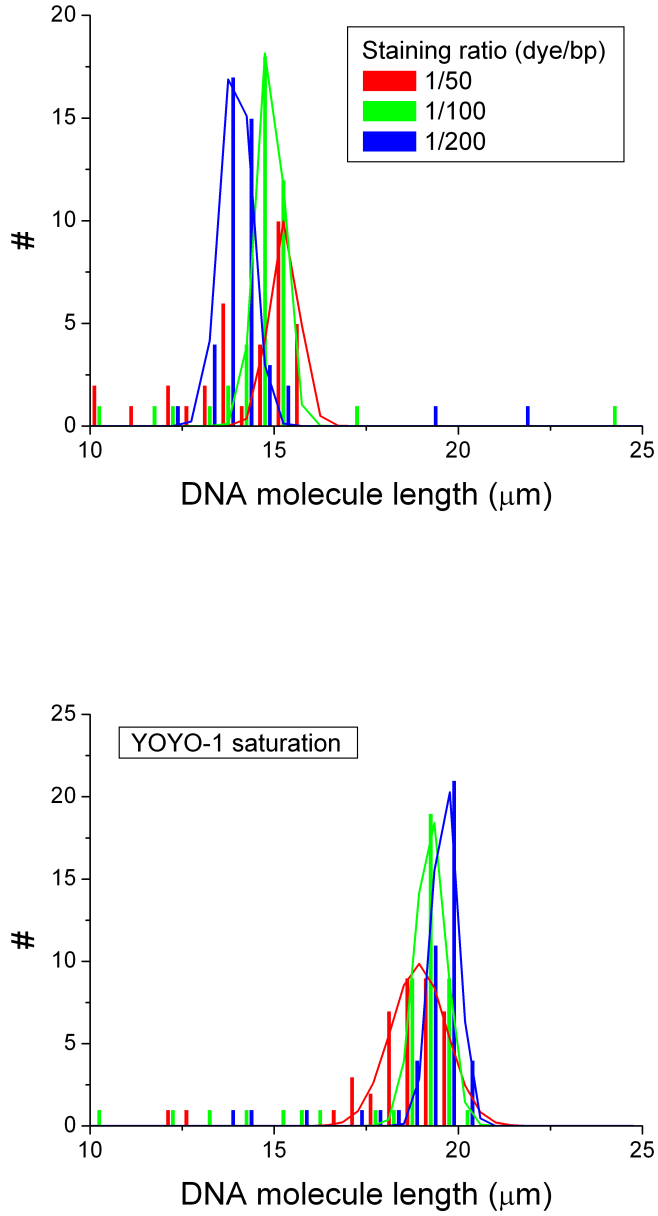

Figure 3.12: Influence of the staining ratio on the apparent DNA molecule length. Upper panel: At a staining ratio of 1/50, 1/100 and 1/200 dye molecules/bp the apparent DNA molecule length is 15.3 ± 0.8, 14.9 ± 0.7 and 14.0 ± 0.8 μm, respectively. Lower panel: After flowing in a buffer solution containing an excess of the intercalation dye YOYO-1 iodide, the mean apparent DNA molecule length for each initial staining ratio (of 1/50, 1/100 and 1/200 dye molecules/bp) was measured again and determined to be 18.9 ± 1.5, 19.2 ± 0.8 and 19.6 ± 0.7 μm, respectively. The bin size is 0.5 μm. 42, 48 and 46 DNA molecules were analysed for the staining ratios 1/50, 1/100 and 1/200 dye molecules/bp, respectively. A constant shear rate σ of 510 s^{-1} was maintained in both series.

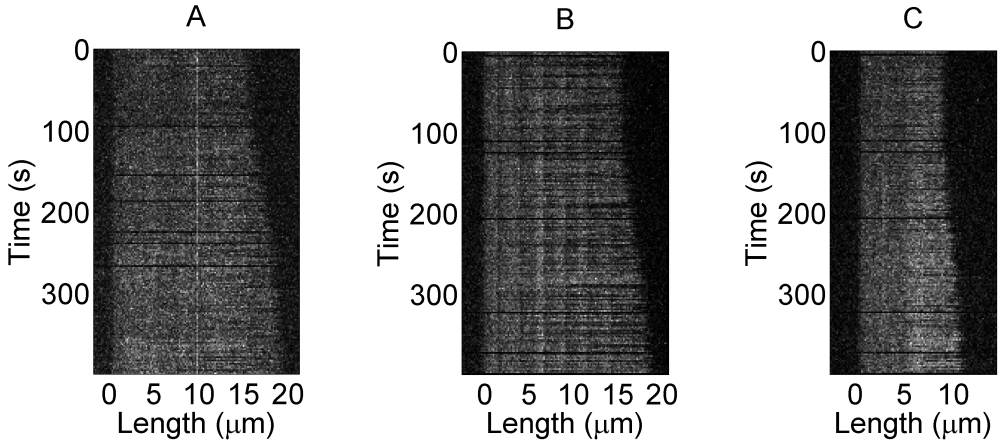

Figure 3.13: Kymographs showing the kinetics of YOYO-1 intercalation into lambda-DNA for an initial staining ratio of 1/50 dye molecules/bp. Panels A and B show non-degraded lambda-DNA molecules that change their length from 15 to 19 μm during intercalation of YOYO-1. Panel C shows a previously sheared (or otherwise degraded) lambda-DNA molecule that changes its length from 9 to 11 μm during intercalation of YOYO-1. A constant shear rate σ of 510 s^{-1} was maintained during the experiments.

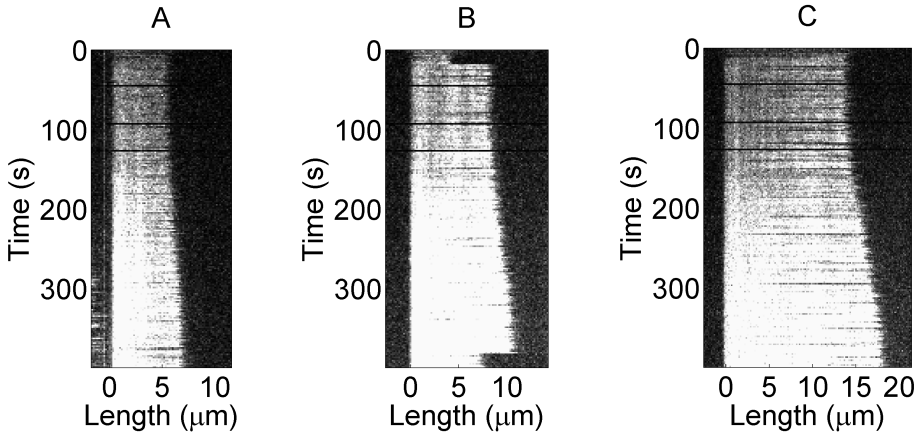

Figure 3.14: Kymographs showing the kinetics of YOYO-1 intercalation into lambda-DNA for an initial staining ratio of 1/100 dye molecules/bp. Panels A and B show previously sheared (or otherwise degraded) lambda-DNA molecules that change their apparent lengths from 5.5 to 7 μm and 8.5 to 11 μm during intercalation of YOYO-1, respectively. The DNA molecule in panel B is bleached at a time point of 380 s with subsequent DNA molecule shortening to an apparent molecule length of 7.5 μm. Panel C shows a non-degraded lambda-DNA molecule that changes its apparent length from 14 to 18 μm during intercalation of YOYO-1. A constant shear rate σ of 510 s^{-1} was maintained during the experiments.

From these traces, it can be clearly derived that YOYO-1 intercalation into

lambda-DNA follows a mono-exponential decay described by the equation $l = l_{end} - (l_{end} - l_{start}) * exp(-t/\tau)$. In this equation, l_{start} and l_{end} are the apparent DNA molecule length l before and after YOYO-1 intercalation, respectively; t is the time and τ is the time constant. During this process the number of free DNA sites gradually decreases, thereby giving rise to an exponential behaviour.

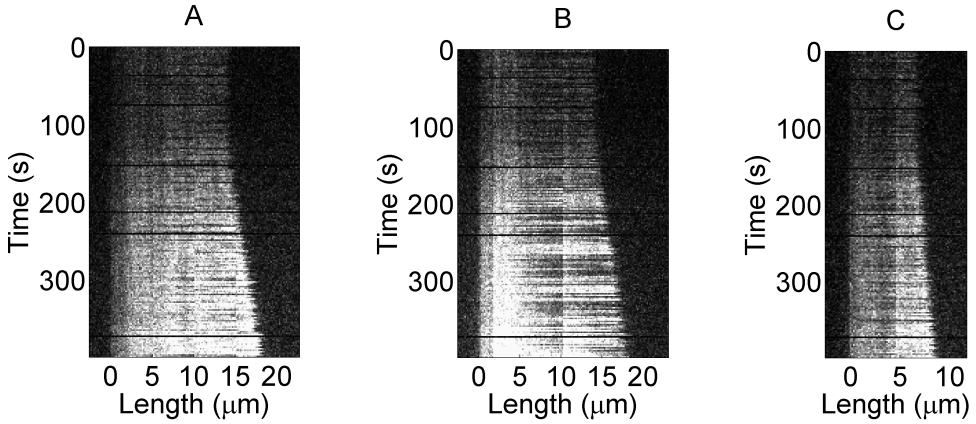

Figure 3.15: Kymographs showing the kinetics of YOYO-1 intercalation into lambda-DNA for an initial staining ratio of 1/200 dye molecules/bp. Panels A and B show non-degraded lambda-DNA molecules that change their apparent length from 14 to 18 μm during intercalation of YOYO-1. Panel C shows a previously sheared (or otherwise degraded) lambda-DNA molecule that changes its apparent length from 6.5 to 8.5 μm during intercalation of YOYO-1. A constant shear rate σ of 510 s^{-1} was maintained during the experiments. (Supplementary video S3-Add-6)

YOYO-1 intercalation kinetic time constants τ		
Initial staining ratio	Mean time constant (s)	Standard deviation of time constant (s)
1/50	199.3	6.7
1/100	162.5	44.1
1/200	95.4	59.9

Table 3.2: Time constants for YOYO-1 intercalation kinetics into lambda-DNA depending on initial staining ratio. The second part of the timetraces of the YOYO-1 intercalation kinetics into lambda-DNA was fitted by a mono-exponential decay function. The mean and standard deviation of the fitted time constants are presented (# molecules fitted for initial staining ratios of 1/50, 1/100 and 1/200: 2, 10 and 10).

10 individual traces for the initial staining ratios of 1/100 and 1/200 were

analysed. Curiously, all data taken at an initial staining ratio of 1/50 had a very low SNR which allowed a reliable fitting only for two traces. However, the qualitative appearance of all kymographs was similar to the ones that permitted fitting, so that the results obtained closely reflect the overall behaviour.

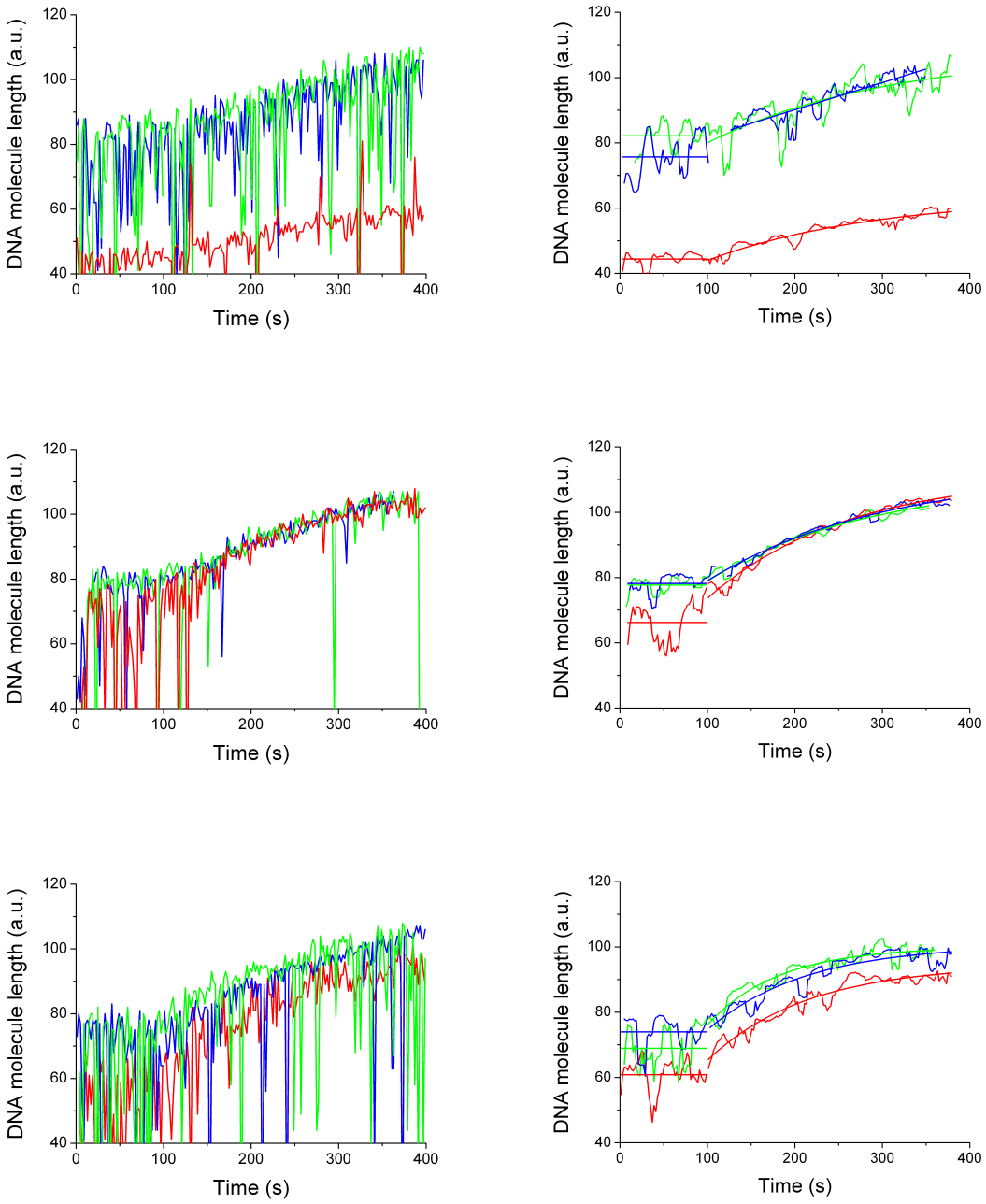

Figure 3.16: Kinetics of YOYO-1 intercalation into lambda-DNA. Three typical timetraces are shown for each initial staining ratio extracted from the raw data with (right panels) and without smoothing (left panels) algorithm (top: 1/50 (the fitting result of the blue curve was not included into the results), middle: 1/100 and bottom: 1/200 dye molecules/bp.)

Table 3.2 shows a summary of the fitting results. With increasing staining ratio, the time constant of the intercalation process becomes larger which is a result of more dye molecules already bound to DNA. At the highest staining ratio of 1/50 the time constant is 199 s which drops to 163 and 95 s for staining ratios of 1/100 and 1/200, respectively. The determined standard deviations are small enough to produce significantly different results for each examined staining ratio.

Figure 3.17. shows histograms with relative DNA molecule length changes directly obtained from kymograph images before and after completed YOYO-1 intercalation. The observed relative DNA molecule length change is 23, 29 and 31% for the initial staining ratios of 1/50, 1/100 and 1/200 dye molecules/bp, respectively, hence showing a characteristic increase for smaller initial staining ratios.

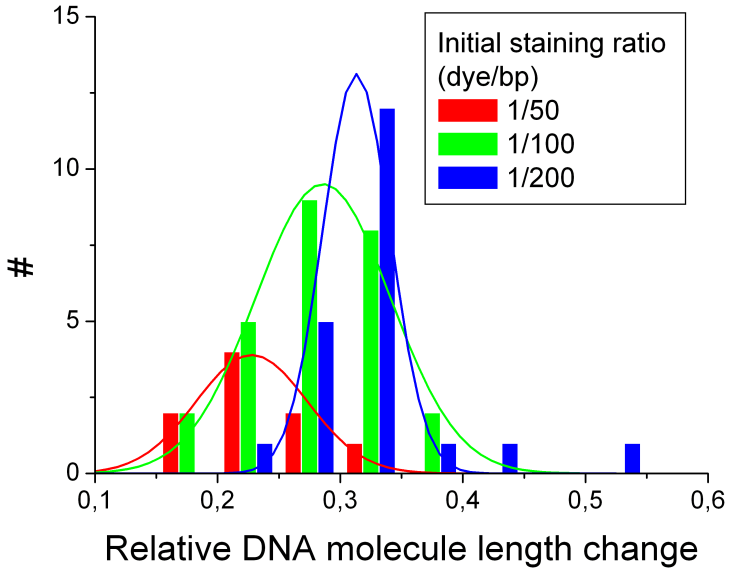

Figure 3.17: Histogram of the relative DNA molecule length change during YOYO-1 intercalation. The relative DNA molecule length change for the initial staining ratios of 1/50, 1/100 and 1/200 dye molecules/bp is 0.23 ± 0.09, 0.29 ± 0.11 and 0.31 ± 0.05, respectively. The bin size is 0.05. A constant shear rate σ of 510 s^{-1} was maintained during the experiments.

3.8 Results: AddAB

3.8.1 AddAB purification

This section describes the AddAB protein purification which adopted a purification method for the analogous AddAB protein from *B. subtilis* (Chedin *et al.*, 2006).

Protein gels were initially also run from samples collected during protein expression to assess the amount of protein expression before and after (an 18 hr) IPTG induction. These two samples are included in the protein gels (lanes 2 and 3, respectively) that were prepared after the first two purification steps to assess their success.

The fourth lane in these two SDS-PAGE gels contains the dialysed protein concentrate that is to be purified. Most of the unwanted proteins are actually eluted in a washing step (lanes 5) that is carried out after protein binding to the column material. At this stage buffer of the initial salt concentration is used which, thereafter, is slowly increased in order to produce a constant NaCl gradient. Depending on the properties of all proteins bound, at a certain salt concentration ionic exchange with the column material takes place which leads to protein unbinding from the column and its subsequent elution.

Eluted fractions of a fixed and relatively small volume (10 ml) were collected throughout the purification procedure and screened for protein size and content.

A Q-sepharose column (fig. 3.18) was used during the first purification step. After applying the NaCl gradient, mainly smaller molecular weight impurities of a size range of 10-25 kDa were eluted from the column in the first 10 fractions that contained protein (which was previously assayed using UV spectrometry). The following 10 fractions contained AddA and AddB clearly seen as a dominant doublet band at 112 and 122 kDa, respectively. These fractions also contained protein impurities of roughly 50, 75 and 100 kDa size. The subsequent fractions contained, besides traces of AddA and AddB, higher (a doublet at 150 kDa) and lower molecular weight protein impurities (65 and 75 kDa).

The eluted fractions containing AddAB were then combined, concentrated and further purified on a hydroxy apatite column (fig. 3.19). When the salt gradient from 50 to 300 mM phosphate was applied, the impurity with a molecular weight between 70 and 75 kDa eluted first from the column. The following 8 fractions contained AddAB and still an impurity of 20-25 kDa size.

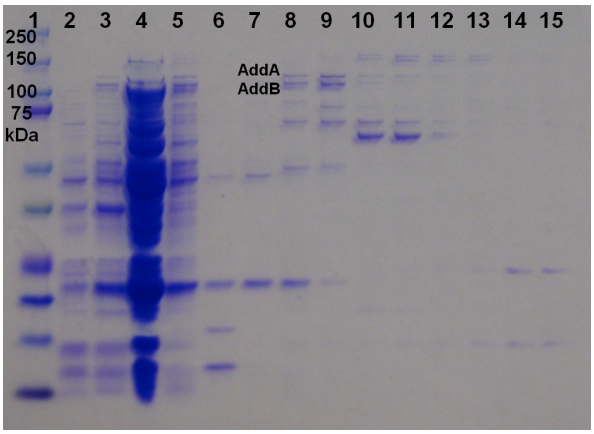

Figure 3.18: AddAB protein purification gel after Q-sepharose column. The different lanes (numbers in brackets) contain, respectively, protein size marker (1), lysate of the uninduced and induced *E. coli* culture (2 and 3), the dialysed protein preparation to be purified on the column (4), the washing fraction of the column (5) and every 5th eluted fraction (6-15) that was obtained while applying a salt gradient (from 100 to 600 mM NaCl).

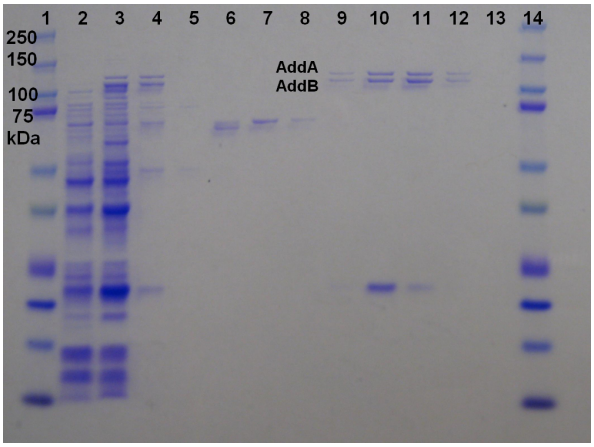

Figure 3.19: AddAB protein purification gel after Hydroxy apatite column. The first five lanes are the same as in the first gel with the fourth lane being the previously purified and combined fractions that contained AddAB. Every second protein containing fraction after applying a gradient from 50 to 300 mM phosphate buffer was then analysed (lanes 6-13).

The final purification step used a Hi-Trap heparin column (fig. 3.20) which was able to remove this impurity upon application of a NaCl gradient from 100 to 600 mM. Four protein fragments (50-75 kDa) were still found after concentrating the AddAB preparation. Mass spectrometry confirmed that these bands (designated 3-6) were all degradation products of AddAB.

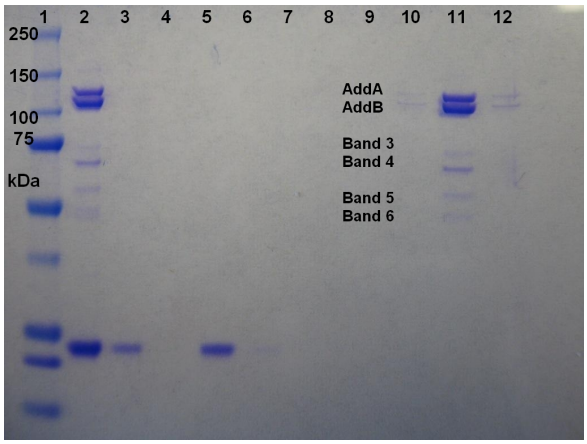

Figure 3.20: AddAB protein purification gel after Hi-Trap Heparin column. The different lanes contain, respectively, protein size marker (1), the dialysed protein preparation to be purified on the column (2), the washing fraction of the column (3) and every 2nd eluted fraction (4-12) that was obtained while applying a salt gradient (from 100 to 600 mM NaCl).

3.8.2 Confirmation of AddAB sequence and functionality

After obtaining a 95% pure AddAB preparation, mass spectrometry and a functional assay were used to confirm the isolation of the correct protein, based on NCBInr database entries, and that it acts as a Mg^{2+}-ATP-dependent nuclease, respectively.

Functional assay

DNA agarose gel electrophoresis was applied to assess whether the AddAB unwinding of lambda-DNA is Mg^{2+}-ATP-dependent or not. Lambda-DNA contains a small enough sticky end to serve as a test DNA molecule for Mg^{2+}-ATP-dependent AddAB unwinding and for the single-molecule experiments. A DNA molecule with either a 6 base ssDNA overhang in the 3'-strand or 10 base ssDNA overhang in the 5'-strand is known to be the best scaffold for RecBCD binding and unwinding (Wong *et al.*, 2005).

AddAB-mediated lambda-DNA unwinding was assayed for different cofactor conditions and reaction times (fig. 3.21). In the absence of either Mg^{2+} or ATP, no DNA unwinding and digestion takes place confirming that Mg^{2+}-ATP is the required cofactor species. With increased reaction time (1 to 15 min), the initial lambda-DNA band (at 48,502 kb) becomes weaker. Simultaneously, the wide size range of digested lambda-DNA appears as a fluorescent shade.

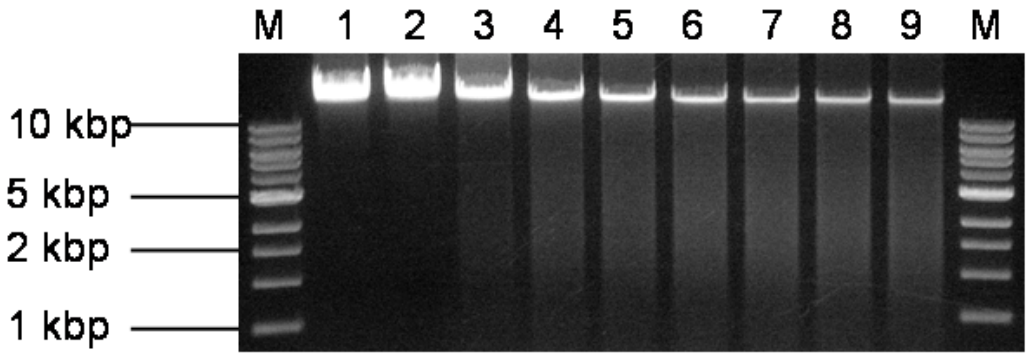

Figure 3.21: DNA agarose gel electrophoresis of AddAB-mediated lambda-DNA unwinding. The lanes contain, respectively, DNA ladder serving as a DNA size marker (M), lambda-DNA incubated with 2 mM Mg^{2+} only (1), lambda-DNA incubated with 1 mM ATP only (2) and lambda-DNA reacted with 1 mM ATP and 2 mM Mg^{2+} for 1, 2, 3, 5, 7, 10 and 15 min (3-9). The AddAB unwinding reaction was stopped by adding an excess of EDTA (10 mM). The reaction was carried out at room temperature using 170 nM AddAB.

3.8.3 Confirmation of an iron-sulfur cluster in AddAB

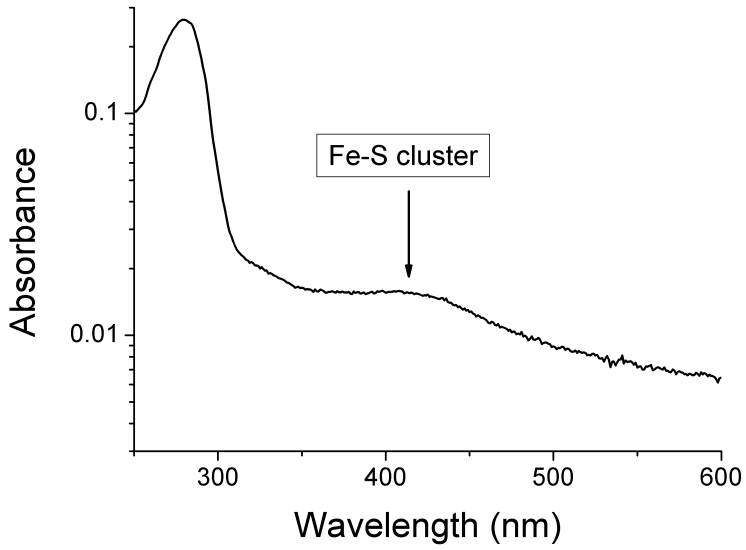

Figure 3.22: UV-VIS spectrum of a concentrated AddAB solution.

The UV-VIS spectrum of AddAB (fig. 3.22) contains an absorption band at 410 nm which indicates the presence of an iron-sulphur cluster, found also in *B.*

subtilis AddAB (Yeeles *et al.*, 2009). This finding is supported by the existence of three conserved cysteine residues near the C-terminus and one additional cysteine residue 200 amino acids further upstream in the AddB sequence.

3.8.4 AddAB single-molecule kinetic experiments

Using surface-tethered and hydrodynamically stretched lambda-DNA molecules, single-molecule AddAB experiments were performed under systematically varied Mg^{2+}-ATP concentration conditions and at different flow (or shear) rates. In addition, two different staining ratios of intercalation dye were probed.

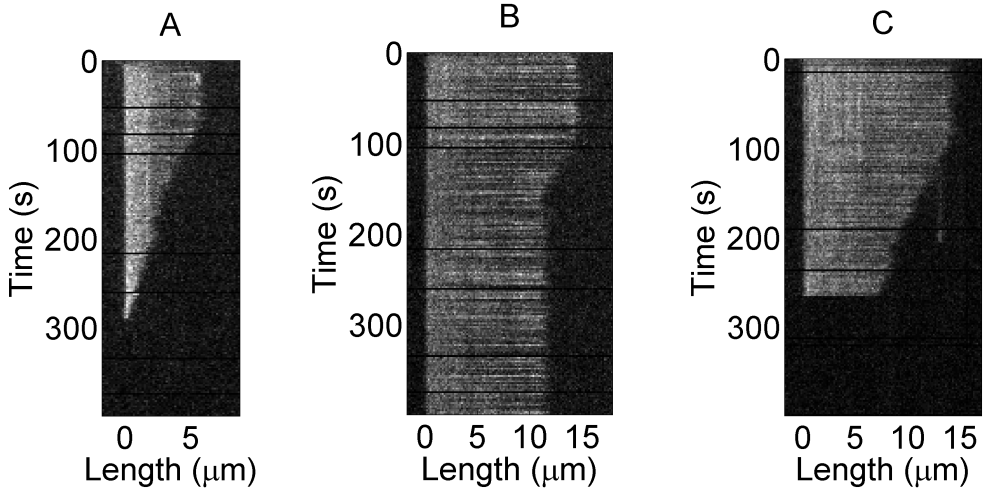

Figure 3.23: Kymographs of AddAB unwinding of lambda-DNA at a Mg^{2+}-ATP concentration of 2 mM. Panel A shows a previously degraded lambda-DNA molecule whose AddAB mediated unwinding is triggered at 80 s which procedes continuously for some 210 s until the complete DNA molecule is digested. Panel B shows a lambda-DNA molecule which is digested to 1/3 by AddAB in a linear and continuous fashion. Probably AddAB unbinding from the DNA is the reason for the cessation of the DNA unwinding. In panel C the observation of lambda-DNA unwinding through action of AddAB is stopped prematurely because of tether instabilities which results in cleavage of the active AddAB-DNA complex from the surface. At the timepoint of 100 s the initial DNA end stuck to the surface and was apparently cut by photobleaching which left a fluorescent trace on the surface. The newly created DNA end was subject to AddAB unwinding. Lambda-DNA in these preparations had a staining ratio of about 1/20 dye molecules/bp. A constant shear rate σ of 510 s^{-1} was maintained during the experiments. (Supplementary video S3-AddAB-1)

In figure 3.23 three typical kymographs for AddAB-mediated lambda-DNA unwinding are shown (at 2 mM Mg^{2+}-ATP). Most of the kinetic time courses

show a linear degradation of the DNA which can be prematurely terminated by either enzyme unbinding or phototoxic damage of DNA and/or protein. In figure 3.23C the tether destabilises and does not allow further observation of this single-molecule.

The figure 3.24 shows control kymographs obtained under exactly the same conditions, but without triggering the enzyme by flushing Mg^{2+}-ATP in the flow-cell. Sudden DNA molecule shortening is a result of photodamage (seen for example in fig. 3.24C).

From these kymograph images two important kinetic measures, the unwinding rate and the processivity, can be derived. The unwinding rate refers to the number of DNA base pairs that are unwound per time unit. The enzyme processivity is defined as the number of base pairs that are degraded by one AddAB enzyme in a single event without pauses.

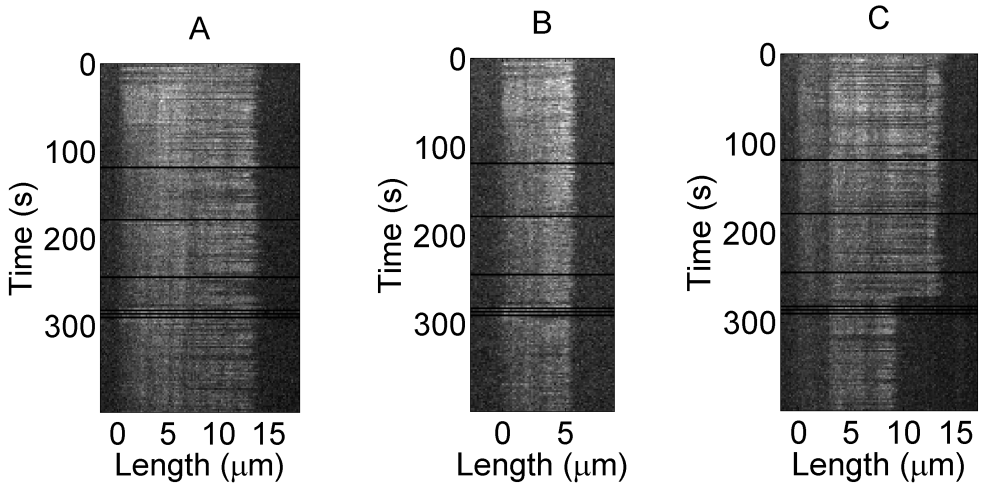

Figure 3.24: Control images (kymographs) for non-triggered lambda-DNA unwinding. The DNA samples were incubated with AddAB in the same way as for the kinetic Mg^{2+}-ATP-dependent unwinding experiments. However, no Mg^{2+}-ATP was added to the flow buffer leaving the DNA molecules undigested. Panel A and C show previously undegraded lambda-DNA molecules at the beginning of observation. Panel B shows a previously degraded, hence shortened, lambda-DNA molecule. The DNA molecule in panel C gets bleached and shortened by some 10,000 bp in one step. No continuous enzymatic unwinding of lambda-DNA was detected in preparations where Mg^{2+}-ATP was omitted in the flow buffer. Lambda-DNA in these preparations had a staining ratio of about 1/20 dye molecules/bp. A constant shear rate σ of 510 s^{-1} was maintained during the experiments. (Supplementary video S3-AddAB-2)

A prerequisite for deriving proper enzyme rate and processivity data is to correlate DNA molecule length with numbers of DNA base pairs. The following

procedure assumes that DNA closer to the tether is not stretched longer than DNA further away from the tether. From all analysed kymographs, the apparent start length of the DNA molecules was determined (still in pxl units) and plotted as a histogram for one condition (fig. 3.25). As this value varied with the amount of intercalation dye and shear rate, a Gaussian fit determined the optimum DNA molecule length which is known and set to be 48,502 bp. Based on this normalisation the enzyme kinetic parameters were calculated.

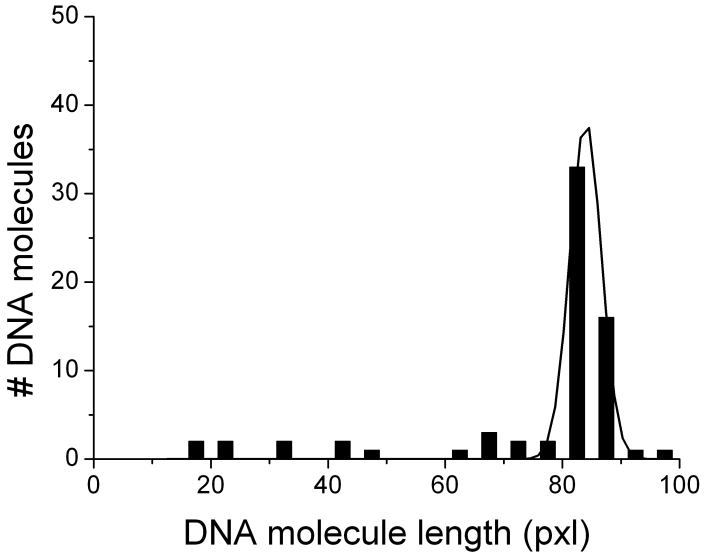

Figure 3.25: Histogram of initial DNA molecule length (1 mM Mg^{2+}-ATP condition). The DNA molecule length measured from the raw data is 84.1 ± 4.8 pxl. The mean value was set to the full lambda-DNA genome of 48,502 bp. Lambda-DNA in these preparations had a staining ratio of about 1/20 dye molecules/bp. The bin size is 5 pxl. (# molecules analysed 68.) A constant shear rate σ of 510 s^{-1} was maintained during the experiments.

3.8.5 Mg^{2+}-ATP dependence of AddAB rate and processivity

The AddAB rates and processivities were investigated for eight different Mg^{2+}-ATP conditions, i.e. 0.01, 0.03, 0.05, 0.1, 0.5, 1, 2 and 5 mM while maintaining a constant shear rate of 510 s^{-1}. For each Mg^{2+}-ATP condition between 44 and 69 single molecules were analysed.

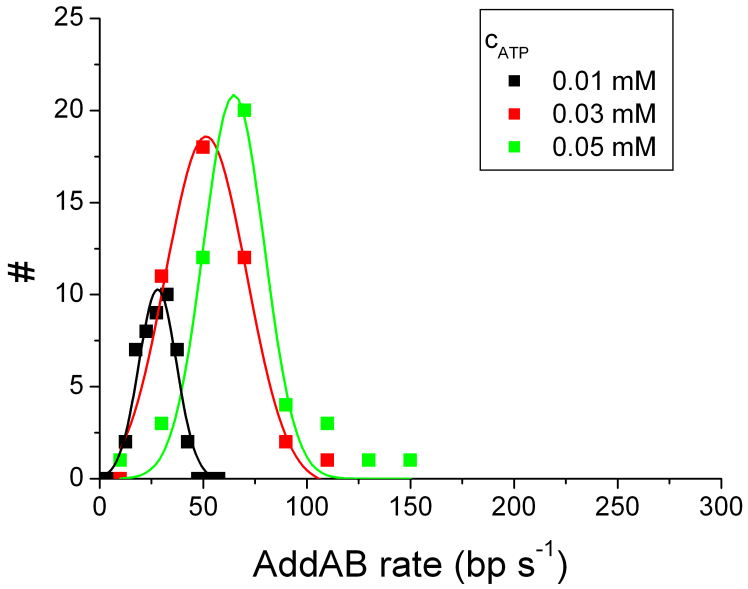

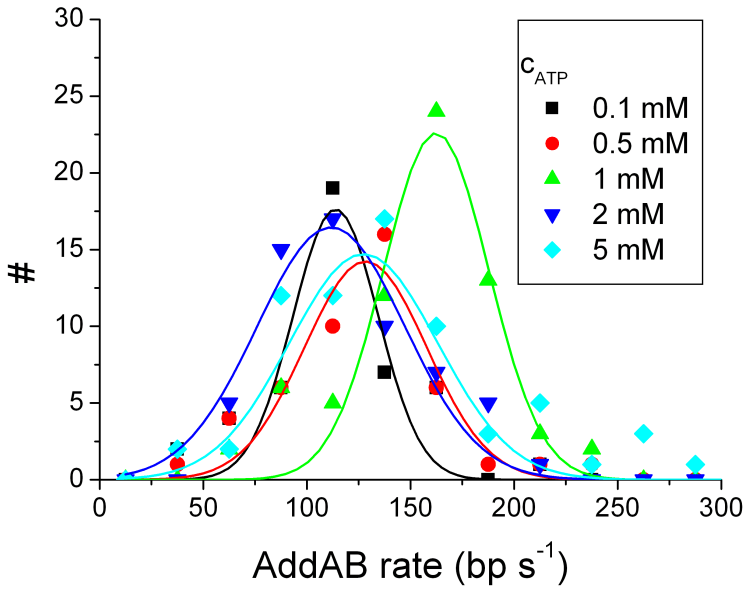

Figure 3.26: Plots of Mg^{2+}-ATP dependence of AddAB rate: Gaussian fit of AddAB rate distributions for different Mg^{2+}-ATP concentrations used. The bin size is 5 bp s^{-1} (0.01 mM Mg^{2+}-ATP), 20 bp s^{-1} (0.03 and 0.05 Mg^{2+}-ATP) and 25 bp s^{-1} (Mg^{2+}-ATP concentraions equal or larger than 0.1 mM). (# molecules analysed for 0.01, 0.03, 0.05, 0.1, 0.5, 1, 2 and 5 mM ATP: 45, 44, 45, 45, 46, 68, 59 and 69.) A constant shear rate σ of 510 s^{-1} was maintained during the experiments.

The distribution of enzyme unwinding rates is quite large, ranging from zero to 50, 100 and 150 bp s^{-1} for the three smallest Mg^{2+}-ATP concentrations 0.01, 0.03 and 0.05 mM, respectively. For all investigated Mg^{2+}-ATP concentrations larger or equal than 0.1 mM the rate range spans from 50 to 250 bp s^{-1}. The obtained data are shown in two distribution plots and can be well described by a Gaussian function (fig. 3.26) because the data are symmetrically distributed around a mean value. The bin size for the 0.01 mM Mg^{2+}-ATP data set was lowered to 5 bp s^{-1} to achieve proper fitting.

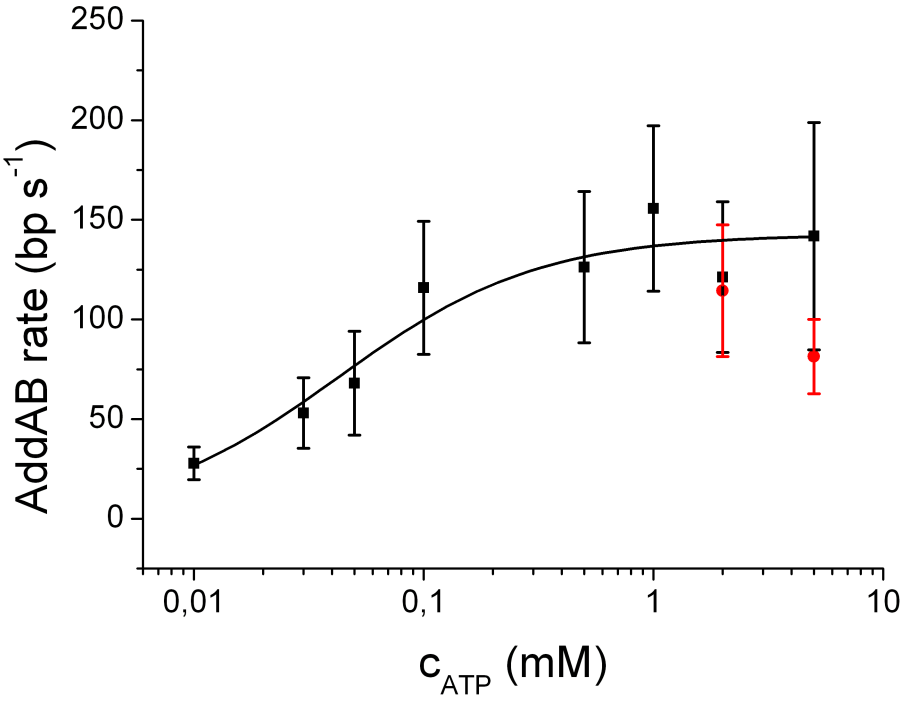

Figure 3.27: Michaelis-Menten plot of mean AddAB rates dependent on Mg^{2+}-ATP concentration. The fit yielded a K_M and an r_{max} of 0.043 ± 0.010 mM and 143 ± 7 bp s^{-1}, respectively. The black data were obtained with Mg^{2+} concentrations of 2 mM for ATP concentrations smaller or equal 1 mM, and 3 and 6 mM Mg^{2+} for 2 and 5 mM ATP, respectively. The red data were obtained for Mg^{2+} concentrations of 2 mM.

In order to derive the Michaelis-Menten parameters for the AddAB enzyme the mean unwinding rate and its standard deviation were calculated for each Mg^{2+}-ATP concentration and plotted in figure 3.27. Starting at a very low Mg^{2+}-ATP concentration of 0.01 mM, the mean rate continuously rises to 150 bp s^{-1} (1 mM Mg^{2+}-ATP). It has to be noted that these very low Mg^{2+}-ATP concentrations ($<$ 0.1 mM) are physiologically not relevant (Dillingham & Kowalczykowski, 2008),

but were assayed in order to obtain clear Michaelis-Menten constants which happen to lie in this Mg^{2+}-ATP concentration range.

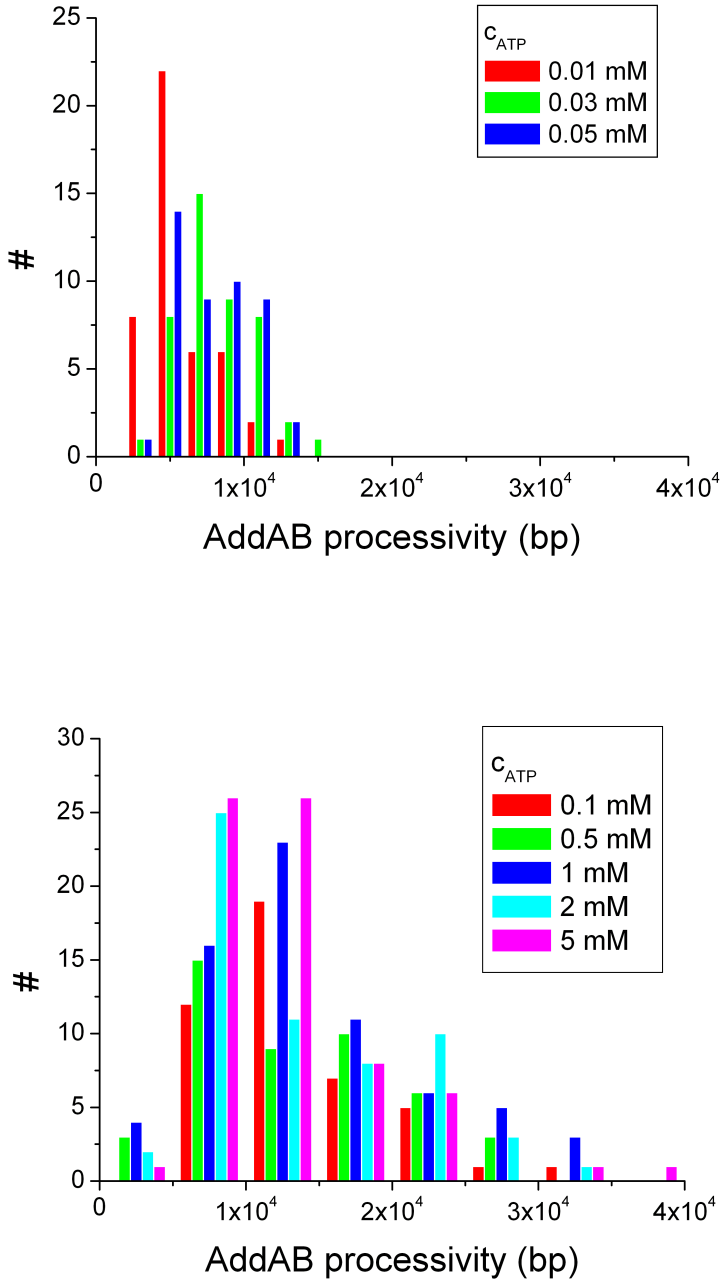

Figure 3.28: Histograms of Mg^{2+}-ATP dependence of AddAB processivity. The bin size is 2000 bp (for Mg^{2+}-ATP concentrations between 0.01 and 0.05 mM) and 5000 bp (for Mg^{2+}-ATP concentrations between 0.1 and 5 mM). (# molecules analysed for 0.01, 0.03, 0.05, 0.1, 0.5, 1, 2 and 5 mM ATP: 45, 44, 45, 45, 46, 68, 59 and 69.) A constant shear rate σ of 510 s^{-1} was maintained during the experiments.

Unexpectedly, the rate at 2 and 5 mM Mg^{2+}-ATP is slightly lower than for 1 mM ATP, but within the error. As kinetic data were obtained from usually three independent preparations which were compared with each other, it can be excluded that one of the preparations was contaminated. When the Mg^{2+} concentration becomes limited with respect to ATP, i.e. when it is lower than the ATP concentration, there is a drop in both AddAB rate and processivity. This reflects that Mg^{2+}-ATP is the actually required cofactor species of the AddAB enzyme. A hyperbolic fit of the rate data yielded a K_M value of 0.043 ± 0.010 mM and a maximum rate r_{max} of 143 ± 7 bp s^{-1}.

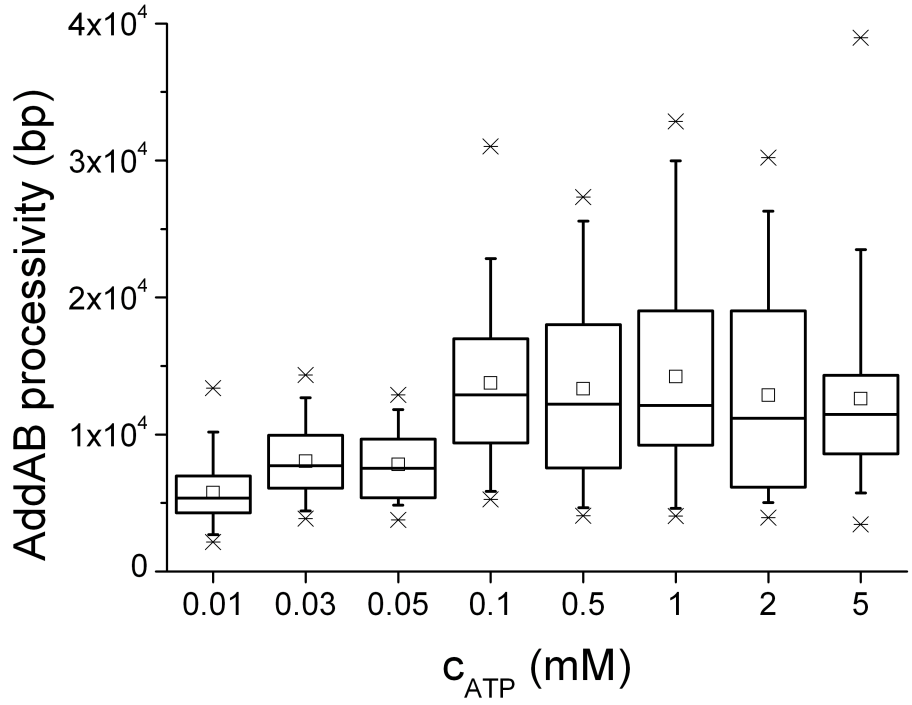

Figure 3.29: Box plot of ATP dependence of AddAB processivity. (# molecules analysed for 0.01, 0.03, 0.05, 0.1, 0.5, 1, 2 and 5 mM ATP: 45, 44, 45, 45, 46, 68, 59 and 69.) A constant shear rate σ of 510 s^{-1} was maintained during the experiments.

The obtained processivity data are skewed and seemingly independent of Mg^{2+}-ATP concentrations larger or equal than 0.1 mM (histograms and box plot in figs. 3.28 and 3.29). Processivities up to 40,000 bp are reached by individual enzymes. The mean value, however, was determined to be around 14,000 bp with standard deviations between 12,000 and 14,000 bp. At small Mg^{2+}-ATP concentrations, 0.01 to 0.05 mM, mean processivity values around 5,000 and 7,000 bp (latter two concentrations) were determined. The box plot (or box-and-whisker diagram) is

a different way to visualise distribution data. It includes the mean of the data (indicated by the small rectangle within the box), the median and the lower and upper quartiles of the distribution (indicated by the box), the whiskers (vertical lines) which extend to at most 1.5 times the box width (the interquartile range) from both ends of the box, as well as the smallest and largest value of the data set (two crosses). Using this way of presentation, it becomes obvious that the processivity data are asymmetric for all Mg^{2+}-ATP concentrations examined.

Fig. 3.30 shows Mg^{2+}-ATP-dependent plots of the determined AddAB rate *versus* processivity for each single-molecule observation. As can be seen, there is a positive linear correlation between AddAB enzyme rate and processivity for 0.01, 0.03, 0.1 and 0.5 mM Mg^{2+}-ATP, i.e. the determined error is smaller than the slope. At 2 mM Mg^{2+}-ATP this correlation becomes negative. All other investigated Mg^{2+}-ATP concentrations did not display significant correlations between AddAB rate and processivity. A slight funnel shape of the data is observed which reflects that at higher enzyme processivity the range of AddAB rates was reduced.

3.8.6 Shear rate dependence of AddAB rate and processivity

Three different shear rates, 306, 510 and 714 s^{-1}, were examined (at 1 mM Mg^{2+}-ATP and a staining ratio of 1/20 dye molecules per DNA base pair) and tested to see whether they influenced AddAB rate and processivity. Figures 3.31 and 3.32 show the data histograms and plots of AddAB processivity and rate, respectively.

It can be clearly seen that the histogram of the AddAB processivity is essentially unaffected by the shear rate. The plotted mean value rises only slighly from 13,600 over 14,200 to 15,000 bp with increased shear rate (slope and error of 3.3 and 21.7 bp s, respectively). In the absence of shear, one would expect a processivity value of 12,600 bp (error 11,260 bp). However, given the very large standard deviations and the error of the abscissa value (when the error bars are included in the fit) this change may not be significant.

Looking at the AddAB rates in the histogram, no clear trend can be observed upon altered shear rate. Nonetheless, the width of the Gaussian fitted curves of the histograms is reduced with increased shear rate from 89 to 60 and 56 bp s^{-1}, respectively. The plot of the mean rates and standard deviations, however, indicates that the AddAB rate is reduced at a higher shear rate from 164 over 156 to 143 bp s^{-1} (slope = -0.05 $\pm$ 0.15 bp). At zero shear a rate value of 182 bp s^{-1} would be obtained (error 94 bp s^{-1}). In analogy to the histograms, the standard deviation is also reduced from 59 to 42 and 33 bp s^{-1} for shear rates of 306, 510 and 714 s^{-1}, respectively.

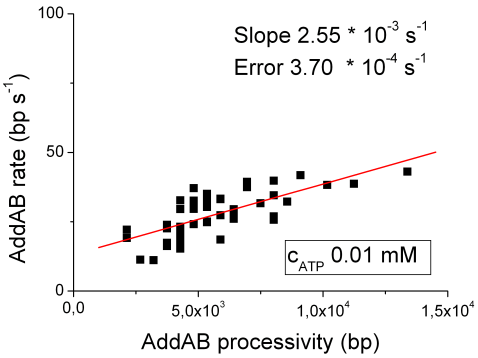
Slope 2.55 * 10-3 s-1
Error 3.70 * 10-4 s-1
cATP 0.01 mM
AddAB rate (bp s-1)
AddAB processivity (bp)

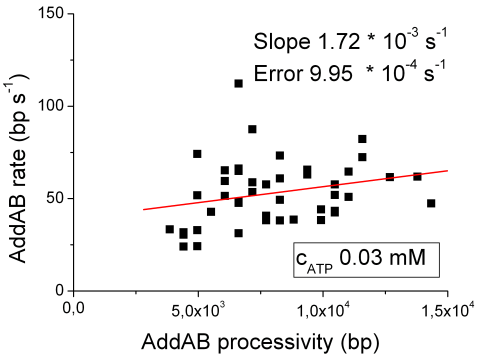
Slope 1.72 * 10-3 s-1
Error 9.95 * 10-4 s-1
cATP 0.03 mM
AddAB rate (bp s-1)
AddAB processivity (bp)

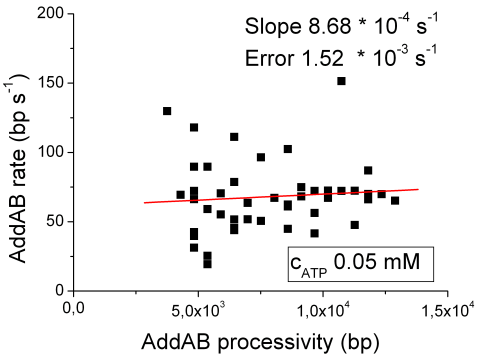
Slope 8.68 * 10-4 s-1
Error 1.52 * 10-3 s-1
cATP 0.05 mM
AddAB rate (bp s-1)
AddAB processivity (bp)

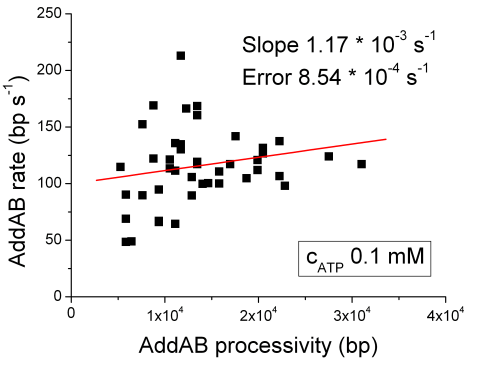
Slope 1.17 * 10-3 s-1
Error 8.54 * 10-4 s-1
cATP 0.1 mM
AddAB rate (bp s-1)
AddAB processivity (bp)

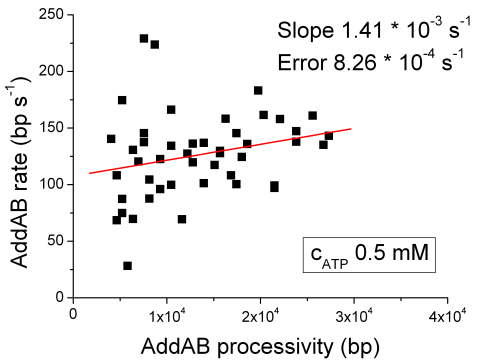
Slope 1.41 * 10-3 s-1
Error 8.26 * 10-4 s-1
cATP 0.5 mM
AddAB rate (bp s-1)
AddAB processivity (bp)

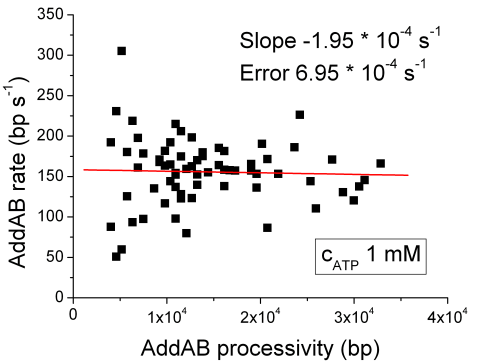
Slope -1.95 * 10-4 s-1
Error 6.95 * 10-4 s-1
cATP 1 mM
AddAB rate (bp s-1)
AddAB processivity (bp)

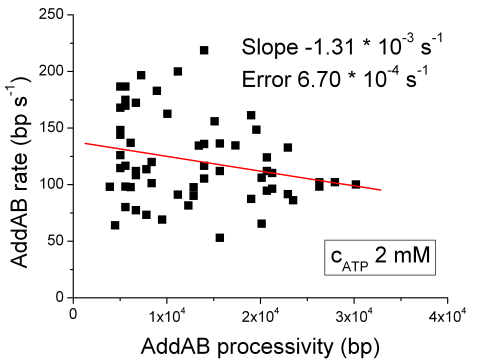
Slope -1.31 * 10-3 s-1
Error 6.70 * 10-4 s-1
cATP 2 mM
AddAB rate (bp s-1)
AddAB processivity (bp)

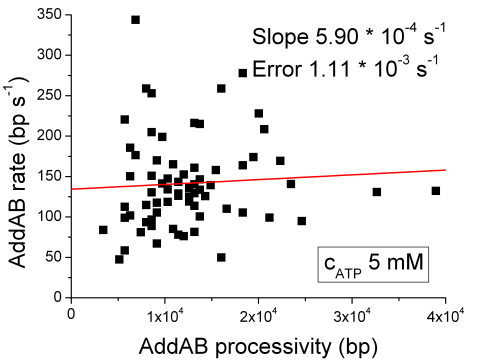
Slope 5.90 * 10-4 s-1
Error 1.11 * 10-3 s-1
cATP 5 mM
AddAB rate (bp s-1)
AddAB processivity (bp)

Figure 3.30: Correlation of AddAB rate with AddAB processivity for 0.01, 0.03, 0.05, 0.1, 0.5, 1, 2 and 5 mM Mg^{2+}-ATP. The data indicate that there is a positive linear correlation between AddAB rate and AddAB processivity at Mg^{2+}-ATP concentrations of 0.01, 0.03, 0.1 and 0.5 mM. For a Mg^{2+}-ATP concentration of 2 mM the linear correlation between AddAB rate and AddAB processivity is negative. For all other Mg^{2+}-ATP concentrations the determined slope values are within error. A constant shear rate σ of 510 s^{-1} was maintained during the experiments.

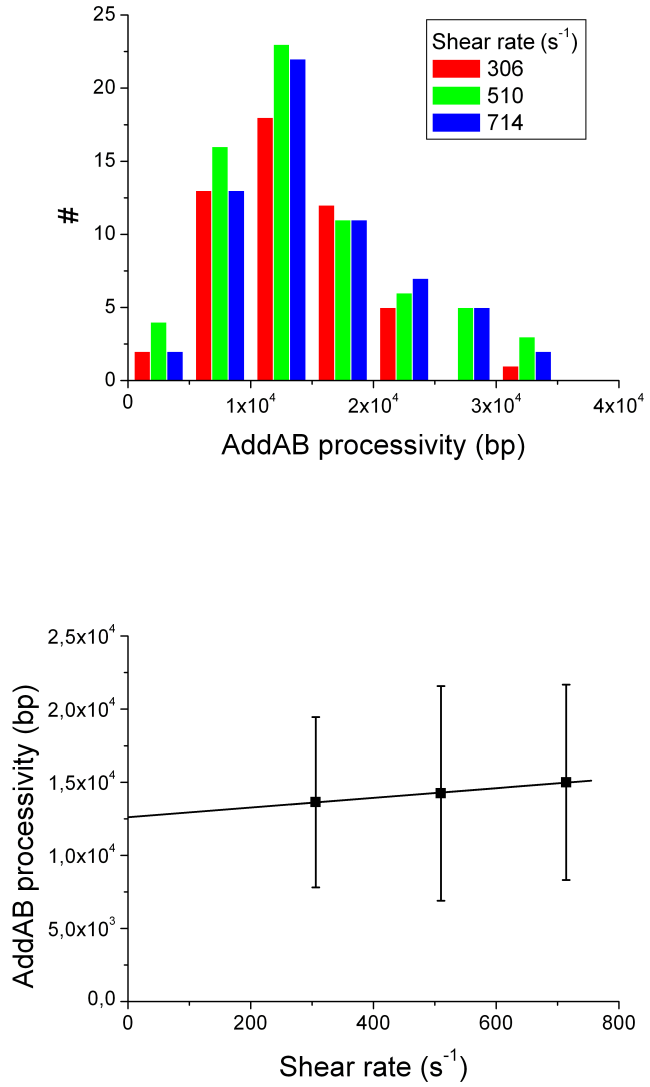

Figure 3.31: Shear rate dependence of AddAB processivity. The bin size in the histogram is 5000 bp. (# molecules analysed for a shear rate σ of 306, 510 and 714 s^{-1}: 50, 68 and 59.) A constant Mg^{2+}-ATP concentration of 1 mM was used during the experiments.

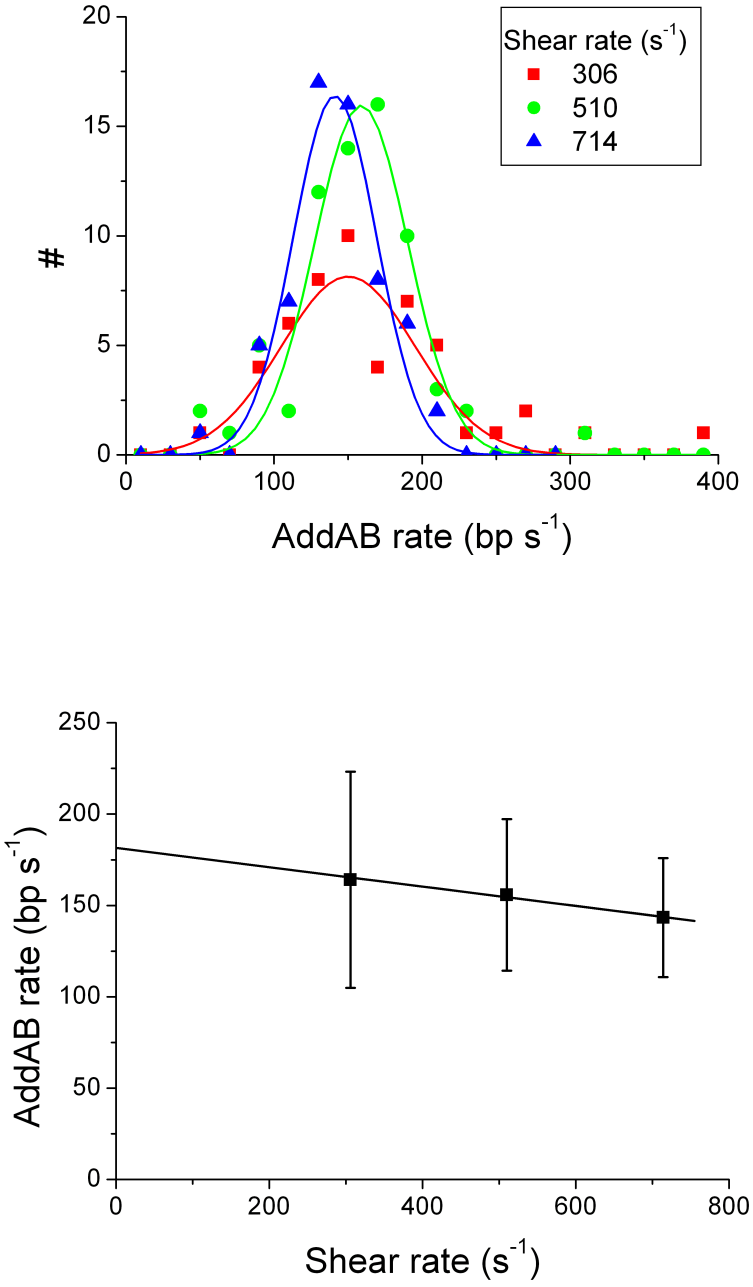

Figure 3.32: Shear rate dependence of AddAB rate. The bin size in the histogram is 20 bp s^{-1}. (# molecules analysed for a shear rate σ of 306, 510 and 714 s^{-1}: 50, 68 and 59.) A constant Mg^{2+}-ATP concentration of 1 mM was used during the experiments.

3.8.7 Staining ratio dependence of AddAB rate and processivity

During the ATP-dependent DNA unwinding, AddAB does not only need to unwind and cut lambda-DNA, it also needs to displace the intercalating dye YOYO-

1 iodide from the DNA. Hence, two different staining ratios of 1/20 and 1/50 dye molecules/bp were investigated with respect to affecting the enzymatic action of AddAB at two different shear rates. The results are shown in figures 3.33 and 3.34.

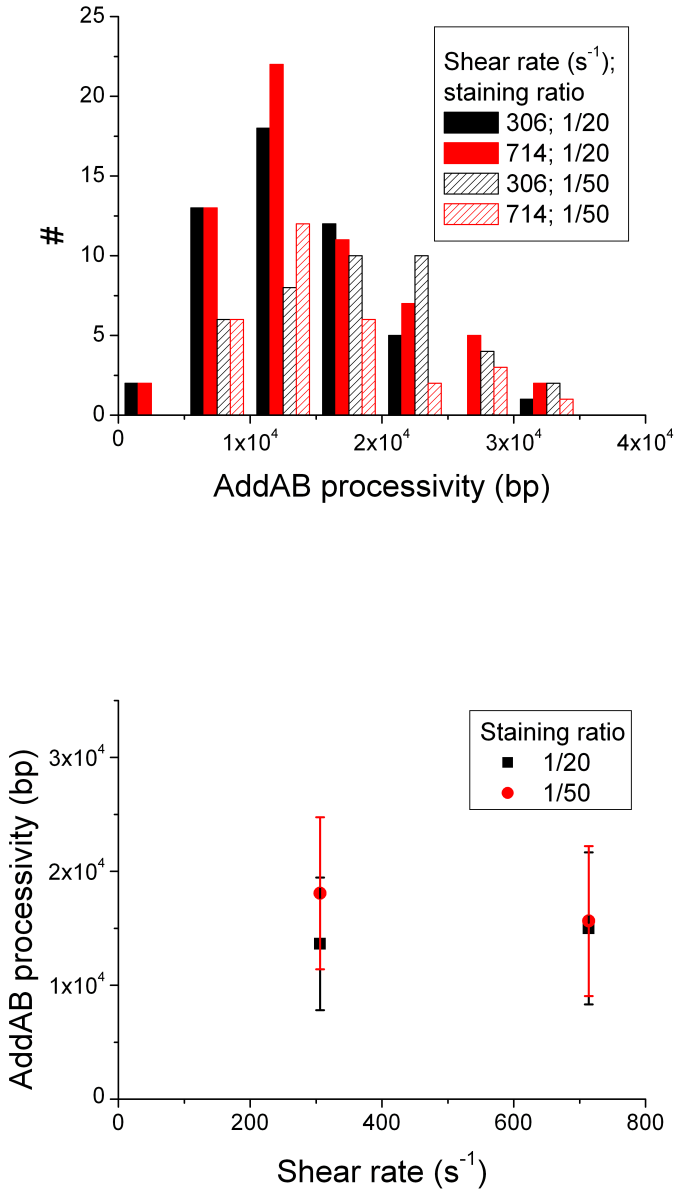

Figure 3.33: Staining ratio dependence of AddAB processivity. The bin size in the histogram is 5000 bp. (# molecules analysed for a shear rate of 306 s^{-1} and a staining ratio of 1/20 and 1/50 dye molecules/bp: 51 and 40. # molecules analysed for a shear rate of 714 s^{-1} and a staining ratio of 1/20 and 1/50 dye molecules/bp: 62 and 30.) A constant Mg^{2+}-ATP concentration of 1 mM was used during the experiments.

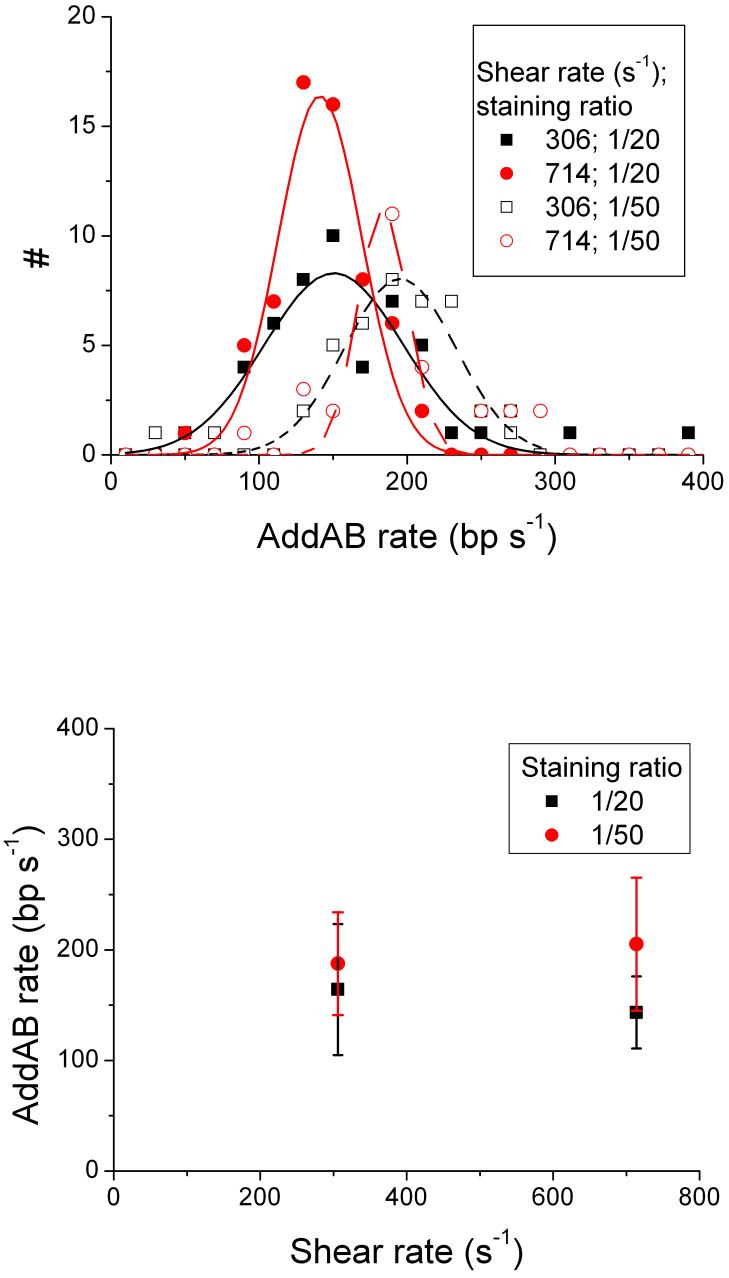

Figure 3.34: Staining ratio dependence of AddAB rate. The bin size in the histogram is 20 bp s^{-1}. (# molecules analysed for a shear rate of 306 s^{-1} and a staining ratio of 1/20 and 1/50 dye molecules/bp: 51 and 40. # molecules analysed for a shear rate of 714 s^{-1} and a staining ratio of 1/20 and 1/50 dye molecules/bp: 62 and 30.) A constant Mg^{2+}-ATP concentration of 1 mM was used during the experiments.

The histogram of the processivity data shows a clear shift for a shear rate of 306 s^{-1} towards higher processivity values for lower staining ratios, suggesting that

bound YOYO-1 iodide molecules impede the enzymatic action. At the highest investigated shear rate, however, both processivity histograms have the same shape. These findings are also clearly seen from the plotted mean processivity values, i.e. the processivity is higher by more than 4,000 bp when the staining ratio is reduced from 1/20 to 1/50 dye molecules/bp (for a shear rate of 306 s^{-1}). Using a shear rate of 714 s^{-1} the difference is much less pronounced with only 600 bp.

The enzyme rate considerably increases upon reducing the staining ratio. Interestingly, between high and low staining ratios the enzyme rate is more affected at higher shear rates. At 714 s^{-1} the rate increases from 143 to 205 bp s^{-1} whereas at 306 s^{-1} the rate only increases from 164 to 188 bp s^{-1}. In case of the enzymatic rate an extrapolation to a shear rate and a staining ratio of zero is not meaningful because of counteracting effects. Under these hypothetical conditions, a maximum AddAB processivity of almost 25,000 bp would be reached.

3.8.8 YOYO-1 iodide bulk assay of AddAB

The ATPase activity of AddAB was determined in a bulk assay which monitors the displacement of YOYO-1 iodide molecules from linear, blunt-end plasmid DNA (pUC18). The measured effect relies on the drastically reduced fluorescence quantum yield of the dye from 80% to less than 1% (DNA-bound *vs.* free dye). A control experiment showed that no fluorescence decay was observed without adding the cofactor Mg^{2+}-ATP.

The linear part of the fluorescence decay curves (fig. 3.35 upper graph), obtained after triggering AddAB unwinding, was fitted and the slope determined from three independent measurements. The mean and standard deviation values were plotted against the Mg^{2+}-ATP concentration (fig. 3.35 lower graph) and fitted with the hyperbolic function $r_{max} * \frac{c_{ATP}}{c_{ATP}+K_M}$ in order to obtain the Michaelis-Menten parameters K_M and r_{max}.

The determined AddAB rate (given in arbitrary units) is biochemically not meaningful, but the K_M value is. The obtained K_M and r_{max} values are 0.41 $\pm$ 0.17 mM and 26.2 $\pm$ 3.1 a.u., respectively.

These experiments were carried out twice and yielded very similar results for the two different days. The measurements at 1 to 5 mM Mg^{2+}-ATP were repeatedly inconsistent in the way that they produced very different rates, although working from the same stock solution. Hence, large error bars were observed for these specific Mg^{2+}-ATP concentrations.

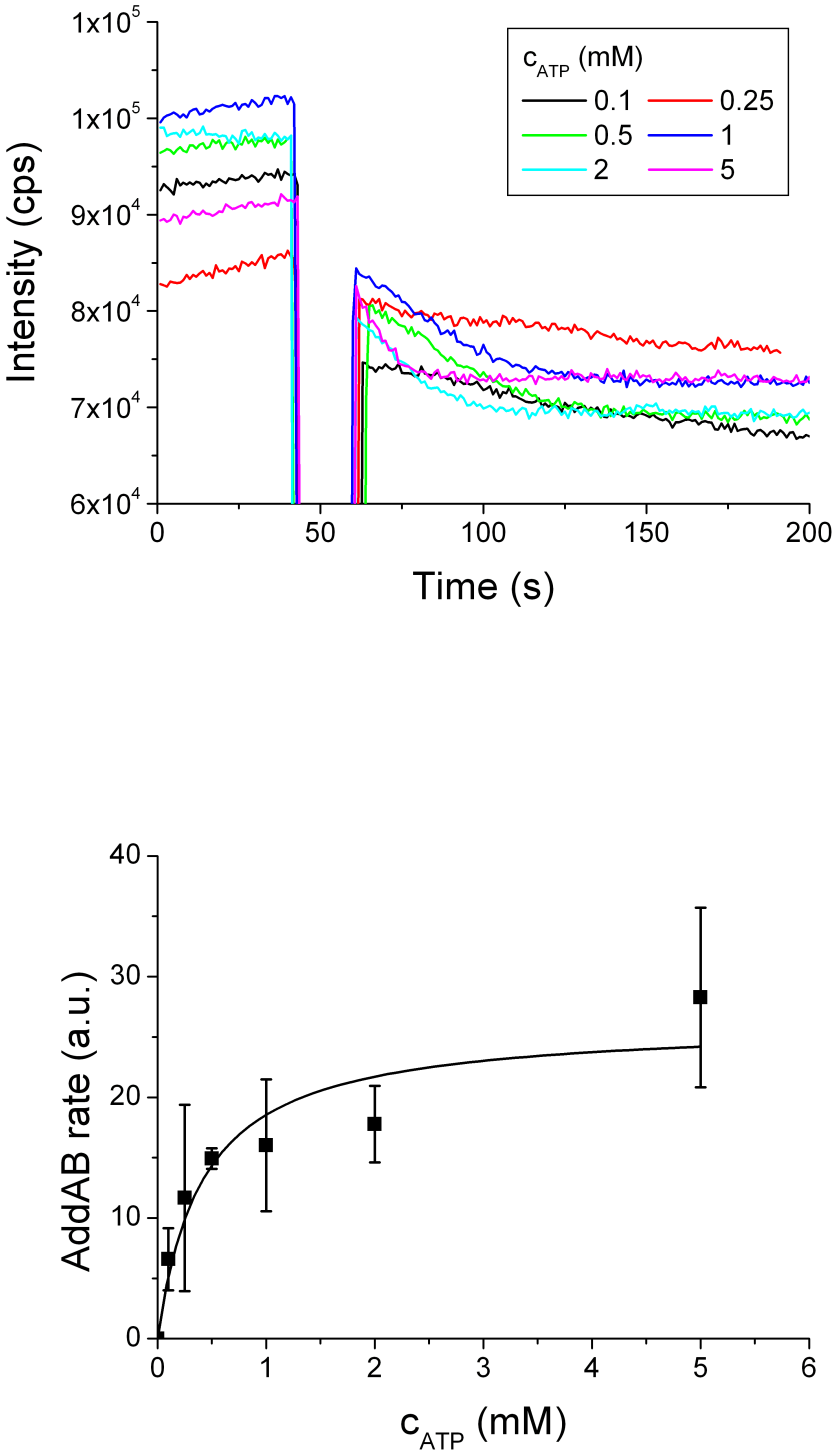

Figure 3.35: AddAB ATPase activity determined from a bulk assay that monitors the YOYO-1 iodide displacement from pUC18 dsDNA through subsequent fluorescence decrease. Upper graph: Time traces of raw data (one example for each Mg^{2+}-ATP concentration). Lower graph: ATPase activity and Michaelis-Menten fit.

3.8.9 Coupled ATPase bulk assay of AddAB

A second way to determine the ATPase activity of an enzyme from a bulk measurement is to use a coupled ATPase NADH assay. Every ATP molecule consumed is linked via a reaction cascade (depicted in fig. 3.6) to the reaction of 1 NADH molecule. NADH has an absorption band at a wavelength of 340 nm which can be spectrophotometrically monitored. The oxidised form of the cofactor, NAD^+, does not absorb at 340 nm, so that the AddAB activity can be monitored by an absorption decrease. Similar to the YOYO-1 iodide bulk assay, the intial part of the obtained absorption traces can be fitted to a linear function (fig. 3.36).

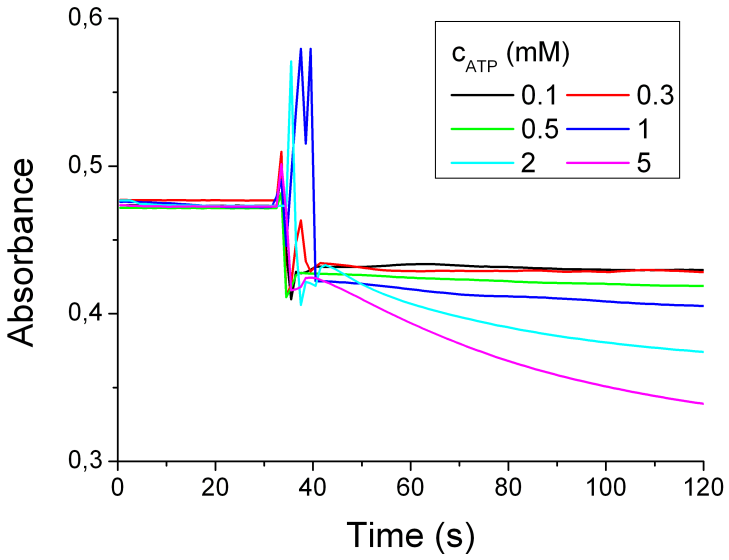

Figure 3.36: Coupled ATPase-NADH assay monitoring the ATP-dependent unwinding of linear plasmid pUC18 DNA by AddAB. One characteristic absorption curve is shown for every examined Mg^{2+}-ATP concentration. After triggering the enzymatic reaction with this cofactor (at about 30 s) a continuous drop in absorption can be seen due to consumed NADH.

Three independent measurements yielded a mean and standard deviation for the ATP consumption, given in nM ATP s^{-1} (nM DNA ends)$^{-1}$ which was corrected for the ATPase activity of AddAB not bound to dsDNA. The plot of these data *versus* the Mg^{2+}-ATP concentration (fig. 3.37) was fitted to a hyperbolic function. The Michaelis-Menten parameters K_M and r_{max} were determined to be 0.98 ± 0.3 mM and 299 ± 31 nM ATP s^{-1} (nM DNA ends)$^{-1}$, respectively.

Two independent assay series yielded the same result, including the large error

bars for the Mg^{2+}-ATP concentrations between 0.3 and 2 mM. More than three repetitions were carried out for these Mg^{2+}-ATP concentrations, however, they always led to inconsistent results.

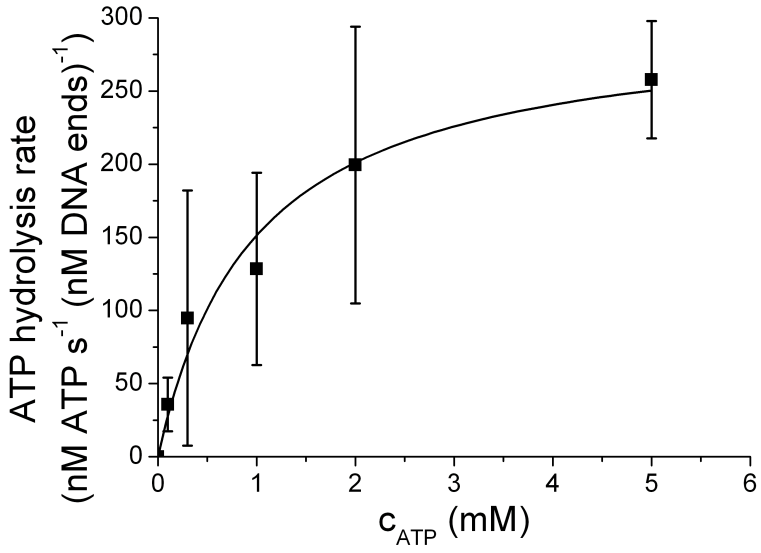

Figure 3.37: AddAB ATPase activity investigated by the coupled enzyme assay. The ATP concentration digested per second and concentration of DNA ends is plotted against the ATP concentration.

3.9 Results: RecBCD

The RecBCD protein has been previously prepared in our laboratory. The ATP-dependent activity and its existence has been shown (Jacob Zipprich, personal communication).

Initially, it served as a test protein to establish single-molecule experiments on hydrodynamically stretched lambda-DNA. Hence, kinetic data obtained at 1 mM Mg^{2+}-ATP condition are presented for comparison with the literature.

Figure 3.38 shows typical kymographs that were obtained during RecBCD-mediated unwinding of lambda-DNA. These are very similar to the ones obtained from AddAB which also show prematurely stopped DNA unwinding by (probably) enzyme unbinding (fig. 3.38A) or photobleaching (fig. 3.38B). Already shortened DNA molecules can be digested to completion (fig. 3.38C). Most of the kinetic traces observed show a linear and continuous unwinding of lambda-DNA.

Fig. 3.39 shows a histogram of the apparent DNA molecule length before

triggering the RecBCD-mediated DNA unwinding with Mg^{2+}-ATP. The optimum length value is 19.75 ± 1 μm (118.5 ± 6.5 pxl). This value reflects that lambda-DNA is stained to completion with YOYO-1 which, at that time, was done in accordance with Bianco *et al.* (2001) who supplemented the flow buffer with 20 nM YOYO-1 iodide.

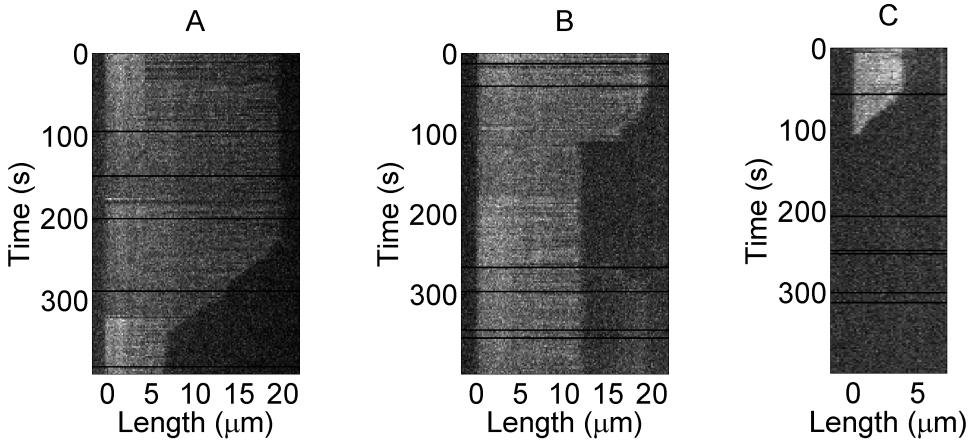

Figure 3.38: Kymographs of RecBCD unwinding of lambda-DNA at a Mg^{2+}-ATP concentration of 1 mM. Panel A shows a lambda-DNA molecule whose RecBCD mediated unwinding is triggered at 220 s which procedes continuously for some 120 s until 2/3 of the DNA molecule is digested. In panel B lambda-DNA unwinding through action of RecBCD is stopped prematurely because of DNA molecule bleaching which results in cleavage of the active RecBCD-DNA complex. Panel C shows a previously degraded lambda-DNA molecule which is digested to completion by RecBCD in a linear and continuous fashion. Lambda-DNA in these preparations was completely loaded with YOYO-1 dye, reaching staining ratios of about 1/5 dye molecules/bp. A constant shear rate σ of 510 s^{-1} was maintained during the experiments.

Figure 3.40 shows the determined RecBCD rates and processivities. The RecBCD processivity has an optimum between 5,000 and 10,000 bp; a maximum processivity value of 35,000 bp has been observed for one individual complex. The RecBCD rate follows a Gaussian distribution and has been determined to be 130 ± 102 bp s^{-1} at a Mg^{2+}-ATP concentration of 1 mM. The maximum rate observed for individual enzyme-DNA complexes goes up to 300 bp s^{-1}.

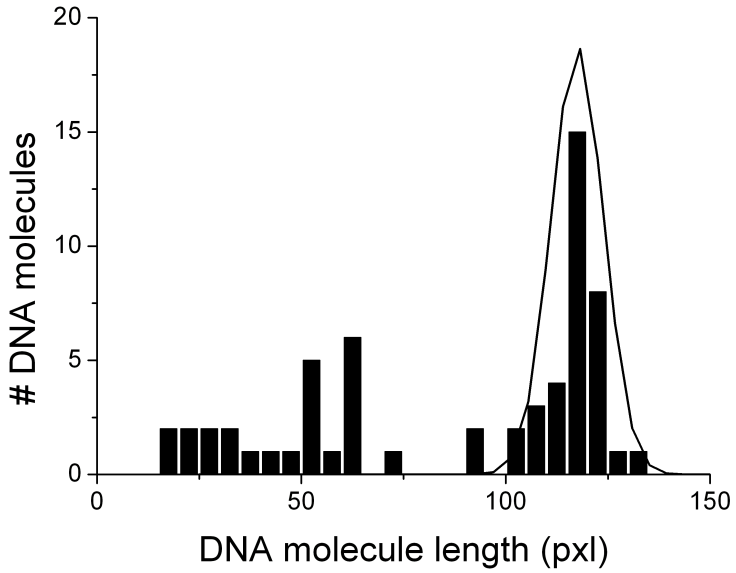

Figure 3.39: Histogram of the initial lambda-DNA molecule length (1 mM Mg^{2+}-ATP condition). The DNA molecule length measured from the raw data is 118.5 ± 6.5 pxl (19.75 ± 1 μm). The bin size is 5 pxl. (# molecules analysed 60.) The mean value was set to the full lambda-DNA genome of 48,502 bp. A constant shear rate σ of 510 s^{-1} was maintained during the experiments.

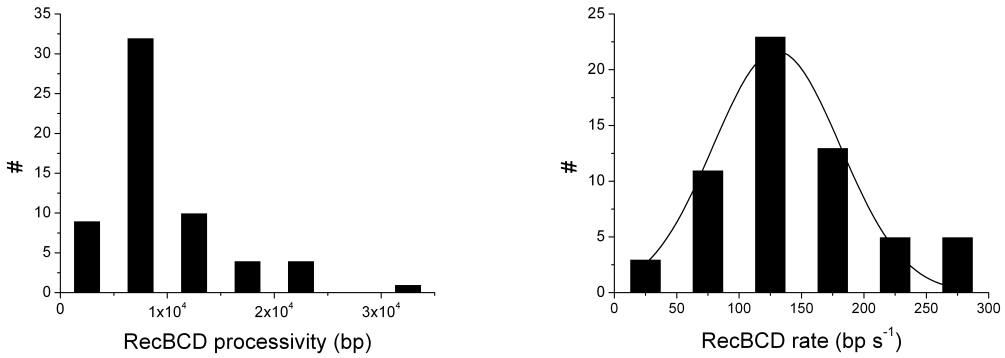

Figure 3.40: Histograms of RecBCD kinetic measures. RecBCD processivity (left) and RecBCD rate (right). The bin sizes are 5000 bp and 50 bp s^{-1}, respectively. The Gaussian fit of the RecBCD rate data yielded a mean unwinding rate of 130 ± 102 bp s^{-1}. (# molecules analysed 60. A constant Mg^{2+}-ATP concentration of 1 mM and a shear rate of 510 s^{-1} was used and maintained during the experiments.

3.10 Discussion

3.10.1 Evaluation of the single-molecule scaffold

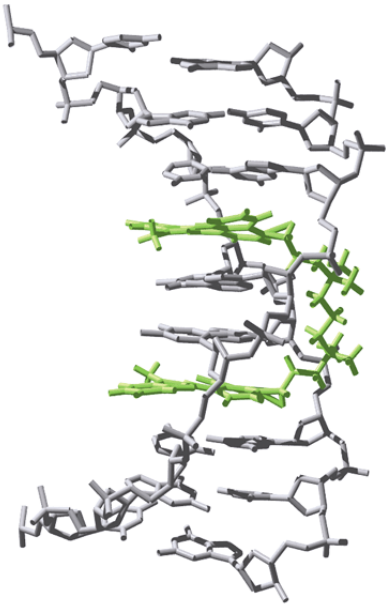

Figure 3.41: NMR solution structure of the TOTO-1 dye bound to dsDNA. (Taken from the Molecular Probes Handbook. Original source: Protein Data Bank PDB 108D.)

Hydrodynamically stretched and visualised lambda-DNA molecules have proven to be an ideal scaffold for probing DNA-protein interactions at the single-molecule level (Bianco *et al.*, 2001; Visnapuu *et al.*, 2008). Implemented approaches use either DNA surface or bead tethering for TIRFM or optical tweezers combined with fluorescence microscopy, respectively. Within this thesis, the TIRFM method was preferentially chosen because it nicely scales up the single-molecule DNA-enzyme experiment.

The commercially available intercalation dye YOYO-1 iodide which has an absorption maximum at 488 nm coinciding with one of the Ar laser lines is used widely for DNA staining purposes. YOYO-1 increases its fluorescence quantum yield upon DNA binding from less than 1% to 80%. A second binding effect of DNA intercalation is the partial unwinding of DNA and the concomitant distortion and elongation of the DNA helix (Johansen & Jacobsen, 1998) which can also be seen in the crystal structure of the analogous TOTO-1 dye bound to DNA (figure 3.41). This structure also shows that the TOTO-1 dye binds DNA through bis-intercalation (Spielmann *et al.*, 1995) which is the same binding mode

for YOYO-1 at low staining ratios (Carlsson *et al.*, 1994; Larsson *et al.*, 1994).

The aspect of DNA distortion already demands a careful characterisation of this single-molecule scaffold before its application to enzyme observation. Thus, both the influence of the flow (or shear) rate and the staining ratio on the apparent DNA molecule length were investigated.

A systematic increase of the flow (shear) rate results in linear DNA extension. At sufficiently low shear rates and during the establishment of DNA stretching (see fig. 3.10, frames 1.8 to 2.6 s), the lambda-DNA molecule shape can be described with the trumpet-shape model (first regime) (Theofanidou *et al.*, 2004). Further increase of the flow rate leads to a stem and flower shape of the DNA chain which is characterised by complete stretching of the DNA molecule near the tether while there is still recognisable agitation of the freely floating DNA end (second regime). At very high shear rates the DNA molecule extension converges to the DNA contour length which is accompanied by full DNA stretching along the whole backbone (third regime). At the examined shear rates of 306, 510 and 714 s^{-1} the observed mean DNA molecule length was 14.3, 15.3 and 15.7 μm indicating the second regime. Higher shear rates were not assayed because they resulted in excessive DNA molecule detachment from the surface. The examined sample must have suffered from previous degradation apparent by two DNA species whose lengths are very similar. Nevertheless, simple Gaussian fitting of the optimal value yielded stable and sensible results. The maximum contour length of lambda-DNA without YOYO-1 intercalation was reported to lie between 16.3 and 16.5 μm (Bellan *et al.*, 2006; Baumann *et al.*, 2000). The shear-rate- or force-dependent stretching of single lambda-DNA molecules was examined before and can be mathematically described with the worm-like-chain model for polymers (Graneli *et al.*, 2006).

$$F = \frac{k_B T}{L_P} \left(\frac{1}{4(1 - \frac{\langle x \rangle}{L})^2} - \frac{1}{4} + \frac{\langle x \rangle}{L} \right) \tag{3.14}$$

In equation 3.14 k_B is the Boltzmann constant, T the absolute temperature, L_P the polymer persistence length and $\langle x \rangle / L$ the relative mean extension of the polymer. The force F is directly proportional to the hydrodynamic flow (or shear) rate. Using $T = 295$ K, $L_P = 50$ nm (Boal, 2002) and $L = 16.4$ μm (average of Bellan *et al.* (2006) and Baumann *et al.* (2000)), this leads to stretching forces of 1.3, 4.6 and 11.2 pN for DNA molecule lengths $\langle x \rangle$ of 14.3, 15.3 and 15.7 μm, respectively. Compared to typical optical tweezers DNA manipulation (see e.g. Bustamante *et al.*, 2003) the presented TIRFM assay works in the low-force stretching regime.

As can be seen from the crystal structure, the intercalation of one YOYO-1 molecule into dsDNA extends the DNA molecule by 0.4 nm (Bellan *et al.*, 2006; Johansen & Jacobsen, 1998). At low DNA staining ratios, i.e. around 1/100 dye molecules/bp this effect is negligible (Graneli *et al.*, 2006). At the three different staining ratios of 1/50, 1/100 and 1/200 slightly decreasing DNA molecule lengths were found, i.e. 15.3 ± 0.8, 14.9 ± 0.7 and 14.0 ± 0.8 μm, respectively. Complete saturation of the lambda-DNA with YOYO-1 dye leads to DNA molecule lengths around 19 μm which matches well the theoretically expected value. As a result of bis-intercalation 1 YOYO-1 molecule binds 4 DNA base pairs. Hence, around 12,000 YOYO-1 molecules can maximally bind lambda-DNA which leads to a length increase of 4.8 μm. This result is in contrast with Perkins *et al.* (1995) and Bensimon *et al.* (1994) who report maximum lambda-DNA length values of 22 μm at the same staining conditions. On the other hand, these groups use different microfluidic devices, DNA-bead tethering and already work from a different initial DNA molecule length.

Previous single-molecule publications have documented the use of intercalation dyes in the reaction trigger buffer (e.g. Bianco *et al.*, 2001). During the course of this project it was found that at low initial dye/base pair staining ratios YOYO-1 molecules intercalate rapidly into dsDNA. Previously, it was reported that the equilibration of YOYO-1 already bound to DNA can take several hours at 50 °C and up to several days at room temperature (Carlsson *et al.*, 1995). In this thesis, the first binding step of YOYO-1 to dsDNA was shown to happen on a timescale of a few minutes depending on the initial dye/base pair staining ratio. For an initial staining ratio of 1/50, 1/100 and 1/200 dye molecules/bp the mono-exponential time constants of YOYO-1 intercalation were found to be 200, 160 and 100 s, respectively.

This finding has implications for both single-molecule and bulk assays using YOYO-1. Control experiments at the single-molecule level have to ensure that the presence of YOYO-1 in the buffer flow does not lead to unwanted transient DNA molecule extension which counteracts any observation of exonuclease activity or that may pretend nucleoprotein filament formation with e.g. the recombination proteins RecA or Rad51.

In bulk experiments one usually monitors exonuclease activity as a result of YOYO-1 deintercalation. Depending on the absolute concentration of YOYO-1 dye and the timescale of the experiment reintercalation of YOYO-1 may happen, hence influencing the recorded timetrace and the final result.

These preliminary results implied several consequences for performing enzyme single-molecule assays using stretched lambda-DNA molecules. The two counter-

acting effects of lambda-DNA lengthening due to YOYO-1 intercalation and the incomplete DNA molecule stretching because of moderate flow rates prevent an absolute measure of the DNA molecule length and require normalisation of this value. During enzymatic reactions, a continuous and intermediate buffer flow of 0.05 ml min^{-1} was maintained to keep the DNA molecules reasonably stretched while avoiding tether instabilities. It is unlikely that enzyme rates determined from single lambda-DNA unwinding are affected by the flow profile experienced by either surface- or bead-tethered DNA molecules. No YOYO-1 was added to any of the flow buffers ensuring a non-perturbed experimental system for exonuclease assays. Control measurements showed that lambda-DNA molecules not subject to enzymatic degradation kept a constant molecule length under these conditions. This also confirms that YOYO-1-DNA complexes are extremely stable and that the dye is not washed off the DNA, at least not on the timescale of minutes.

3.10.2 RecBCD

The RecBCD enzyme is well-characterised in the literature (Dillingham & Kowalczykowski, 2008) and hence served as a model enzyme to establish single-molecule exonuclease assays using hydrodynamically stretched lambda-DNA molecules. As a proof of principle a relevant sample size of 60 individual molecules was collected at 22 °C using a cofactor concentration of 1 mM Mg^{2+}-ATP. The mean enzyme rate and processivity were determined with 130 ± 102 bp s^{-1} and 9,600 ± 5,900 bp, respectively. However, Bianco *et al.* (2001) reported a RecBCD rate of 502 ± 243 bp s^{-1} and a RecBCD processivity of 27,000 ± 9,800 bp (at 23 °C), respectively, which were also determined with a single-molecule lambda-DNA stretching assay. This discrepancy may be due to an inactivated or lost RecD subunit in the assayed enzyme. Earlier, it was found that the RecBC complex where the D subunit was missing or inactivated had a two-fold reduced enzyme rate and six-fold decreased processivity (Dillingham *et al.*, 2005; Bianco & Kowalczykowski, 2000). The preparation of RecBCD is very challenging and time consuming, hence no attempts were made to repeat the TIRFM experiments with a newly prepared enzyme stock.

It is also worth mentioning that the data obtained were done according to experimental conditions described by Bianco *et al.* (2001) where the lambda-DNA molecules were stained to saturation with the YOYO-1 dye. This group also supplemented the flow buffer with this dye which was not done to collect the data set described in this thesis. During the characterisation of the AddAB

enzyme, discussed in detail in the following section, it was found that an increasing amount of intercalation dye has a negative influence on both the enzyme rate and processivity. The remaining discrepancy found for the RecBCD enzyme may be due to the different assays. Optical tweezers as used by Bianco *et al.* (2001) allow maintenance of the bead-tethered DNA-enzyme complex freely in solution whereas TIRFM looks at surface-tethered DNA molecules. The latter technique may have two disadvantages: If the surface is not completely passivated with BSA, the free DNA-enzyme end may transiently stick to it. Furthermore, very high laser light intensities are reached near the surface with TIRFM which may damage the biological sample more vigorously than epi-fluorescence conditions used in combination with optical tweezers. Both effects can have a negative influence on the enzyme behaviour and may theoretically reduce enzyme rate and processivity. In principle, it would have been possible to compare both the TIRFM over the optical tweezers assay using facilities in COSMIC. However, given the limited time and the requirement for sample modification (using DNA bead tethering), this comparison could not be carried out. To the best of my knowledge, no laboratory has done such a validation yet in which a single enzyme stock, e.g. RecBCD, was investigated with the two methods.

3.10.3 *B. fragilis* AddAB

The *B. fragilis* AddAB enzyme (BfAddAB) was expressed and purified as described in the materials and methods and results section. The AddAB sequence was confirmed by mass spectrometry through comparison with entries in the NCBInr database. Global protein alignment with the *B. subtilis* AddAB (BsAddAB) enzyme has yielded 17% and 16% amino acid identity for the AddA and AddB protein, respectively (Garry Blakely, personal communication). The presence of an iron-sulfur cluster indicated by three conserved and one additional cysteine residue 200 amino acids further upstream in the sequence was confirmed by UV spectroscopy which showed an absorption band at 410 nm. This iron-sulfur cluster was shown to be essential for DNA end binding in BsAddAB (Yeeles *et al.*, 2009; Cromie, 2009). AddAB functions as a Mg^{2+}-ATP-dependent DNA exonuclease which was confirmed by DNA gel electrophoresis. The helicase activity was demonstrated in a bulk assay and by a single-molecule experiment which both revealed continuous YOYO-1 displacement from dsDNA. The ATPase activity of BfAddAB was analysed with a coupled enzyme assay.

The BsAddAB enzyme is known to have only one single motor for DNA helicase activity due to the presence of an N-terminal SF1 helicase domain in AddA

(Dillingham & Kowalczykowski, 2008). Within this context, the function of the putatively intact Walker A motif (helicase motif 1), used for binding and hydrolysis of ATP, in the AddB subunit remains to be elucidated. The remaining six SF1 helicase motifs are missing in this protein. Based on protein sequence alignments, the BfAddAB enzyme is also known to have only one active helicase motor in the AddA subunit. This helicase activity is clearly supported by a single-molecule and a bulk YOYO-1 displacement assay from dsDNA. The enzymatic behaviour of AddAB is analogous to *E. coli* RecBCD which is a well-known two-motor helicase. On this basis, claims that BfAddAB acts either as a DNA translocase or exonuclease can be rejected. Regarding the functional and sequence similarity of BfAddAB with RecBCD and BsAddAB who were proven to bind dsDNA in a 1:1 ratio (Dillingham & Kowalczykowski, 2008; Chedin & Kowalczykowski, 2002), BfAddAB can also be assumed to bind in the same ratio to dsDNA. The fact that multiple enzyme species can theoretically bind to a single dsDNA end was not addressed within this thesis, but could be assayed by applying varied enzyme concentrations in excess over DNA. Such a strategy would reveal cooperative enzyme binding and nuclease effects.

Given the highly abundant and short chi sequence in the *B. subtilis* genome it was speculated that the AddAB enzymes are not required to be as processive and fast as the RecBCD enzyme. So far, there exists no report in the literature on the rate and processivity of any AddAB enzyme. Within this thesis, the BfAddAB processivity and rate is characterised at the single-molecule level for different Mg^{2+}-ATP concentrations, different shear rates and YOYO-1 concentrations bound to the DNA.

Single-molecule experiments have the power to look at individual active DNA-enzyme complexes. The recorded traces, shown as kymogaphs, give the most direct insight into the AddAB enzyme rate and processivity without being obscured by inactive DNA-enzyme species, as present during bulk observations. The predominant mode of single enzyme-mediated DNA unwinding occurs at a constant rate which is referred to as static disorder. The enzyme rate ranges mostly from 50 to 250 bp s^{-1} at Mg^{2+}-ATP concentrations larger or equal than 0.1 mM. Once an individual enzyme has started to unwind DNA at a certain rate, it will keep this rate until it unbinds from the DNA and, thus, naturally stops or is subject to laser degradation. The static disorder effect was also found for the RecBCD enzyme including the large rate range (Bianco *et al.*, 2001). Dynamic disorder refers to the phenomenon that individual translocases change their rate during the translocation process. Apparent dynamic disorder was discovered only in a subset of the AddAB data (10-20%) and may be most likely the result of

an artefact coming from surface interactions of the free DNA tail which has the AddAB complex bound. This artefact always led to a decrease in enzyme rate and was usually accompanied by fluorescent traces left on the surface (e.g. seen in figure 3.23C). However, as obvious in this example, this interaction itself does not necessarily lead to AddAB rate lowering.

The determined mean ATP-dependent AddAB rates (at 22 °C) are 3-fold or 2-fold lower than for RecBCD measured at the single-molecule level or in bulk, respectively (Bianco *et al.*, 2001; Roman & Kowalczykowski, 1989 b). The mean AddAB rates determined at a Mg^{2+}-ATP concentration of 2 mM and 5 mM were lower than for 1 mM Mg^{2+}-ATP. But, these values deviate within the experimental error. The AddAB processivity is, in contrast to RecBCD, independent of the Mg^{2+}-ATP concentration for concentrations larger or equal than 0.1 mM and has mean values and standard deviations of around 14,000 bp which is half the value reported for RecBCD at 1 mM Mg^{2+}-ATP (Bianco *et al.*, 2001). At Mg^{2+}-ATP concentrations smaller than 0.1 mM, which are physiologically irrelevant (Dillingham & Kowalczykowski, 2008), the AddAB processivity decreases.

Measurements of the AddAB rate and processivity at altered shear rates and YOYO-1 staining ratios confirm that these parameters have a slight influence on the enzyme behaviour, as expected. At a reduced shear rate the enzyme rate increases, whereas the enzyme processivity stays almost constant. As YOYO-1 needs to be displaced from the dsDNA during AddAB unwinding the dye presents an impediment to the enzyme which reduces both enzyme rate and processivity. Nevertheless, none of these effects has a clear statistical significance which is in part a result of the naturally wide range of AddAB enzyme rate and processivity.

The *B. fragilis* chi site is not known at present. No hint from the single-molecule data of enzyme pausing at a specific site on lambda-DNA, was observed. The limitation of the single-molecule assay for the detection of enzyme pausing was estimated to be around 10 seconds matching 5 camera frames. Even if pausing had occurred within that time window, it should have resulted in a noticeable change of enzyme rate in one single kymograph, but this was not observed. The BsAddAB was found to bind tightly to its chi site for 15 min (half-life) (Chedin *et al.*, 2006). This mechanistic aspect is thought to protect the 3'-terminated DNA strand from further nuclease degradation.

The characterisation of the BfAddAB enzyme finally allows a kinetic comparison to the well-characterised RecBCD enzyme. In particular, one can address the question why bacteria have evolved two different enzymes for the same functions, DNA recombination and repair, and whether the number of helicase domains used by each enzyme plays a significant role. The data suggest that the AddAB

processivity plays a dominant role for the action of the enzyme. The main reason is most obviously that the enzyme needs to exceed the average spacing between any two chi sites in order to properly fulfil its biological function. However, without knowing the *B. fragilis* chi sequence and its distribution on the *B. fragilis* genome, it remains to be assessed how well the BfAddAB enzyme has itself adapted to this natural context. The unwinding rate of the single-motor enzyme AddAB is significantly smaller than the RecBCD rate and is apparently of less importance than the (high) processivity. Although powered by only one helicase motor, BfAddAB can unwind on average 14,000 bp per event, with some individual enzymes unwinding up to 40,000 bp. This puts it in the same range as RecBCD and makes it the most processive single-motor SF1 helicase known to date. The AddAB unwinding rate is similar to another SF1 helicase, UvrD, which was reported to have a maximum translocation rate of 275 bp s^{-1} at 25 °C (Dessinges *et al.*, 2004). However, the processivity of UvrD is on average 256 bp which is strikingly lower than BfAddAB. The high AddAB processivity is, hence, surprising as it is more similar to a two-helicase rather than a one-helicase motor. These findings prove that two helicases are not an *a priori* requirement for a highly processive molecular motor, as is the case for RecBCD whose rate and processivity decrease upon disabling of the RecD motor (Dillingham *et al.*, 2005). In addition, these results clearly show that independent of the homologous recombination enzyme used by bacterial cells - either RecBCD or AddAB - the high processivity is an absolute requirement for the proper *in vivo* functioning of these enzymes.

In table 3.3 the Michaelis-Menten constants obtained from the single-molecule and the two different bulk assays are compared. This is also visualised in figure 3.42 which show the kinetic data obtained from the two bulk and the single-molecule assay. Curiously, all K_M values differ from each other which suggests that the used methods bias the result. Nevertheless, the two bulk assays display very similar BfAddAB activity with K_M values differing by a factor of 2. In the single-molecule assay, there is an implicit selection for active DNA-enzyme complexes whereas both bulk assays do not allow such a selection. Also, looking at figure 3.42 clearly underlines that the single-molecule method is much more sensitive in detecting enzyme function than a standard bulk spectroscopy assay. This criterion is a reasonable explanation for why the Michaelis-Menten curve is much steeper for the single-molecule data than compared to the bulk data. In addition, the absolute DNA concentration in the single-molecule experiment is much lower than in the bulk and a continuously fresh reaction buffer is flowed into the microfluidics which maintains a constant and high ATP concentration.

The fact that this experiment uses surface-tethered DNA molecules which are in a stretched configuration should not impact the result.

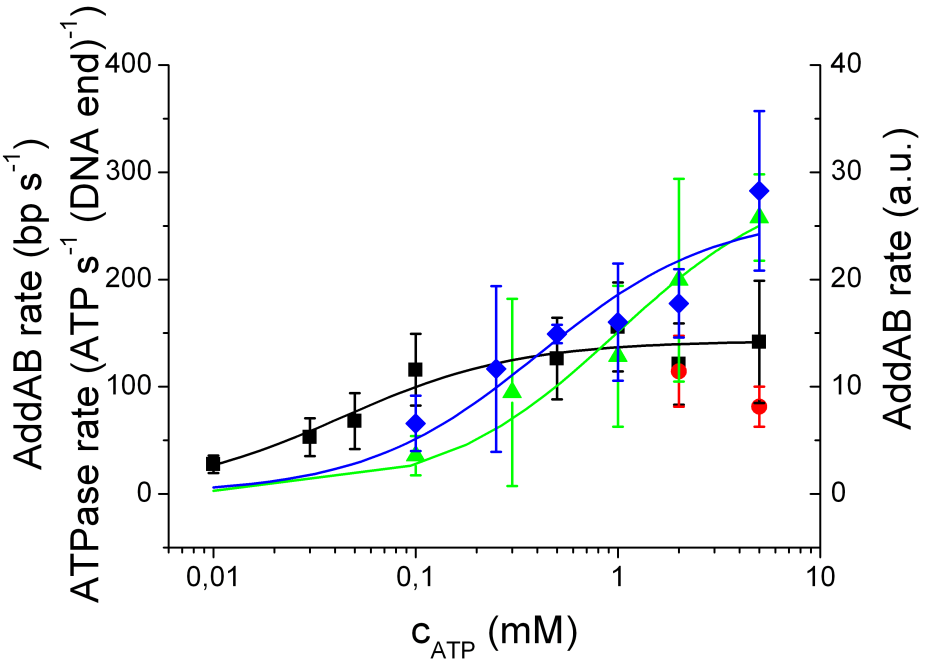

Figure 3.42: Comparison of the kinetic data obtained from the single-molecule assay (AddAB rate (bp s^{-1}), black squares, left axis; red circles, limiting Mg^{2+} concentration of 2mM), the coupled ATPase assay (ATPase rate (nM ATP s^{-1} (nM DNA ends)$^{-1}$), green triangles, left axis) and the YOYO-1 helicase assay (AddAB rate (a.u.), blue diamonds, right axis).

The two bulk assays monitor completely independent aspects. The YOYO-1 displacement assay measures actual DNA unwinding. A problem with the time-traces taken is that the number of active DNA-enzyme complexes is not known. Hence, it is impossible to derive a meaningful enzyme rate and processivity. These traces are further complicated by the finding that YOYO-1 reintercalates rapidly into remaining dsDNA which does not become unwound. The coupled enzyme assay, on the other hand, does not reveal to which extent DNA is unwound. Over the used Mg^{2+}-ATP concentration range of 0.1 to 5 mM there is a steady increase in Mg^{2+}-ATP consumption which was found to slightly decrease and, hence minimally deviate from the Michaelis-Menten curve, (almost) within error at 1 and 2 mM Mg^{2+}-ATP for the YOYO-1 displacement assay at the single-molecule level and in bulk, respectively. This finding may also reflect that the AddB subunit has an intact Walker A motif which binds and digests ATP although not contributing to DNA unwinding.

As pointed out earlier, the obtained r_{max} values are only meaningful for the

BfAddAB Michaelis-Menten fit results		
Assay	K_M (mM)	r_{max}
Single-molecule assay	0.043 ± 0.010	143 ± 7 bp s^{-1}
YOYO-1 bulk assay	0.41 ± 0.17	26.2 ± 3.1 a.u.
ATPase assay	0.98 ± 0.3	299 ± 31 nM ATP s^{-1} (nM DNA ends)$^{-1}$

Table 3.3: BfAddAB Michaelis-Menten fit results shown for the different kinetic assays used.

single-molecule and the coupled enzyme assay. Knowing that the two-helicase motor RecBCD consumes 3-4 ATP molecules/bp unwound (Roman & Kowalczykowski, 1989 b), one can well relate the r_{max} value of 143 bp s^{-1} to the concentration of ATP digested per single DNA-enzyme complex (299 ± 31 nM ATP s^{-1} (nM DNA ends)$^{-1}$) which yields roughly 2 ATP molecules/bp unwound for the single-motor helicase BfAddAB. This, however, also assumes that all of the dsDNA ends present in solution have an active AddAB enzyme bound.

3.11 Outlook

The presented data have furthered our understanding of the AddAB homologous recombination enzymes, in particular a first characterisation of the BfAddAB enzyme rate and processivity was undertaken. To arrive at a more complete picture for the AddAB mechanism chi site interactions will have to be performed at both the single-molecule level and in bulk. This, however, involves finding the *B. fragilis* chi site in the first place. The chi site of the BsAddAB enzyme is known and Chedin *et al.* (2006) found that a very stable complex between both structures is formed with a half-time of 15 minutes. This raises further fundamental questions about the initiation and regulation of DNA repair by AddAB enzymes. In comparison, the switching behaviour of the *E. coli* RecBCD enzyme after encountering its chi sequence takes place within seconds (Spies *et al.*, 2003; Handa *et al.*, 2005). In addition, it remains to be shown that, in analogy to RecBCD, AddAB has evolved to maintain DNA processivities that are much higher than the average intersite distance between two chi sites on a bacterial genome. At present, only the BfAddAB processivity is known but not the chi site and its distribution on the *B. fragilis* genome and *vive versa* for BsAddAB.

The ultimate goal for elucidating the AddAB mechanism is to obtain a crystal structure. This will shed light on the enzyme's exact mechanism and allow detailed comparison with RecBCD. Complementary enzyme mutant studies should then solve many of the remaing questions.

A fundamental aspect that has not been solved yet for either RecBCD or AddAB is the static disorder of the enzyme rates observed in single-molecule experiments. Mere speculation suggests that internal enzyme folding influences the exact rate of DNA progression and unwinding. Single-molecule studies may hence be performed on proteins that can be specifically labelled with non-natural, fluorescent amino acids which can serve as reporter molecules.

Chapter 4

Image analysis of single-molecule kinetic data using lambda-DNA

4.1 Preface

This project was carried out with Dr Martin Oheim and Mr Marcel van 't Hoff at the University Paris V Descartes (Paris, France) who are part of my Marie-Curie Research-Training-Network.

The group has developed a lot of expertise in TIRFM applied to single-cell and single-vesicle imaging used for neurological sciences. In the initial stages of the project described in chapter 3 I had very nice interactions with this group which has given me the opportunity to learn the TIRF technique. Using the lambda-DNA scaffold described earlier, we evaluated the performance of a previously built TIRF setup which uses a parabolic reflector. All measurements were performed by the PhD student Marcel van 't Hoff and by myself.

I have implemented several quantitative image analysis approaches that are decribed in this chapter.

A publication on this work has appeared in which I share the first authorship with Mr Marcel van 't Hoff (van 't Hoff *et al.*, 2009).

4.2 Quantitative image analysis

Quantitative image analysis is defined as the extraction of information from data that are in the form of pictures (Glasbey & Horgan, 1995). It recognises five different stages that are usually followed in this order.

1. The display of the image can be chosen, after careful consideration, as binary, greyscale or multivariate.
2. Filters are used for transformation and noise reduction in the images.
3. Segmentation divides the image in different regions (of interest).
4. Mathematical morphology studies the shapes and sizes of objects.
5. Measurement is done to extract quantitative information from the images.

4.3 Aim and motivation

As mentioned in chapter 1, the position of individual fluorescent molecules can be determined with high precision (e.g. Yildiz *et al.*, 2003). In analogy to the point-spread-function fitting procedure the aim of this sub-project was to use quantitative image analysis to accurately determine the length of single lambda-DNA molecules with high precision. However, during the continuation of this project and the application of surface-tethered lambda-DNA molecules to homologous recombination enzymes (chapter 3), it became obvious that the exact DNA length cannot be determined. The main reasons are that the shear rate influences the apparent DNA molecule length and that the intercalation dye YOYO-1 stretches the DNA. In addition, DNA degradation poses a problem.

Hence, this chapter describes approaches that reduce noise in images showing fluorescently labelled, stretched lambda-DNA. In addition, it offers a straightforward way to extraxt the relative DNA molecule length from single kymograph images. After analysis of many kymographs and data normalisation, the DNA length in base pairs can be obtained as in chapter 3.

4.4 Materials and Methods

The parabolic-reflector TIRF setup used for image acquisition was not built by me. It is described in detail in the appended publication (van 't Hoff *et al.*, 2009). Hence, I am not describing it in this chapter.

The preparation of biotinylated DNA for surface NeutrAvidin attachment was done as described in chapter 3 and carried out by me. Borosilicate capillaries with 0.1 x 1.0 mm inner dimensions and 5 cm length were used instead of Perspex flowcells and purchased from Composite Metal Services, Ltd. (Ilkley, UK).

All image analysis approaches were implemented by me using the software MatLab R2008a (The MathWorks, Cambridge).

4.5 Approaches and results

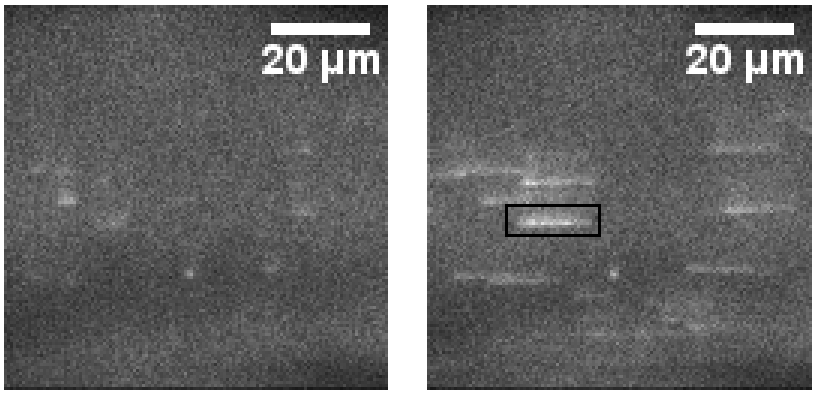

Figure 4.1: Single frame of coiled (left) and stretched (right) lambda-DNA molecules taken from a video sequence obtained with the parabolic-reflector TIRF setup. (Supplementary video S4-1)

As outlined in chapter 3 the uncoiling of surface-tethered fluorescently labelled lambda-DNA molecules can be visualised. Figure 4.1 shows one field-of-view of coiled and stretched lambda-DNA molecules. These first data suffered from many problems that were solved during the course of my PhD:

- The sample was completely bleached within 20 s leaving no single DNA molecule on the surface.
- Individual DNA molecules showed blinking behaviour because of DNA tail fluctuations in and out of the evanescent-field layer (see supplementary movie). (Very shallow laser incidence angles were used which produce an evanescent-field of a few 10s of nanometres.)
- The samples also suffered from unstable linkers (NeutrAvidin binding to biotinylated DNA). Hence, detachment and vanishing of DNA molecules from the surface was observed with high frequency.

At that stage, the lambda-DNA scaffold could not be applied to observation of enzymatic action.

In the following the outlined approach described in section 4.2 is adopted to address the aim of this project. First, one image frame extracted from one of the videos (fig. 4.1 right panel) was taken as a working basis and converted into a coloured look-up-table (LUT) to assess the noise level more easily by vision (fig. 4.2 Raw data). The pixel values were normalised to match the LUT (step

1). Different noise reduction techniques were applied to this frame and viewed for comparison with the raw image (step 2, figures 4.2). After this step an example DNA molecule (arbitrarily chosen and marked in figure 4.1) was plotted to assess whether the "molecule shape" is clear and can be recognised by a general mathematical feature. The noise reduction techniques used were the Laplace transformation, the first derivative, combinations of both and the singular value decomposition (SVD).

4.5.1 Laplace transformation

The Laplace transformation is also known as Kernel function. It is similar to a moving average or box filter which replaces each pixel value by the average of pixel values centred around it. If we denote f_{ij} as pixel values in the initial image with $i, j = 1, ..., n$, w as a weight matrix and the output pixel values as $g_{i,j}$, this can be expressed with the following equation

$$g_{ij} = \sum_{k=-m}^{m} \sum_{l=-m}^{m} w_{k-m+1,l-m+1} f_{i+k,j+l} \quad \text{for } i, j = (m+1), ..., (n-m). \tag{4.1}$$

If $m = 1$ the averaging window consists of a 3×3 matrix. Note that the resulting image is shortened in both dimensions by a pixel difference of $2m$. The way equation 4.1 is defined does not change the size of the resulting image matrix. However, the image frame (in case of $m = 1$ one layer) remains unchanged. The bigger the window chosen the larger the smoothing effect in the final image.

Depending on the resolving structure and feature of the initial image this weight matrix can be redesigned. In case of the stretched DNA molecules which we wish to resolve, it was found that a 5×5 Kernel matrix with the following entries works best in the images.

$$w = \begin{pmatrix} -1 & -1 & -1 & -1 & -1 \\ -1 & -1 & -1 & -1 & -1 \\ 5.5 & 5.5 & 5.5 & 5.5 & 5.5 \\ -1 & -1 & -1 & -1 & -1 \\ -1 & -1 & -1 & -1 & -1 \end{pmatrix} \tag{4.2}$$

The middle row consists of reasonably large numbers to amplify the stream of an imaged stretched DNA molecule (fig. 4.2 Laplace transformation (5×5 Kernel)).

4.5.2 First derivative

A particularly useful tool which reveals edges in the images is the performance of the first derivative in column direction. This is because the stretched DNA takes a horizontal position.

$$g_{ij} = f_{i+1,j} - f_{i,j} \quad \text{for } i = 1, ..., n-1 \text{ and } j = 1, ..., n. \tag{4.3}$$

After this transformation negative values g_{ij} occur which were automatically set to zero. A combination of the first derivative with subsequent application of the 5×5 Kernel function has proven useful to amplify the objects of interest (fig. 4.2 First derivative and first derivative followed by 5×5 Kernel).

4.5.3 Singular value decomposition (SVD)

The Singular value decomposition (SVD) is a very powerful method for de-noising and data compression (Hou, 2003). SVD decomposes the initial $m \times n$ image matrix A into three matrices U, Σ and V which are related by

$$A = U\Sigma V^* \tag{4.4}$$

Σ is a diagonal $m \times n$ matrix and U and V are unitary matrices (whose columns are orthonormal) having $m \times m$ and $n \times n$ dimensions, respectively. (The asterisk denotes the adjoint matrix.) The SVD calculates the eigenvalues and eigenvectors of AA^* and A^*A. The eigenvectors of AA^* and A^*A are the columns of U and V, respectively. The eigenvalues are the squares of the singular values for A which are the diagonal entries of the Σ matrix arranged in descending order.

$$\Sigma = \begin{pmatrix} \sigma_1 & 0 & 0 & & 0 & 0 & & 0 \\ 0 & \sigma_2 & 0 & \dots & 0 & 0 & \dots & 0 \\ 0 & 0 & \sigma_3 & & 0 & 0 & & 0 \\ & \vdots & & \ddots & & & & \vdots \\ 0 & 0 & 0 & & \sigma_r & 0 & & 0 \\ 0 & 0 & 0 & & 0 & 0 & \dots & 0 \\ & \vdots & & & & \vdots & & \vdots \\ 0 & 0 & 0 & \dots & 0 & 0 & \dots & 0 \end{pmatrix} \tag{4.5}$$

Looking at the Σ matrix, the SVD can now be used to discriminate between signal and noise. The four largest values ($\sigma_i \gg 0$) were systematically taken to reconstruct a noise-reduced image according equation 4.4. All other values in the

Σ matrix were quite small and set to zero as they simply contribute to noise in the images (fig. 4.2 SVD).

Raw data/image

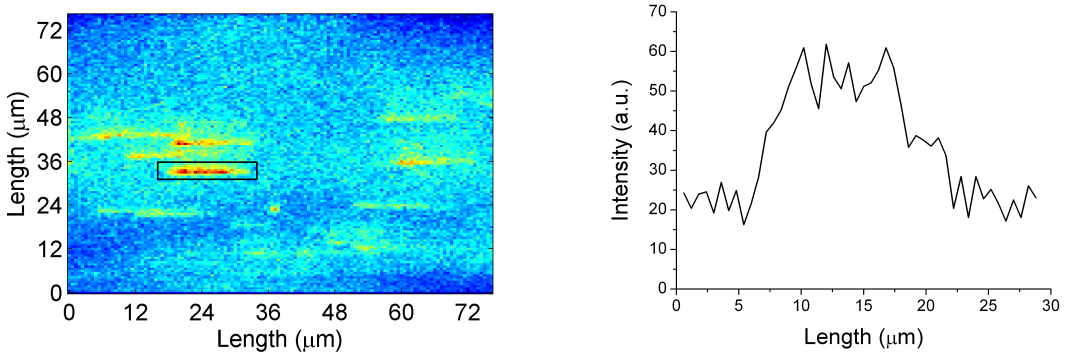

Laplace transformation (5×5 Kernel)

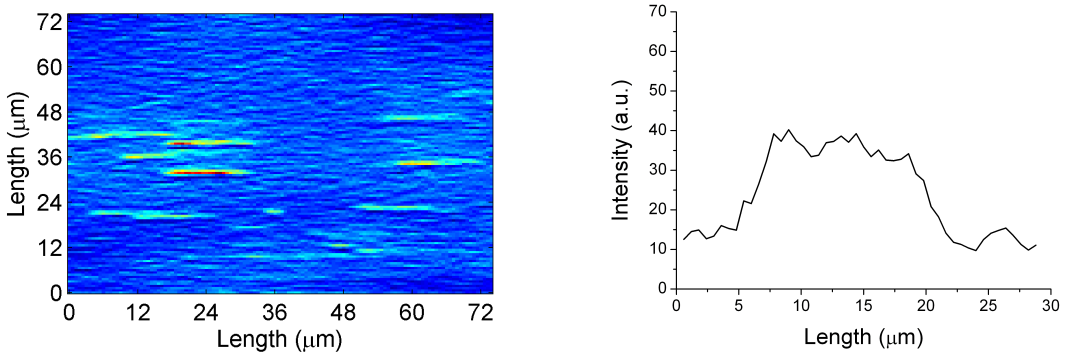

First derivative

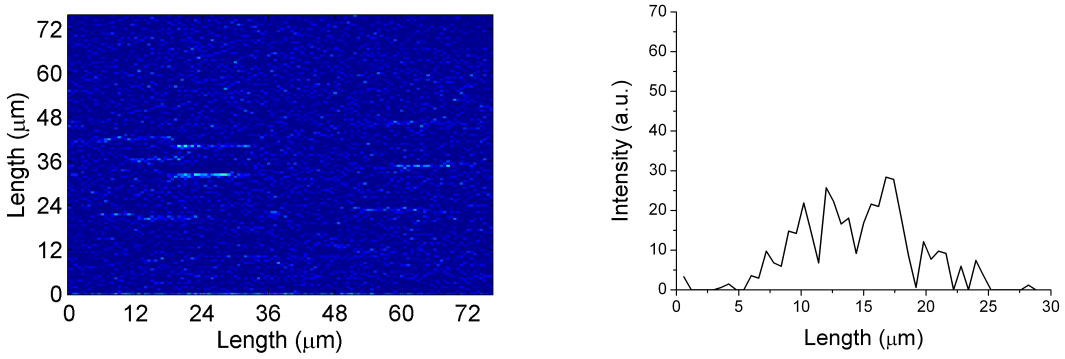

First derivative followed by 5×5 Kernel

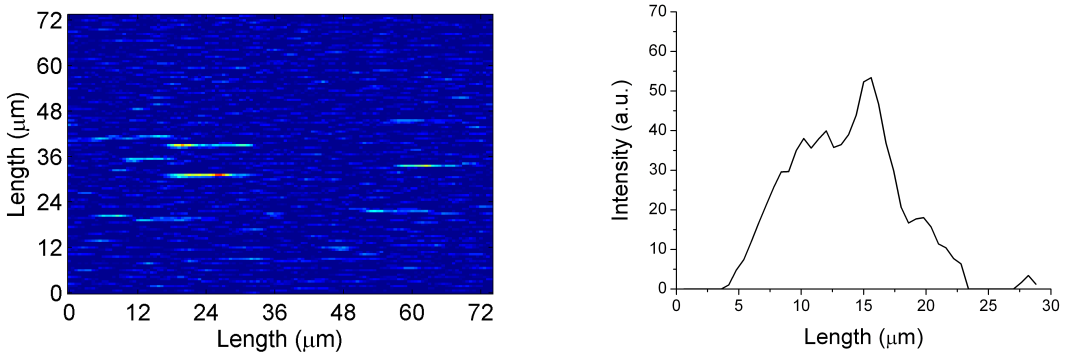

SVD

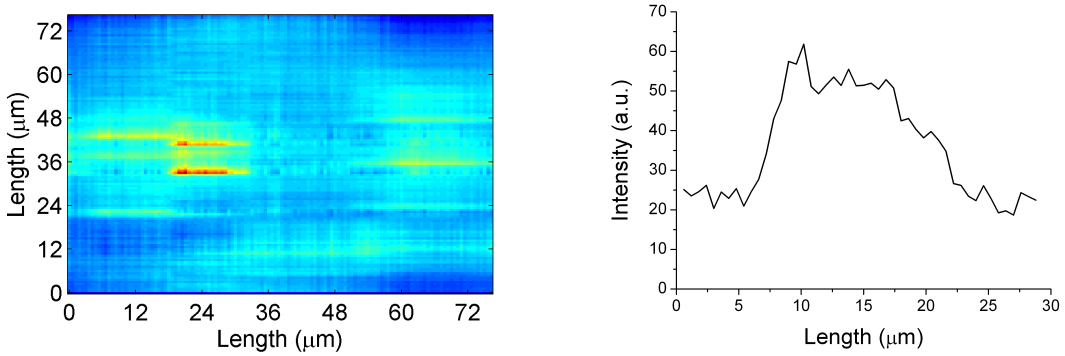

Figure 4.2: Application of noise reduction techniques to a raw image showing around 8 individual stretched lambda-DNA molecules.

Figure 4.2 (raw data/image) shows a typical image with around 8 stretched DNA molecules clearly distinguished by eye to which the different noise reduction techniques were applied. The intensity trace of the most intense DNA molecule (always the same, marked in figs. 4.1 and 4.2 Raw image) is plotted after each treatment in the graph on the right side. The raw image (top row) is very noisy which is also true for the intensity of the chosen DNA molecule. Application of the 5×5 Kernel function takes out a lot of this noise in both the image and the intensity trace. Although the first derivative alone and in combination with the 5×5 Kernel improves the image to the eye, the obtained intensity traces are noisier than the raw image or become distorted, respectively. The SVD applied to the raw images did not prove useful as it removed a few of the previously resolved DNA molecules and as it seemed to distort the image.

An obvious problem with most of the noise reduction techniques is image distortion, i.e. mathematical DNA molecule lengthening as for example with

the 5×5 Kernel function. In addition the most clearly resolved DNA molecule was picked in the image for intensity trace display. The resolution of the other DNA molecules was less efficient. Hence, no mathematical approach could be developed to divide the image in several regions of interest containing each one DNA molecule (segmentation step 3). The fourth step, mathematical morphology, is not of interest within this study, as stretched DNA molecules have an *a priori* well-defined shape.

Based on these findings, kymographs were produced manually from the raw video files saving steps 3 and 4 (figure 4.3). As the DNA traces in each row (coming from individual frames in the raw video) are still quite noisy, the SVD was applied to reduce the noise in the kymograph images. In particular, as seen in figure 4.3 the SVD method is very effective for rectangular patterns and does neither change the feature of the reconstructed kymograph nor the DNA length in the intensity trace. But, it clearly removes all the noise in the DNA streams which is a perfect basis for DNA molecule length determination.

4.5.4 DNA molecule length determination

Each row in the kymograph (fig. 4.3) represented a single video frame showing, after flow application and before loss by bleaching or detachment, a stretched DNA molecule. To determine the DNA molecule length from the kymographs, both DNA molecule ends were fitted with the sigmoidal function

$$y = A_2 + \frac{A_1 - A_2}{1 + exp(\frac{x - x_0}{dx})} \tag{4.6}$$

to determine the start and end position x_0, respectively. The difference between the left and right x_0 value determined the DNA molecule length. Frames dominated by blinking or subject to photobleaching yielded aberrant fit parameters, e.g. R^2 values larger than a set threshold of 1000 and DNA lengths smaller than 10 μm, and were systematically discarded from analysis. This procedure allowed multiple determinations of DNA molecule length from one and the same DNA molecule in one kymograph (fig. 4.4). Furthermore, the whole ensemble of DNA molecules imaged could be analysed one by one (fig. 4.5).

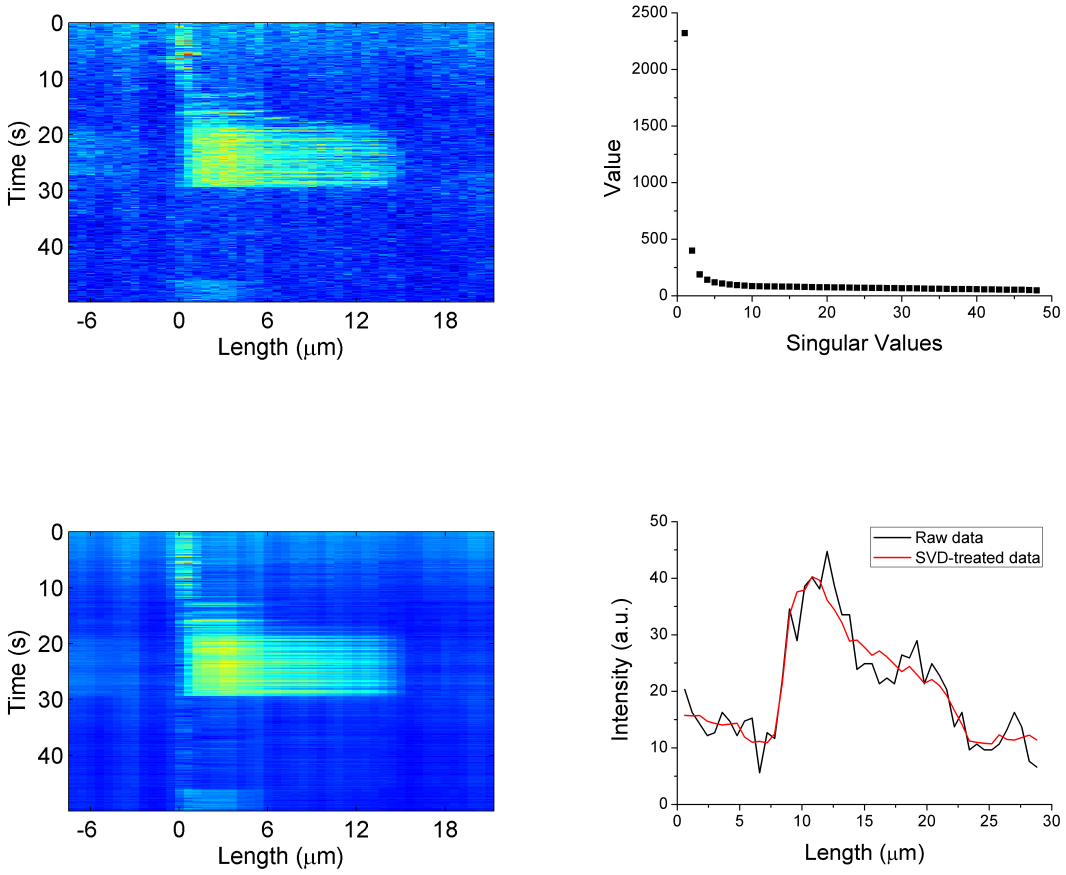

Figure 4.3: SVD analysis of a single kymograph. A typical kymograph obtained from a raw video before and after application of the SVD (top left and bottom left), respectively. The kymograph shows lambda-DNA stretching at 15 s, initiated by a shear rate of 300 s^{-1}, and DNA detachment at 29 s. The singular values calculated from the raw image were plotted (top right). An example stream at frame 200 (time point of 20 s) was plotted from the raw image and after subjection to SVD (bottom right).

4.6 Discussion

Different noise reduction approaches, such as the Laplace transformation, the first derivative, combinations of both and the singular value decomposition, were implemented to improve the resolution of individual, stained lambda-DNA molecules imaged with TIRFM. None of these approaches proved to be good enough to automate the detection and readout of single lambda-DNA molecules from the raw video files for DNA length determination.

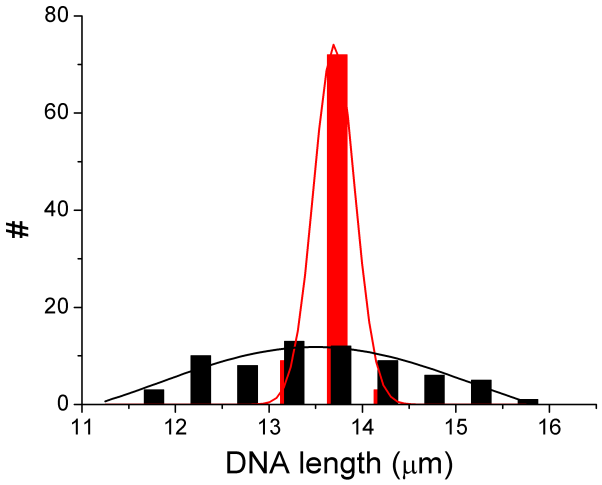

Figure 4.4: Analysis of one kymograph displaying one stretched DNA molecule. Histograms showing the DNA molecule length determined in each frame by sigmoidal fitting to the left and right ends of the DNA molecule. The precision of a Gaussian fit is increased 6-fold following SVD (number of frames analysed: n = 67 and 84 for raw (black) and SVD data (red) yielding DNA molecule lengths of 13.50 ± 1.00 μm vs. 13.68 ± 0.17 μm , respectively). The bin size is 0.5 μm.

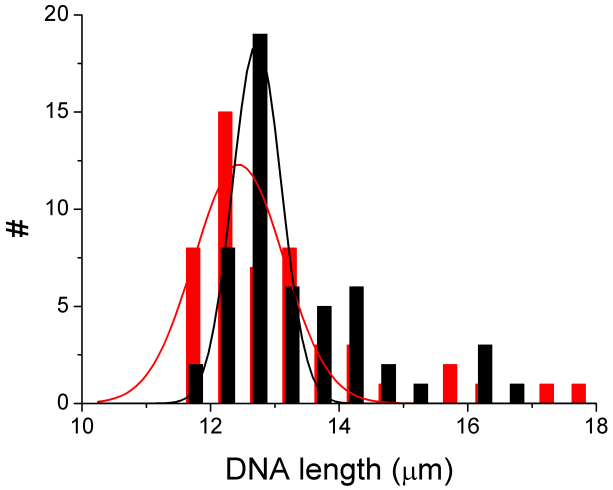

Figure 4.5: Summary of the analysed kymograph images derived from a total of ten TIRF time-lapse movies. The average DNA contour lengths measured in the uncoiled state for n = 53 DNA molecules and n = 50 DNA molecules for raw (black) and SVD treated data (red), respectively, were 12.7 ± 0.7 μm and 12.4 ± 1.2 μm. The bin size is 0.5 μm.

Based on manually selected kymographs which were subjected to SVD and a sigmoidal function fitting routine, the lambda-DNA molecule length was determined for each individual molecule multiple times and then analysed for all kymograph images derived from the raw video files. Fig. 4.4 shows, for an extended lambda-DNA molecule, how SVD improves the accuracy of such length measurements. The gain in precision is about six-fold, as judged from the width of the histogram (13.50 ± 1.00 μm vs. 13.68 ± 0.17 μm, n = 67 and 84 image planes, respectively). Thus, SVD improves the accuracy of single-molecule DNA length measurements without affecting the mean length value determined (values lieing within the range of standard deviation).

The DNA length determination could be still improved by applying higher flow rates in the microfluidic devices which would restrict remaining fluctuations of the DNA tail. Larger objective magnifications would allow a better DNA molecule resolution and, hence, benefit the fitting process.

The population histogram (fig. 4.5), however, shows quite a large distribution of DNA molecule lengths, for both raw and SVD-treated data. This is a result of influences analysed earlier (chapter 3.7), i.e. the actually low shear rate of 300 s^{-1} leading to incomplete DNA molecule stretching and the influence of the staining dye YOYO-1. In addition, it seems that the data obtained were prone to some early probably shear degradation as the determined mean DNA molecule length values were in the range of 12 to 13 μm. According to Bellan *et al.* (2006) and Baumann *et al.* (2000) the DNA contour length should be approximately 16.3 or 16.5 μm, respectively.

One of the aims of this project was to apply these findings and developmental ideas to enzyme kinetic traces on lambda-DNA, as presented in chapter 3. Unfortunately, the only viable way to determine DNA molecule lengths with high precision leads to artifacts in the kymographs. The subjection of these kymographs to SVD introduced step patterns in the DNA unwinding trace because the SVD method searches for rectangular patterns and superimposes these on any structure revealed. Hence, the AddAB- and RecBCD-mediated lambda-DNA unwinding traces had to be analysed manually.

Chapter 5

Conclusion

Bacteroides fragilis and *Escherichia coli* are among the most dominant bacterial species in the gut of human beings and mammals. Under normal circumstances, both the host and the bacteria lead a good relation of symbiosis which does them both well. However, these two bacterial species can also act as opportunistic pathogens (Szabo *et al.*, 1986; Karch *et al.*, 2005; Wexler, 2007) which usually happens outside the mammalian gut. The host immune system then produces reactive oxygen species (ROS) which are directed against the bacteria to kill them (McGlynn & Lloyd, 2002). Homologous recombination systems repair damaged DNA resulting from the ROS to protect the bacteria and maintain their viability. A common side effect of such an infectious struggle is the mammal suffering from diarrhoea which leads to the ejection of the good-natured bacteria (of the same species) in the gut into a low-salt environment where they experience a drastic hypo-osmotic shock. Indeed, the bacteria jumped out of the frying pan into the fire. Fortunately, most species have evolved mechanosensitive channels (Pivetti *et al.*, 2003) to protect themselves against cell lysis due to an extreme rise in osmotic pressure.

Homologous recombination enzymes and mechanosensitive channels which represent two bacterial stress response systems were analysed using biophysical single-molecule and single-cell techniques. Both TIRF microscopy and optical tweezers have proven to be very valuable tools to get insights into the underlying mechanisms of the studied protein complexes at the level of single entities, either molecules or cells.

The homologous recombination enzymes AddAB and RecBCD from the bacterial species *B. fragilis* and *E. coli*, respectively, were studied. While RecBCD is extremely well characterised (Dillingham & Kowalczykowski, 2008), only little was known about the analogous single-motor helicase AddAB which is much

more prevalent in the bacterial world (Cromie, 2009). The important enzyme parameters of DNA unwinding rate and processivity were characterised. TIRF microscopy of fluorescently labelled single stretched lambda-DNA molecules revealed the strikingly high processivity of BfAddAB which is apparently an important requirement for the enzyme to fulfil its biological function. More work, however, is needed to characterise the interaction of the BfAddAB enzyme with its regulating chi site. Mutant enzymes need to be examined as well to get a full and clear understanding of this particular recombination system.

Single-cell studies of hypo-osmotically shocked *E. coli* have provided astonishing insights into the diverse cellular response and have shed light on cell wall and membrane lesions. While the damage to these cellular features varies from cell to cell and differs from tiny lesions to large ruptures, it still remains impossible to elucidate what is really happening on a molecular scale. On the one hand a consistent and generally accepted model for the bacterial cell wall is still missing (Dmitriev *et al.*, 2005; Vollmer, 2008). On the other hand, optical microscopy still provides limitations to our observations as both high temporal and spatial resolution are not simultaneoulsy achievable yet. PALM and STED for example currently work on static samples only (Hell, 2007). Likewise, although dynamic experiments seem to be difficult to perform with AFM and EM approaches, this may be the most promising way to further our insight as no sample staining is required. Alternatively, using the same optical tweezers and microfluidic system described in this thesis, the application of a cell wall and cell membrane stain to hypo-osmotically shocked *E. coli* cells would already provide much more information on the fate of these entities. Using faster CCD cameras which work at the millisecond timescale would also provide clearer insight into the processes happening on the few millisecond time scale during hypo-osmotic shock.

In this thesis, single-molecule *in vitro* experiments and single-cell manipulation were carried out independently. Recently, it has become possible to carry out single-molecule imaging in living cells (Xie *et al.*, 2008). The advantage of these experiments is that an *in vivo* environment better reflects the biological conditions of the mechanism of interest. However, as apparent in chapter 2, working with living cells is experimentally challenging as well as intrinsically complex and difficult in terms of data interpretation. The area of genomics and proteomics (Graves & Haystead, 2002) which analysis these complex molecular circuits may soon feed back valuable information into the area of single-molecule science *in vivo* as well as into many others. Nevertheless, *in vitro* experiments of any kind are still valuable tools to complement cellular assays and to understand isolated biological circuits. To better reflect the situation in the living cell, Ellis (2001) has

suggested to take into account crowding effects which are an important driving force for e.g. protein-protein interactions.

In the area of single-molecule and single-cell science there is a constant need for further refinement of technical equipment and analysis techniques. Especially, scientific instruments need to be both sturdy and sensitive while performing many complex tasks simultaneously that give access to as much information as possible. To accomplish this, many methods still work on the basis of post-acquisition analysis. However, it would be desirable to perform online analysis of acquired data which provides instantaneous insights into the investigated experimental system. Such approaches also allow saving of precious hard-disk space as raw data do not need to be stored anymore (see e.g. Laurens *et al.*, 2009). Method validation is, in many cases, also required to exploit the full power of single-molecule techniques and not to analyse artefacts.

The phenomenon of fast YOYO-1 intercalation into dsDNA is apparently unknown to the research community or has been ignored in the past. Within the framework of using hydrodynamically stretched lambda-DNA to perform protein-DNA interaction studies at the single-molecule level, it has been very useful to further characterise this experimental system and to understand the kinetics of YOYO-1 DNA intercalation to prevent unwanted side effects.

Single-molecule methods rely on very large data sets to provide good statistics of observed parameters. Although we are able to scale up most single-molecule approaches, currently there seems to be a lag behind image and more general data analysis development. Rather than analysing all data by hand and extracting desired parameters in hours of work, attempts were made to automate the analysis of video streams showing stretched molecules of lambda-DNA. Some approaches, like the Kernel transformation and the singular value decomposition, seem to follow the right path. However, the video data are overall too complex to fully automate this analysis. In the first place, many experimental artefacts need to be discriminated, camera noise needs to be optimally reduced, a single-molecule needs to be unambiguously recognised and then analysed in terms of molecule length in each frame (in case of lambda-DNA). More developmental work and more effective algorithms are needed here to keep up with the pace of instrument development.

The application of single-entity methods has proven very useful to understand complex biophysical systems, exemplified in this thesis and in the literature (Joo *et al.*, 2008; Xie *et al.*, 2008). The combined efforts of the single-molecule community, which nowadays includes biologists, physicists and chemists, will further our understanding of such systems and, hence, contribute to solve current funda-

mental problems like cancer and neurodegenerative diseases. The basis for this work, however, will remain in the area of fundamental research.

Appendix A: Hypo-osmotic shock videos

This section provides supplementary video material for chapter 2 which shows the image sequences as a video stream as well as additional videos to gain further insight into the experiment.

All videos in the appendices are .avi files which can be played with common players, e.g. the Windows Media Player and the Quicktime Player. The latter has the advantage to allow scrolling through the videos frame by frame as well as allowing enlargement of the video size.

Video S2-1-Downshock-Loss-from-trap-and-survivor-phase-contrast.avi
The phase-contrast video shows two *E. coli* cells which are optically trapped in a microfluidic device and subjected to a hypo-osmotic shock from minimal medium + 0.5 M NaCl via minimal medium + 0.5 M NaCl + 50 μM H_2O_2 into distilled water. The left cell is lost from the trap indicated by floating away from the trap position and the cell in the right trap apparently survives the hypo-osmotic shock. After a complete shift into the distilled water stream the cell does not change its appearance in the phase-contrast image.

S2-2-Downshock-Unclear-event-vs-loss-from-trap-phase-contrast.avi
Two optically trapped *E. coli* cells are lost simultaneously from the optical trap during a hypo-osmotic shock. Just before the *E. coli* cells float away from the trap position they slightly fade which is an indication for cell lysis. However, due to cell loss the fate of both cells cannot be properly assessed making the experimental outcome unclear.

S2-3-Downshock-Vanishing-cell-phase-contrast.avi

A hypo-osmotically shocked *E. coli* cell which bursts fast and vanishes between two recorded video frames. The initial field of view was about 5 times larger in both dimensions in which no cell remnant was observed.

S2-4-Downshock-Bursting-cell-phase-contrast.avi
Two optically trapped *E. coli* cells which burst sequentually upon hypo-osmotic shock.

S2-5-Downshock-Swelling-cell-phase-contrast.avi
An optically trapped *E. coli* cell which swells first upon hypo-osmotic shock and then suddenly vanishes from the entire field of view as a result of fast bursting. The cell was incubated for 1.5 hr at 37 °C in minimal medium + 0.5 M NaCl which may provoke this artefact which was never observed in one of the cultures without further incubation.

S2-6-Downshock-Leaking-cell-phase-contrast.avi
The optically trapped *E. coli* cell leaks upon hypo-osmotic shock, but the cell ghost remains in the trap.

S2-7-Downshock-Leaking-cell-Ghost-loss-phase-contrast.avi
The optically trapped *E. coli* cell leaks upon hypo-osmotic shock with the cell ghost eventually lost from the trap.

S2-8-Downshock-Bursting-cell-epi-fluorescence.avi
The epi-fluorescence video shows one GFP expressing *E. coli* cell which is subjected to a hypo-osmotic shock from minimal medium + 0.5 M NaCl via minimal medium + 0.5 M NaCl + 50 μM H_2O_2 into distilled water. The *E. coli* cell clearly burst upon hypo-osmotic shock releasing a cloud of GFP. This was a rare event observed only two times.

S2-9-Downshock-GFP-leaking-cell-epi-fluorescence.avi
The GFP expressing *E. coli* cell is subjected to a hypo-osmotic shock and continuously leaks GFP through cell membrane lesions. At a time of 28 s, the imaging mode is shortly changed from epi-fluorescence to phase-contrast which shows that the *E. coli* cell has not changed its appearance in the latter mode which was also the case for all other GFP leaking cells.

S2-10-Downshock-GFP-bleaching-cell-epi-fluorescence.avi

A GFP expressing *E. coli* cell is subjected to control conditions, i.e. kept at minimal medium + 0.5 M NaCl. Continuous epi-fluorescence imaging purely leads to GFP photobleaching which is hardly noticeable on the timescale shown.

Appendix B: AddAB single-molecule lambda-DNA videos and MatLab files

Additional videos

S3-Add-1-TIRF-Fluorescent-1um-beads.avi
Fluorescent microspheres of 1 μm size are floating in a buffer solution and are imaged with TIRF microscopy. The evanescent field only excites fluorescent beads close to the surface which produces the classical blinking effect upon floating towards and away from the glass/buffer interface.

S3-Add-2-DNA-dynamics-objective-TIRF-DNA-un-and-recoiling.avi
A TIRFM video shows uncoiling and recoiling of fluorescently labelled, surface-tethered lambda-DNA molecules in a hydrodynamic flow with a shear rate of 510 s^{-1}.

S3-Add-3-DNA-dynamics-Two-site-tether.avi
A TIRFM video shows the uncoiling and recoiling of a single-site bound fluorescently labelled lambda-DNA molecules in a hydrodynamic flow with a shear rate of 510 s^{-1}. Due to an artefact, the second molecule is attached at both ends and oscillates orthogonally to the DNA molecule extension.

S3-Add-4-DNA-dynamics-Brownian-motion-wo-flow.avi
Brownian dynamics of fluorescently labelled, surface-tethered lambda-DNA molecules without hydrodynamic flow.

S3-Add-5-DNA-dynamics-DNA-loops-in-flow.avi
A TIRFM video shows the uncoiling and recoiling of several fluorescently labelled lambda-DNA molecules in a hydrodynamic flow with a shear rate of 510 s^{-1}. Due to an artefact, some DNA molecules are attached at both molecule ends and at a distance much smaller than the lambda-DNA contour length leading to the formation of dynamic DNA loops in the flow.

S3-Add-6-YOYO-1-intercalation.avi
Continuously stretched lambda-DNA molecules at a shear rate of 510 s^{-1} are subjected to a 20 nM YOYO-1 solution. Dye intercalation into dsDNA and subsequent lengthening of the lambda-DNA molecules can be observed within minutes. The initial staining ratio was 1/200 dye molecules per DNA base pair.

AddAB videos

S3-AddAB-1-AddAB-unwinding.avi
A hydrodynamically stretched lambda-DNA molecule is continuously unwound by a single AddAB enzyme triggered with 1 mM Mg^{2+}-ATP.

S3-AddAB-2-Control.avi
A hydrodynamically stretched lambda-DNA molecule was incubated in the presence of AddAB enzyme. Omission of Mg^{2+}-ATP prevented enzyme-mediated DNA unwinding (control conditions). At the timepoint of 268 s photobleaching leads to a sudden DNA molecule shortening, accompanied by a loss of more than 10,000 bp.

S3-AddAB-3-DNA-dynamics-Attachment-migration-cut-digestion.avi
A hydrodynamically stretched single-site tethered lambda-DNA molecule wiggles in solution. The second DNA end then suddenly sticks to the surface. Thereafter, DNA molecule migration with transient loop formation takes place. Photobleaching produces two short one site-tethered DNA molecules. The smaller DNA molecule is recognised by AddAB which binds and unwinds the DNA under Mg^{2+}-ATP consumption.

RecBCD videos

S3-RecBCD-1-RecBCD-unwinding.avi
Hydrodynamically stretched lambda-DNA molecules are continuously unwound by single RecBCD enzymes triggered with 1 mM Mg^{2+}-ATP.

MatLab programmes

MatLab Picture export routine

The provided .m files can be run with MatLab R2008a to produce kymographs images with labelled time and length axes. The main file from which the routine has to be run is "kinetics.m".

MatLab YOYO-1 intercalation

The provided .m files were used to read out (un)smoothed DNA molecule length data from the kymographs showing YOYO-1 intercalation into lambda-DNA. The main files from which the routines have to be run are "kinetics.m" and "kinetics-smoothing.m".

Appendix C: MatLab and video files for image analysis

Lambda-DNA uncoiling

S4-1-TIRF-parabolic-mirror-Lambda-DNA-uncoiling.avi
A parabolic-mirror TIRFM video shows uncoiling of fluorescently labelled, surface-tethered lambda-DNA molecules in a hydrodynamic flow with a shear rate of 300 s^{-1}. The evanescent field is very shallow, hence the DNA tails fluctuate in and out of the evanescent field showing a characteristic blinking effect.

MatLab programmes

MatLab Kernel-functions and First-derivative

The provided .m files were used to convolve single image frames showing hydrodynamically stretched DNA molecules with Kernel functions and to apply a first-derivative routine. The main file from which the routine has to be run is "test01.m".

MatLab SVD and DNA length determination

The provided .m files were used to treat kymographs showing a hydrodynamically stretched DNA molecule with the singular value decomposition and to extract the DNA molecule length using a sigmoidal function fitting routine. The main file from which the routine has to be run is "test01.m".

Bibliography

[1] H. Akama, M. Kanemaki, M. Yoshimura, T. Tsukihara, T. Kashiwagi, H. Yoneyama, S. I. Narita, A. Nakagawa, and T. Nakae. Crystal structure of the drug discharge outer membrane protein, OprM, of *Pseudomonas aeruginosa*: dual modes of membrane anchoring and occluded cavity end. *J Biol Chem*, 279:52816–52819, 2004.

[2] B. Alberts, A. Johnson, J. Lewis, M. Raff, K. Roberts, and P. Walter. *Molecular Biology of the Cell Fifth Edition*. Garland Science, 2008.

[3] S. K. Amundsen, A. F. Taylor, and G. R. Smith. The RecD subunit of the *Escherichia coli* RecBCD enzyme inhibits RecA loading, homologous recombination, and DNA repair. *Proc Natl Acad Sci U S A*, 97:7399–7404, 2000.

[4] S. K. Amundsen, J. Fero, L. M. Hansen, G. A. Cromie, J. V. Solnick, G. R. Smith, and N. R. Salama. *Helicobacter pylori* AddAB helicase-nuclease and RecA promote recombination-related DNA repair and survival during stomach colonization. *Mol Microbiol*, 69:994–1007, 2008.

[5] D. G. Anderson, J. J. Churchill, and S. C. Kowalczykowski. Chi-activated RecBCD enzyme possesses 5'–>3' nucleolytic activity, but RecBC enzyme does not: evidence suggesting that the alteration induced by chi is not simply ejection of the RecD subunit. *Genes Cells*, 2:117–128, 1997.

[6] D. G. Anderson and S. C. Kowalczykowski. The recombination hot spot chi is a regulatory element that switches the polarity of DNA degradation by the RecBCD enzyme. *Genes Dev*, 11:571–581, 1997.

[7] A. Anishkin and S. Sukharev. Water dynamics and dewetting transitions in the small mechanosensitive channel MscS. *Biophys J*, 86:2883–2895, 2004.

[8] K. Arakawa, R. Uno, Y. Nakayama, and M. Tomita. Validating the significance of genomic properties of chi sites from the distribution of all octamers in *Escherichia coli*. *Gene*, 392:239–246, 2007.

[9] L. Aravind, K. S. Makarova, and E. V. Koonin. Holliday junction resolvases and related nucleases: identification of new families, phyletic distribution and evolutionary trajectories. *Nucleic Acids Res*, 28:3417–3432, 2000.

[10] D. A. Arnold, P. R. Bianco, and S. C. Kowalczykowski. The reduced levels of chi recognition exhibited by the RecBC1004D enzyme reflect its recombination defect *in vivo*. *J Biol Chem*, 273:16476–16486, 1998.

[11] D. A. Arnold and S. C. Kowalczykowski. Facilitated loading of RecA protein is essential to recombination by RecBCD enzyme. *J Biol Chem*, 275:12261–12265, 2000.

[12] M. Arnoldi, M. Fritz, E. Bäuerlein, M. Radmacher, E. Sackmann, and A. Boulbitch. Bacterial turgor pressure can be measured by atomic force microscopy. *Phys Rev E Stat Phys Plasmas Fluids Relat Interdiscip Topics*, 62:1034–1044, 2000.

[13] A. Ashkin, J. M. Dziedzic, J. E. Bjorkholm, and S. Chu. Observation of a single-beam gradient force optical trap for dielectric particles. *Opt Lett*, 11:288–290, 1986.

[14] D. Axelrod. Selective imaging of surface fluorescence with very high aperture microscope objectives. *J Biomed Opt*, 6:6–13, 2001.

[15] D. Axelrod. Total internal reflection fluorescence microscopy in cell biology. *Traffic*, 2:764–774, 2001.

[16] D. Axelrod. Total internal reflection fluorescence microscopy in cell biology. *Methods Enzymol*, 361:1–33, 2003.

[17] N. Q. Balaban, J. Merrin, R. Chait, L. Kowalik, and S. Leibler. Bacterial persistence as a phenotypic switch. *Science*, 305:1622–1625, 2004.

[18] R. B. Bass, P. Strop, M. Barclay, and D. C. Rees. Crystal structure of *Escherichia coli* MscS, a voltage-modulated and mechanosensitive channel. *Science*, 298:1582–1587, 2002.

[19] C. G. Baumann, V. A. Bloomfield, S. B. Smith, C. Bustamante, M. D. Wang, and S. M. Block. Stretching of single collapsed DNA molecules. *Biophys J*, 78:1965–1978, 2000.

[20] M. H. Bayer, W. Keck, and M. E. Bayer. Localization of penicillin-binding protein 1B in *Escherichia coli*: immunoelectron microscopy and immunotransfer studies. *J Bacteriol*, 172:125–135, 1990.

[21] L. M. Bellan, J. D. Cross, E. A. Strychalski, J. Moran-Mirabal, and H. G. Craighead. Individually resolved DNA molecules stretched and embedded in electrospun polymer nanofibers. *Nano Lett*, 6:2526–2530, 2006.

[22] R. J. Bennett and J. L. Keck. Structure and function of RecQ DNA helicases. *Crit Rev Biochem Mol Biol*, 39:79–97, 2004.

[23] A. Bensimon, A. Simon, A. Chiffaudel, V. Croquette, F. Heslot, and D. Bensimon. Alignment and sensitive detection of DNA by a moving interface. *Science*, 265:2096–2098, 1994.

[24] K. Berg-Sorensen and H. Flyvbjerg. Power spectrum analysis for optical tweezers. *Rev Sci Instr*, 75:1–19, 2004.

[25] P. R. Bianco, L. R. Brewer, M. Corzett, R. Balhorn, Y. Yeh, S. C. Kowalczykowski, and R. J. Baskin. Processive translocation and DNA unwinding by individual RecBCD enzyme molecules. *Nature*, 409:374–378, 2001.

[26] P. R. Bianco and S. C. Kowalczykowski. The recombination hotspot chi is recognized by the translocating RecBCD enzyme as the single strand of DNA containing the sequence 5'-gctggtgg-3'. *Proc Natl Acad Sci U S A*, 94:6706–6711, 1997.

[27] P. R. Bianco and S. C. Kowalczykowski. Translocation step size and mechanism of the RecBC DNA helicase. *Nature*, 405:368–372, 2000.

[28] W. B. Bigger. Treatment of staphylococcal infections with penicillin by intermittent sterilization. *Lancet*, 2:497–500, 1944.

[29] S. Blumberg, A. Gajraj, M. W. Pennington, and J.-C. Meiners. Three-dimensional characterization of tethered microspheres by total internal reflection fluorescence microscopy. *Biophys J*, 89:1272–1281, 2005.

[30] D. Boal. *Mechanics of the Cell*. Cambridge University Press, 2002.

[31] U. Bockelmann. Single-molecule manipulation of nucleic acids. *Curr Opin Struct Biol*, 14:368–373, 2004.

[32] P. E. Boehmer and P. T. Emmerson. The RecB subunit of the *Escherichia coli* RecBCD enzyme couples ATP hydrolysis to DNA unwinding. *J Biol Chem*, 267:4981–4987, 1992.

[33] I. R. Booth, M. D. Edwards, S. Black, U. Schumann, and S. Miller. Mechanosensitive channels in bacteria: signs of closure? *Nat Rev Microbiol*, 5:431–440, 2007.

[34] I. R. Booth, M. D. Edwards, and S. Miller. Bacterial ion channels. *Biochemistry*, 42:10045–10053, 2003.

[35] L. R. Brewer and P. R. Bianco. Laminar flow cells for single-molecule studies of DNA-protein interactions. *Nat Methods*, 5:517–525, 2008.

[36] N. A. Busch, T. Kim, and V. A. Bloomfield. Tracer diffusion of proteins in DNA solutions. 2. Green fluorescent protein in crowded DNA solutions. *Macromolecules*, 33:5932–5937, 2000.

[37] H. J. Busscher and H. C. van der Mei. Microbial adhesion in flow displacement systems. *Clin Microbiol Rev*, 19:127–141, 2006.

[38] C. Bustamante, Z. Bryant, and S. B. Smith. Ten years of tension: single-molecule DNA mechanics. *Nature*, 421:423–427, 2003.

[39] C. Bustamante. *In singulo* Biochemistry: When Less Is More. *Annu Rev Biochem*, 77:45–50, 2008.

[40] D. A. Cano, M. G. Pucciarelli, F. García del Portillo, and J. Casadesús. Role of the RecBCD recombination pathway in *Salmonella* virulence. *J Bacteriol*, 184:592–595, 2002.

[41] C. Carlsson, M. Jonsson, and B. Akerman. Double bands in DNA gel electrophoresis caused by bis-intercalating dyes. *Nucleic Acids Res*, 23:2413–2420, 1995.

[42] C. Carlsson, A. Larsson, M. Jonsson, B. Albinsson, and B. Norden. Optical and photophysical properties of the oxazole yellow DNA probes YO and YOYO. *J Phys Chem*, 98:10313-10321, 1994.

[43] G. Chang, R. H. Spencer, A. T. Lee, M. T. Barclay, and D. C. Rees. Structure of the MscL homolog from *Mycobacterium tuberculosis*: a gated mechanosensitive ion channel. *Science*, 282:2220–2226, 1998.

[44] M. K. Cheezum, W. F. Walker, and W. H. Guilford. Quantitative comparison of algorithms for tracking single fluorescent particles. *Biophys J*, 81:2378–2388, 2001.

[45] H. W. Chen, B. Ruan, M. Yu, J. Wang, and D. A. Julin. The RecD subunit of the RecBCD enzyme from *Escherichia coli* is a single-stranded DNA-dependent ATPase. *J Biol Chem*, 272:10072–10079, 1997.

[46] J. J. Churchill and S. C. Kowalczykowski. Identification of the RecA protein-loading domain of RecBCD enzyme. *J Mol Biol*, 297:537–542, 2000.

[47] F. Chédin, S. D. Ehrlich, and S. C. Kowalczykowski. The *Bacillus subtilis* AddAB helicase/nuclease is regulated by its cognate chi sequence *in vitro*. *J Mol Biol*, 298:7–20, 2000.

[48] F. Chédin, N. Handa, M. S. Dillingham, and S. C. Kowalczykowski. The AddAB helicase/nuclease forms a stable complex with its cognate chi sequence during translocation. *J Biol Chem*, 281:18610–18617, 2006.

[49] F. Chédin and S. C. Kowalczykowski. A novel family of regulated helicases/nucleases from gram-positive bacteria: insights into the initiation of DNA recombination. *Mol Microbiol*, 43:823–834, 2002.

[50] O. Cordin, J. Banroques, N. K. Tanner, and P. Linder. The dead-box protein family of RNA helicases. *Gene*, 367:17–37, 2006.

[51] M. M. Cox, M. F. Goodman, K. N. Kreuzer, D. J. Sherratt, S. J. Sandler, and K. J. Marians. The importance of repairing stalled replication forks. *Nature*, 404:37–41, 2000.

[52] M. M. Cox. Motoring along with the bacterial RecA protein. *Nat Rev Mol Cell Biol*, 8:127–138, 2007.

[53] N. Crampton, M. Yokokawa, D. T. F. Dryden, J. M. Edwardson, D. N. Rao, K. Takeyasu, S. H. Yoshimura, and R. M. Henderson. Fast-scan atomic force microscopy reveals that the type III restriction enzyme EcoP15I is capable of DNA translocation and looping. *Proc Natl Acad Sci U S A*, 104:12755–12760, 2007.

[54] G. A. Cromie. Phylogenetic ubiquity and shuffling of the bacterial RecBCD and AddAB recombination complexes. *J Bacteriol*, 191:5076–5084, 2009.

[55] C. Cui, D. O. Smith, and J. Adler. Characterization of mechanosensitive channels in *Escherichia coli* cytoplasmic membrane by whole-cell patch clamp recording. *J Membr Biol*, 144:31–42, 1995.

[56] R. J. Davenport, G. J. Wuite, R. Landick, and C. Bustamante. Single-molecule study of transcriptional pausing and arrest by *E. coli* RNA polymerase. *Science*, 287:2497–2500, 2000.

[57] C. J. Davidson and M. G. Surette. Individuality in bacteria. *Annu Rev Genet*, 42:253–268, 2008.

[58] F. de Fornel. *Evanescent Waves From Newtonian Optics to Atomic Optics*. Springer-Verlag Berlin Heidelberg New York, 2001.

[59] P. Demchick and A. L. Koch. The permeability of the wall fabric of *Escherichia coli* and *Bacillus subtilis*. *J Bacteriol*, 178:768–773, 1996.

[60] M.-N. Dessinges, T. Lionnet, X. G. Xi, D. Bensimon, and V. Croquette. Single-molecule assay reveals strand switching and enhanced processivity of UvrD. *Proc Natl Acad Sci U S A*, 101:6439–6444, 2004.

[61] M. S. Dillingham and S. C. Kowalczykowski. RecBCD enzyme and the repair of double-stranded DNA breaks. *Microbiol Mol Biol Rev*, 72:642–71, 2008.

[62] M. S. Dillingham, M. Spies, and S. C. Kowalczykowski. RecBCD enzyme is a bipolar DNA helicase. *Nature*, 423:893–897, 2003.

[63] M. S. Dillingham, M. R. Webb, and S. C. Kowalczykowski. Bipolar DNA translocation contributes to highly processive DNA unwinding by RecBCD enzyme. *J Biol Chem*, 280:37069–37077, 2005.

[64] D. A. Dixon and S. C. Kowalczykowski. The recombination hotspot chi is a regulatory sequence that acts by attenuating the nuclease activity of the *E. coli* RecBCD enzyme. *Cell*, 73:87–96, 1993.

[65] D. A. Dixon and S. C. Kowalczykowski. Role of the *Escherichia coli* recombination hotspot, chi, in RecABCD-dependent homologous pairing. *J Biol Chem*, 270:16360–16370, 1995.

[66] B. A. Dmitriev, S. Ehlers, and E. T. Rietschel. Layered murein revisited: a fundamentally new concept of bacterial cell wall structure, biogenesis and function. *Med Microbiol Immunol*, 187:173–181, 1999.

[67] B. Dmitriev, F. Toukach, and S. Ehlers. Towards a comprehensive view of the bacterial cell wall. *Trends Microbiol*, 13:569–574, 2005.

[68] B. A. Dmitriev, F. V. Toukach, K.-J. Schaper, O. Holst, E. T. Rietschel, and S. Ehlers. Tertiary structure of bacterial murein: the scaffold model. *J Bacteriol*, 185:3458–3468, 2003.

[69] K. M. Dohoney and J. Gelles. Chi-sequence recognition and DNA translocation by single RecBCD helicase/nuclease molecules. *Nature*, 409:370–374, 2001.

[70] C. C. Dykstra, K. M. Palas, and S. R. Kushner. Purification and characterization of exonuclease V from *Escherichia coli* K-12. *Cold Spring Harb Symp Quant Biol*, 49:463–467, 1984.

[71] M. D. Edwards, I. R. Booth, and S. Miller. Gating the bacterial mechanosensitive channels: MscS a new paradigm? *Curr Opin Microbiol*, 7:163–167, 2004.

[72] M. D. Edwards, Y. Li, S. Kim, S. Miller, W. Bartlett, S. Black, S. Dennison, I. Iscla, P. Blount, J. U. Bowie, and I. R. Booth. Pivotal role of the glycine-rich TM3 helix in gating the MscS mechanosensitive channel. *Nat Struct Mol Biol*, 12:113–119, 2005.

[73] D. C. Eichler and I. R. Lehman. On the role of ATP in phosphodiester bond hydrolysis catalyzed by the RecBC deoxyribonuclease of *Escherichia coli*. *J Biol Chem*, 252:499–503, 1977.

[74] M. El Karoui, D. Ehrlich, and A. Gruss. Identification of the lactococcal exonuclease/recombinase and its modulation by the putative chi sequence. *Proc Natl Acad Sci U S A*, 95:626–631, 1998.

[75] R. J. Ellis. Macromolecular crowding: an important but neglected aspect of the intracellular environment. *Curr Op Struct Biol*, 11:114–119, 2001.

[76] J. P. Erzberger and J. M. Berger. Evolutionary relationships and structural mechanisms of AAA^+ proteins. *Annu Rev Biophys Biomol Struct*, 35:93–114, 2006.

[77] A. Flaus, D. M. A. Martin, G. J. Barton, and T. Owen-Hughes. Identification of multiple distinct Snf2 subfamilies with conserved structural motifs. *Nucleic Acids Res*, 34:2887–2905, 2006.

[78] A. Flaus and T. Owen-Hughes. Mechanisms for ATP-dependent chromatin remodelling: farewell to the tuna-can octamer? *Curr Opin Genet Dev*, 14:165–173, 2004.

[79] S. C. Gill and P. H. von Hippel. Calculation of protein extinction coefficients from amino acid sequence data. *Anal Biochem*, 182:319–326, 1989.

[80] C. A. Glasbey and G. W. Horgan. *Image analysis for the biological sciences*. John Wiley & Sons Ltd, 1995.

[81] B. Glauner, J. V. Höltje, and U. Schwarz. The composition of the murein of *Escherichia coli*. *J Biol Chem*, 263:10088–10095, 1988.

[82] A. E. Gorbalenya and E. V. Koonin. Helicases: amino acid sequence comparisons and structure-function relationships. *Curr Opin Struct Biol*, 3:419–429, 1993.

[83] A. Granéli, C. C. Yeykal, T. K. Prasad, and E. C. Greene. Organized arrays of individual DNA molecules tethered to supported lipid bilayers. *Langmuir*, 22:292–299, 2006.

[84] P. R. Graves, and T. A. J. Haystead. Molecular Biologist's Guide to Proteomics. *Microbiol Mol Biol Rev*, 66:39–63, 2002.

[85] N. Handa, P. R. Bianco, R. J. Baskin, and S. C. Kowalczykowski. Direct visualization of RecBCD movement reveals cotranslocation of the RecD motor after chi recognition. *Mol Cell*, 17:745–750, 2005.

[86] E. Haustein and P. Schwille. Ultrasensitive investigations of biological systems by fluorescence correlation spectroscopy. *Methods*, 29:153–166, 2003.

[87] E. Haustein and P. Schwille. Fluorescence correlation spectroscopy: novel variations of an established technique. *Annu Rev Biophys Biomol Struct*, 36:151–169, 2007.

[88] E. Hecht. *Optik*. Addison-Wesley (Deutschland) GmbH, 1992.

[89] S. W. Hell. Toward fluorescence nanoscopy. *Nat Biotechnol*, 21:1347–1355, 2003.

[90] S. W. Hell. Far-field optical nanoscopy. *Science*, 316:1153–1158, 2007.

[91] R. E. Henkel. *Tests of significance*. Sage Publications - Beverly Hills - London, 1976.

[92] I. D. Hickson, C. N. Robson, K. E. Atkinson, L. Hutton, and P. T. Emmerson. Reconstitution of RecBC DNAse activity from purified *Escherichia coli* RecB and RecC proteins. *J Biol Chem*, 260:1224–1229, 1985.

[93] J. V. Höltje. Growth of the stress-bearing and shape-maintaining murein sacculus of *Escherichia coli*. *Microbiol Mol Biol Rev*, 62:181–203, 1998.

[94] R. Holliday. A mechanism for gene conversion in fungi. *Genet Res Camb*, 5:282–304, 1964.

[95] S. Hormeño and J. R. Arias-Gonzalez. Exploring mechanochemical processes in the cell with optical tweezers. *Biol Cell*, 98:679–695, 2006.

[96] Z. Hou. Adaptive singular value decomposition in wavelet domain for image denoising. *Pattern Recognit*, 36:1747–1763, 2003.

[97] K. C. Huang, R. Mukhopadhyay, B. Wen, Z. Gitai, and N. S. Wingreen. Cell shape and cell-wall organization in Gram-negative bacteria. *Proc Natl Acad Sci U S A*, 105:19282–19287, 2008.

[98] T. V. Ilyina, A. E. Gorbalenya, and E. V. Koonin. Organization and evolution of bacterial and bacteriophage primase-helicase systems. *J Mol Evol*, 34:351–357, 1992.

[99] K. Ishidate, E. S. Creeger, J. Zrike, S. Deb, B. Glauner, T. J. MacAlister, and L. I. Rothfield. Isolation of differentiated membrane domains from *Escherichia coli* and *Salmonella typhimurium*, including a fraction containing attachment sites between the inner and outer membranes and the murein skeleton of the cell envelope. *J Biol Chem*, 261:428–443, 1986.

[100] F. Johansen and J. P. Jacobsen. 1H NMR studies of the bis-intercalation of a homodimeric oxazole yellow dye in DNA oligonucleotides. *J Biomol Struct Dyn*, 16:205–222, 1998.

[101] C. Joo, H. Balci, Y. Ishitsuka, C. Buranachai, and T. Ha. Advances in Single-Molecule Fluorescence Methods for Molecular Biology *Annu Rev Biochem*, 77:18.1–26, 2008.

[102] H. Karch, P. I. Tarr, and M. Bielaszewska. Enterohaemorrhagic *Escherichia coli* in human medicine. *Int J Med Microbiol*, 295:405–418, 2005.

[103] G. W. C. Kaye and T. H. Laby. *Tables of Physical and Chemical Constants*. Longman Scientific & Technical, 1986.

[104] K. Kitano, E. Tuomanen, and A. Tomasz. Transglycosylase and endopeptidase participate in the degradation of murein during autolysis of *Escherichia coli*. *J Bacteriol*, 167:759–765, 1986.

[105] J. Kooistra, B. J. Haijema, and G. Venema. The *Bacillus subtilis* AddAB genes are fully functional in *Escherichia coli*. *Mol Microbiol*, 7:915–923, 1993.

[106] F. Korangy and D. A. Julin. Kinetics and processivity of ATP hydrolysis and DNA unwinding by the RecBC enzyme from *Escherichia coli*. *Biochemistry*, 32:4873–4880, 1993.

[107] S. Korolev, J. Hsieh, G. H. Gauss, T. M. Lohman, and G. Waksman. Major domain swiveling revealed by the crystal structures of complexes of *E. coli* Rep helicase bound to single-stranded DNA and ADP. *Cell*, 90:635–647, 1997.

[108] V. Koronakis, A. Sharff, E. Koronakis, B. Luisi, and C. Hughes. Crystal structure of the bacterial membrane protein TolC central to multidrug efflux and protein export. *Nature*, 405:914–919, 2000.

[109] C. Kung. A possible unifying principle for mechanosensation. *Nature*, 436:647–654, 2005.

[110] S. T. Lam, M. M. Stahl, K. D. McMilin, and F. W. Stahl. Rec-mediated recombinational hot spot activity in bacteriophage lambda. II. A mutation which causes hot spot activity. *Genetics*, 77:425–433, 1974.

[111] A. Larsson, C. Carlsson, M. Jonsson, and B. Albinsson. Characterization of the binding of the fluorescent dyes YO and YOYO to DNA by polarized light spectroscopy. *J Am Chem Soc*, 116:8459-8465, 1994.

[112] N. Laurens, S. R. W. Bellamy, A. F. Harms, Y. S. Kovacheva, S. E. Halford, and G. J. L. Wuite. Dissecting protein-induced DNA looping dynamics in real time. *Nucl Acids Res*, 37:5454–5464, 2009.

[113] J. Lederberg and T. Iino. Phase variation in *Salmonella*. *Genetics*, 41:743–757, 1956.

[114] M. Leduc, C. Frehel, and J. van Heijenoort. Correlation between degradation and ultrastructure of peptidoglycan during autolysis of *Escherichia coli*. *J Bacteriol*, 161:627–635, 1985.

[115] N. Levina, S. Tötemeyer, N. R. Stokes, P. Louis, M. A. Jones, and I. R. Booth. Protection of *Escherichia coli* cells against extreme turgor by activation of MscS and MscL mechanosensitive channels: identification of genes required for MscS activity. *EMBO J*, 18:1730–1737, 1999.

[116] Y. Li, P. C. Moe, S. Chandrasekaran, I. R. Booth, and P. Blount. Ionic regulation of MscK, a mechanosensitive channel from *Escherichia coli*. *EMBO J*, 21:5323–5330, 2002.

[117] S. Liu, G. Bokinsky, N. G. Walter, and X. Zhuang. Dissecting the multistep reaction pathway of an RNA enzyme by single-molecule kinetic "fingerprinting". *Proc Natl Acad Sci U S A*, 104:12634–12639, 2007.

[118] Z. Liu, C. S. Gandhi, and D. C. Rees. Structure of a tetrameric MscL in an expanded intermediate state. *Nature*, 461:120–124, 2009.

[119] J. C. Locke and M. B. Elowitz. Using movies to analyse gene circuit dynamics in single cells. *Nat Rev Microbiol*, 7:383–392, 2009.

[120] S. W. Magennis, E. M. Graham, and A. C. Jones. Quantitative spatial mapping of mixing in microfluidic systems. *Angew Chem Int Ed Engl*, 44:6512–6516, 2005.

[121] P. Mangeol, D. Côte, T. Bizebard, O. Legrand, and U. Bockelmann. Probing DNA and RNA single molecules with a double optical tweezer. *Eur Phys J E Soft Matter*, 19:311–317, 2006.

[122] B. Martinac, M. Buechner, A. H. Delcour, J. Adler, and C. Kung. Pressure-sensitive ion channel in *Escherichia coli*. *Proc Natl Acad Sci U S A*, 84:2297–2301, 1987.

[123] C. Masterson, P. E. Boehmer, F. McDonald, S. Chaudhuri, I. D. Hickson, and P. T. Emmerson. Reconstitution of the activities of the RecBCD holoenzyme of *Escherichia coli* from the purified subunits. *J Biol Chem*, 267:13564–13572, 1992.

[124] P. McGlynn and R. G. Lloyd. Recombinational repair and restart of damaged replication forks. *Nat Rev Mol Cell Biol*, 3:859–870, 2002.

[125] S. O. Meroueh, K. Z. Bencze, D. Hesek, M. Lee, J. F. Fisher, T. L. Stemmler, and S. Mobashery. Three-dimensional structure of the bacterial cell wall peptidoglycan. *Proc Natl Acad Sci U S A*, 103:4404–4409, 2006.

[126] B. Michel, H. Boubakri, Z. Baharoglu, M. LeMasson, and R. Lestini. Recombination proteins and rescue of arrested replication forks. *DNA Repair (Amst)*, 6:967–980, 2007.

[127] S. Miller, W. Bartlett, S. Chandrasekaran, S. Simpson, M. Edwards, and I. R. Booth. Domain organization of the MscS mechanosensitive channel of *Escherichia coli*. *EMBO J*, 22:36–46, 2003.

[128] K. Morimatsu and S. C. Kowalczykowski. RecFOR proteins load RecA protein onto gapped DNA to accelerate DNA strand exchange: a universal step of recombinational repair. *Mol Cell*, 11:1337–1347, 2003.

[129] B. Nanduri, A. K. Byrd, R. L. Eoff, A. J. Tackett, and K. D. Raney. Pre-steady-state DNA unwinding by bacteriophage T4 Dda helicase reveals a monomeric molecular motor. *Proc Natl Acad Sci U S A*, 99:14722–14727, 2002.

[130] F. C. Neidhardt, R. Curtiss, J. L. Ingraham, E. C. C. Lin, K. B. Low, B. Magasanik, W. S. Reznikoff, M. Riley, M. Schaechter, and H. E. Um-

barger. *Escherichia coli and Salmonella: Cellular and Molecular Biology*. American Society for Microbiology, 1996.

[131] P. Nelson. *Biological Physics*. W. H. Freeman and Company, 2004.

[132] K. C. Neuman and S. M. Block. Optical trapping. *Rev Sci Instrum*, 75:2787–2809, 2004.

[133] K. C. Neuman, E. H. Chadd, G. F. Liou, K. Bergman, and S. M. Block. Characterization of Photodamage to *Escherichia coli* in Optical Traps. *Biophys J*, 77:2856–2863, 1999.

[134] A. Novick and M. Weiner. Enzyme induction as an all-or-none phenomenon. *Proc Natl Acad Sci U S A*, 43:553–566, 1957.

[135] T. Nyström. A bacterial kind of aging. *PLoS Genet*, 3:e224, 2007.

[136] D. J. Pappin, P. Hojrup, and A. J. Bleasby. Rapid identification of proteins by peptide-mass fingerprinting. *Curr Biol*, 3:327–332, 1993.

[137] S. Patrick. *Molecular Medical Microbiology*, chapter Bacteroides, pages 1921–1948. Academic Press, London, 2002.

[138] T. T. Perkins, D. E. Smith, R. G. Larson, and S. Chu. Stretching of a single tethered polymer in a uniform flow. *Science*, 268:83–87, 1995.

[139] T. T. Perkins, H.-W. Li, R. V. Dalal, J. Gelles, and S. M. Block. Forward and reverse motion of single RecBCD molecules on DNA. *Biophys J*, 86:1640–1648, 2004.

[140] E. Perozo, D. M. Cortes, P. Sompornpisut, A. Kloda, and B. Martinac. Open channel structure of MscL and the gating mechanism of mechanosensitive channels. *Nature*, 418:942–948, 2002.

[141] E. Perozo, A. Kloda, D. M. Cortes, and B. Martinac. Physical principles underlying the transduction of bilayer deformation forces during mechanosensitive channel gating. *Nat Struct Biol*, 9:696–703, 2002.

[142] C. D. Pivetti, M.-R. Yen, S. Miller, W. Busch, Y.-H. Tseng, I. R. Booth, and M. H. Saier. Two families of mechanosensitive channel proteins. *Microbiol Mol Biol Rev*, 67:66–85, 2003.

[143] J. Postgate. *The outer reaches of life*. Cambridge University Press, 1994.

[144] A. M. Powl, J. M. East, and A. G. Lee. Lipid-protein interactions studied by introduction of a tryptophan residue: the mechanosensitive channel MscL. *Biochemistry*, 42:14306–14317, 2003.

[145] M. E. Pullman, H. S. Penefsky, A. Datta, and E. Racker. Partial resolution of the enzymes catalyzing oxidative phosphorylation. I. purification and properties of soluble dinitrophenol-stimulated adenosine triphosphatase. *J Biol Chem*, 235:3322–3329, 1960.

[146] A. Quiberoni, I. Biswas, M. El Karoui, L. Rezaïki, P. Tailliez, and A. Gruss. *In vivo* evidence for two active nuclease motifs in the double-strand break repair enzyme RexAB of *Lactococcus lactis*. *J Bacteriol*, 183:4071–4078, 2001.

[147] E. P. C. Rocha, E. Cornet, and B. Michel. Comparative and evolutionary analysis of the bacterial homologous recombination systems. *PLoS Genet*, 1:e15, 2005.

[148] L. J. Roman and S. C. Kowalczykowski. Characterization of the adenosinetriphosphatase activity of the *Escherichia coli* RecBCD enzyme: relationship of ATP hydrolysis to the unwinding of duplex DNA. *Biochemistry*, 28:2873–2881, 1989.

[149] L. J. Roman and S. C. Kowalczykowski. Characterization of the helicase activity of the *Escherichia coli* RecBCD enzyme using a novel helicase assay. *Biochemistry*, 28:2863–2873, 1989.

[150] L. J. Roman and S. C. Kowalczykowski. Formation of heteroduplex DNA promoted by the combined activities of *Escherichia coli* RecA and RecBCD proteins. *J Biol Chem*, 264:18340–18348, 1989.

[151] J. Rosamond, K. M. Telander, and S. Linn. Modulation of the action of the RecBC enzyme of *Escherichia coli* K-12 by Ca^{2+}. *J Biol Chem*, 254:8646–8652, 1979.

[152] D. W. Sambrook, and J. Russell. *Molecular Cloning - A Laboratory Manual*. Cold Spring Harbor Laboratory Press, New York, 2001.

[153] D. A. Schafer, J. Gelles, M. P. Sheetz, and R. Landick. Transcription by single molecules of RNA polymerase observed by light microscopy. *Nature*, 352:444–448, 1991.

[154] K. Scheffzek, M. R. Ahmadian, W. Kabsch, L. Wiesmüller, A. Lautwein, F. Schmitz, and A. Wittinghofer. The Ras-RasGap complex: structural

basis for GTPase activation and its loss in oncogenic Ras mutants. *Science*, 277:333–338, 1997.

[155] M. Schleyer, R. Schmid, and E. P. Bakker. Transient, specific and extremely rapid release of osmolytes from growing cells of *Escherichia coli* K-12 exposed to hypoosmotic shock. *Arch Microbiol*, 160:424–431, 1993.

[156] W. Schumann. *Dynamics of the Bacterial Chromosome*. Wiley-VCH Verlag GmbH & Co. KGaA, Weinheim, 2006.

[157] R. Seidel, J. G. P. Bloom, J. van Noort, C. F. Dutta, N. H. Dekker, K. Firman, M. D. Szczelkun, and C. Dekker. Dynamics of initiation, termination and reinitiation of DNA translocation by the motor protein EcoR124I. *EMBO J*, 24:4188–4197, 2005.

[158] M. R. Singleton, M. S. Dillingham, M. Gaudier, S. C. Kowalczykowski, and D. B. Wigley. Crystal structure of RecBCD enzyme reveals a machine for processing DNA breaks. *Nature*, 432:187–193, 2004.

[159] M. R. Singleton, M. S. Dillingham, and D. B. Wigley. Structure and mechanism of helicases and nucleic acid translocases. *Annu Rev Biochem*, 76:23–50, 2007.

[160] J. M. Skordalakes, and E. Berger. Structure of the Rho transcription terminator: Mechanism of mRNA recognition and helicase loading. *Cell*, 114:135–146, 2003.

[161] G. R. Smith. Homologous recombination near and far from DNA breaks: alternative roles and contrasting views. *Annu Rev Genet*, 35:243–274, 2001.

[162] G. R. Smith, S. M. Kunes, D. W. Schultz, A. Taylor, and K. L. Triman. Structure of Chi hotspots of generalized recombination. *Cell*, 24:429–436, 1981.

[163] H. P. Spielmann, D. E. Wemmer, and J. P. Jacobsen. Solution structure of a DNA complex with the fluorescent bis-intercalator TOTO determined by NMR spectroscopy. *Biochemistry*, 34:8542–8553, 1995.

[164] M. Spies, P. R. Bianco, M. S. Dillingham, N. Handa, R. J. Baskin, and S. C. Kowalczykowski. A molecular throttle: the recombination hotspot chi controls DNA translocation by the RecBCD helicase. *Cell*, 114:647–654, 2003.

[165] M. Spies, M. S. Dillingham, and S. C. Kowalczykowski. Translocation by the RecB motor is an absolute requirement for chi-recognition and RecA protein loading by RecBCD enzyme. *J Biol Chem*, 280:37078–37087, 2005.

[166] J. L. Spudich and D. E. Koshland. Non-genetic individuality: chance in the single cell. *Nature*, 262:467–471, 1976.

[167] G. C. Stewart. Taking shape: control of bacterial cell wall biosynthesis. *Mol Microbiol*, 57:1177–1181, 2005.

[168] F. W. Stahl, J. M. Crasemann, and M. M. Stahl. Rec-mediated recombinational hot spot activity in bacteriophage lambda. III. Chi mutations are site-mutations stimulating rec-mediated recombination. *J Mol Biol*, 94:203–212, 1974.

[169] N. R. Stokes, H. D. Murray, C. Subramaniam, R. L. Gourse, P. Louis, W. Bartlett, S. Miller, and I. R. Booth. A role for mechanosensitive channels in survival of stationary phase: regulation of channel expression by RpoS. *Proc Natl Acad Sci U S A*, 100:15959–15964, 2003.

[170] H. S. Subramanya, L. E. Bird, J. A. Brannigan, and D. B. Wigley. Crystal structure of a DExx box DNA helicase. *Nature*, 384:379–383, 1996.

[171] S. Sukharev, M. Betanzos, C. S. Chiang, and H. R. Guy. The gating mechanism of the large mechanosensitive channel MscL. *Nature*, 409:720–724, 2001.

[172] S. I. Sukharev, P. Blount, B. Martinac, F. R. Blattner, and C. Kung. A large-conductance mechanosensitive channel in *E. coli* encoded by *mscl* alone. *Nature*, 368:265–268, 1994.

[173] J.-Z. Sun, D. A. Julin, and J.-S. Hu. The nuclease domain of the *Escherichia coli* RecBCD enzyme catalyzes degradation of linear and circular single-stranded and double-stranded DNA. *Biochemistry*, 45:131–140, 2006.

[174] R. A. Szabo, E. C. D. Todd, and A. Jean. Method to isolate *Escherichia coli* O157:H7 from food. *J Food Prot*, 49:768–772, 1986.

[175] N. Tamura, S. Murakami, Y. Oyama, M. Ishiguro, and A. Yamaguchi. Direct interaction of multidrug efflux transporter AcrB and outer membrane channel TolC detected via site-directed disulfide cross-linking. *Biochemistry*, 44:11115–11121, 2005.

[176] A. F. Taylor and G. R. Smith. Monomeric RecBCD enzyme binds and unwinds DNA. *J Biol Chem*, 270:24451–24458, 1995.

[177] A. F. Taylor and G. R. Smith. RecBCD enzyme is a DNA helicase with fast and slow motors of opposite polarity. *Nature*, 423:889–893, 2003.

[178] E. Theofanidou, T. J. Su, J. Arlt, D. T. F. Dryden, W. J. Hossack, J. Crain, and W. C. K. Poon. Study of DNA deformation under flow using optical tweezers. *Proceedings of the SPIE*, 5514:712–723, 2004.

[179] R. E. Thompson, D. R. Larson, and W. W. Webb. Precise nanometer localization analysis for individual fluorescent probes. *Biophys J*, 82:2775–2783, 2002.

[180] A. Touhami, M. H. Jericho, and T. J. Beveridge. Atomic force microscopy of cell growth and division in *Staphylococcus aureus*. *J Bacteriol*, 186:3286–3295, 2004.

[181] R. Y. Tsien. The green fluorescent protein. *Annu Rev Biochem*, 67:509–544, 1998.

[182] B. van den Broek, F. Vanzi, D. Normanno, F. S. Pavone, and G. J. L. Wuite. Real-time observation of DNA looping dynamics of type IIE restriction enzymes NaeI and NarI. *Nucleic Acids Res*, 34:167–174, 2006.

[183] J. van Mameren, M. Modesti, R. Kanaar, C. Wyman, E. J. G. Peterman, and G. J. L. Wuite. Counting Rad51 proteins disassembling from nucleoprotein filaments under tension. *Nature*, 457:745–748, 2009.

[184] M. van 't Hoff, M. Reuter, D. T. F. Dryden, and M. Oheim. A parabolic variable-angle TIRF reflector for multiplexed high-precision imaging of single lambda-DNA molecules. *Phys Chem Chem Phys*, 11:7713–7720, 2009.

[185] A. Varma and K. D. Young. FtsZ collaborates with penicillin binding proteins to generate bacterial cell shape in *Escherichia coli*. *J Bacteriol*, 186:6768–6774, 2004.

[186] N. Vazquez-Laslop, H. Lee, R. Hu, and A. A. Neyfakh. Molecular sieve mechanism of selective release of cytoplasmic proteins by osmotically shocked *Escherichia coli*. *J Bacteriol*, 183:2399–2404, 2001.

[187] M.-L. Visnapuu, T. Fazio, S. Wind, and E. C. Greene. Parallel arrays of geometric nanowells for assembling curtains of DNA with controlled lateral dispersion. *Langmuir*, 24:11293–11299, 2008.

[188] W. Vollmer, D. Blanot, and M. A. de Pedro. Peptidoglycan structure and architecture. *FEMS Microbiol Rev*, 32:149–167, 2008.

[189] W. Vollmer and J.-V. Höltje. The architecture of the murein (peptidoglycan) in gram-negative bacteria: vertical scaffold or horizontal layer(s)? *J Bacteriol*, 186:5978–5987, 2004.

[190] J. E. Walker, M. Saraste, M. J. Runswick, and N. J. Gay. Distantly related sequences in the alpha- and beta-subunits of ATP synthase, myosin, kinases and other ATP-requiring enzymes and a common nucleotide binding fold. *EMBO J*, 1:945–951, 1982.

[191] J. Wang, R. Chen, and D. A. Julin. A single nuclease active site of the *Escherichia coli* RecBCD enzyme catalyzes single-stranded DNA degradation in both directions. *J Biol Chem*, 275:507–513, 2000.

[192] W. Wang, S. S. Black, M. D. Edwards, S. Miller, E. L. Morrison, W. Bartlett, C. Dong, J. H. Naismith, and I. R. Booth. The structure of an open form of an *E. coli* mechanosensitive channel at 3.45 Å resolution. *Science*, 321:1179–1183, 2008.

[193] Website *E. coli* statistics
http://gchelpdesk.ualberta.ca/CCDB/cgi-bin/STAT-NEW.cgi

[194] Website Molecular Genetics, Leiden Institute of Chemistry
http://molgen.lic.leidenuniv.nl/research/chromatin

[195] H. M. Wexler. *Bacteroides*: the Good, the Bad, and the Nitty-Gritty. *Clin Microbiol Rev*, 20:593–621, 2007.

[196] P. Wiggins and R. Phillips. Membrane-protein interactions in mechanosensitive channels. *Biophys J*, 88:880–902, 2005.

[197] R. Winter and F. Noll. *Methoden der Biophysikalischen Chemie*. B.G. Teubner Stuttgart, 1998.

[198] C. J. Wong, A. L. Lucius, and T. M. Lohman. Energetics of DNA end binding by *E. coli* RecBC and RecBCD helicases indicate loop formation in the 3'-single-stranded DNA tail. *J Mol Biol*, 352:765–782, 2005.

[199] A. K. Wozniak, G. F. Schröder, H. Grubmüller, C. A. M. Seidel, and F. Oesterhelt. Single-molecule FRET measures bends and kinks in DNA. *Proc Natl Acad Sci U S A*, 105:18337–18342, 2008.

[200] G. D. Wright, J. Arlt, W. C. K. Poon, and N. D. Read. Optical tweezer micromanipulation of filamentous fungi. *Fungal Genet Biol*, 44:1–13, 2007.

[201] X. S. Xie, P. J. Choi, G.-W. Li, N. K. Lee, and G. Lia. Single-molecule approach to molecular biology in living bacterial cells. *Annu Rev Biophys*, 37:417–444, 2008.

[202] J. Ye, A. R. Osborne, M. Groll, and T. A. Rapoport. RecA-like motor ATPases–lessons from structures. *Biochim Biophys Acta*, 1659:1–18, 2004.

[203] J. T. P. Yeeles, R. Cammack, and M. S. Dillingham. An iron-sulfur cluster is essential for the binding of broken DNA by AddAB-type helicase-nucleases. *J Biol Chem*, 284:7746–7755, 2009.

[204] J. T. P. Yeeles and M. S. Dillingham. A dual-nuclease mechanism for DNA break processing by AddAB-type helicase-nucleases. *J Mol Biol*, 371:66–78, 2007.

[205] A. Yildiz, J. N. Forkey, S. A. McKinney, T. Ha, Y. E. Goldman, and P. R. Selvin. Myosin V walks hand-over-hand: single fluorophore imaging with 1.5-nm localization. *Science*, 300:2061–2065, 2003.

[206] K. D. Young. Bacterial shape. *Mol Microbiol*, 49:571–580, 2003.

[207] X. Yu, M. J. Jezewska, W. Bujalowski, and E. H. Egelman. The hexameric *E. coli* DnaB helicase can exist in different quaternary states. *J Mol Biol*, 259:7–14, 1996.

Publications

M. van 't Hoff*, **M. Reuter***, D. T. F. Dryden, and M. Oheim. A parabolic variable-angle TIRF reflector for multiplexed high-precision imaging of single lambda-DNA molecules. *Phys Chem Chem Phys*, 11:7713-7720, 2009, * shared first-authorship.

M. Reuter, F. Parry, D. T. F. Dryden, and G. W. Blakely. Single molecule imaging of *Bacteroides fragilis* AddAB reveals the highly processive translocation of a single motor helicase. *Nucl Acids Res* (accepted).